AD_____

Award Number: DAMD17-97-1-7261

TITLE: Non-Invasive Determination of Breast Cancer Oxygen Tension by F-19 NMR and Breast Cancer Physiology in Response to Radiotherapy

PRINCIPAL INVESTIGATOR: Yulin Song

CONTRACTING ORGANIZATION: The University of Texas Southwestern Medical Center at Dallas
Dallas, Texas 75390-9105

REPORT DATE: August 2001

TYPE OF REPORT: Final

PREPARED FOR: U.S. Army Medical Research and Materiel Command
Fort Detrick, Maryland 21702-5012

DISTRIBUTION STATEMENT: Approved for Public Release;
Distribution Unlimited

The views, opinions and/or findings contained in this report are those of the author(s) and should not be construed as an official Department of the Army position, policy or decision unless so designated by other documentation.

20020903 061

# REPORT DOCUMENTATION PAGE

Form Approved
OMB No. 074-0188

Public reporting burden for this collection of information is estimated to average 1 hour per response, including the time for reviewing instructions, searching existing data sources, gathering and maintaining the data needed, and completing and reviewing this collection of information. Send comments regarding this burden estimate or any other aspect of this collection of information, including suggestions for reducing this burden to Washington Headquarters Services, Directorate for Information Operations and Reports, 1215 Jefferson Davis Highway, Suite 1204, Arlington, VA 22202-4302, and to the Office of Management and Budget, Paperwork Reduction Project (0704-0188), Washington, DC 20503

| 1. AGENCY USE ONLY (Leave blank) | 2. REPORT DATE | 3. REPORT TYPE AND DATES COVERED |
|---|---|---|
| | August 2001 | Final (1 Aug 97 - 31 Jul 01) |

**4. TITLE AND SUBTITLE**
Non-Invasive Determination of Breast Cancer Oxygen Tension by F-19 NMR and Breast Cancer Physiology in Response to Radiotherapy

**5. FUNDING NUMBERS**
DAMD17-97-1-7261

**6. AUTHOR(S)**
Yulin Song

**7. PERFORMING ORGANIZATION NAME(S) AND ADDRESS(ES)**
The University of Texas Southwestern Medical Center at Dallas
Dallas, Texas 75390-9105

E-Mail: song1058@hotmail.com

**8. PERFORMING ORGANIZATION REPORT NUMBER**

**9. SPONSORING / MONITORING AGENCY NAME(S) AND ADDRESS(ES)**
U.S. Army Medical Research and Materiel Command
Fort Detrick, Maryland 21702-5012

**10. SPONSORING / MONITORING AGENCY REPORT NUMBER**

**11. SUPPLEMENTARY NOTES**

**12a. DISTRIBUTION / AVAILABILITY STATEMENT**
Approved for Public Release; Distribution Unlimited

**12b. DISTRIBUTION CODE**

**13. ABSTRACT** *(Maximum 200 Words)*

The goals of this **Predoctoral Traineeship** were two-fold: 1) To provide me with the solid and extensive training and valuable experience in a modern NMR laboratory for a career as a clinical medical physicist and a breast cancer research scientist; 2) To develop and investigate a non-invasive technique of measuring oxygen tension in breast cancer based on $^{19}F$ MRI of hexafluorobenzene(HFB). For the past three years, I have learned tumor biology, tumor histology, tumor modeling, surgical techniques for implanting tumors, electronic techniques of designing, constructing, and testing MRI RF coils, MRI data acquisitions, Computer programming, digital signal and image processing, near-infrared spectroscopy (NIRS), and operation of advanced medical systems and instruments. In addition, I designed and constructed a double-tuned ($^{19}F$-$^{1}H$) birdcage resonator and a switchable slotted tube resonator. I wrote several computer programs for acquiring and processing MRI and NIRS data. I developed a mathematical model for describing tumor hemodynamics following physiological perturbations, and a second mathematical model for computing tumor oxygen consumption following KCl-induced cardiac arrest using NIRS. I found that the HFB signal intensity decays exponentially with a typical biological half-life ranging from $T_{1/2}$ = 700 to 1200 minutes. The global and regional clearance and redistribution of HFB within the tumors did not interfere with $^{19}F$ MRI oximetry. The local response to respiratory challenge depended strongly on initial baseline $pO_2$ in breast tumor NF13762, with voxels of high baseline $pO_2$ showing significant changes in $pO_2$, while voxels of low baseline $pO_2$ showed small changes. Irradiation delayed tumor growth and caused changes in tumor oxygenation.

**14. SUBJECT TERMS**
Breast Cancer, Hexafluorobenzene (HFB), Perfluorocarbon (PFC), $^{19}F$ NMR, Echo Planar Imaging (EPI), Near-Infrared Spectroscopy (NIRS) $pO_2$, $sO_2$, Hemoglobin.

**15. NUMBER OF PAGES**
200

**16. PRICE CODE**

| 17. SECURITY CLASSIFICATION OF REPORT | 18. SECURITY CLASSIFICATION OF THIS PAGE | 19. SECURITY CLASSIFICATION OF ABSTRACT | 20. LIMITATION OF ABSTRACT |
|---|---|---|---|
| Unclassified | Unclassified | Unclassified | Unlimited |

# TABLE OF CONTENTS

**Front Cover** ..... 1

**Report Documentation Page (Standard Form 298)** ..... 2

**Table of Contents** ..... 3

1. **Introduction** ..... 4

2. **Training Accomplishments** ..... 4

3. **Research Accomplishments** ..... 5

   1) Background Information ..... 5

   2) Tumor Transplantation and Handling, Tumor Volume Doubling Time (VDT), and Tumor Histology ..... 8

      Tumor Model ..... 9

      Tumor Transplantation and Handling ..... 9

      Tumor Growth and Mathematical Model for Computing *VDT* ..... 9

      Tumor Histology ..... 12

   3) Design and Construction of MRI RF Resonators ..... 13

      Double-Tuned ($^{1}H$-$^{19}F$) Birdcage Resonator ..... 14

      Slotted Tube Resonator ..... 21

   4) Assessment of Hexafluorobenzene (HFB) Distribution ..... 26

      Animal Preparation ..... 26

      $^{1}H$ Magnetic Resonance Imaging ..... 27

      $^{19}F$ MRI and Assessment of HFB Distribution ..... 27

      Determination of HFB Redistribution and Clearance ..... 28

   5) Software Development ..... 30

      A Computer Program to Assess the Goodness of T1 Relaxation Curve Fit ..... 30

      A Computer Program to Compute HFB Clearance Rate ..... 32

      A Computer Program to Process $pO_2$ Data ..... 32

      A Computer Program to Process NIRS Data ..... 33

6) Investigation of Tumor Oyxgenation during Untreated Growth .....34
Investigation of Tumor Tissue $pO_2$ .....34
Investigation of Tumor Vascular $\Delta[HbO_2]$ or $sO_2$ and $\Delta[Hb]_{Total}$ .....53
Investigation of Tumor Physiology in Response to Irradiation .....86
7) Dissertation .....95
4. **Key Research Accomplishments** .....96
5. **Reportable Outcomes** .....99
6. **Conclusions** .....102
7. **References** .....103
8. **Appendices** .....111

# 1. INTRODUCTION

The fundamental goals of this **Predoctoral Traineeship** were three-fold: 1) to provide me with an opportunity to continue to learn and apply the state of the art NMR technology and radiotherapy techniques to cancer diagnosis and treatment; 2) to provide me with a solid and extensive training, and valuable experience in a modern NMR laboratory for a career as a clinical medical physicist and a breast cancer research scientist; and 3) to develop and investigate a non-invasive technique of measuring oxygen tension ($pO_2$) in breast cancers in an animal model based on $^{19}F$ MRI of hexafluorobenzene (HFB), now called the **FREDOM** (**F**luorocarbon **R**elaxometry using **E**cho planar imaging for **D**ynamic **O**xygen **M**apping). In this report, I will summarize the highlights of my past three-year's training and research as originally proposed in my **Predoctoral Traineeship** application.

# 2. TRAINING ACCOMPLISHMENTS

For the past three years, under the guidance of my mentor, Dr. Ralph P. Mason, I have gone through a rigorous training in tumor biology, tumor histology, tumor modeling, tumor implantation and transplantation, radiation biology, MRI physics, MRI RF coil design, construction, and testing, MRI data acquisitions, computer programming, digital signal and image processing, near-infrared spectroscopy (**NIRS**), experimental design, and data analysis. I have learned how to use many advanced medical systems and instruments. As an important part of my doctoral curriculum training and research, I needed to use an Omega CSI 4.7 T MR system with actively shielded gradients (Acustar$^{TM}$, Bruker Instruments, Inc., Fremont, CA, USA). This system, based on a 40-cm diameter bore horizontal magnet, is located in the Rogers Magnetic Resonance Center of the University of Texas Southwestern Medical Center at Dallas, which is an NIH Biotechnology Resource Facility. I had immediate access to the system and other resources in the center, and, on average, I used the system three days per week in the past for either experiments or data processing and programming. Now I can operate the magnet independently for both imaging and spectroscopy experiments. To meet our particular experimental needs, I modified and wrote several data acquisition and post-processing programs. These include an NMR-shell script program for computing the biological half-life of hexafluorobenzene (**HFB**) in rat breast tumors, an NMR-shell script program for displaying the T1 relaxation curve of individual voxels of MR EPI images, a C and NMR-shell script program for acquiring BOLD and Gd-DTPA data, a C program for converting MRI image files among different platforms, a Visual Basic program for processing MRI EPI data, and a LabView program for processing near-infrared spectroscopy (**NIRS**) data. In addition, I have also learned how to use electronic

instruments commonly seen in modern RF labs, including a sophisticated HP Frequency Analyzer, and how to operate center lathes and milling machines frequently encountered in the machine shops of radiology and radiation oncology departments. These are the necessary skills required for a professional medical physicist and biomedical engineer. With these skills, I designed, constructed, and tested a double-tuned ($^{19}$F-$^{1}$H) birdcage resonator and a switchable slotted tube resonator. Both phantom testing and *in vivo* imaging experiments indicated that the two resonators worked well. In addition, I have been working on a new type of RF coils, which combines a traditional RF coil with NIRS. These coils will allow simultaneous measurement of tumor tissue $pO_2$ by $^{19}$F MRI, tumor vascular oxyhemoglobin concentration [$HbO_2$], and total hemoglobin concentration $[Hb]_{Total}$ by NIRS. This is a challenging task and successful completion of these RF coils would be significant in tumor oximetry. Another goal of this **Predoctoral Traineeship** was to investigate breast tumor physiology in response to therapeutic interventions. This required the use of rat mammary adenocarcinoma 13762NF. Implanting this type of tumor in female Fisher 344 rats in a pedicle model was a complicated and lengthy surgical procedure. Now I have learned the techniques and can do the surgery without any difficulties. I have also learned the techniques of blood gas analysis using fiber optic pulse oximeter and the operation of automated microelectrode systems. Besides comprehensive hands-on training, I developed a mathematical model for describing tumor hemodynamics following physiological perturbations, and a second mathematical model for computing tumor oxygen consumption following KCl-induced cardiac arrest using NIRS.

# 3. RESEARCH ACCOMPLISHMENTS

## 1) Background Information

Solid tumors develop regions of hypoxia during their growth due to an imbalance between the rate of tumor cell proliferation and the proliferation and branching of the blood vessels [**1-3**], leading to diffusion-limited or chronic hypoxia. However, tumor hypoxia can also occur due to another important reason, the deficient oxygen-carrying capacity of the blood, *i.e.*, low blood hemoglobin concentration, as observed in the case of anemic cancer patients [**4-6**]. Substantial clinical evidence has indicated that it is the hypoxia that is responsible for the failure of radiotherapy [**7-10**], some forms of chemotherapy [**11**, **12**], and photodynamic therapy [**13**]. Moreover, considerable clinical studies have also shown that tumor hypoxia plays a key role for increased expression of many genes that relate to tumor angiogenesis and growth, including vascular endothelial growth factor (**VEGF**), platelet-derived growth factor (**PDGF**), and p53 [**14**, **15**], and low oxygenation levels in tumors correlate with a higher metastatic rate [**16-18**]. Although the mechanism for the latter effect has not been fully understood, some studies have suggested that it could be caused by increased DNA mutation rate and overreplication

under the hypoxic condition **[19-21]**. In addition, a number of clinical trials have found that patient survival, measured either as tumor regression or as local control, depends largely on tumor oxygenation [**10, 16, 22, 23**].

Recently, the use of erythropoietin treatment and blood transfusion has gained increasing attention and popularity in tumor therapy community [**24**, **25**] because many clinical studies have shown that there is a relationship between hemoglobin concentrations and therapeutic outcome [**26**, **27**]. Results of several other clinical trials have indicated that higher hemoglobin concentrations correlate with improved local tumor control and a higher overall survival rate [**28**, **29**], suggesting that hemoglobin concentration could be an independent prognostic factor in tumor therapy. However, the exact mechanism how hemoglobin concentrations affect tumor therapy and radiotherapy in particular is still being debated [**30**]. Available experimental and clinical data seem to support the hypothesis that low hemoglobin concentrations impair oxygen-transporting capacity of blood and eventually lead to tumor hypoxia. In view of the important role of hemoglobin in tumor therapy, it is necessary to have a means to measure and manipulate hemoglobin levels in tumor.

The critical effects of oxygenation on tumor therapy, angiogenesis, metastasis, and prognosis have stimulated the development of novel tumor oximetry techniques. Over the past several decades, substantial progress has been made in developing techniques for measuring tumor tissue oxygen tension ($pO_2$) and hypoxia. These include microelectrodes [**31**, **32**], ESR/EPR [**33**, **34**], the comet assay [**35**], phosphorescence quenching imaging [**36**], nitroimidazole binding assays [**37**], paired survival assay [**37**] and NMR [**38-40**]. However, none of these has been recognized generally as a perfect noninvasive method. Electrodes are highly invasive and only sample a limited region. ESR has two major drawbacks compared with NMR: lack of tissue penetration at very high frequencies (GHz) and the inability to obtain functional information at multiple locations (mapping). $^{31}$P NMR is perhaps the most attractive indicator of tumor oxygenation since it is entirely non-invasive with observation of endogenous metabolites. However, it is relatively insensitive, sampling a large volume, and metabolic hypoxia may occur at an oxygen tension that considerably exceeds radiobiological hypoxia [**41**]. Recent studies have indicated that tissue contrast changes in $^{1}$H MRI on the basis of the blood oxygen level dependent (**BOLD**) method provide a qualitative approach to tissue oxygenation. However, changes in blood flow affect the signal intensity and therefore, complicate the interpretation of results [**42, 43**]. $^{19}$F NMR techniques can provide a direct measurement of $pO_2$ based on the principle that the $^{19}$F NMR spin-lattice relaxation rates R1 (=1/T1) of perfluorocarbon (**PFC**) emulsions are linearly proportional to oxygen tension [**44-46**]. $^{19}$F has 100% natural isotopic abundance and an 83% sensitivity relative to $^{1}$H. $^{19}$F occurs in exceedingly low concentrations in biological systems (as the fluoride ion), thus, there is essentially no background noise to interfere with *in vivo* studies. In

addition, $^{19}F$ NMR techniques have the potential advantages of being non-invasive, repeatable, and able to produce local tumor $pO_2$ maps with high spatial resolution.

Tumor oxyhemoglobin concentration [$HbO_2$] or $sO_2$ is another important indicator of tumor oxygenation. However, for many years, very little progress has been made in developing techniques to measure it. One promising technique is near-infrared spectroscopy (**NIRS**). The NIRS tumor oximetry is based on the fact that there exists a substantial absorption difference of light in NIR region (700 ~ 900 nm) between deoxyhemoglobin [Hb] and oxyhemoglogin [$HbO_2$], while absorption of light by other macromolecules and water is insignificant. Based on light modulation mechanisms, NIRS techniques can be classified as: continuous wave (**CW**) light spectroscopy in DC format, amplitude-modulated laser light spectroscopy in frequency domain, and pulsed-laser light spectroscopy in time domain. Using NIRS techniques, *in vivo* measurements of $sO_2$ have been carried out in a wide variety of biological systems such as exercised muscles [**47-49**] and brain [**50-52**]. However, so far, very limited studies have been done in *in vivo* measurements of tumor $sO_2$. Among the published studies, NIRS has been used to evaluate the effects of anesthetics on vascular $sO_2$ in RIF-1 tumors [**53**] and in 9L gliosarcoma [**54**], and to assess the effects of hypoxia, hyperoxia, and asphyxia on BA1112 rhabdomyosarcoma [**55**]. Recently, Mariya *et. al.* [**56**] has published their data on monitoring tumor oxygenation status during fractionated irradiation in two murine tumor cell lines using NIR reflection spectroscopy. NIRS is completely non-invasive, inexpensive, portable, and amenable to real-time measurements. It can be used to measure tumor vascular hemoglobin oxygen saturation $sO_2$, hemoglobin concentration [Hb], and tumor blood flow, and to monitor tumor transient response to therapeutic interventions. However, because of inhomogeneous nature and limited dimension of tumors, classical diffusion theory does not hold. Absolute quantification of tumor oxygenation based on photon diffusion approximation approach still remains a challenging issue. An alternative approach is to modify Beer-Lambert's law and use the measured transmitted light amplitude to compute the trends in the changing absorption coefficients and, thus, changes in [$HbO_2$] or $sO_2$ and $[Hb]_{Total}$.

We have surveyed the relative sensitivity of several PFCs and found that hexafluorobenzene (**HFB**) offers exceptional sensitivity to changes in $pO_2$ with relatively little response to temperature. HFB has a single resonance, providing optimal signal-to-noise ratio (**SNR**). I have applied the $^{19}F$ MRI of HFB technique to investigate dynamic changes in $pO_2$ in tumors in response to respiratory challenges and the feasibility of mapping the clearance rate of HFB. In addition, I have also investigated hemodynamic changes in [$HbO_2$] and $[Hb]_{Total}$ in tumors in response to therapeutic interventions using a newly developed NIRS system.

## 2) Tumor Transplantation and Handling, Tumor Volume Doubling Time (VDT), and Tumor Histology

**Tumor Model**

Murine mammary adenocarcinomas 13762NF [**57**] were used in this study. The 13762NF is a subline of mammary adenocarcinoma 13762. This tumor model was chosen because it demonstrates substantially different therapeutic sensitivity and metastatic characteristics from other tumor types. The 13762NF is less differentiated. It is inhibited by estrogen in young female rats and stimulated in adult female rats. It metastasizes to regional lymph nodes, and lung, and occasionally to liver, but not to brain. It is highly responsive to alkylating agents and platinum chemotherapeutic agents.

**Tumor Transplantation and Handling**

Our lab has successfully developed a tumor transplantation model, the pedicle model [**58**]. Murine mammary adenocarcinomas 13762NF were implanted in skin pedicles on the forebacks of adult female Fischer 344 rats (~250 g). To identify them, each tumor was assigned a unique code. The surgical procedure for creating a pedicle tumor model is as follows. A flap of depilated skin was raised from the body of the rat and held in position with a non-traumatic curved bull-dog clip. A 3-cm incision was made through the skin using the curved edge of the clip as a guide. Wound clips were used to joint the edges of the skin, producing a tube resembling a suitcase handle. Animals were housed separately after the surgery and during the entire course of experiments. Two weeks later, the clips were removed and the distal end of the pedicle severed. A piece of fresh tumor tissue (~ 2× 2 × 2 $mm^3$) from the fourth generation of mammary adenocarcinomas 13762NF was implanted in the lumen and cut closed with a wound clip.

One of the major advantages of the pedicle model is that it is basically isolated from the body proper and perfectly suited for *in vivo* NIRS and MRI studies, therapy, and manipulation. In addition, the pedicle model allows accurate measurement of tumor size. It has been shown to have no significant difference from the traditional subcutaneous site in the thigh in terms of growth [**58**].

**Tumor Growth and Mathematical Model for Computing *VDT***

After tumors were implanted, they first entered a two-week silent period of undetected growth and then an accelerating period in which most tumors grew exponentially. Some, though they may not appear to grow exponentially over their entire life spans, did show exponential growth over short periods of time. The time for the tumors to grow to a predetermined size spanned a wide range. In some cases, the silent periods lasted more than three weeks. Once the implanted tumor tissue grew into a detectable tumor, tumor's three orthogonal dimensions were measured at least once every two days with a caliper. Depending on tumor growth rate, tumors were measured daily in some cases to improve the goodness of curve fit when computing volume doubling time (**VDT**). Prior to the measurements, the rats were anesthetized with 50μl ketamine hydrochloride (100 mg/ml) and the tumors' hair was cut with a pair of surgical scissors to

improve the accuracy of the measurements. Using an ellipsoidal approximation, tumor volume was determined using formula

$$V = (\frac{4\pi}{3}) \cdot (\frac{a}{2}) \cdot (\frac{b}{2}) \cdot (\frac{c}{2}) = (\frac{\pi}{6}) \cdot a \cdot b \cdot c \qquad (1)$$

where $a$, $b$, and $c$ were the diameters along the three major orthogonal axes of the tumor. A very important proliferative feature of the solid tumors is their volume doubling time (*VDT*) (day), a kinetic parameter closely related to the underlying mathematical growth model.

Historically, a growing tumor is modeled as a deterministic dynamic system mathematically described by ordinary differential equations. The central concept of a dynamic system is the trajectory. In the case of tumor growth, the trajectory is the growth curve that describes the change in tumor size as a function of time from the start of proliferation of initial tumor cells. The tumor size can be expressed as dimensions or volume or mass or cellularity, depending on personal choice. For tumor modeling, these quantities are interchangeably used, because they are linearly proportional to each other for solid tumors. Unfortunately, most of these tumor growth models have been seldom validated against experimental tumor growth curves, either because of the relative scarcity of high quality tumor growth data [**59**]. Limited accurately measured tumor data revealed that growth curves for some human tumors are very close to exponential function [**60**], yielding a constant volume doubling time. However, other studies indicated that many human tumors also show irregular or decelerating growth, giving a progressively longer volume doubling time [**60**]. Such curves can be fitted with a variety of mathematical models, but the most prominent one is the Gompertz model [**61**]. However, the empirical Gompertz model lacks a truly fundamental biological explanation.

In an attempt to obtain an analytical expression for computing the tumor volume doubling time, I used a first order, autonomous differential equation to model the tumor growth

$$\frac{dV}{dt} = \lambda V, \qquad \lambda > 0 \qquad (2)$$

where $\lambda$ is the tumor growth rate constant. The model is based on the fundamental biological argument that tumor growth results from exponential cell proliferation. If, for example, each healthy tumor cell divides to produce two proliferative daughters, then the growth of the tumor cell population is: 1, 2, 4, 8, .... $2^n$, an exponential function, *i.e.*, the population size will increase exponentially with time. This model describes unrestricted

tumor growth as the time goes to infinity, a phenomenon not supported by experimental data. However, for a reasonable period of growth, it gives excellent description of tumor growth curves. Most importantly, we can derive an analytical expression for computing the tumor volume doubling time from this model.

The solution of Equation (2) is an exponential function: $V = V_0 \cdot \exp(\lambda t)$ or $V = V_0 \cdot \exp(t/\tau)$, where $V_0 (cm^3)$ is the initial tumor volume at time $t$ = 0 (day) and $\tau$ (day) is the time constant of the exponential growth curve. A very important property of exponential tumor growth is that the tumor volume doubling time (*VDT*) is a constant. Thus, when time increases by one *VDT*, the tumor volume will be doubled. Mathematically, this is written as

$$2V = V_0 \cdot \exp(\frac{t + VDT}{\tau}) \tag{3}$$

Dividing Equation (3) by $V = V_0 \cdot \exp(t/\tau)$ gives

$$\frac{2V}{V} = \frac{V_0 \cdot \exp(\frac{t + VDT}{\tau})}{V_0 \cdot \exp(\frac{t}{\tau})} \quad \Rightarrow \quad 2 = \exp(\frac{VDT}{\tau}) \tag{4}$$

Taking natural log on both sides of Equation (4) gives an equation for computing *VDT*

$$VDT = \tau \ln 2 \tag{5}$$

where $\tau$ is obtained by fitting the experimental tumor data to $V = V_0 \cdot \exp(t/\tau)$.

**Figure 1** shows the growth curve of a representative mammary adenocarcinoma 13762NF. This particular tumor had a "silent interval" of about 10 days. When its growth was detected, the tumor volume increased exponentially with time ($R$ = 0.954) over a fairly long period of time as seen in **Figure 1**, indicating that the assumption for the exponential growth model was correct. The volume doubling time (*VDT*) as determined by Equation (5) was approximately 5.2 days. It is important to point out that, first of all, the long silent phase of undetected growth was not included in the plot. If it were to be included, the entire curve would shift 10 days to the right and the shape of the exponential part of the growth curve would not changed at all. This would not, in any way, affect the result of *VDT* computation as the volume doubling time is a kinetic parameter used to describe the accelerating phase or, in most cases, the exponential phase of a tumor growth. Secondly, in measuring the tumor dimensions, especially when

tumors were small, the skin thickness was subtracted from the measured dimensions. Last, the *VDT*s were computed solely based on the data obtained from intact tumors. During their late growth stage, some tumors might bleed due to a variety of reasons. When this happened, the data gathered after this point were not included in the final computation of *VDT*s.

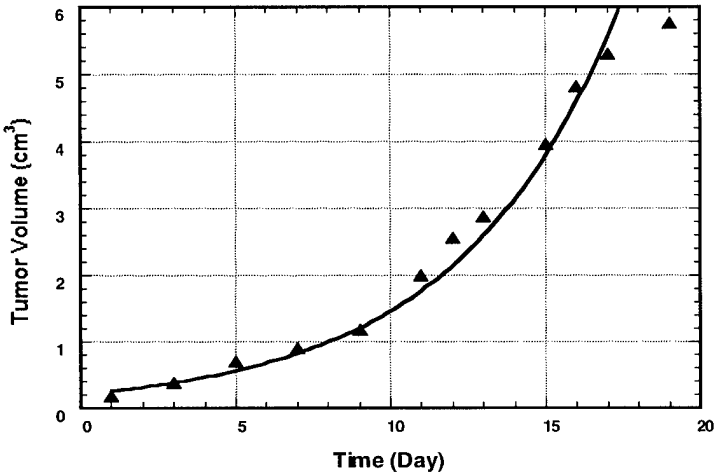


**Figure 1.** Tumor volume of a representative 13762NF breast tumor as a function of time after implantation. The tumor volume was computed using an ellipsoidal model: $V = (\pi/6)abc$. An excellent curve fit ($R = 0.954$) was obtained using an exponential growth model.

**Table 1.** A summary of tumor volume doubling time for a group of six 13762NF breast tumors.

| Tumor No. | *VDT* (Day) |
|---|---|
| 1 | 3.2 |
| 2 | 4.0 |
| 3 | 3.3 |
| 4 | 3.6 |
| 5 | 5.2 |
| 6 | 4.4 |
| **Mean *VDT* (Day)** | **3.95 ±0.76** |

## Tumor Histology

Conventional tumor histology was performed to gather information regarding tumor size, gross morphology, presence and extension of tumor necrosis, histological type and grade. Randomly chosen tumors were sacrificed by tail injection of a lethal dose of KCl. Immediately following the death of the rats, the tumors were excised and fixed in

10% neutral buffered formalin. The tumors were subsequently processed through graded ethanols and xylene, and embedded in paraffin. After embedding, sections were cut at 5μm thickness and routine hematoxylin and eosin (H&E) staining performed according to established protocols. Selected central and peripheral regions of the stained histological sections were photomicrographed using brightfield optics with a magnification of ten. Figure 2 shows histological sections of a representative 13762NF breast tumor.

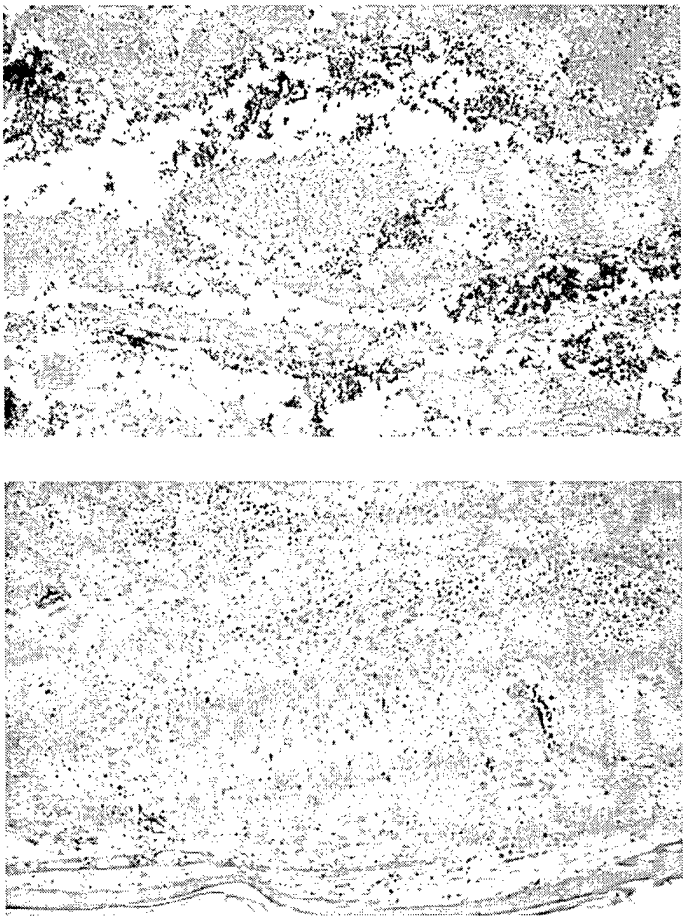

**Figure 2.** Histological sections of a representative 13762NF breast tumor: central (top) and peripheral (bottom) regions of the tumor.

## 3) Design and Construction of MRI RF Resonators

This project involved $^{19}F$ and $^{1}H$ MR imaging with living rats in a single experiment, so it was highly desirable to be able to change the resonant frequency without retuning the resonator and disturbing the animal. The desired imaging and spectroscopy resonator for our purposes would be the one that provides the highest

possible signal-to-noise ratio (**SNR**), a good filling factor, a high $Q$ factor, minimum resistance losses, and a highly homogeneous $\boldsymbol{B}_1$ field. To address these issues, I designed, constructed, and tested two RF resonators, one being a double-tuned birdcage resonator ($^1$H/$^{19}$F) and another one a swithable slotted tube resonator.

## Double-Tuned ($^1$H-$^{19}$F) Birdcage Resonator

A birdcage resonator consists of a set of $N$ (2, 4, 8, 16, etc.) copper wires or sheets arranged axially on the surface of a plastic cylinder and connected by high quality RF capacitors at each end. In this configuration, the effective current density in the wires or sheets varies in proportion to $cos(\phi)$, where $\phi$ is the azimuthal angle in cylindrical coordinates [**62**], and there exist several possible modes of resonance, two of which have the desired sinusoidal dependence of current on $\phi$ [**63**].

- **Design Theory**

Assuming perfectly conducting copper sheets, Figure 3 shows part of the simplified circuit model of a birdcage resonator with 16 identical legs (copper sheets), where $L_i$ is the self inductance of the $i$th copper sheet and $C_i$ is the capacitor connected between the $i$th and the $(i+1)$th copper sheet. The self inductance of the short copper sheet used to connect the capacitors at the ends is neglected. This is based on the fact that the electric current in the resonator is longitudinal (along the copper sheet) and maximal at the ends of the resonator.

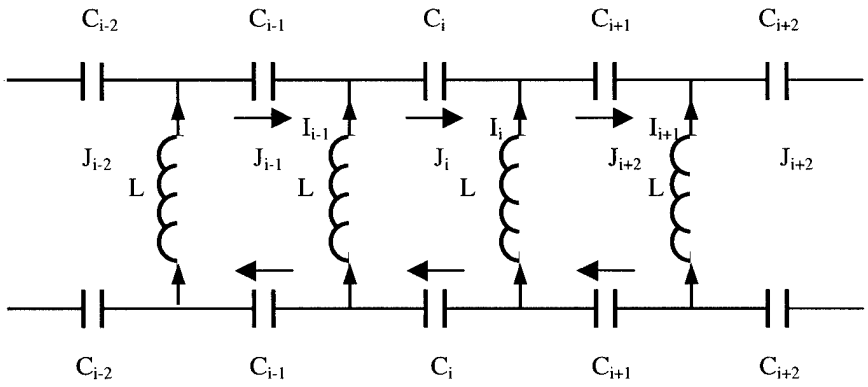


**Figure 3.** Part of the equivalent circuit for the high-pass double-tuned whole body birdcage resonator.

By applying Kirchhoff's Law to the $i$th loop made up of $i$th and $(i+1)$th copper sheets and $i$th capacitor $C_i$ and using the complex number notation for AC current and impedance, we can get a linear system of equations:

$$\sum_k i\omega M_{i,k} I_k - \sum_k i\omega M_{i+1,k} I_k - \frac{2i}{\omega C_i} J_i = 0 \qquad (6)$$

where $M_{i,k}$ is the mutual inductance between the $i$th and $k$th copper sheets, $J_i$ is the current in the $i$th capacitor, $I_k$ is the current in the $k$th copper sheet, $i$ is the imaginary number, and the summation is carried out over all possible values of index $k$ from 0 to $N - 1$.

There are many ways of solving Equation (6), either analytically or numerically. The solution will represent the various resonant modes of operation of the resonator. This circuit model is a simplified one and does not take into account the complications that exist in any real implementation, such as the self-inductance of the capacitors and the inductance of the end rings. Nevertheless, the general form of the model is not altered by these factors, and the qualitative description is still valid.

- **Computer Simulation**

Instead of solving the above-described complex equation, I simulated this circuit model on a PC computer using P-Spice [**64**]. The desired resonant frequencies are 188.22 MHz for $^{19}$F and 200.16 MHz for $^{1}$H in a 4.7 T magnet. The inductance produced by the end rings was neglected in this simulation circuit, since it only accounts for ~ 5% of the total inductance. However, the circuit model is adequate for analyzing the essential frequency characteristics of the resonator. The first step in simulating this problem was to estimate the inductance of the copper sheets, which is given by [**63**].

$$L = 2h[\ \ln (2h/b) + 1/2\ ] \qquad (7)$$

where $L$ is the inductance in nanoHenries, $h$ is the height in centimeters, and $b$ is the width in centimeters. The copper sheets have a height of 16.5 cm and a width of 1.0 cm, with a thickness of ~ 0.2 mm. The calculated value of the inductance based on Equation (7) was 113 nH.

The second step was to substitute this value into the simulation circuit, apply an AC current source to the circuit, vary the value of each of the 32 capacitors, and observe the amplitudes of output voltages and resonant frequencies of the circuit until two sharp resonant peaks (188.22 MHz for $^{19}$F and 200.16 MHz for $^{1}$H in a 4.7 T magnet) with the maximum output voltages were achieved. The capacitance values for the end ring capacitors obtained from the P-Spice simulation are tabulated in Table 1. Theoretically speaking, all the capacitance values should be equal for a single-tuned resonator and close to each other for a double-tuned resonator in order to generate a homogeneous $\boldsymbol{B}_1$ field. The circuit model presented here is a simplified one. Therefore, the capacitance values obtained are not quite close to each other. The simulation study indicates that C10,

C26, C11, C27, C12, and C28 are relatively insensitive to $^{19}F$ resonant frequency; thus, they could be connected to the $^{1}H$ tuning circuit. I chose to place the tuning circuit in parallel to C10 since this placement provides both the best tuning for $^{1}H$ mode and also stabilizes the $^{19}F$ mode.

**Table 1** Capacitance values determined by P-Spice simulation (unit: pF)

| C1 | C2 | C3 | C4 | C5 | C6 | C7 | C8 |
|---|---|---|---|---|---|---|---|
| 40 | 130 | 130 | 130 | 120 | 115 | 108 | 115 |
| **C9** | **C10** | **C11** | **C12** | **C13** | **C14** | **C15** | **C16** |
| 42 | 159 | 185 | 120 | 120 | 102 | 90 | 90 |
| **C17** | **C18** | **C19** | **C20** | **C21** | **C22** | **C23** | **C24** |
| 40 | 130 | 130 | 130 | 120 | 115 | 108 | 106 |
| **C25** | **C26** | **C27** | **C28** | **C29** | **C30** | **C31** | **C32** |
| 42 | 159 | 185 | 120 | 120 | 102 | 90 | 90 |

Fine tuning of $^{19}F$ mode is achieved by connecting another capacitor CF19T in parallel with C6. When $^{19}F$ tuning capacitor CF19T varies from 0 pF to 2000 pF, $^{19}F$ resonant peak varies from (188.224 $MH_z$, 14.727 V) to (184.871 $MH_z$, 16.606 V) while $^{1}H$ resonant peak changes only from (200.435 $MH_z$, 13.905 V) to (200.535 MHz, 13.602 V), which is a clear indication that each mode is independently tuned.

- **Construction**

A 16-leg high-pass double-tuned birdcage resonator was constructed according to the design principles and the simulation results described above. The resonator is tunable to both 188.2 $MH_z$ and 200.1 $MH_z$ for operation at $^{19}F$ and $^{1}H$ frequencies on a 4.7 T magnet. The cylindrical resonator body is 24.60 cm in length and has an outer diameter of 24.00 cm. The outer structure of the resonator is made of a 5 mm thick plexiglass cylinder, which provides mechanical support and structural stability for the resonator. A 0.2 mm thick copper sheet shield, connected to the ground, is mounted on the inner wall of the outer plexiglass cylinder.

The critical part of the resonator is its inner structure. The inner structure, made from a 5 mm thick plexiglass cylinder, has an outer diameter of 10.50 cm. On the inner wall of the plexiglass cylinder are mounted directly 16 copper sheets (legs) with 1.5 mm gaps and 32 capacitors. The size of the uniform region of $\boldsymbol{B}_1$ magnetic field generated by the resonator is directly related to the number of legs. The more numerous the legs, the more uniform the $\boldsymbol{B}_1$ magnetic field in the radial direction. I chose to build a birdcage resonator with sixteen legs because the $\boldsymbol{B}_1$ magnetic field generated should, in principle,

be uniform enough for my applications and should produce strong NMR signal. The legs are made from 0.1 mm thick copper foil. Each of the sixteen legs is 16.5 cm in length, 1.0 cm in width in the central part and 1.5 cm in width at the two ends (Figure 4).

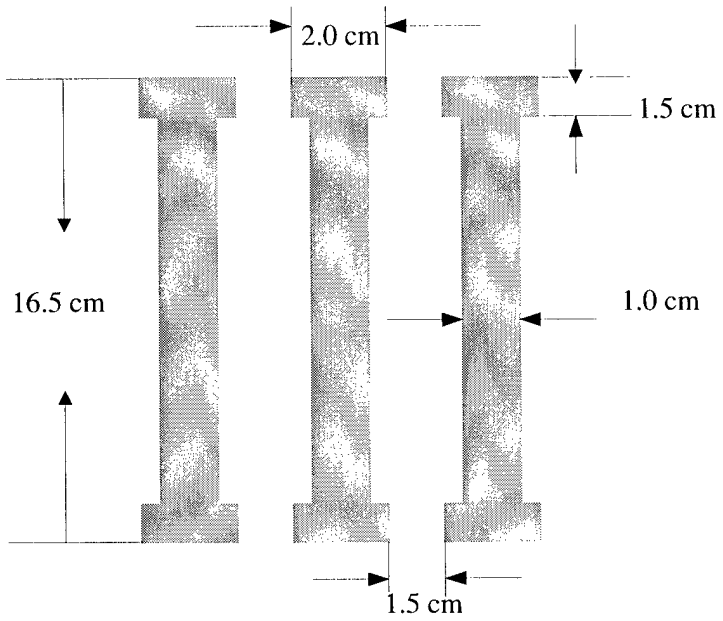


**Figure 4.** Geometry of the legs (copper sheets).

The structure of the two end rings, *i.e.*, the two circular bands at the ends of the resonator, consisted of capacitors and was made identical to achieve electrical balance so that the loading effects of the sample could be reduced. The resonator is double-tuned, and is driven between equivalent points on the two rings halfway between two adjacent parallel legs. The resonator was tuned by individually adjusting the CF19T and CH1T at each of the resonant frequencies. The capacitively coupled tuning loops were placed between legs 11 and 13 and legs 19 and 21. These loops were connected by standard coaxial cables to the external tuning capacitors CF19T and CH1T that allowed each resonant mode to be independently tuned. Special care was taken to ensure that there was little tuning interaction between the two resonant frequencies as possible. The resonator was matched capacitively through a variable capacitor $C_{match.}$

- **Bench Testing**

The laboratory bench testing was carried out using a frequency analyzer (HP8752A). To test the resonator's performance, it was essential to have a set of standard samples that simulated the type of *in vivo* samples used in the magnet. Two NMR

phantoms were prepared for this purpose, which roughly had the same loading effects (lowering $Q$ and shifting resonant frequencies) as a male adult rat (~ 250 g). A 444 ml phantom was made of an NMR compatible plastic bottle filled with a solution of saline and trifluoroacetic acid (TFA, 5% v/v). A smaller 250 ml phantom, also made of an NMR compatible plastic bottle, was filled with a solution of TFA (5% V/V) and $CuSO_4$ (1 g/liter) in distilled water. The major chemical components and their concentrations of the phantoms are listed in Table 2.

**Table 2.** Major chemical components and their concentrations of the saline phantoms.

| CHEMICAL NAME | CONCENTRATION (g/l) |
|---|---|
| *NaCl* | 6.90 |
| *KCl* | 0.375 |
| $MgSO_4$ | 0.145 |
| $CaCl_2$ | 0.185 |
| $Na_2HCO_3$ | 2.10 |
| *Glucose* | 1.80 |

The resonator's resonant frequencies, unloaded and loaded $Q$ values (quality factors) and $Q$ damping for each of the resonant modes as measured by the frequency analyzer are presented in Table 3. $Q_0$ is the unloaded $Q$ value measured with the resonator in air (without the phantom), while $Q_L$ is the $Q$ value measured when the saline phantom was placed centrally inside the resonator. The $Q$ damping is defined as the ratio of $Q_0/Q_L$. The results are the means of three measurements. The loaded $Q$ values are affected by the dimensions of the phantom and its position in the resonator. In general, the loaded $Q$ values are dominated by the effect of the RF lossy sample. The $Q$ values decrease as the dimensions of the sample increases.

**Table 3.** Results of the laboratory bench testing of the birdcage resonator. $Q_0$ and $Q_L$ were measured with the 444 ml phantom.

| Resonant Mode | Resonant Frequency (MHz) | Unloaded $Q_0$ | Loaded $Q_L$ | $Q_0/Q_L$ |
|---|---|---|---|---|
| $^{19}F$ | 188.22 | 14 | 9 | 1.56 |
| $^{1}H$ | 200.16 | 13 | 8 | 1.63 |

It can be seen from Table 3 that the unloaded $Q_0$, loaded $Q_L$, and the $Q$ damping $Q_0/Q_L$ for both resonant modes are similar. The relatively low $Q$ values may be attributed to the relatively long coaxial cables used to connect the tuning and match circuits. Another possible reason could be the large size of the resonator because the longer the legs, the larger their resistance, causing increased resistance losses and significantly lowering $Q$ values. One of the consequences of the low $Q$ values on the NMR experiments would be to increase the $90^0$ pulse width for a given RF power level. This can be verified by the following equation [**64**]:

$$PW = K\left(\frac{V_R}{Q}\right)^{1/2} \tag{8}$$

where $PW$ is the $90^0$ pulse width, $V_R$ is the resonator volume, $Q$ is the quality factor of the resonator, and the factor $K$ is roughly a constant for all resonator designs. This equation indicates that the $90^0$ pulse width is linearly proportional to the square root of resonator' volume and inversely proportional to the square root of resonator's $Q$ value.

- **Phantom Imaging**

The double-tuned birdcage resonator's NMR performance was tested on the Omega CSI 4.7 T magnet, which operates at a proton frequency of 200.106 $MH_Z$ and a fluorine frequency of 188.273 $MH_Z$. The phantom was centered in the resonator and the resonator was positioned in the isocenter of the magnet, with its axis being aligned with the direction of the magnet's static magnetic field $\boldsymbol{B}_0$. The $90^0$ pulse widths were determined from a $180^0$ null of the whole sample. Typical $90^0$ pulse widths were 700 μs for proton and 350 μs for fluorine. Shimming was accomplished on the water proton FID of the saline solution in the phantom, with the resonator tuned to the double resonant modes. The goal was to obtain a $\boldsymbol{B}_0$ of homogeneous strength over the entire imaging sample volume. Fourteen shim currents were adjusted on the proton FID throught the system automated shimming utility until a symmetrical and long FID was obtained. The proton spectral linewidth at half height after shimming was 34 Hz, which was sufficient for imaging experiments.

To minimize acquisition time, a driven equilibrium spin-echo pulse sequence with a fairly short echo time (TE = 8ms) was employed so that the $T_2$ dephasing effects were not significant. Proton transaxial (transverse) images were acquired as a 3-D data set with a repetition time TR = 150 ms, echo time TE = 8 ms, and a 128 x 64 x 8 matrix size over 100 mm x 100 mm field of view (FOV), providing 0.78 mm x 1.56 mm x 25 mm digital resolution. To improve signal-to-noise ratio (SNR), two acquisitions were averaged for each image, thus, giving a total acquisition time of 2 min 33 sec. Proton coronal and sagittal images were also acquired with the same imaging parameters.

SNRs for the images with 2 averages were measured using a standard routine. The values for signal were measured from a randomly chosen portion of images by a square crop and the values for noise were taken from the four corners of the image background. For each measurement, the square crop covered a reasonably large area of the image or background, so that the data obtained were unbiased. The results of SNR measurements for the proton images are listed in Table 4. The resonator's $B_1$ field homogeneity was estimated by visual inspection of the images.

**Table 4.** Results of SNR measurements for the proton images.

| | Upper-Left SNR | Upper-Right SNR | Lower-Left SNR | Lower-Right SNR | Mean SNR | SD |
|---|---|---|---|---|---|---|
| **Transaxial Section** | 88.0 | 97.4 | 93.0 | 93.3 | 92.9 | 3.9 |
| **Sagittal Section** | 279.8 | 272.7 | 278.7 | 294.0 | 281.3 | 9.0 |
| **Coronal Section** | 287.5 | 114.3 | 267.7 | 125.8 | 198.8 | 91.4 |

The magnet frequency was then set on resonance for the $CF_3$ group of TFA, without retuning the resonator. The $90^0$ pulse was 360 ms. The $^{19}F$ spin-echo images were acquired as transaxial, saggital and coronal projections. The images were fluorine density-weighted with TR = 150 ms and TE = 8 ms and were averaged 16 times to achieve an acceptable SNR. Thus, each image was acquired in 2 min 33 sec. The image matrix size was 128 x 64 with a field of view of 100 x 100 mm for the tranaxial projection and 200 x 200 mm for the sagittal and coronal projections, respectively.

**Table 5.** Results of SNR measurements for the $^{19}F$ images.

| | Upper-Left SNR | Upper-Right SNR | Lower-Left SNR | Lower-Right SNR | Mean SNR | SD |
|---|---|---|---|---|---|---|
| **Transaxial Section** | 3.2 | 3.3 | 3.4 | 3.5 | 3.3 | 0.1 |
| **Sagittal Section** | 5.9 | 6.7 | 7.3 | 6.9 | 6.7 | 0.6 |
| **Coronal Section** | 4.3 | 4.5 | 3.8 | 3.7 | 4.1 | 0.4 |

The image SNRs were measured in the same way as the proton images and the results are presented in Table 5. The spin-lattice relaxation time T1 of the $CF_3$ group was estimated by applying a non-spatially selective inversion recovery (IR) RF pulse. Seven different IR delays ($\tau$) increasing in the range between 800 ms to 20 sec were used (Table

6). The T1 value was calculated based on the Levenberg-Marquardt three-parameter fitting algorithm [**65**] on peak intensity values (Table 6).

**Table 6.** Results of T1 measurement for TFA solution and delay list ( $\tau$ ) of the inversion recovery pulse sequence.

**Function: y = A*(1-(W+1)*exp(-τ/T1)**
**A = 1.92e+06 ± 26484**
**W = 0.026 ± 0.042**
**T1 = 2.3 ± 0.19**
**Standard Error = 41129.6**
**Y Standard Deviation = 31091.1**

| τ | Intensity | Calculated | Difference | SD |
|---|---|---|---|---|
| 20.000 | 1923050.524 | 1923610.434 | 559.911 | 0.018 |
| 16.000 | 1932423.278 | 1921888.260 | -10535.018 | -0.339 |
| 8.000 | 1857983.273 | 1859578.430 | 1595.157 | 0.051 |
| 4.000 | 1534324.010 | 1567419.792 | 33095.782 | 1.064 |
| 2.000 | 1135584.863 | 1085041.321 | -50543.542 | -1.626 |
| 1.000 | 587685.972 | 637132.244 | 49446.272 | 1.590 |
| 0.800 | 545796.816 | 522178.645 | -23618.170 | -0.760 |

## Slotted Tube Resonator

The slotted-tube resonator was originally developed to efficiently provide $^1$H decoupling to samples in high-field magnets [**66**]. The common slotted tube resonator consists of a conducting tube with two slots cut symmetrically along both sides of the tube. The surface current distribution produced by the slotted tube resonator peaks near the edges of the conducting tube adjacent to the slots. The conducting tube of the slotted tube resonator is opaque to RF field and diverts all the $\boldsymbol{B}_1$ field flux through the two slots. Thus, the aperture angle of the slots must be optimized in order for the resonator to generate a homogeneous field. The fundamental feature of the slotted tube resonator is that the conducting component has a low inductance, and hence, large volume resonators can be constructed. At the RF frequencies encountered in clinical MRI systems, this means that the slotted tube resonators can be designed to contain samples of size comparable to that of the human head. The major applications of the slotted tube resonator are for imaging and for localized spectroscopy techniques demanding a uniform flip angle over the entire sample.

- **Design Theory**

The circuit model is illustrated in Figure 5. $L_s$ and $R_s$ are sample inductance and resistance, respectively. This circuit model can be further simplified in terms of equivalent circuit (Figure 6) with

$$Z'_2 = \frac{i(L_3C_3\omega^2 - 1)}{\omega(C_3 - C_2(L_3C_3\omega^2 - 1))} \tag{9}$$

where $\omega$ is the resonant frequency of the circuit and $i$ is the imaginary number. Thus, the tuning impedance $Z_T$ is given by the following expression:

$$\begin{aligned} Z_T &= Z_1 + Z_2' = \frac{-i}{C_1\omega} + Z_2' \\ &= i\frac{C_1(L_3C_3\omega^2 - 1) - \omega(C_3 - C_2(L_3C_3\omega^2 - 1))}{\omega C_1(C_3 - C_2(L_3C_3C^2 - 1))} \end{aligned} \tag{10}$$

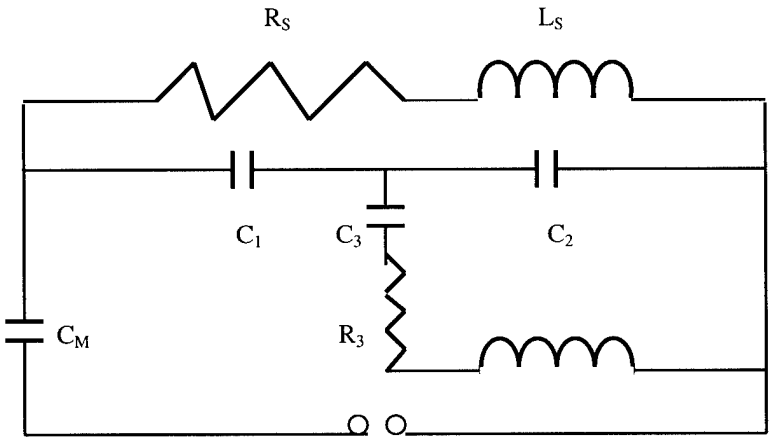


**Figure 5.** The circuit model of the switchable slotted tube resonator. $R_s$ is the sample resistance and $L_s$ the sample inductance. $R_3$ is the equivalent resistance of the tuning loop.

When the resonator operates at the higher frequency $\omega = \omega_h$, the tuning impedance $Z_T$ is a function of the total capacitance of the tuning circuit and is given by the expression

$$Z_T = -i\frac{(C_1 + C_2')}{\omega_h C_1 C_2'} \tag{11}$$

where

$$C'_2 = \frac{C_2(L_3C_3\omega_h^2 - 1) - C_3}{L_3C_3\omega_h^2 - 1} \tag{12}$$

Thus, the tuning is achieved by adjusting all the capacitors. When the resonator operates at the lower frequency $\omega = \omega_l$, the series $L_3 C_3$ circuit has a zero impedance and the total tuning impedance is reduced to

$$Z_T = -\frac{i}{C_1\omega_l} \tag{13}$$

Thus, tuning is obtained by adjusting $C_1$ only.

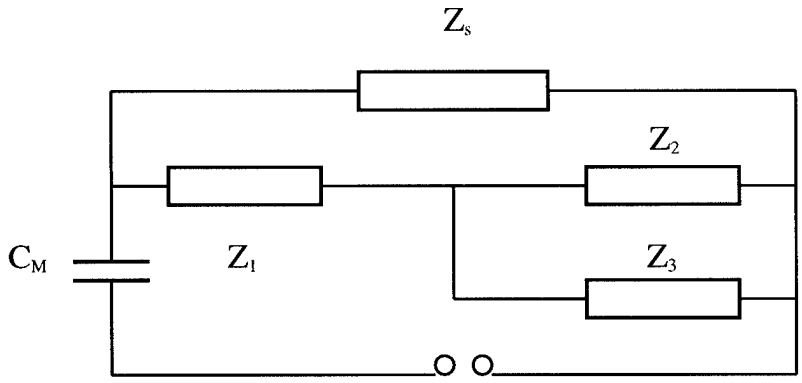


**Figure 6.** Equivalent circuit model of the slotted tube resonator.

- **Construction**

A switchable slotted tube resonator was constructed based on the above design theory using two copper sheets, which cover an $80^0$ arc [**67**] for optimal $\boldsymbol{B}_1$ field homogeneity. The cylindrical resonator body is 23.5 cm long with outer diameter 25.4 cm. The outer structure of the resonator is made of a 5mm thick plexiglass cylinder. The inner structure is made of a 3 mm thick plexiglass cylinder, having a small outer diameter of 7.6 cm to increase the filling factor and reduce the pulse width. The two ends of the resonator are covered by two 6 mm thick plexiglass boards stabilized by 6 nonmagnetic screws on each end, respectively. The two boards, along with the outer structure, provide very stable mechanical support for the resonator. Three capacitors of 20.0 pF were positioned symmetrically between the guard rings and the copper sheets to obtain uniform surface current distribution.

The resonator has a usable length of 15.5 cm, sufficient for *in vivo* adult rat NMR experiments. The two guard rings and two copper sheets are made from 0.3 mm thick copper foil. The width of each of the guard rings is 1.0 cm and there is a spacing of

approximately 0.5 cm between the guard ring and the vertical copper sheets, which are joined with capacitors. The copper sheets have a length of 12.5 cm and their width covers about $80^0$. The resonator is tunable to $^{19}F$ (188.22 MHz) and $^1H$ (200.16 MHz), and is driven between one copper sheet and one guard ring. The tuning of the resonator was achieved by three variable capacitors $C_1$, $C_2$, and $C_3$, which are V2145H family high $Q$ RF capacitors (Voltronics Corporation, Denville, New Jersey). $C_1$ and $C_2$ (NMTM38GE) have a capacitance range of 1.0 ~ 38.0 pF, $C_3$ (NMTM120CE) has a capacitance range of 2.0 ~ 120.0 pF, and $C_M$ (NMQM22GE) has a capacitance range of 1.0 ~ 22.0 pF. $^{19}F$ resonance was obtained by adjusting $C_1$ and $^1H$ resonance was achieved by adjusting $C_1$, $C_2$, and $C_3$, respectively. The resonator was matched capacitively through $C_M$.

- **Bench Testing**

The resonator was tuned and matched on the laboratory bench with the help of a frequency analyzer (HP8752A). The resonant frequencies, unloaded $Q_0$ and loaded $Q_L$ values and $Q$ damping for each of the resonant modes are presented in Table 7. $Q_0$ is the unloaded $Q$ value measured with the resonator in air, while $Q_L$ is the $Q$ value measured when the phantom was placed centrally inside the resonator. The $Q$ damping is defined as the ratio of $Q_0/Q_L$. The results are the means of three measurements.

**Table 7.** Results of the laboratory bench testing of the slotted tube resonator. $Q_0$ and $Q_L$ were measured with the 250 ml phantom.

| Resonant Mode | Resonant Frequency (MHz) | Unloaded $Q_0$ | Loaded $Q_L$ | $Q_0/Q_L$ |
|---|---|---|---|---|
| $^{19}F$ | 188.22 | 97.5 | 54.2 | 1.80 |
| $^1H$ | 200.16 | 63.8 | 53.6 | 1.19 |

As can be seen from Table 7, the unloaded $Q_0$ for $^{19}F$ is much higher than that for $^1H$, and the loaded $Q_L$ for both resonant frequencies is essentially same. The $Q$ damping, $Q_0/Q_L$, for $^{19}F$ is 1.5 times higher than that for $^1H$. This means that the RF lossy phantom has a much stronger effect on the $^{19}F$ resonance than on the $^1H$ resonance. The high $Q$ values could be the result of several factors, including a relatively small usable volume, minimized length of connecting wires, and a structure without a copper shield. The high $Q$ values guarantee that the resonator has a higher excitation efficiency, *i.e.*, the $90^0$ pulse width for a given RF power level is short or the magnitude of the $\boldsymbol{B}_1$ field generated with a given RF power level is high. The results of the laboratory bench testing also indicated that the resonator was easy to tune and match and both resonant frequencies were stable and immune to external electromagnetic interference.

- **Phantom Imaging**

Once again, the NMR performance of the slotted tube resonator was tested on the Omega CSI 4.7 T magnet. The *in vitro* resonator sensitivity for proton and fluorine was determined using the 250 ml phantom, which was filled with a solution of TFA (5%v/v) and $CuSO_4$ (1g/liter) in distilled water. Measurements of $90^0$ pulse width were performed from a $180^0$ null of the whole sample. Typical $90^0$ pulse widths were around 170 μs for proton and 110 μs for fluorine. Shimming was performed on the water proton FID of the saline solution with resonator tuned to the $^1H$ resonance, to a typical spectral linewidth of 32 Hz. The driven equilibrium spin-echo pulse sequence was used for the imaging experiment. Imaging parameters were: TR= 150ms, TE = 8ms, and matrix size =128 x 64 x 8. The field of view (FOV) was 80 mm x 80 mm for transaxial images, 100 mm x 100 mm for coronal, and 200 mm x 200 mm for sagittal images. The images were acquired with one excitation, thus giving a total acquisition time of 1.16 min. The image signal-to-noise ratios (SNRs) were measured as described before. The results of SNR measurements for the proton images are listed in Table 8.

**Table 8.** Results of SNR measurements for the proton images.

| | Upper-Left SNR | Upper-Right SNR | Lower-Left SNR | Lower-Right SNR | Mean SNR | SD |
|---|---|---|---|---|---|---|
| **Transaxial Section** | 389.3 | 199.5 | 897.8 | 666.3 | 538.2 | 177.1 |
| **Sagittal Section** | 494.2 | 517.5 | 478.8 | 450.5 | 485.3 | 28.1 |
| **Coronal Section** | 190.3 | 30.2 | 164.6 | 22.8 | 102.0 | 87.9 |

Following the $^1H$ imaging experiment, the resonator was retuned in place to 188.27 MHz and corresponding $^{19}F$ imaging experiment was carried out. The $90^0$ pulse was 108 μs and the spectral linewidth after shimming was 46 Hz. The spin-echo (SE) images were acquired with the imaging parameters: TR = 150 ms, TE = 8 ms, FOV = 100 x 100 mm, NA = 16, and matrix size = 64 x 32. The image SNR measurements were performed in the same way as the proton images and the results are given in Table 9.

**Table 9.** Results of SNR measurements for the fluorine images.

| | Upper-Left SNR | Upper-Right SNR | Lower-Left SNR | Lower-Right SNR | Mean SNR | SD |
|---|---|---|---|---|---|---|
| **Transaxial Section** | 3.1 | 2.9 | 2.6 | 3.0 | 2.9 | 0.2 |
| **Sagittal Section** | 4.2 | 5.1 | 4.0 | 4.2 | 4.4 | 0.5 |
| **Coronal Section** | 4.2 | 4.3 | 4.7 | 4.6 | 4.5 | 0.2 |

## 4) Assessment of Hexafluorobenzene (HFB) Distribution

### Animal Preparation

Once the tumors reached ~1 cm diameter (~ 0.5 $cm^3$), corresponding to a typical lower limit of tumor detected in patients, the rats were anesthetized with 200 μl ketamine hydrochloride i.p. (100 mg/ml; Aveco, Fort Dodge, IA) and were maintained under general gaseous anesthesia using a small animal anesthesia unit with air (1.0 $dm^3$/min) and 1.0% isoflurane (Ohmeda PPD Inc., Fort Dodge, IA). Tumor hair was cut with a pair of surgical scissors for reduction of the NIR light scattering and ease of HFB injection. The rats were placed on their sides in a specially designed NMR bed. The body temperature was maintained at about 37°C by a warm water blanket with a feedback system (K-MOD 100, Baxter Healthcare Co., Deerfield, IL). A fiber optic pulse oximeter (Nonin Medical, Inc., Plymouth, MN) was placed on the hind foot to monitor arterial hemoglobin saturation ($s_aO_2$) and heart rate (HR), and a thermocouple (Cole-Parmer Instrument Co., Vernon Hills, IL) was inserted rectally to monitor core temperature. 40 μl HFB (99.9%, Aldrich Chemical Co., St. Louis, MO) was injected directly into selected areas of tumor central and peripheral regions at the same plane using a Hamilton syringe with a 32 G needle. The needle was inserted manually to penetrate across the whole tumor and withdrawn ~ 1 mm to reduce the tissue pressure and 2~5 μl HFB injected. The needle was repeatedly withdrawn at a step size 1~2 mm and further HFB injected. A total of 2 ~ 3 tracks of HFB was injected in the form of a fan.

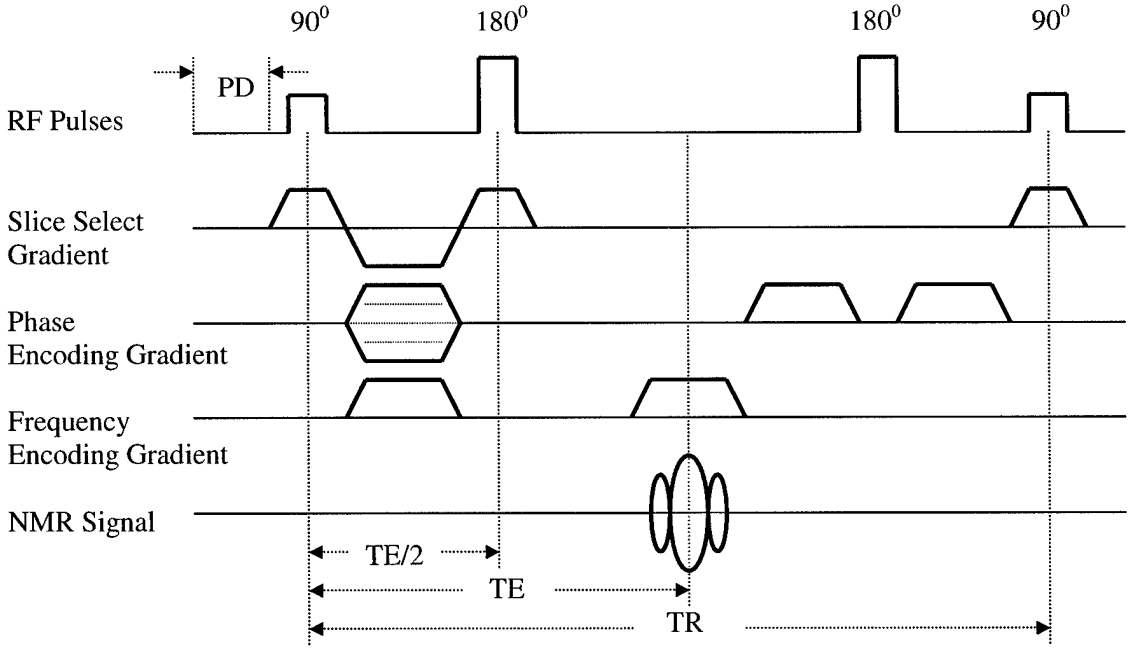


**Figure 7.** Pulse diagram of the driven equilibrium spin-echo pulse sequence

## $^1$H Magnetic Resonance Imaging

For each tumor, high resolution 3-D $^1$H MR imaging was first performed for anatomical reference. A frequency switchable ($^1$H/$^{19}$F) RF coil was placed around the tumor with the tumor centered in the coil. The rat was then be placed on its side in the bed and positioned in the isocenter of the magnet, with the coil axis being aligned perpendicular to the direction of the magnet's static magnetic field $\boldsymbol{B}_0$. The $90^0$ pulse width was determined from a $180^0$ null of the whole tumor. Shimming was performed on the tumor tissue water proton FID to a typical linewidth of 70 Hz. This was accomplished by adjusting fourteen shim currents on the FID through the system automated shimming utility until a symmetrical and long FID was obtained. The goal was to obtain a $\boldsymbol{B}_0$ of homogeneous strength over the entire tumor.

**Table 10**. $^1$H imaging parameters

| | |
|---|---|
| Repetition Time (**TR**) | 1500 ms |
| Echo Time (**TE**) | 80 ms |
| Matrix Size | 128x64x8 |
| Field of View (**FOV**) | 20x20x20 mm |
| Digital Resolution | 156 μm x 312 μm x 2.5 mm |
| Number of Acquisitions (**NA**) | 2 |
| Total Acquisition Time | 25 min 36 sec |

To minimize acquisition time, the driven-equilibrium spin-echo pulse sequence with a short echo time (TE = 80 ms) (Figure 7) was used so that the $T_2$ dephasing effects was not significant. $^1$H images were acquired as a 3-D date set. Imaging parameters used are shown in Table 10. These T2-weighted images showed the tumor anatomy and its position relative to the back of the rat. Following the $^1$H imaging, the corresponding $^{19}$F imaging was then performed to show the distribution of HFB in the tumor.

## $^{19}$F MRI and Assessment of HFB Distribution

The magnet frequency was then set on resonance for the CF group of HFB and the coil was retuned in place to 188.273 MHz. Corresponding fluorine density-weighted images was acquired as a 3-D data set using the driven-equilibrium spin-echo pulse sequence. The imaging parameters are shown in Table 11. Gradients were compensated to account for the difference in gyromagnetic ratios. Data were processed using sine-bell apodization to improve SNR and zero-filling in the first phase encoding direction for the execution of fast Fourier transform (**FFT**). Images were transferred to a PC and further processed off line using a SCION imaging software.

**Table 11.** $^{19}F$ imaging parameters

| | |
|---|---|
| Repetition Time (**TR**) | 150 ms |
| Echo Time (**TE**) | 8 ms |
| Matrix Size | 128x64x8 |
| Field of View (**FOV**) | 20x20x20 mm |
| Digital Resolution | 156 μm x 312 μm x 2.5 mm |
| Number of Acquisitions (**NA**) | 8 |
| Total Acquisition Time | 10 min 15 sec |

**Determination of HFB Redistribution and Clearance**

HFB clears from tissue relatively rapidly as compared to traditional PFCs, which exhibit excessive tissue retention. To verify that HFB clearance was not so rapid as to interfere with relaxometry, an NMR shell script program was written to compute the elimination rate constant of HFB using $^{19}F$ MR EPI images with the longest delay time (90 sec). The program was based on a plasma clearance model commonly used in pharmacokinetic analysis. Plasma clearance is the term used to represent the sum of all the drug elimination processes of the body. These include two primary processes, *i.e.*, metabolism and the function of the kidneys, and other secondary processes such as sweating, bile production, respiration, and feces generation. Each of these elimination processes has its own characteristic elimination constant. The plasma clearance model, taking into account all the elimination processes, describes the change in drug concentration with time. Mathematically, it is written as

$$C(t) = C(0)\exp(-\lambda \cdot t) \quad \text{or} \tag{14}$$

$$C(t) = C(0)\exp(-\frac{t}{T}), \tag{15}$$

where $C(0)$ represents the initial drug concentration, $C(t)$ the drug concentration at time $t$, $\lambda$ the total elimination rate constant (1/min), and $T$ the total elimination time constant (min). The biological half-life of a drug is defined as the time needed for the drug concentration in the plasma to be reduced by half. By using the plasma clearance model, this time can be shown to be

$$t_{1/2} = \frac{\ln 2}{\lambda} = T \cdot \ln 2, \tag{16}$$

Since, for a given set of imaging parameters, the NMR signal intensity of HFB was linearly proportional to its concentration in the tumor, analysis of the changes in signal intensity of $^{19}$F MR EPI images with time gave the values for the elimination rate constant or the elimination time constant of HFB. This was accomplished by rewriting Equation (15) as a discrete form

$$C_{i,j}^{n}(n\Delta t) = C_{i,j}^{1}(0)\exp(-\frac{n\cdot\Delta t}{T_{i,j}}), \tag{17}$$

where $n$ was the image index in the time series, $\Delta t$ was the time interval between two successive images, $C_{i,j}^{n}(n\Delta t)$ was the signal intensity of voxel $(i, j)$ in the $n$th image at time $n\Delta t$, $C_{i,j}^{1}(0)$ was the signal intensity of voxel $(i, j)$ in the first image (at time zero), and $T_{i,j}$ was the elimination time constant of voxel $(i, j)$. $T_{i,j}$ was obtained by fitting the signal intensity of $^{19}$F MR EPI images to Equation (17). In practice, however, Equation (17) was transformed into a logarithmic form so that the curve fit of the time series data yielded a straight line and the slope gave the value of $T_{i,j}$.

$$\ln(C_{i,j}^{n}(n\Delta t)) = \ln(C_{i,j}^{1}(0)) - \frac{n\cdot\Delta t}{T_{i,j}}, \tag{18}$$

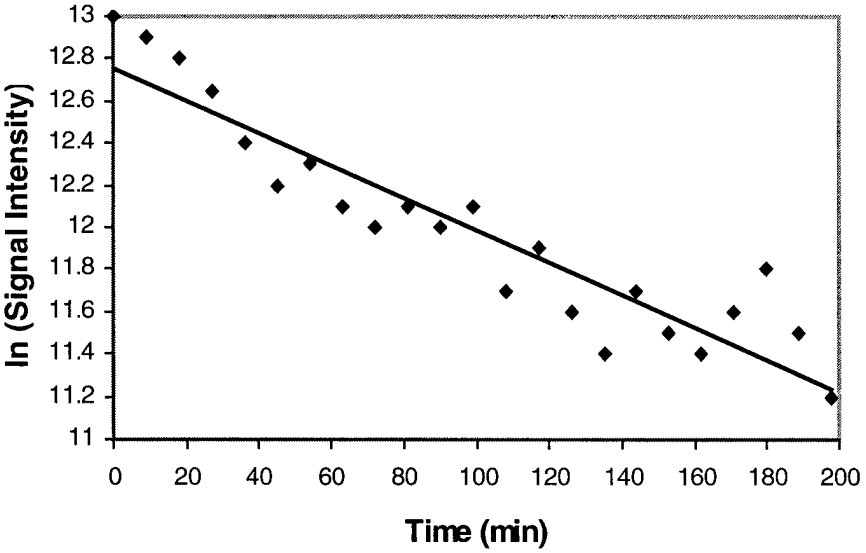


**Figure 8.** HFB clearance curve of a typical voxel from a 13762NF breast tumor. $\tau$ = 160 min.

Figure 8 shows the HFB clearance curve of a representative voxel from a 13762NF breast tumor during the 3 hours period of a typical experiment. For many regions, the HFB signal intensity was found to decay exponentially with a typical biological half-life ranging from $T_{1/2}$ = 700 to 1200 min. Since our $^{19}F$ MR EPI oximetry experiments lasted about three hours, this means the global and regional clearance and redistribution of HFB within the tumors did not interfere with $^{19}F$ MR EPI oximetry. By analyzing the clearance of individual voxels, it was found that as a whole $^{19}F$ signal intensity decreased with time, some voxels, however, showed increases in signal intensity as shown in Figure 9. This could be due to the inflow of HFB from the surrounding voxels. Since HFB concentration only affects the SNR of $^{19}F$ signal intensity and does not have a direct impact on relaxation rate $R1$, this local redistribution of HFB will not compromise the quality of our tumor oxygenation studies.

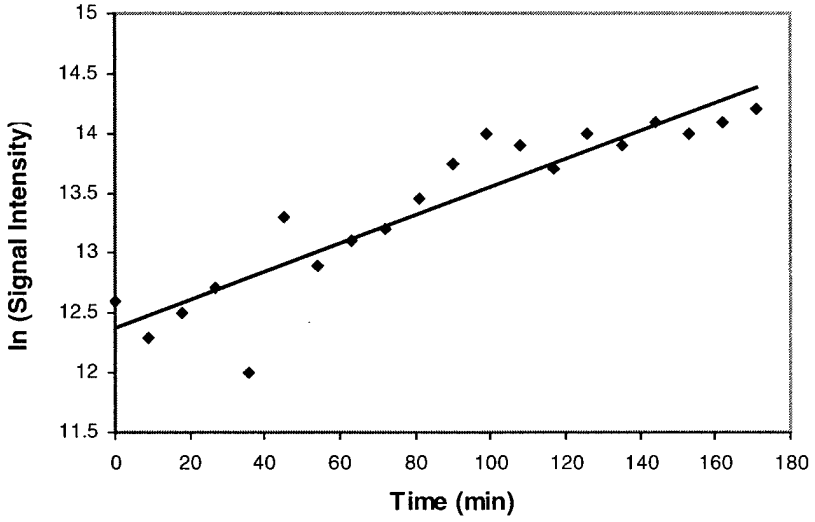


**Figure 9.** HFB clearance curve of a voxel from a 13762NF breast tumor that showed an increase in signal intensity with time

## 5) Software Development

### A Computer Program to Assess the Goodness of T1 Relaxation Curve Fit

$^{19}F$ EPI was used as a basic building block for $^{19}F$ MR EPI oximetry. To measure spin-lattice relaxation time (T1) and hence $pO_2$ maps, a pulse burst saturating (PBSR) pulse train was applied immediately prior to the EPI sequence. This led to some loss of dynamic range in the results, but substantially shortened the time required for a T1 experiment and thus, improved the temporal resolution. Fourteen data sets were acquired with delay time in a geometric progression ranging from 200 ms to 90 sec. Since the

longest and shortest delays were alternated during data acquisitions to reduce systematic bias, it was necessary to restore the images to the correct order, *i.e.*, from the shortest to the longest delay (200 ms $\cdots\cdots \rightarrow$ 90 sec) prior to the curve fit

In order to obtain the spatial distribution (map) of $pO_2$ in breast tumors, we needed to solve for the R1 map of injected HFB first. This was done by fitting the signal intensity in each of the voxels of the fourteen images to a three-parameter exponential relaxation model:

$$\begin{aligned} y_n(i,j) &= A(i,j)\cdot[1-(1+W)\cdot\exp(-R1(i,j)\cdot\tau_n)] \\ &(n=1,2,\cdots\cdots,14) \\ &(i,j=1,2,\cdots\cdots 32) \end{aligned} \tag{19}$$

by the Levenberg-Marquardt least-squares algorithm, where $y_n(i,j)$ was the measured signal intensity corresponding to delay time $\tau_n$(the $n$th image) of voxel $(i,j)$, $A(i,j)$ was the fully relaxed signal intensity amplitude of voxel $(i,j)$, $W$ was a dimensionless scaling factor allowing for imperfect signal conversion, and $R1(i,j)$ was the relaxation rate of voxel $(i,j)$ in unit of $\sec^{-1}$.

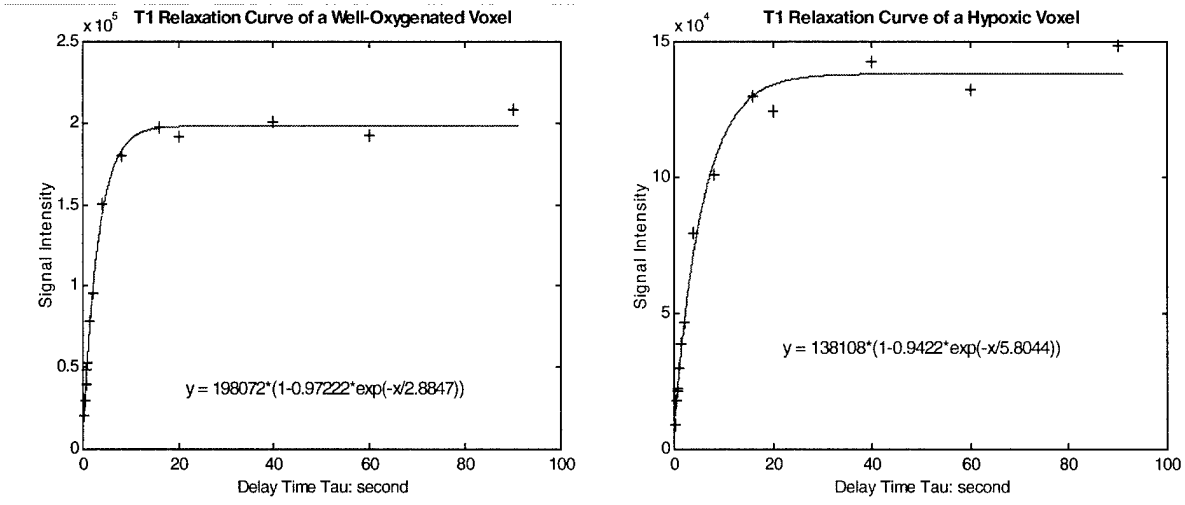


**Figure 10.** T1 relaxation curves of a well-oxygenated voxel (left) and a hypoxic voxel (right).

Good T1 relaxation curve fit was crucial in $^{19}F$ PBSR-EPI oximetry. It was relatively easy to obtain excellent curve fits, provided SNR > 10 for most intense signals.

To assess the goodness of curve fit, I wrote a Unix based NMR-shell script program to display the T1 relaxation curve of individual voxels of PBSR-EPI images. The graphical representation of the data, relaxation model, and goodness of fit provided a quick and convenient way of assessing the quality of the data. Based on the rms error of fit, the goodness of curve fit could be classified into three categories: good, intermediate, and poor.

For typical good relaxation data, the global least squares minimization was achieved with a very small rms error. These data, related to strong $^{19}F$ signal, represented those voxels within the region of interest (ROI). For typical intermediate data, the global least squares minimization was achieved with a relatively large rms error due to a single bad data point, which led to a big T1 error. To improve the relaxation curve fit, a threshold was applied to the raw data, which eliminated those data points $\geq 3\sigma$ from the curve. The remaining data, thus, provided a better curve fit. In applying the threshold, only one data point was eliminated from the raw data per curve. These relaxation data represented those voxels within the ROI, but had relatively strong $^{19}F$ signals. In general, they gave good T1 values. For poor relaxation data, the global least squares minimization either failed or converged slowly with a very large rms error. These relaxation data, associated with those voxels outside the ROI, represented either very week $^{19}F$ signals or background noise. They gave unreliable T1 values. Figure 10 shows T1 relaxation curves of a well-oxygenated voxel (left) and a hypoxic voxel (right).

**A Computer Program to Compute HFB Clearance Rate**

A C-program was written to compute the clearance rate $T_{i,j}$ of individual voxels by fitting the signal intensity of PBSR-EPI images to Equation (18). A clearance rate map was then produced by displaying $T_{i,j}$ as a color-coded image. This program is capable of computing the global and regional clearance rates of HFB.

**A Computer Program to Process $pO_2$ Data**

A windows-based Visual Basic program was written to process $pO_2$ data. The program can display and process images in the following formats:

- BMP Bitmap
- GIP Graphics Interchange Format
- JPG Joint Photographic Experts Group
- DIB Device Independent Bitmap
- WMF Windows MetaFile
- EMF Enhanced MetaFile
- ICO Icons

More functions are being added to the program.

## A Computer Program to Process NIRS Data

NIRS signal and biomedical signals in general are commonly contaminated by a number of sources. To reduce the contamination (noise), I employed digital signal processing techniques: averaging and filtering. Averaging was to improve the SNR of the signal and filtering was to remove the unwanted frequency components contained in the signal. Digital filters are mathematical algorithms implemented in hardware and/or software that operate on a digital signal to produce a desired digital output signal. I wrote a LabView$^{TM}$ program to implement these techniques. LabView$^{TM}$ is a graphical programming development environment based on the G-programming language for data acquisition and control, data analysis, and data presentation. It is more powerful and, at the same time, easier to learn and implement than the traditional text-based programming languages, such as C.

- **Averaging**

The first step in processing the NIRS data was averaging. Four adjacent data points were averaged to produce a new data point according to:

$$y(n) = \frac{x(n) + x(n+1) + x(n+2) + x(n+3)}{4} \tag{20}$$

where $x(n)$ represented the $n$th input data point and $y(n)$ the $n$th output data point. Since the NIRS data were acquired at relatively high sampling frequency, this averaging operation improved the SNR of the signal but not at the expense of losing detailed information in the data.

- **Digital Filtering**

Following averaging, the data were fed into a high order Butterworth low-pass filter with a cut-off frequency of 1.0 Hz. Butterworth filters are one of the infinite impulse response (IIR) filters. The main characteristics of the IIR filters is that the output depends not only on the current and past input data, but also on the past output data as shown in the following recursive equation [**68**]:

$$y(n) = \sum_{k=0}^{N} a_k x(n-k) - \sum_{k=1}^{M} b_k y(n-k) \tag{21}$$

where $a_k$ are called the forward coefficients, $b_k$ the reverse coefficients, $x(n)$ and $y(n)$ are the input and output to the filter, and $N$ and $M$ are the number of forward and reverse coefficients, respectively. Given the filter specifications (Table 12), $a_k$, $b_k$, $N$ and $M$ were computed using either a standard procedure.

The rationale for me to use a high order low-pass Butterworth filter was two-fold. Firstly, a Butterworth filter requires fewer coefficients. Thus, it executes faster and does not require extra memory. Secondly, a Butterworth filter has no ripple in either the passband or the stopband, and has a smooth, monotonically decreasing frequency response in the transition band.

**Table 12.** Specifications for the low-pass Butterworth filter

| Parameters | Specifications |
|---|---|
| Passband | 0 -1.0 Hz |
| Stopband | > 2.0 Hz |
| Stoppband attenuation | > 20 dB |
| Filter Order | 15 |

## 6) Investigation of Tumor Oyxgenation during Untreated Growth

### Investigation of Tumor Tissue $pO_2$

- **$^{19}$F MR EPI Oximetry**

EPI is a high-speed imaging technique first developed by Mansfield [69]. EPI can be divided into single-shot EPI and multiple-shot EPI. For this project, I used a variation of the original single-shot EPI, pulse burst saturation recovery echo-planar imaging (PBSR-EPI). It has been shown to be very effective and efficient in oxygen dynamic studies [70-72]. A typical PBSR-EPI pulse sequence diagram is shown in **Figure 11**.

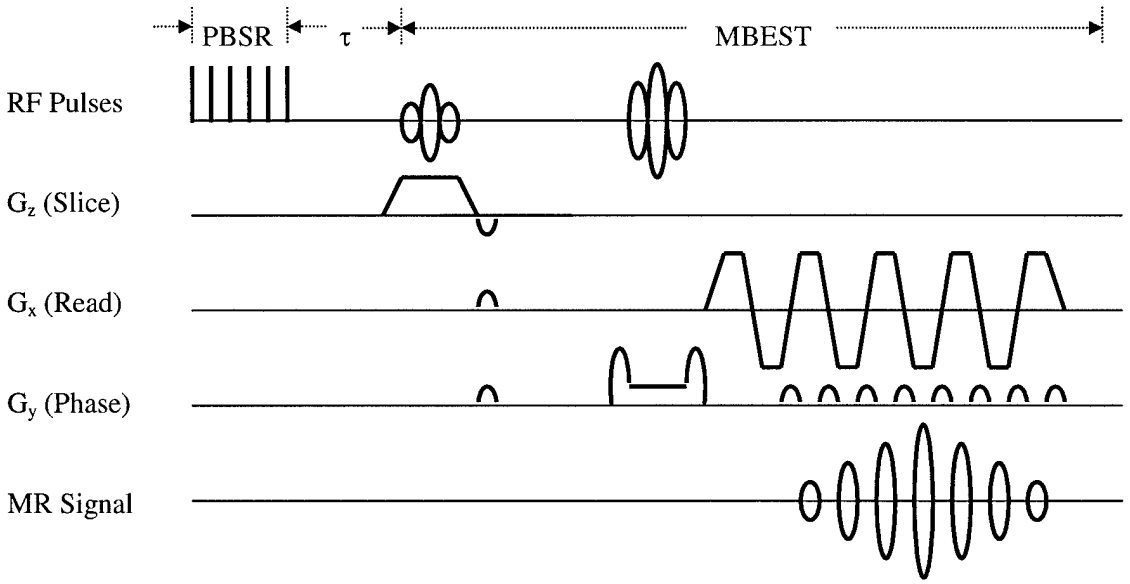


**Figure 11.** A typical PBSR-EPI pulse sequence diagram.

The PBSR-EPI consists of three basic building blocks: a preparation pulse sequence (PBSR), a variable delay time $\tau$, and a single shot spin-echo EPI with "blipped" phase encoding gradient. The PBSR is a pulse train of 20 non-spatially selective $90^0$ pulses with 50 ms spacing to saturate $^{19}F$ nuclei. Fourteen different $\tau$ values, ranging from 200 ms to 90 s, are used to modulate image intensities so that good T1 relaxation curves can be obtained. The function of the brief "blipped" phase encoding gradient between each echo is to increment phase in the $k_y$ direction to form a blipped echo image. Fourteen EPI images are acquired with 32x32 in-plane resolution. PBSR-EPI may result in some loss of dynamic range in signal intensity, but substantially shortens the data acquisition time for a T1 experiment. By incorporating a PBSR preparation pulse sequence into EPI, each R1 (1/T1) map can be produced with a temporal resolution of ~ 6 min, facilitating measurements of dynamic changes in $pO_2$ accompanying therapeutic interventions and allowing the fate of individual voxels to be traced.

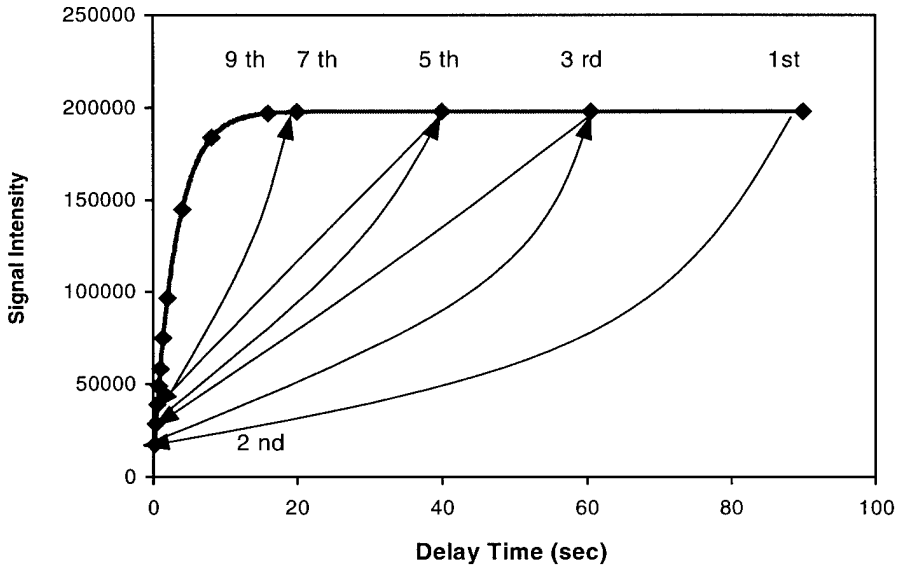


**Figure 12.** A schematic representation of the ARDVARC protocol.

To enhance SNR of the $^{19}F$ EPI images, and thus, improve the precision of R1 measurements, I used a novel data acquisition protocol developed in our lab: ARDVARC (**A**lternated **R**1 **D**elays with **V**ariable **A**cquisitions to **R**educe **C**learance effects) (**Figure 12**). The ARDVARC has two new features in comparison with the traditional approach. Firstly, the number of acquisitions (NA) varies with $\tau$ values. This innovation significantly improves the SNR for short delays and provides a better curve fit by additional acquisitions. Data are amplitude-corrected, *i.e.*, divided by the number of

acquisitions to maintain correct signal amplitude. Secondly, longest and shortest delays are alternated to reduce bias resulting from HFB clearance or fluctuations in R1 (Table 13). In order to determine R1, and hence $pO_2$, signal intensity in each voxel was fitted to a three-parameter exponential relaxation model:

$$y_n(i,j) = A(i,j)\cdot[1-(1+W(i,j))\cdot\exp(-R1(i,j)\cdot\tau_n)] \quad (n = 1, 2, \ldots\ldots, 14) \quad (i,\ j = 1, 2, \ldots\ldots 32) \tag{22}$$

by the Levenberg-Marquardt least-squares algorithm, where $y_n(i, j)$ was the measured signal intensity of voxel $(i, j)$ at delay time $\tau_n$ (the $n$th image), $A(i, j)$ was the fully relaxed signal intensity of voxel $(i, j)$, $W(i, j)$ was a dimensionless scaling factor used for imperfect signal conversion, and $R1(i, j)$ is the relaxation rate of voxel $(i, j)$ in unit of $sec^{-1}$.

**Table 13.** ARDVARC parameters

| Order of Acquisition | Order in Curve Fit (n) | Delay Time τ (sec) | Number of Acquisitions (NA) |
|---|---|---|---|
| 1 | 14 | 90 | 1 |
| 2 | 1 | 0.2 | 12 |
| 3 | 13 | 60 | 1 |
| 4 | 2 | 0.4 | 12 |
| 5 | 12 | 40 | 1 |
| 6 | 3 | 0.6 | 12 |
| 7 | 11 | 20 | 1 |
| 8 | 4 | 0.8 | 12 |
| 9 | 10 | 16 | 2 |
| 10 | 5 | 1 | 8 |
| 11 | 9 | 8 | 2 |
| 12 | 6 | 1.5 | 4 |
| 13 | 8 | 4 | 4 |
| 14 | 7 | 2 | 4 |

Regional tumor $pO_2$ maps were produced by applying the calibration curve to $R1$ maps. It was found that at $37C^0$ and 4.7 T:

$$pO_2(i,j) = \left[\frac{R1(i,j) - 0.0835}{0.001876}\right] (\text{torr}) \tag{23}$$

using PBSR-EPI for HFB.

- **Respiratory Challenge Paradigms**

One of the important issues in radiotherapy is how to manipulate oxygenation in tumors and monitor its dynamic response to various therapeutic interventions noninvasively. Many protocols and techniques have been proposed. A simple intervention is respiratory challenge, *i.e.*, attempting to elevate tumor oxygenation with inhaled gas. For this project, two respiratory challenge paradigms were used to manipulate oxygenation in tumors. $^{19}$F MR EPI and NIRS were used to monitor oxygen dynamic response and assess its temporal characteristics and changes in the extent of hypoxia.

(1) ***Air*** ($21\%\ O_2$) → ***Carbogen*** ($95\%\ O_2 + 5\%\ O_2$) → ***Air*** → ***Carbogen*** → ***Air***

(2) ***Air*** → ***Carbogen*** → ***Air*** → ***100% $O_2$*** → ***Air***

Most experiments were performed using paradigm (1). However, in some cases, repeated carbogen interventions were performed sequentially to evaluate the reproducibility of the time course profiles of the tumors.

- **Investigation of Tumor Tissue Oxygen Dynamics by $^{19}$F MR EPI**

Following $^{1}$H and $^{19}$F MRI to determine the tumor anatomy and the distribution of HFB, a series of $^{19}$F MR EPI oximetry experiments were performed according to the respiratory challenge paradigms described above. During the imaging sessions, initially, rats inhaled medical grade compressed air ($21\%\ O_2$) and three measurements were taken for the first phase. Subsequently, five measurements were taken for each gas switch, giving a total of twenty-three measurements. The complete five-phase imaging session took about 2.5 hours. **Figure 13** shows four contiguous slices of conventional spin echo (SE) $^{1}$H MR images (upper panel) of breast tumor No. 1 (2.4 $cm^3$). Corresponding $^{19}$F MR images (lower panel) reveal the discrete distribution of HFB in the tumor. 40 µl HFB was directly injected into the tumor and about ~ 7% of the total tumor volume was labeled in the central regions. **Figure 14** shows representative $pO_2$ maps of a selected subregion obtained from breast tumor No.1 with respect to respiratory challenge. The $pO_2$ maps were acquired using $^{19}$F EPI with a temporal resolution of 6.5 min. Gray background represents all possible voxels that fitted to the three-parameter exponential relaxation model. Because of random electronic noise, not all fitted voxels provided meaningful data. To select only those reliable and consistent voxels, thresholds were applied to the raw $pO_2$ maps. As seen in the $pO_2$ maps, not all voxels met the thresholds. The colored voxels represent valid $pO_2$ data. In this particular subregion, 52 voxels provided good $pO_2$ data. **Figure 15** shows the time course profile of $pO_2$ in response to respiratory challenge for tumor No.1. Each data point represents mean ± SD of all voxels for one measurement or one $pO_2$ map.

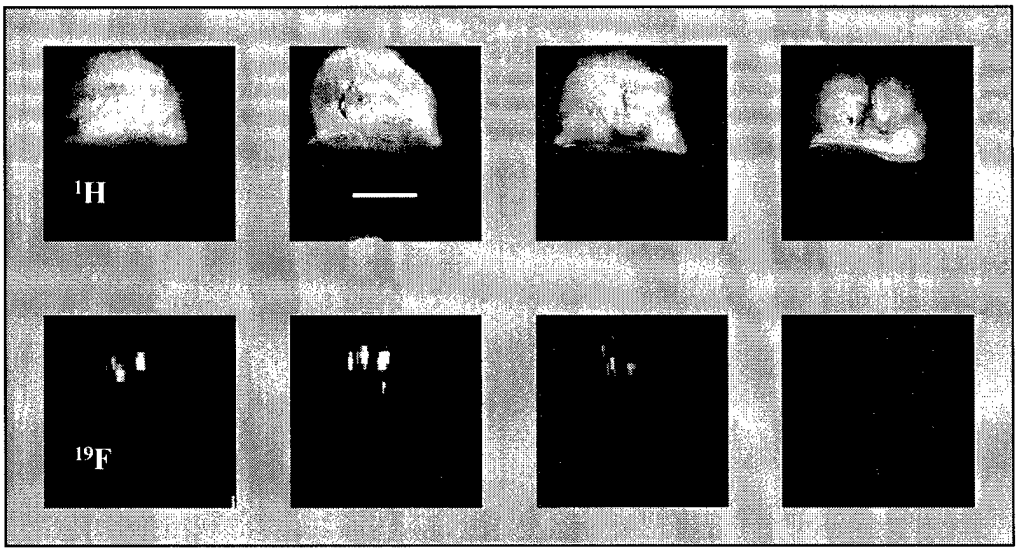


**Figure 13** Four contiguous $^{1}$H and $^{19}$F MR coronal images from respective 3D data sets of breast tumor No.1 (2.4 $cm^3$). Slice thickness = 4 mm, bar = 1 cm.

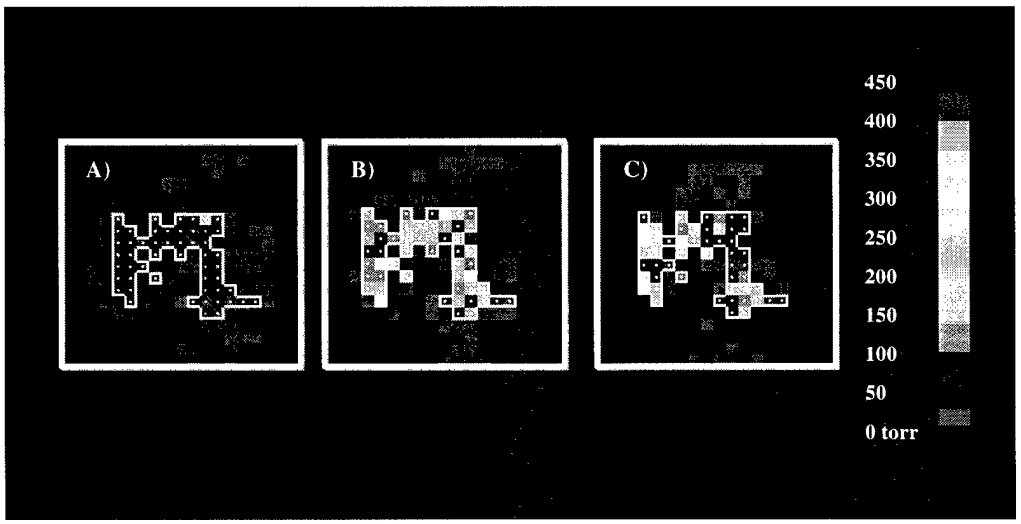


**Figure 14** Representative $pO_2$ maps (expanded) obtained from breast tumor No.1 (2.4 $cm^3$) using $^{19}$F EPI. (**A**) Rat breathing 33% $O_2$, (**B**) 100% $O_2$ and (**C**) carbogen (95% $O_2$ + 5% $CO_2$).

Three baseline measurements (33% $O_2$) gave mean $pO_2$ of 19.4 ± 2.6, 19.6 ± 2.8, and 15.6 ± 2.1 (torr), respectively, indicating that tumor baseline $pO_2$ was consistent and stable. Breathing 100% oxygen induced rapid and significant changes in $pO_2$ compared

with baseline values. Following the onset of pure oxygen breathing, tumor oxygen tension increased to 68.8 ± 11.8, and 72 ± 16.1 (torr) for the fourth and fifth measurements, respectively ($p < 0.01$). Oxygen tension continued to increase further for the last three measurements, yielding 100.2 ± 22.1, 132.1 ± 28.6, and 167.2 ± 40.3 (torr) ($p < 0.008$ and $p < 0.004$). As seen in the plot, $pO_2$ did not reach the steady state. After the gas was switched back to baseline 33% $O_2$, $pO_2$ dropped quickly and significantly initially ($p < 0.008$) and then slowly afterwards for the next four measurements. However, the final $pO_2$ remained elevated above the initial baseline value, a phenomenon also observed in some other breast tumors. This was consistent with my tumor vascular oxygenation study using NIRS, in which many tumors showed an elevated $\Delta[HbO_2]$ following a gas switch from carbogen to air. Altering inhaled gas to carbogen produced a similar time course response pattern in $pO_2$ in terms of the rate of response and magnitude. The $pO_2$ values for the last three measurements during carbogen breathing were 136.4 ± 35.3, 142.2 ± 3.9, and 166.2 ± 50.6 (torr), respectively ($p < 0.008$ and $p < 0.004$). No statistically significant difference was observed between pure oxygen breathing and carbogen breathing in this case (**Figure 15**). Upon return to baseline 33% $O_2$ breathing for the last phase of the experiment, $pO_2$ returned to the baseline level, as expected. **Figure 16** shows the mean $pO_2$ for each gas switch for breast tumor No. 1. Error bars in the figure represent standard error (SE). The mean $pO_2$ was 108.1 ± 41.8 (torr) when the rat was breathing pure oxygen ($p < 0.0036$). Following a gas switch to 33% $O_2$, $pO_2$ decreased to 75 ± 8.5 (torr) ($p < 0.049$). $pO_2$ increased to 110.9 ± 24 (torr) during carbogen breathing ($p < 0.0029$).

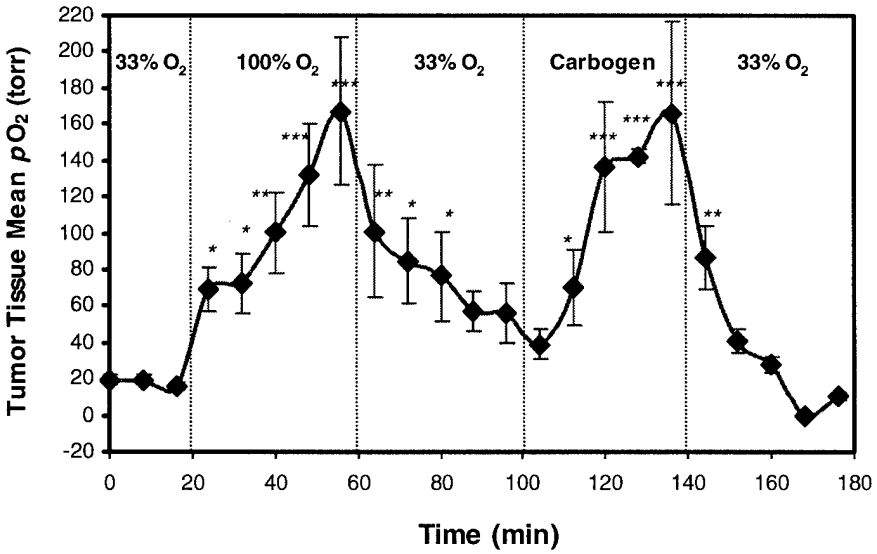


**Figure 15** Time course profile of $pO_2$ in response to respiratory challenge for breast tumor No.1 (2.4 $cm^3$). Each data point representing mean ± SD. Statistical significance with respect to baseline: (*** $p < 0.004$, ** $p < 0.008$, * $p < 0.01$).

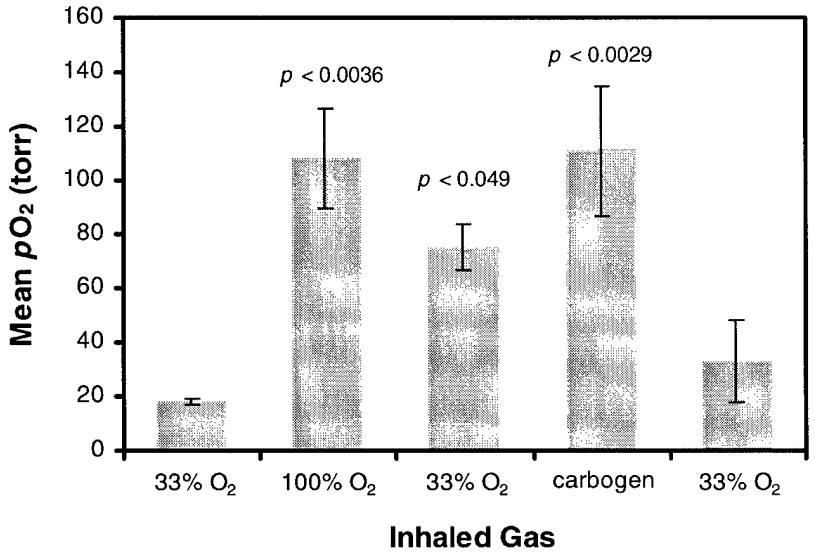


**Figure 16** Mean $pO_2$ for each gas switch obtained from breast tumor No.1 (2.4 $cm^3$). Error bars representing SE.

The rate of $pO_2$ response to gas intervention is an important dynamic parameter because it was related to the status of tumor perfusion. To estimate this parameter quantitatively, the data corresponding to pure oxygen breathing was fitted a mono-exponential model: $pO_2 = A \cdot \exp[(t - t_0) / \tau]$, where $\tau$ is the time constant of the response. Since there were only six data points available for the curve fit in each case, sometimes, the data may not provide a good fit. For this particular example, the mono-exponential curve fit gave $\tau = 18 \pm 15$ (min). As a comparison, typical fast time constant for tumor vascular hemoglobin oxygen saturation $\Delta[HbO_2]$ ranged from 10 to 80 sec and typical slow time constant ranged from 5 to 12 min. This strongly indicated that the tumor tissue $pO_2$ had a much slower response than tumor vascular $\Delta[HbO_2]$.

**Figure 17** shows three representative $pO_2$ histograms obtained by FREDOM of HFB for breast tumor No.1 with respect to inhaled gas. The histograms show the heterogeneity of $pO_2$ values within the tumor as well as the mean $pO_2$ values. The data are presented as relative frequency, defined as the number of voxels falling within a particular $pO_2$ range divided by the total number of voxels. As is demonstrated in **Figure 17 (A)**, $pO_2$ distribution concentrated on the low $pO_2$ range with a mean $pO_2$ of $20 \pm 2$ (torr) and a median $pO_2$ of 10 (torr) while the rat was breathing baseline 33% $O_2$. 100% $O_2$ breathing caused a significant shift of the histogram towards the higher $pO_2$ value ($p < 0.001$), yielding a mean $pO_2$ of $80 \pm 8$ (torr) and a median $pO_2$ of 68.3 (torr). Carbogen breathing also caused a significant shift of the histogram towards the higher $pO_2$ value ($p < 0.0008$), giving a mean $pO_2$ of $121 \pm 14$ (torr) and a median $pO_2$ of 116 (torr).

Presenting $pO_2$ distribution by histograms is similar to the data presentation used by clinical Eppendorf Histograph. However, $^{19}F$ EPI technique is non-invasive and repeatable. The data presented in **Figure 17** were further illustrated in **Figure 18**, which shows the cumulative fractions as function of inhaled gas. If, for simplicity, the threshold for tumor hypoxia was 10 (torr), then there was a significant drop in tumor hypoxic fraction, from 0.27 to 0.082 when compared with 100% $O_2$ breathing ($p < 0.03$) (**Figure 18 (B)**). Carbogen breathing reduced the hypoxic fraction to 0.077 ($p < 0.03$), thus more hypoxic regions became better oxygenated (**Figure 18 (C)**).

The $^{19}F$ EPI oximetry has the distinct advantage over other techniques that subsequent measurements are completely non-invasive. The greatest strength of this method is the ability to trace the fate of individual voxels (regions) with respect to therapeutic interventions. **Figure 19** shows dynamic changes in $pO_2$ of six specific voxels of breast tumor No. 2 (3.5 $cm^3$) with respect to different inhaled gases. It is noteworthy that voxels with high baseline $pO_2$ had significantly different response characteristics from those with initially low $pO_2$, which showed small changes. **Figure 20** shows dynamic changes in $pO_2$ of 44 specific voxels in tumor No. 3 in response to carbogen breathing. Once again, the local response both in terms of rate and magnitude depended strongly on initial baseline $pO_2$. A strong linear correlation was observed in most of the 13762NF breast tumors between initial mean baseline $pO_2$ and the maximum $pO_2$ for a given group of voxels with respect to carbogen or oxygen breathing. An ROI of 83 voxels was selected from breast tumor No. 1 (**Figure 21**). In this example, the linear coefficient $R$ was found to be 0.95. This finding is of potential clinical significance and could help predict tumor response to elevated oxygen breathing based on the initial baseline value.

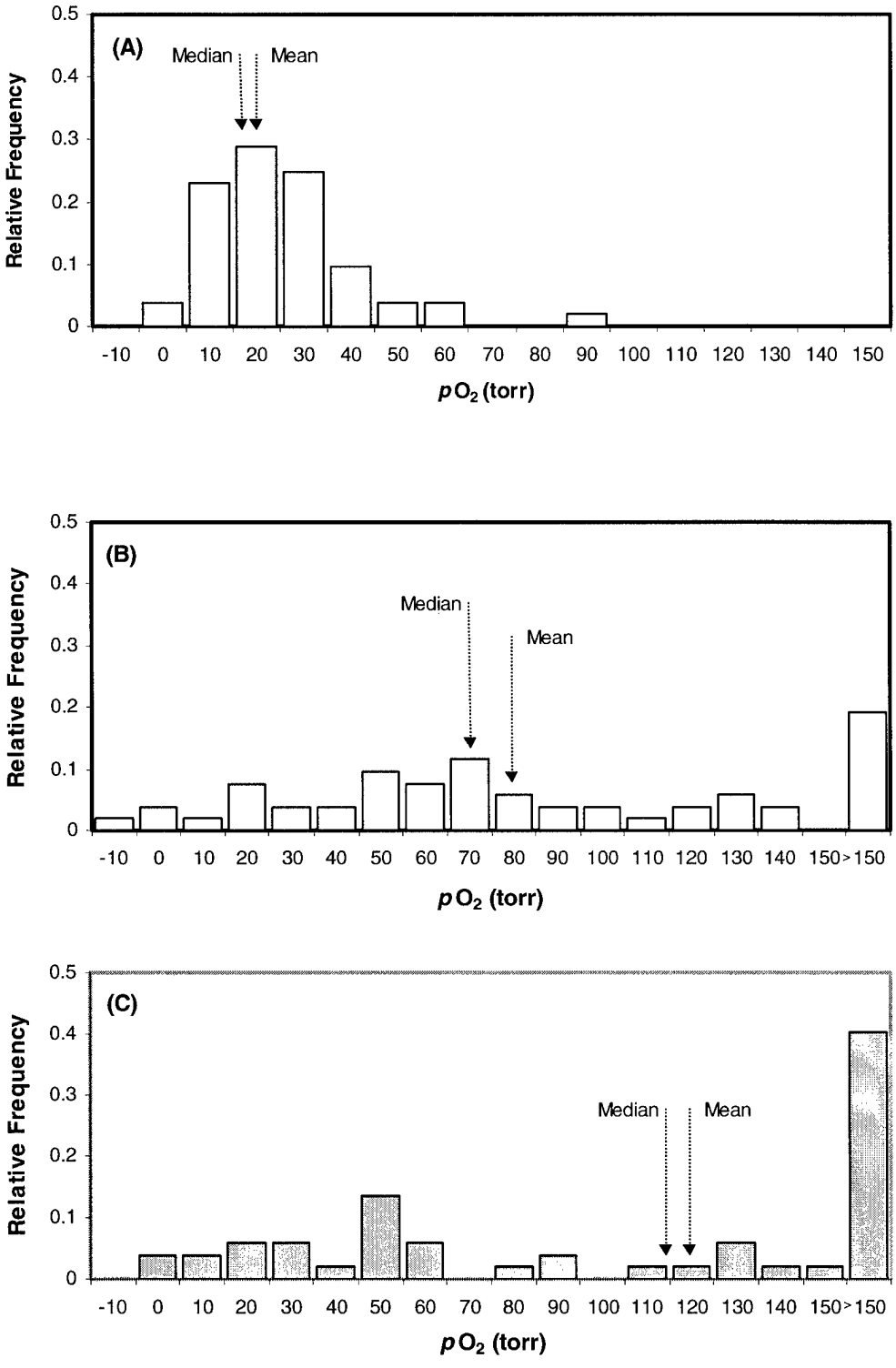


**Figure 17** Representative $pO_2$ histograms obtained by FREDOM of HFB for breast tumor No. 1 with respect to inhaled gas. (**A**) 33% $O_2$ (**B**) 100% $O_2$ (**C**) carbogen.

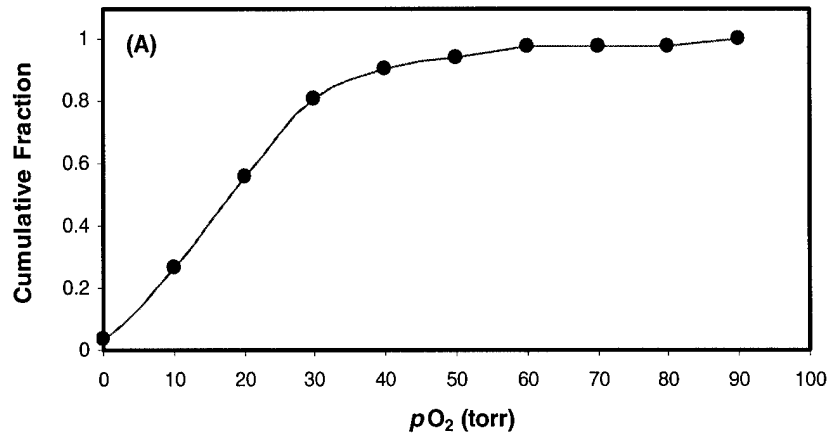


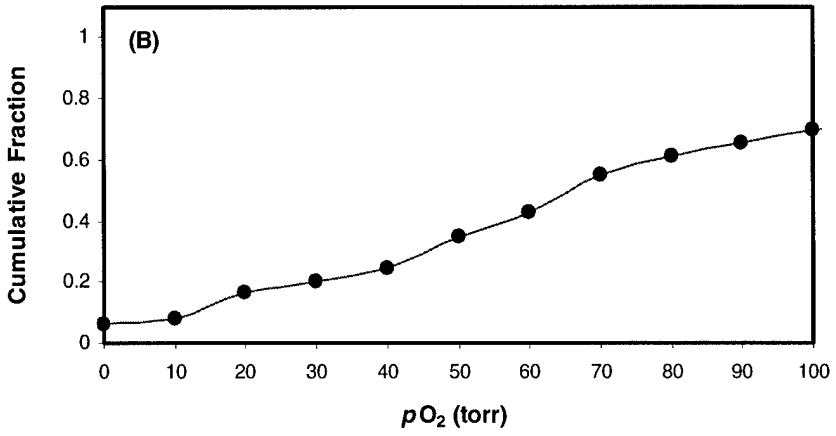


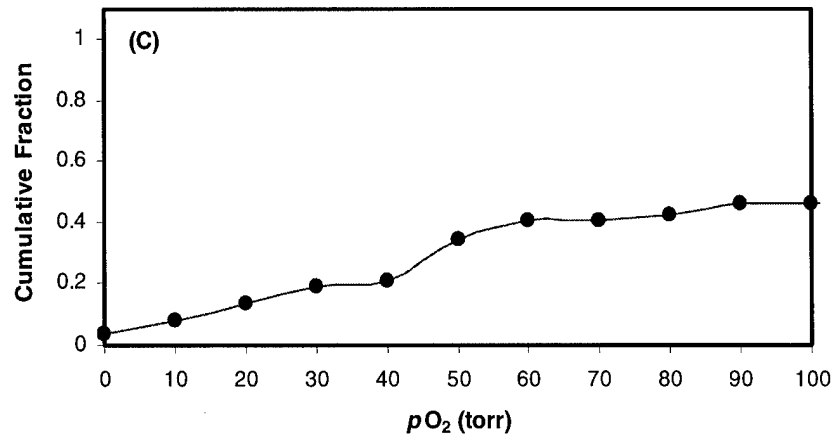


**Figure 18** Cumulative fractions as function of inhaled gas for tumor No.1. (**A**) 33% $O_2$ (**B**) 100% $O_2$, and (**C**) carbogen.

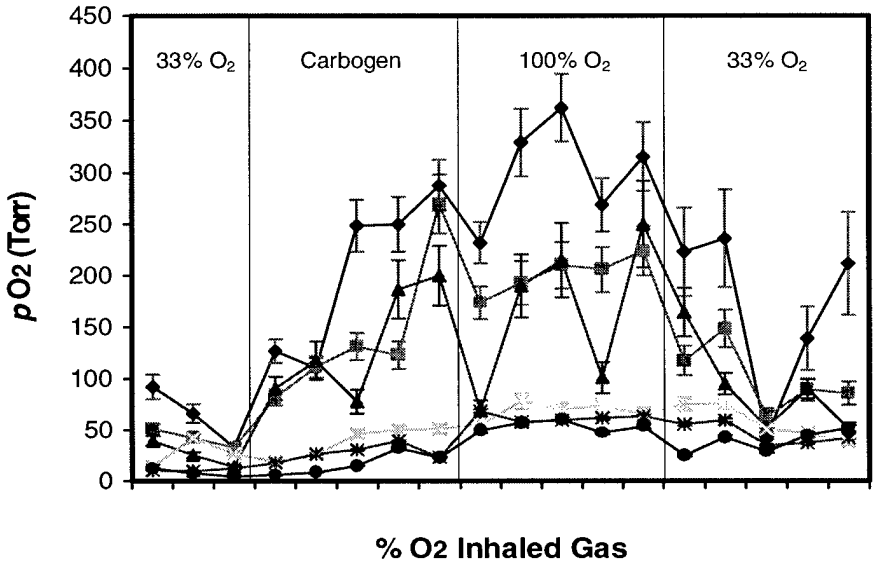


**Figure 19** Dynamic changes in $pO_2$ of six specific voxels in tumor No.2. The local response both in terms of rate and magnitude depended strongly on initial baseline $pO_2$.

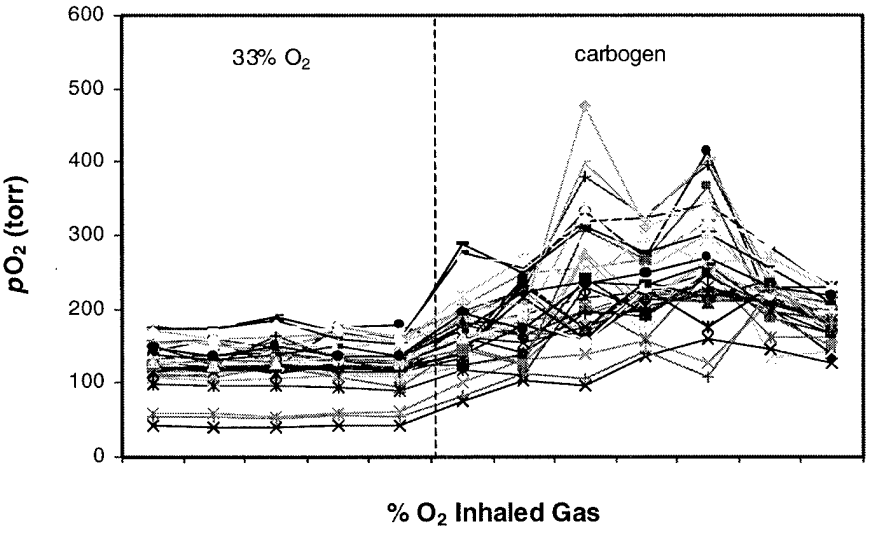


**Figure 20** Dynamic changes in $pO_2$ of 44 specific voxels in tumor No.3 in response to carbogen breathing.

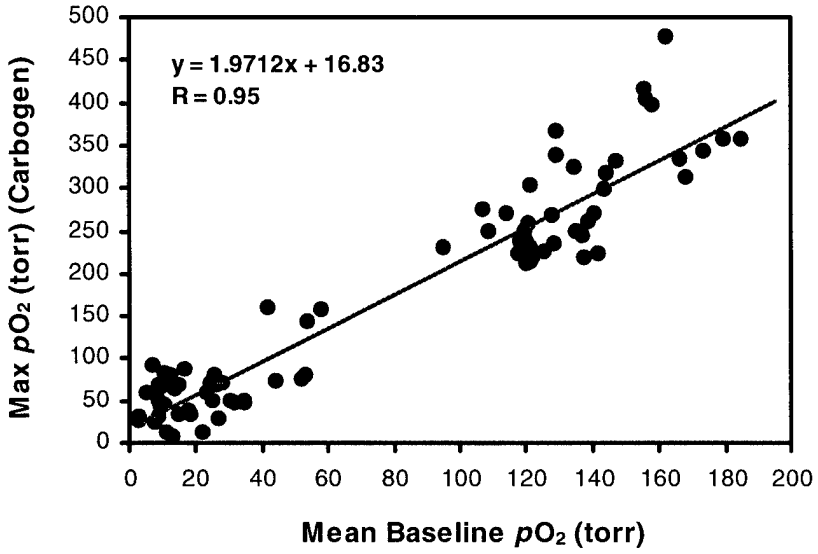


**Figure 21** Maximum $pO_2$ vs. initial mean baseline $pO_2$ for a group of voxels selected from breast tumor No.1 ($R = 0.95$).

**Figure 22** shows representative $pO_2$ maps of a selected subregion obtained from breast tumor No. 4 (1.7 $cm^3$). **Figure 23** shows the time course profile of $pO_2$ in response to respiratory challenge in the same subregion for tumor No. 4. **Figure 24** shows the mean $pO_2$ for each gas switch for breast tumor No. 4. In this case, the initial mean baseline $pO_2$ was 62.3 ± 4.6 (torr). Following a gas switch from 33% $O_2$ to 100% $O_2$, the mean $pO_2$ increased to 197.5 ± 23.8 (torr) ($p < 0.0004$). After the gas was switched to 33% $O_2$ again, the mean $pO_2$ remained significantly higher than the initial mean baseline $pO_2$ (118.7 ± 10.5 (torr), $p < 0.08$). $pO_2$ increased even more significantly (270.4 ± 21.5 (torr)) when the gas was switched to carbogen ($p < 0.0001$). **Figure 25** shows the mean hypoxic fraction as a function of inhaled gas for breast tumor No. 4. The mean baseline hypoxic fraction was 0.147 ± 0.062, which decreased to 0.06 ± 0.03 during 100% $O_2$ breathing ($p < 0.066$) and 0.049 ± 0.02 during carbogen breathing ($p < 0.058$). **Figure 26** shows the $pO_2$ histograms corresponding to **Figure 22** for breast tumor No.4 with respect to inhaled gas. Once again, both 100% $O_2$ and carbogen breathing caused a significant shift of the histogram towards the higher $pO_2$ value. A fairly strong linear relationship was also observed between the initial mean baseline $pO_2$ and the maximum $pO_2$ for a group of voxels selected from breast tumor No.4 ($R = 0.68$), as seen in **Figure 27**.

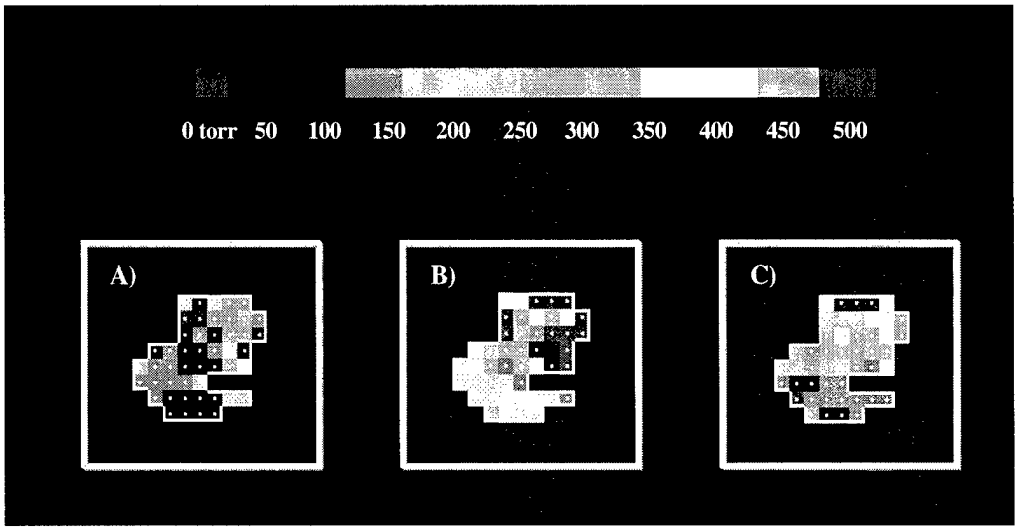


**Figure 22** Representative $pO_2$ maps (expanded) obtained from breast tumor No.4 (1.7 $cm^3$) using $^{19}F$ EPI. (**A**) Rat breathing 33% $O_2$, (**C**) 100% $O_2$ and (**B**) carbogen.

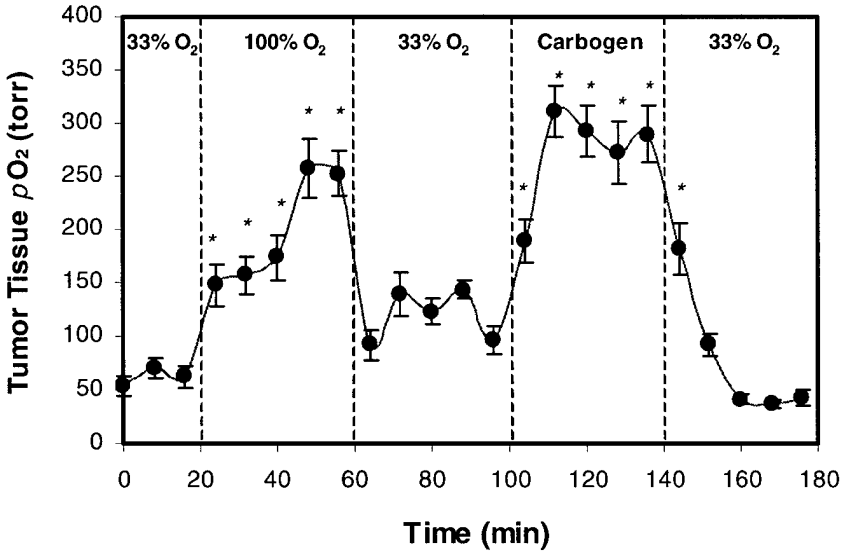


**Figure 23** Time course profile of $pO_2$ in response to respiratory challenge for breast tumor No.4 (1.7 $cm^3$). Each data point representing mean ± SD. Statistical significance with respect to baseline: (* $p < 0.0001$).

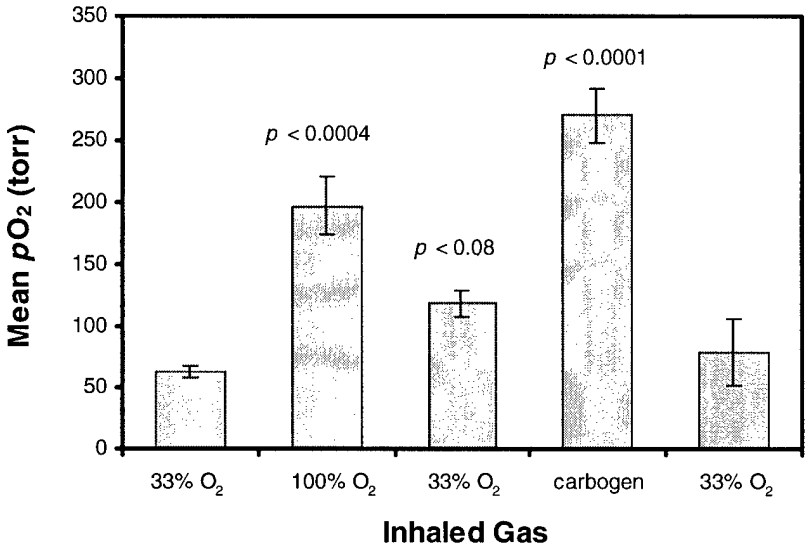


**Figure 24** Mean $pO_2$ in response to respiratory challenge for breast tumor No. 4 (1.7 $cm^3$). Error bars representing SE.

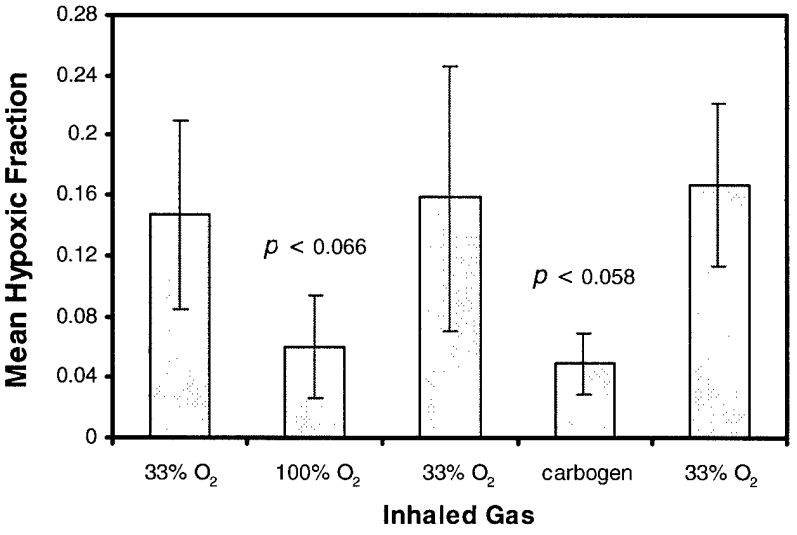


**Figure 25** Mean hypoxic fraction as a function of inhaled gas for breast tumor No. 4 (1.7 $cm^3$). Error bars representing SE.

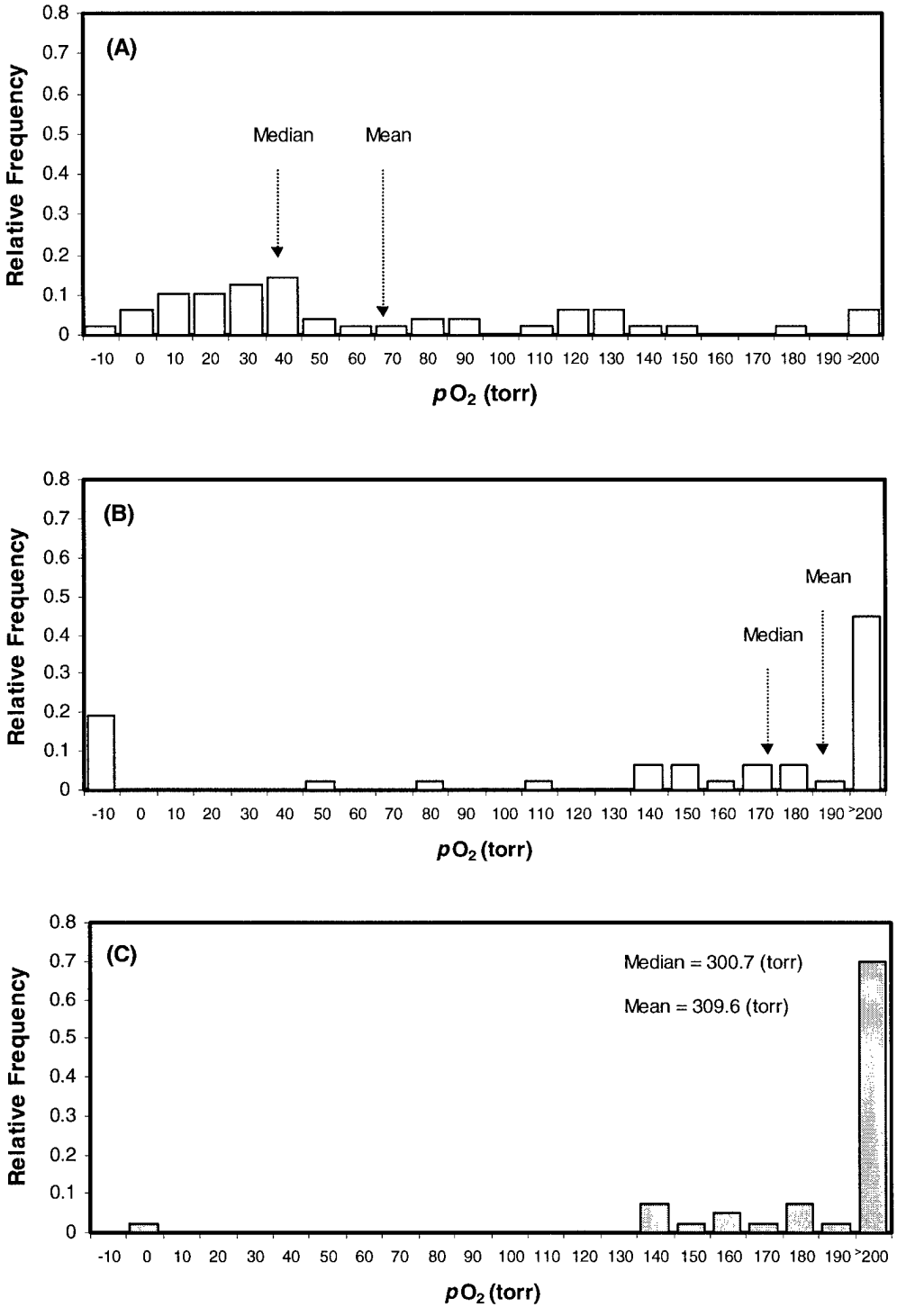


**Figure 26** $pO_2$ histograms corresponding to **Figure 22** for breast tumor No. 4 with respect to inhaled gas. (**A**) 33% $O_2$ (**B**) 100% $O_2$ (**C**) carbogen.

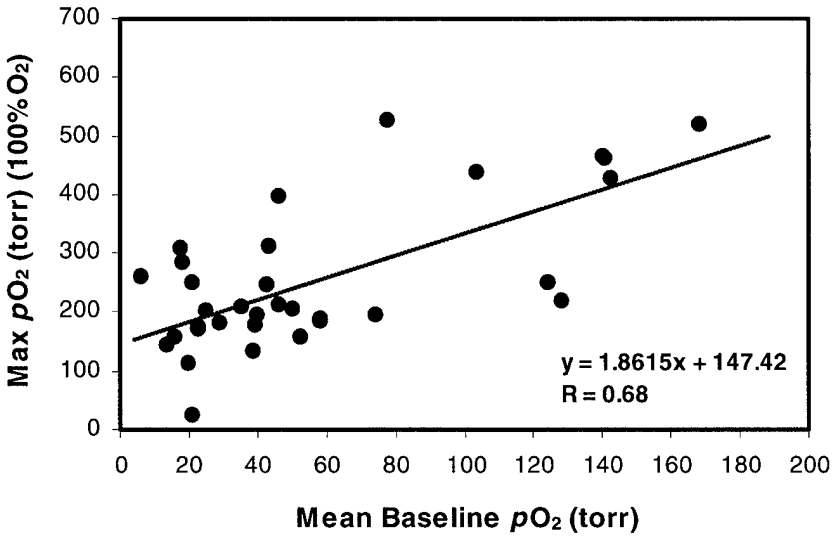


**Figure 27** Maximum $pO_2$ vs. initial mean baseline $pO_2$ for a group of voxels selected from breast tumor No.4 ($R$= 0.68).

In this study, all tumors showed a significant increase in $pO_2$ when the rats inhaled either 100% $O_2$ or carbogen. As expected, the level of increase was tumor dependent. The results for a group of seven tumors are summarized in **Figure 28**. Generally, tumors with lower baseline $pO_2$ tended to respond poorly to either 100% $O_2$ or carbogen breathing compared to those with higher baseline $pO_2$. The baseline hypoxic fraction for each individual tumor was also determined using the threshold $pO_2 < 10$ torr. It was found that there was a fairly strong linear relationship between baseline hypoxic fraction and baseline $pO_2$, as shown in **Figure 29**. It was also found that baseline hypoxic fraction correlated well with tumor volume (**Figure 30**). In addition, there was a fairly strong linear relationship between mean baseline $pO_2$ and tumor volume, as shown in **Figure 31**. **Table 7.6** summarizes the results of tumor tissue $pO_2$.

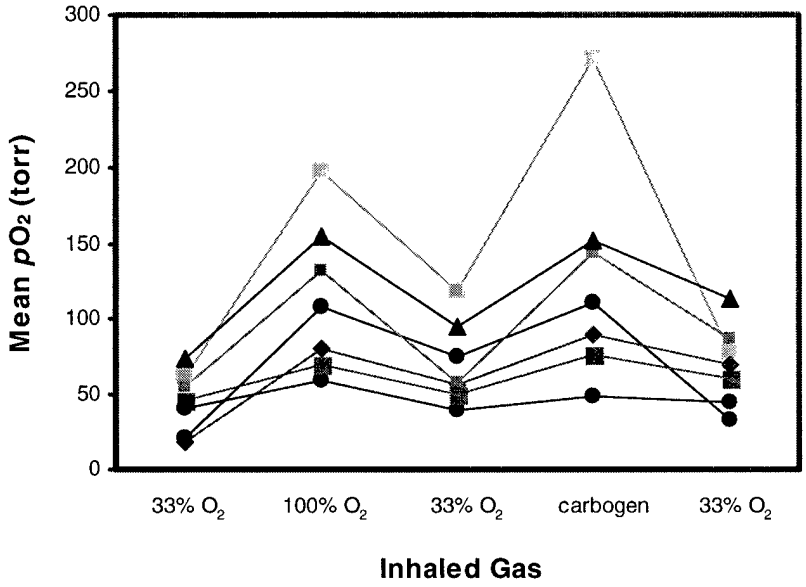


**Figure 28** Impact of inhaled gas on tumor oxygenation for a group of seven tumors.

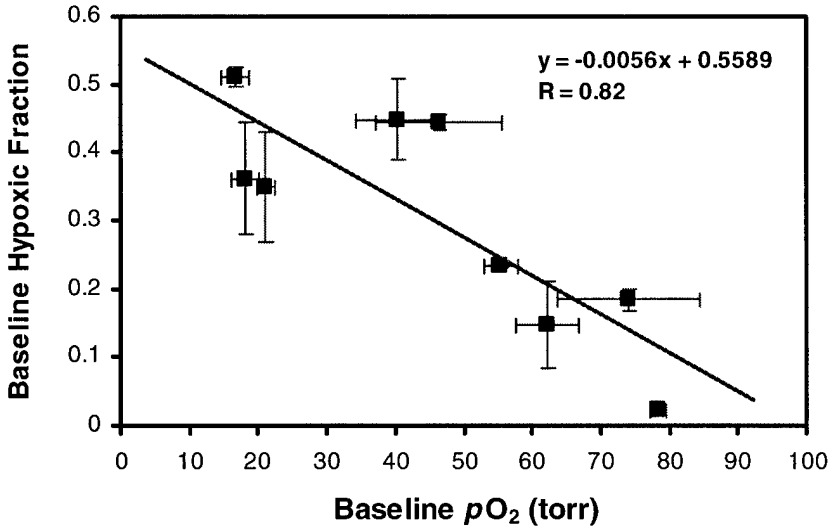


**Figure 29** Relationship between baseline $pO_2$ and baseline hypoxic fraction for a group of nine breast tumors.

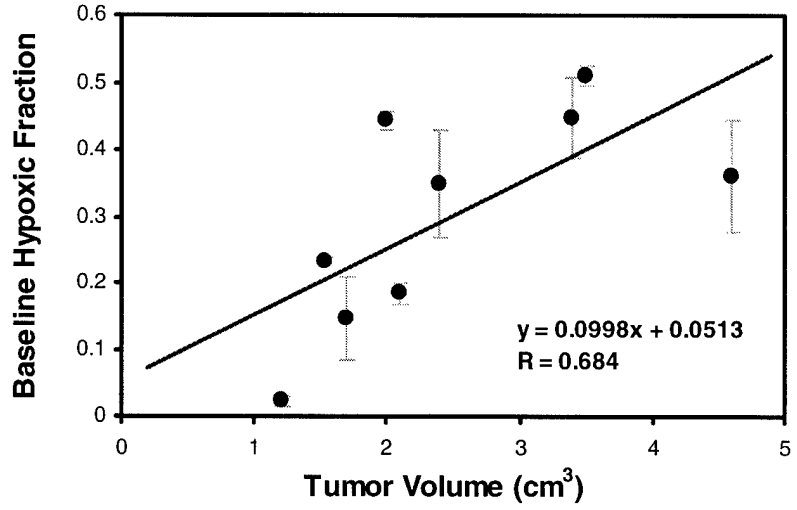


**Figure 30** Relationship between baseline hypoxic fraction and tumor volume for a group of nine breast tumors.

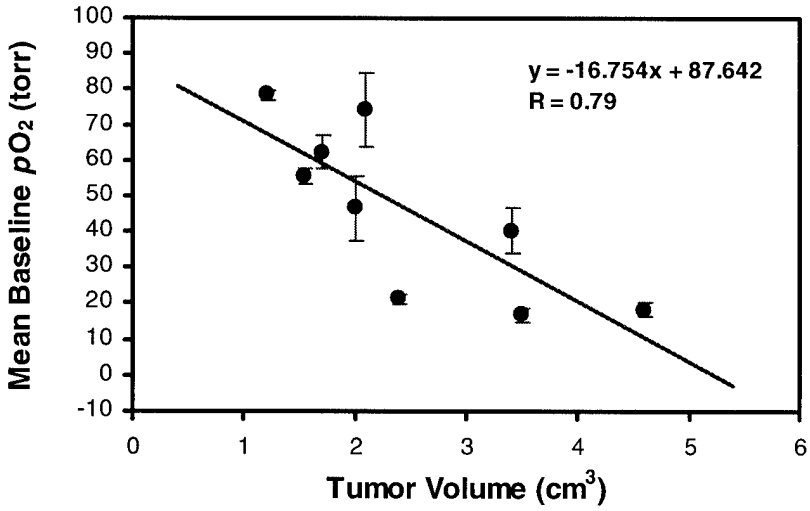


**Figure 31** Relationship between mean baseline $pO_2$ and tumor volume for a group of nine breast tumors.

**Table 14** Summary of tumor tissue $pO_2$ (Mean ± SE).

| Tumor Volume ($cm^3$) | Mean τ (min) | Mean Baseline $pO_2$ (torr) | Mean 100% $O_2$ $pO_2$ (torr) | Mean Carbogen $pO_2$ (torr) | Mean Baseline Hypoxic Fraction (< 10 torr) |
|---|---|---|---|---|---|
| **Small Tumors (Vol. < 2.0)** | 21.5 ± 8.3 | 63.3 ± 6.8 | 138.5 ± 19.4 | 156.6 ± 15.7 | 0.21 ± 0.08 |
| **Large Tumors (Vol. > 2.5)** | 27.4 ± 7.8 | 24.1 ± 5.5 | 80.6 ± 5.5 | 72.3 ± 10.3 | 0.42 ± 0.04 |

- **Discussion**

Since poorly oxygenated tumors tend to resist conventional therapy, there have been many efforts to re-oxygenate tumors prior to therapy. A simple intervention is respiratory challenge, i.e., attempting to elevate the oxygen concentration of the inhaled gas. Past clinical trials were often disappointing, but it is now thought that results were significantly influenced by the inability to identify hypoxic tumors (i.e., those that would benefit from manipulation). As techniques become available to measure tumor oxygenation, it is appropriate to reevaluate approaches to manipulating tumor oxygenation. By increasing the oxygen tension of the inspired gas, the arterial $s_aO_2$ should increase, leading to increased hemoglobin saturation of the tumor vasculature $\Delta[HbO_2]$, and hence, increased tumor tissue $pO_2$. The data presented in this report indicate that breathing elevated $O_2$ does indeed have a significant effect on tumor arterial $s_aO_2$, vascular $\Delta[HbO_2]$, and tissue $pO_2$. Significant changes were found in tumor vascular $\Delta[HbO_2]$ and in tissue $pO_2$ by ANOVA in both carbogen inhalation and 100% oxygen inhalation. There has been a debate as to whether carbogen is more effective at modulating tumor oxygenation than 100% oxygen since $CO_2$ is a peripheral vasoconstrictor. Indeed, recent work in a human glioma xenografts suggests that oxygen alone has no influence on tumor vascular oxygenation, whereas carbogen produces a pronounced effect. My results obtained with $^{19}$F-EPI seem to suggest that carbogen breathing is more effective than 100% $O_2$ breathing.

It is important to point out that some voxels gave negative $pO_2$ values even under the condition of breathing carbogen or 100% $O_2$. Several factors may contribute to this phenomenon; firstly, the temperature variations during the course of experiments; secondly, the uncertainty in the $R1$ estimate due to low SNR for certain voxels; and thirdly, uncertainty in the calibration constants. The second factor could be the dominant one. However, application of the proper thresholds based on $R1$ error rejects most unreliable data.

In this study, the rat rectal temperature was closely monitored during the course of experiments. Typically, the temperature variation was within 2 $^0$C, *i.e.*, $\Delta T \leq \pm 2\ ^0$C over a period of 4 ~ 5 hours. Since $R1$ of HFB is relatively insensitive to changes in temperature, the error in $pO_2$ introduced by temperature variation was insignificant. The order of the error can be estimated in the following way. From the general calibration equation , $R1$ can be expressed as

$$R1 = a + b \cdot T + c \cdot P + d \cdot T \cdot P \tag{24}$$

where $P$ is oxygen tension (torr), $a$ ($sec^{-1}$), $b$ ($sec^{-1}/^0C$), $c$ ($sec^{-1}$/torr), and $d$ ($sec^{1}/^0C \cdot torr$) are four calibration constants, and $T$ is temperature ($^0$C). Assuming a constant oxygen tension $P$, differentiating Equation (24) with respect to $T$ gives

$$\Delta R1 = b \cdot \Delta T + d \cdot P \cdot \Delta T \quad \text{or} \tag{25}$$

$$\Delta R1 = (b + d \cdot P) \cdot \Delta T \tag{26}$$

Equation (26) describes the relationship between the change in temperature, $\Delta T$, and the error in $R1$ caused by $\Delta T$, $\Delta R$. Using the calibration constants given in reference **[72]** and assuming $P = 5$ (torr), we obtain

$$\Delta R1 = \pm 0.00008888 \cdot \Delta T \tag{27}$$

Considering the worst case in which temperature changes by $\Delta T = \pm 2\ ^0$C, the corresponding change in $R1$, according to Equation (27), is

$$\Delta R1 = \pm 0.00017776\ (sec^{-1})$$

which gives an error in $pO_2$ of $\pm$ 0.095 (torr) $\approx \pm$ 0.1 (torr) using Equation (23). Clearly, the error in $pO_2$ caused by temperature variation was insignificant.

## Investigation of Tumor Vascular $\Delta[HbO_2]$ or $sO_2$ and $\Delta\ [Hb]_{Total}$

- **Oximetry Based on Near-Infrared Spectroscopy (NIRS)**

Near-Infrared Spectroscopy (NIRS) can be used to measure total hemoglobin concentration $[Hb]_{Total}$, oxyhemoglobin concentration $[HbO_2]$, and oxygen saturation ($sO_2$) based on observed phenomena: firstly, the absorption of light by deoxyhemoglobin (Hb) and oxyhemoglobin ($HbO_2$) predominates over water and other macromolecules at the selected wavelengths; secondly, the absorption coefficient of deoxyhemoglobin (Hb)

differs substantially from that of oxyhemoglobin ($HbO_2$) in the NIR region (700 – 900 nm). The traditional continuous wave spectroscopy (CWS) uses the classical Beer-Lambert's law to determine the absorption coefficient of the sample over a known optical path length and thus the concentration of the sample. Current available CWS techniques include dual-wavelength and multi-wavelength light spectroscopy, pulse oximetry, and CW brain functional imaging systems. The essence of Beer-Lambert's law states that equal thickness of an absorbing material will absorb a constant fraction of the energy incident upon it. Mathematically, it can be written as:

$$\begin{cases} \mu_a = -\frac{1}{L} \cdot \ln(\frac{I}{I_0}) \\ C = \frac{\mu_a}{\varepsilon} \end{cases}, \tag{28}$$

where $\mu_a$ is the absorption coefficient of the sample ($cm^{-1}$), $L$ is the optical path length of the light (cm), $I_0$ and $I$ are the incident and transmitted light intensity, respectively, $\varepsilon$ is the extinction coefficient of the sample ($cm^{-1}mM^{-1}$), and $C$ is the concentration of the sample (mM).

Theoretically speaking, however, Beer-Lambert's law is valid only for homogenous translucent solutions that do not scatter light. In a continuous medium, light photons travel at the speed of light that is dependent only on the refractive index of the medium. If this is a scattering medium, photons travel with the constant speed and direction until they collide elastically with a scatterer, resulting in a change in traveling direction. Depending on the scattering properties of the medium, the scattered photons may travel in a random direction, or in a preferential forward or backward direction. The total distance or optical path length traveled by photons between the source and detector is much longer than the geometric distance between the source and detector. In this case, Beer-Lambert's law is not valid since exact $L$ is not known. In the absence of scatterers, the total optical path length traveled by photons before detection is simply the geometric distance between the source and detector. Thus, $L$ is known and Beer-Lambert's law is valid. Since biological tissues are highly inhomogeneous and optically turbid, it is obvious that we cannot directly apply Beer-Lambert's law to biological tissues. Light attenuation results not only from tissue absorption, but also from tissue scattering. Light absorption results mainly from absorption of oxyhemoglobin and deoxyhemoglobin, myoglobin, and cytochrome oxidase. The amount of light absorption depends on the concentrations of these molecules. Light scattering results from mitochondrion, protein, and various ions. Scattering gives rise to distributed path lengths that are significantly

longer than the geometric distance between the source and detector used in Beer-Lambert's law, leading to a distorted absorption spectrum of the sample. To take scattering into account, we need to use the photon diffusion approximation theory [**73**] based on a general mass transfer diffusion equation. This equation allows us to describe photon migration in scattering media and compute both absorption and scattering coefficients. For this study, I used a new dual wavelength, homodyne frequency-domain near-infrared spectroscopy (NIRS) system to measure changes in tumor vascular oxyhemoglobin concentration [$HbO_2$] and total hemoglobin concentration $[Hb]_{Total}$. The theoretical formulation of the system is based on a modified Beer-Lambert's law.

- **In-Phase and Quadrature Phase Detection System**

The dual wavelength, homodyne NIRS system (wavelengths 758 nm and 782 nm) is based on an In-phase and Quadrature-phase chip (I&Q chip). These wavelengths were chosen because they not only allow the calculation of [$HbO_2$] and $[Hb]_{Total}$, but also fall into the range of wavelengths compatible with the low cost photo multiplier tube (PMT). The system uses only one RF source to modulate the light emitted by two laser diodes and lets the I&Q chip to determine amplitude and phase changes of light attenuated by the sample [**74**].

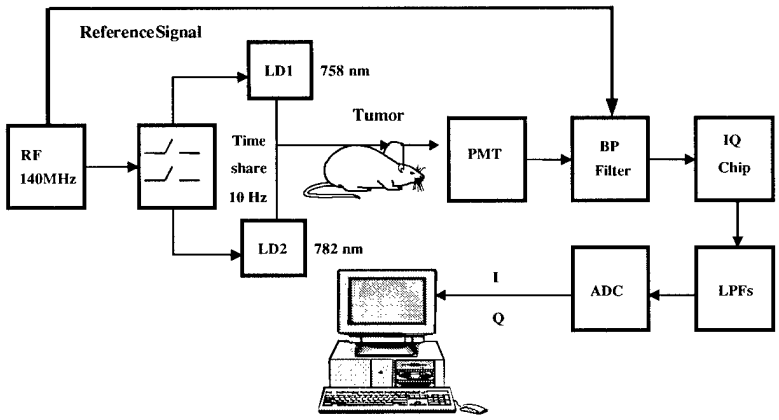


**Figure 32.** A schematic diagram of the NIRS I&Q system.

**Figure 32** shows a schematic diagram of the NIRS system. An RF source modulates the light from two laser diodes (LD1 and LD2) at 140 MHz through a time-sharing system. The light passes through fiber optic cables, is transmitted through the tumor tissue, and collected by a second fiber bundle. The light is then amplified by a photo multiplier tube (PMT) and filtered by a bandpass (BP) filter to pick up only the signal being modulated at 140 MHz. The signal is demodulated into I and Q components by the I&Q chip and filtered again by two lowpass filters (LPFs) to select the DC

components. These final DC signals are digitized by a 12-bit analog to digital converter (ADC) and stored in a computer. Light amplitude and phase changes caused by the tumor attenuation are used to compute changes in tumor vascular oxyhemoglobin concentration [$HbO_2$] and total hemoglobin concentration [Hb]$_{Total}$. The NIRS system is interfaced to a laptop via a National Instruments data acquisition card (DAQCard-1200) that is fully software-configurable. A National Instruments DAQ driver, NI-DAQ, is used to control the operations of the card. The graphical programming language LabView$^{TM}$ is used to create a graphical user interface (GUI) for controlling data acquisition, processing, and display [**75**]. The raw data are saved in a text format and can be further processed using a variety of digital signal processing (DSP) techniques.

- **Algorithms for Computing Tumor Vascular [$HbO_2$] and [Hb]$_{Total}$**

In principle, it is possible to obtain absolute values of [Hb]$_{Total}$, [$HbO_2$], and the percent oxyhemoglobin saturation $sO_2$ (defined as [$HbO_2$]/[Hb]$_{Total}$), given both amplitude and phase information [**76**]. However, because of tumors' inhomogeneous nature and limited dimensions, classical photon diffusion approximation does not hold and such an absolute quantification would be erroneous using traditional methods. An alternative approach is to modify Beer-Lambert's law and use the measured transmitted light amplitude to compute the trends in the changing absorption coefficients, and thus, changes in [Hb]$_{Total}$ and [$HbO_2$], *i.e.*, $\Delta$[Hb]$_{Total}$ and $\Delta$[$HbO_2$] [**77**]. The modified Beer-Lambert's law can be written as:

$$\Delta\mu_a = \mu_{aP} - \mu_{aB} = \frac{1}{L}\log(\frac{A_B}{A_P}), \tag{29}$$

where letters P and B stand for perturbation and baseline, respectively, $A_B$ is the transmitted baseline light amplitude, $A_P$ is the transmitted light amplitude under the physiological perturbation, and $L$ is the optical path length between the source and detector. The quantity $(A_B / A_P)$ can be obtained by direct measurement and $L$ can be estimated from an empirical formula [**76**, **78**]:

$$L = DPF \times d, \tag{30}$$

where $DPF$ is a dimensionless factor, called the differential path length factor and $d$ is the direct source to detector separation (cm). Since $DPF$ is not a very well defined quantity for solid rat tumors, it is assumed to be 1 for simplicity in this study.

To obtain the absorption coefficients of deoxyhemoglobin and oxyhemoglobin, it is also assumed that in the NIR region background absorbance is negligible and deoxyhemoglobin and oxyhemoglobin are the predominant light absorbing molecules in the tumor tissue. Therefore, the absorption coefficient of the tumor can be approximated

as the product of the extinction coefficients for deoxyhemoglobin and oxyhemoglobin and their respective concentrations:

$$\mu_a^{\lambda} = \varepsilon_{\mathrm{Hb}}^{\lambda}[\mathrm{Hb}] + \varepsilon_{\mathrm{HbO_2}}^{\lambda}[\mathrm{HbO_2}], \tag{31}$$

Equation (31) has two unknowns: [Hb] and [$HbO_2$] and we can not solve for them with only one equation. If we use NIR light at two different wavelengths, then we have two equations and [Hb] and [$HbO_2$] can be obtained by solving following linear system of equations

$$\mu_a^{758} = \varepsilon_{\mathrm{Hb}}^{758} \cdot [\mathrm{Hb}] + \varepsilon_{\mathrm{HbO_2}}^{758} \cdot [\mathrm{HbO_2}], \tag{32}$$

$$\mu_a^{782} = \varepsilon_{\mathrm{Hb}}^{782} \cdot [\mathrm{Hb}] + \varepsilon_{\mathrm{HbO_2}}^{782} \cdot [\mathrm{HbO_2}], \tag{33}$$

where $\mu_a^{758}$ and $\mu_a^{782}$ are the absorption coefficients, $\varepsilon_{\mathrm{Hb}}^{758}$ and $\varepsilon_{\mathrm{Hb}}^{782}$ are the extinction coefficients for deoxyhemoglobin, $\varepsilon_{\mathrm{HbO_2}}^{758}$ and $\varepsilon_{\mathrm{HbO_2}}^{782}$ are the extinction coefficients for oxyhemoglobin at the wavelengths 758 nm and 782 nm, respectively, and [Hb] and [$HbO_2$] are the deoxyhemoglobin and oxyhemoglobin concentrations, respectively. Since $\varepsilon_{\mathrm{Hb}}^{758}, \varepsilon_{\mathrm{Hb}}^{782}, \varepsilon_{\mathrm{HbO_2}}^{758}$, and $\varepsilon_{\mathrm{HbO_2}}^{782}$ are physical constants, changes in [$HbO_2$] and [Hb] in tumor tissue vasculature cause changes in $\mu_a^{758}$ and $\mu_a^{782}$ according to Equations (32) and (33). Thus, by measuring changes in $\mu_a^{758}$ and $\mu_a^{782}$, we can determine changes in [$HbO_2$] and [Hb]. Combining Equations (29), (32), and (33) yields equations for computing changes in [Hb] and [$HbO_2$] [**77**].

$$\Delta[\mathrm{Hb}] = [\mathrm{Hb}]_{\mathrm{P}} - [\mathrm{Hb}]_{\mathrm{B}} = \frac{\varepsilon_{\mathrm{HbO_2}}^{758} \log(\frac{A_{\mathrm{B}}}{A_{\mathrm{P}}})^{782} - \varepsilon_{\mathrm{HbO_2}}^{782} \log(\frac{A_{\mathrm{B}}}{A_{\mathrm{P}}})^{758}}{L(\varepsilon_{\mathrm{Hb}}^{782}\varepsilon_{\mathrm{HbO_2}}^{758} - \varepsilon_{\mathrm{Hb}}^{758}\varepsilon_{\mathrm{HbO_2}}^{782})}, \tag{34}$$

$$\Delta[\mathrm{HbO_2}] = [\mathrm{HbO_2}]_{\mathrm{P}} - [\mathrm{HbO_2}]_{\mathrm{B}} = \frac{\varepsilon_{\mathrm{Hb}}^{782} \log(\frac{A_{\mathrm{B}}}{A_{\mathrm{P}}})^{758} - \varepsilon_{\mathrm{Hb}}^{758} \log(\frac{A_{\mathrm{B}}}{A_{\mathrm{P}}})^{782}}{L(\varepsilon_{\mathrm{Hb}}^{782}\varepsilon_{\mathrm{HbO_2}}^{758} - \varepsilon_{\mathrm{Hb}}^{758}\varepsilon_{\mathrm{HbO_2}}^{782})}, \tag{35}$$

where $\Delta[]$ represents a change in concentration. At room temperature (20 ~ 24 $^0$C) and a *p*H of 7.172, $\varepsilon_{\mathrm{Hb}}^{758} = 0.359$ $\mathrm{cm^{-1}mM^{-1}}$, $\varepsilon_{\mathrm{HbO_2}}^{758} = 0.1496$ $\mathrm{cm^{-1}mM^{-1}}$, $\varepsilon_{\mathrm{Hb}}^{782} = 0.265$ $\mathrm{cm^{-1}mM^{-1}}$, and $\varepsilon_{\mathrm{HbO_2}}^{782} = 0.178$ $\mathrm{cm^{-1}mM^{-1}}$, which were obtained by linear interpolation based on the data published by Zijlstra *et al.* [**79**]. Thus, the final expressions for computing changes in [Hb] (mM), [$HbO_2$] (mM), and $[\mathrm{Hb}]_{\mathrm{Total}}$ (mM) are:

$$\Delta[\mathrm{Hb}] = \frac{1}{L}\left[7.34 \cdot \log(\frac{A_B}{A_P})^{758} - 6.17 \cdot \log(\frac{A_B}{A_P})^{782}\right], \quad (36)$$

$$\Delta[\mathrm{HbO_2}] = \frac{1}{L}\left[-10.92 \cdot \log(\frac{A_B}{A_P})^{758} + 14.80 \cdot \log(\frac{A_B}{A_P})^{782}\right], \quad (37)$$

$$\begin{aligned}\Delta[\mathrm{Hb}]_{\mathrm{Total}} &= \Delta\{[\mathrm{HbO_2}] + [\mathrm{Hb}]\} \\ &= \frac{1}{L}\left[-3.58 \cdot \log(\frac{A_B}{A_P})^{758} + 8.63 \cdot \log(\frac{A_B}{A_P})^{782}\right],\end{aligned} \quad (38)$$

where Equation (38) represents a change in total hemoglobin concentration in the tumor, a physiological parameter that is linearly proportional to a change in total blood volume in the tumor, assuming a constant hematocrit.

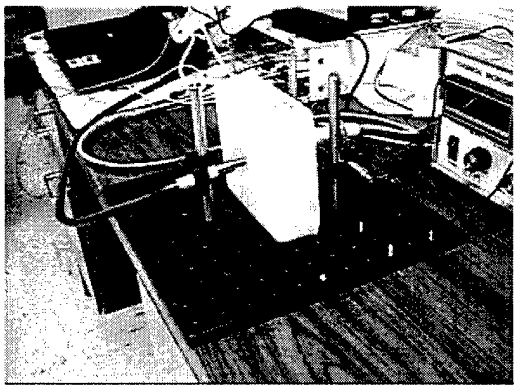

**Figure 33** Stability of the I&Q system was evaluated using a 4-cm thick tissue equivalent phantom.

- **I&Q System Drift Test**

Good stability and reproducibility of the I&Q system was crucial in tumor oxygenation measurements. Poor stability and reproducibility gave unreliable, even incorrect measurements. Thus, it was necessary to systematically evaluate and validate the performance of the I&Q system using established protocols. The first evaluation performed was the drift test. Prior to the tests, the I&Q system was warmed up for about 20 - 30 minutes. Then, the stability of the I&Q system was evaluated using a 4-cm thick tissue equivalent phantom with stable optical properties [**80**] in transmittance mode

(**Figure 33**). The data were acquired with a sampling frequency of 2.22 Hz for about 30 minutes, giving a total of 4000 data points. The same test procedure was repeated several times to assess the reproducibility of the I&Q system. In addition, the stability and reproducibility of of the I&Q system was further evaluated using a chunk of fresh red pork meat (3 x 3 x 4 $cm^3$), also configured in transmittance mode. However, in this case, the source-to-detector separation was 3.0 cm. **Figure 34** shows the results of a representative system drift test for $\Delta[HbO_2]$ and $\Delta[Hb]_{Total}$ over a period of 33 minutes. The test was performed using a tissue equivalent phantom with a source-to-detector separation of 4.0 cm. For this particular drift test, the standard deviations (SD) for $\Delta[HbO_2]$ and $\Delta[Hb]_{Total}$ were 0.0056 (mM) and 0.0034 (mM), respectively, indicating that the I&Q system had an excellent stability. Since SD is the most commonly used statistic for describing variability or stability, mean $\Delta[HbO_2]$ and mean $\Delta[Hb]_{Total}$ were not computed.

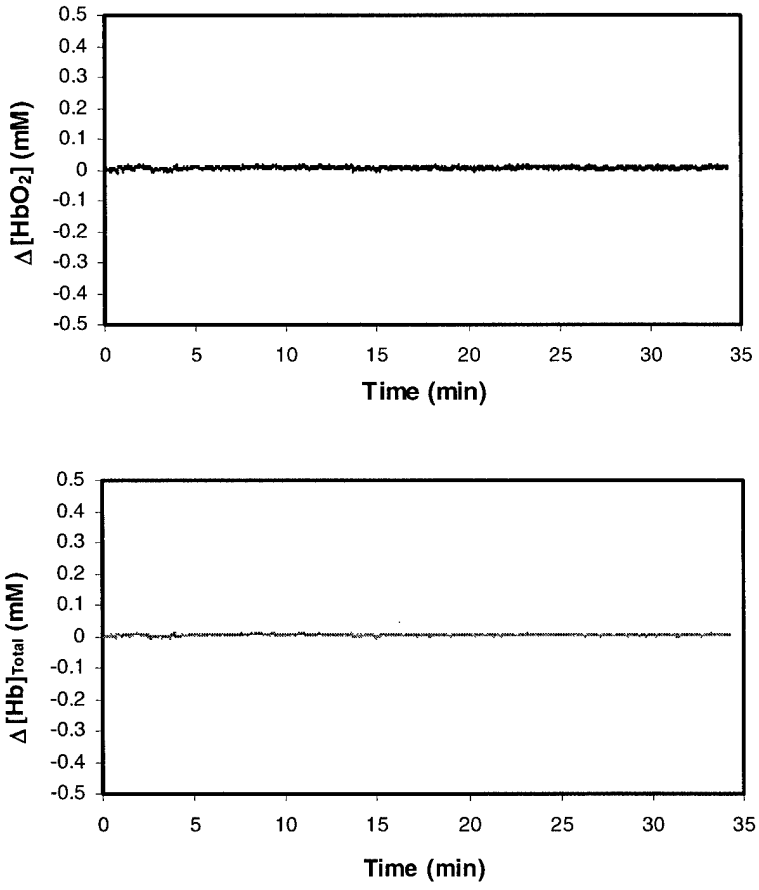


**Figure 34** Results of a representative system drift test for $\Delta[HbO_2]$ and $\Delta[Hb]_{Total}$.

**Table 15** is a summary of five system drift tests obtained under the similar experimental conditions. As can be seen from **Table 15**, the standard deviations for all drift tests were of the same order, suggesting the I&Q system was very stable in terms of variability. The standard error (SE) fell in the range of $3.0 \times 10^{-5} \sim 7.45 \times 10^{-5}$.

**Table 15** Summary of five system drift tests obtained using a tissue phantom (SD = Standard Deviation). The range of standard error (SE): $3.0 \times 10^{-5} \sim 7.45 \times 10^{-5}$

| No | SD of $\Delta[HbO_2]$ | SD of $\Delta[Hb]_{Total}$ |
|---|---|---|
| 1 | 0.0053 | 0.0037 |
| 2 | 0.0043 | 0.0025 |
| 3 | 0.0056 | 0.0034 |
| 4 | 0.0066 | 0.0032 |
| 5 | 0.0046 | 0.0023 |

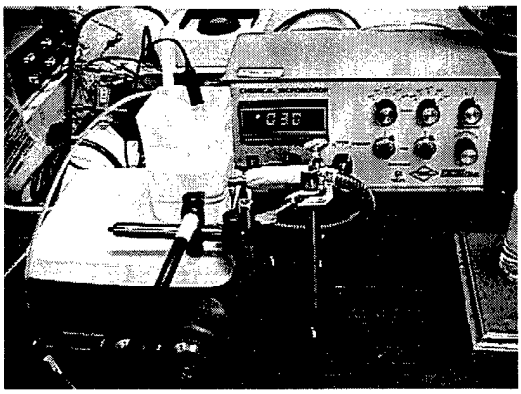

**Figure 35** The I&Q system was validated using 250 ml of a 0.5% intralipid solution and repeated addition of 2 ml fresh rabbit blood.

- **Blood Test**

In general, two factors have direct impact on the accuracy and sensitivity of a medical instrument: the precision of the instrument itself and the mathematical algorithm used to compute the desired physiological parameters from the measured electrical signal, voltage or current. To validate the sensitivity of the I&Q system, two different kinds of experiments were performed using intralipid, a milk-like product used to treat patients

with malnutrition, and fresh rabbit blood. The first was to validate sensitivity of the I&Q system in response to a change in $[Hb]_{Total}$. The second was aimed at validating sensitivity of the I&Q system in response to a change in $[HbO_2]$. In the first case, a vessel with a squared cross section was filled with 250 ml of a 0.5% intralipid solution (intralipid + physiological saline) and then sealed with parafilm. The vessel was placed on a magnetic stirrer/heater. A plastic tube connected to different gases was inserted into the solution in the vessel. In some cases, a $pO_2$ electrode was also inserted into the solution to monitor oxygen tension of the solution. The temperature of the solution was maintained at 37 $^0$C by the heater. The light source and the detector were attached to the side of the vessel at $90^0$ relative to each other and maintained in place by a mechanical holder (**Figure 35**). Initially, air was bubbled through the solution until a steady state was obtained. 2-ml fresh rabbit blood, collected on heparin to prevent blood from clotting, was then added to the intralipid solution. In the meantime, air, $N_2$, and $O_2$ were continuously bubbled through the solution alternatively. In the second case, in order to validate $\Delta[HbO_2]$ measurement, 3-ml fresh rabbit blood was added to the intralipid solution first. Air was then bubbled through the solution until a steady state was reached. Next, the blood was deoxygenated by bubbling pure nitrogen through the solution. Once $\Delta[HbO_2]$ reached a steady state, the blood was reoxygenated by bubbling air through the solution. This oxy-deoxy cycle was repeated three times to evaluate the reproducibility of the I&Q system.

**Figure 36** shows the results of a representative blood test. 2 ml fresh rat blood was added to an intralipid solution twice, followed by 2 ml fresh rabbit blood once to test any possible significant difference in terms of NIR absorptivity. As is seen in **Figure 36**, $\Delta[HbO_2]$ and $\Delta[Hb]_{Total}$ increased linearly with the repeated addition of blood, while air was bubbling through the intralipid solution. With the sensitivity of our current NIRS system, no significant differences in increases in $\Delta[HbO_2]$ and $\Delta[Hb]_{Total}$ were detected with respect to different hemoglobin species. Results of the blood test are summarized in **Table 16**.

**Table 16** Summary of the blood test.

| Blood Volume (ml) | Change in $\Delta[HbO_2]$ (mM) | Change in $\Delta[Hb]_{Total}$ (mM) |
|---|---|---|
| 2 (rat) | 0.543 ± 0.006 | 0.355 ± 0.003 |
| 2 (rat) | 0.558 ± 0.006 | 0.366 ± 0.003 |
| 2 (rabbit) | 0.523 ± 0.006 | 0.343 ± 0.003 |

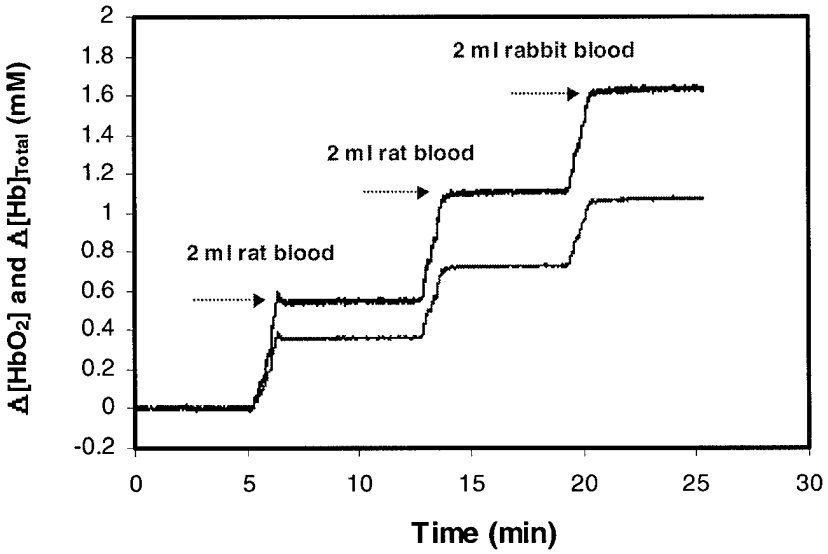


**Figure 36** Results of a representative blood test.

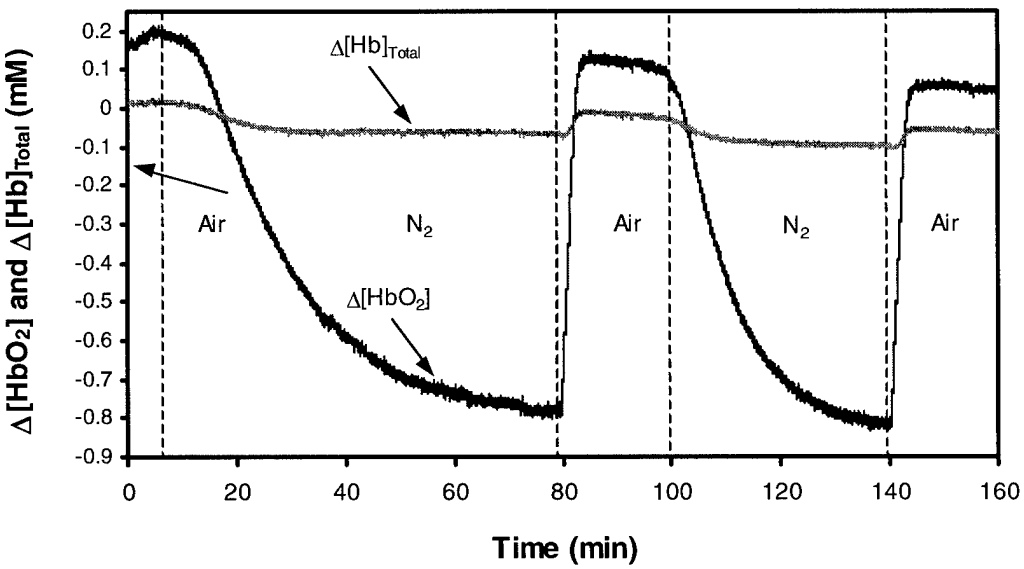


**Figure 37** Repeated oxygenation-deoxygenation cycles of 3-ml fresh rabbit blood by continuously bubbling air and $N_2$ alternately through the intralipid solution.

**Figure 37** shows the repeated oxygenation-deoxygenation cycles of 3-ml fresh rabbit blood mixed with 250-ml intralipid solution by continuously bubbling air and $N_2$ alternately through the intralipid solution. The slight fluctuation in $\Delta[Hb]_{Total}$ was related to air bubbling. The temperature of the intralipid solution was maintained at 23 $^0$C. The I&Q system demonstrated a good reproducibility with respect to repeated oxygenation-deoxygenation interventions.

- **Arm Ischemia Test**

The accuracy and sensitivity of the I&Q system were also evaluated by *in vivo* arm ischemia tests on human subjects. Four physically healthy fellow BME students were recruited in this study after giving their informed consent. The source and detector were placed on the anterior (flexor) compartment of the forearm in reflectance mode with a separation of 3 cm and secured by a circular brace. A blood pressure cuff was then placed around the biceps brachii muscle in the upper arm. The subjects were asked to sit still and not to move the arm during the course of the experiments. The experiments were initiated after the subjects' $\Delta[HbO_2]$ and $\Delta[Hb]_{Total}$ had reached a steady state. Two different experimental protocols were used. In the first case, baseline $\Delta[HbO_2]$ and $\Delta[Hb]_{Total}$ were measured for 8 minutes. Then, the blood pressure cuff was inflated to 100 mmHg to occlude the venous blood outflow and $\Delta[HbO_2]$ and $\Delta[Hb]_{Total}$ were measured for 8 minutes again. Following the cuff deflation, $\Delta[HbO_2]$ and $\Delta[Hb]_{Total}$ were measured for another 8 minutes. In the second case, both arterial inflow and venous outflow were occluded by inflating the blood pressure cuff to 230 mmHg.

Representative $\Delta[HbO_2]$ and $\Delta[Hb]_{Total}$ during a forearm venous occlusion test are shown in **Figure 38**. Prior to venous occlusion, the mean baseline $\Delta[HbO_2]$ and $\Delta[Hb]_{Total}$ values were 0.015 ± 0.02 (mM) and 0.016 ± 0.01 (mM), respectively. Immediately following venous occlusion, $\Delta[HbO_2]$ and $\Delta[Hb]_{Total}$ increased gradually and significantly ($p < 0.0001$), yielding final mean values of 0.84 ± 0.02 (mM) and 0.81 ± 0.04 (mM), respectively. After the blood pressure cuff was deflated, $\Delta[HbO_2]$ and $\Delta[Hb]_{Total}$ returned to the initial baseline values very rapidly. **Figure 39** shows the results of a second forearm occlusion test. However, in this example, both arterial blood inflow and venous blood outflow were occluded by inflating the blood pressure cuff to 230 mmHg. Thus, the time course profiles of $\Delta[HbO_2]$ and $\Delta[Hb]_{Total}$ were very different from those shown in **Figure 38**. The noise in the data was caused by accidental arm movements. Prior to the cuff inflation, $\Delta[HbO_2]$ and $\Delta[Hb]_{Total}$ were basically constant. After the blood pressure cuff was inflated to 230 mmHg, $\Delta[HbO_2]$ dropped slowly, but significantly ($p < 0.0001$) as the oxygen was being consumed in aerobic respiration by the forearm. As expected, $\Delta[Hb]_{Total}$ did not change because both arterial blood inflow and venous blood outflow were occluded and the total blood volume in the forearm was constant. Immediately following the deflation of the blood pressure cuff, both $\Delta[HbO_2]$ and $\Delta[Hb]_{Total}$ showed

significant momentary overshoot ($p < 0.0001$) as the oxygenated blood flushed into the forearm, followed by a fast drop and a slow return to initial baseline values as the venous outflow returned the blood to the heart.

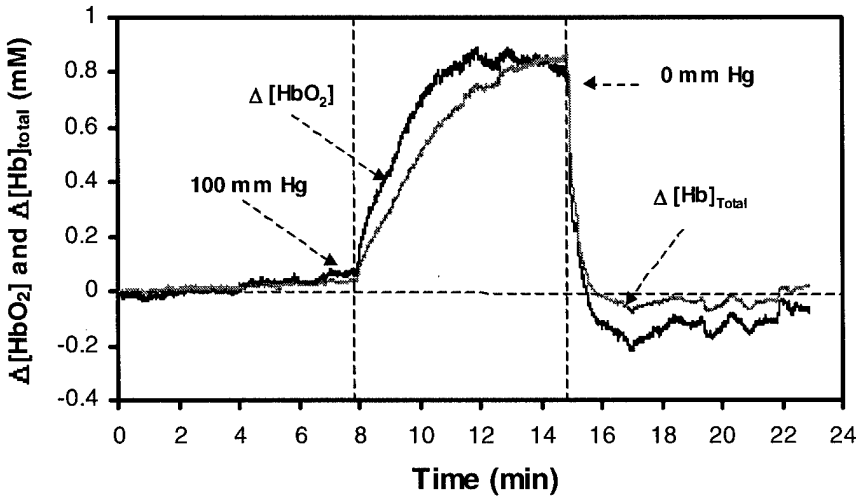


**Figure 38** Representative $\Delta[HbO_2]$ and $\Delta[Hb]_{Total}$ during a forearm venous occlusion experiment.

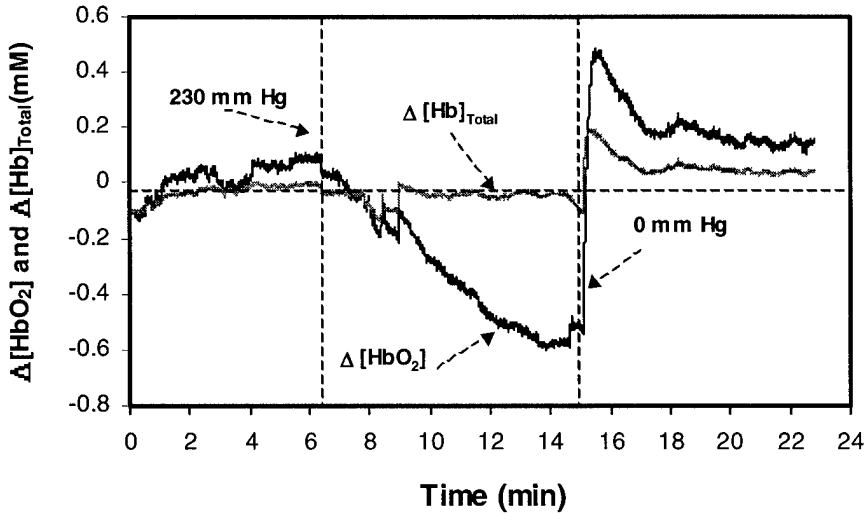


**Figure 39** Results of a second forearm occlusion test. In this case, the blood pressure cuff was inflated to 230 mmHg.

- **Investigation of Tumor Vascular $\Delta[HbO_2]$ and $\Delta[Hb]_{Total}$ by NIRS**

Once the mammary tumors reached ~1 cm diameter (~ 0.5 $cm^3$), corresponding to a typical lower limit of tumor detected in patients, experiments were initiated. I chose to use relatively large tumors in order to ensure that the NIRS interrogated only the tumor tissue rather than the surrounding normal skin tissue. The rats were anesthetized with 200 μl ketamine hydrochloride i.p. (100 mg/ml; Aveco, Fort Dodge, IA) and were maintained under general gaseous anesthesia using a small animal anesthesia unit with air (1.0 l/min) and 1.0% isoflurane (Ohmeda PPD Inc., Fort Dodge, IA). Prior to experiments, tumor hair was cut with a pair of surgical scissors to reduce NIR light scattering and tumor's three orthogonal diameters were measured with a caliper for estimating tumor volume. The rats were placed on their sides in an animal bed and stabilized using tape to reduce motion artifacts caused by rats' breathing movements. The body temperature was maintained at about 37 °C by a warm water blanket connected a water pump (K-MOD 100, Baxter Healthcare Co., Deerfield, IL). A fiber optic pulse oximeter (Nonin Medical, Inc., Plymouth, MN) was placed on the hind foot to monitor arterial hemoglobin saturation ($s_aO_2$) and heart rate (HR), and a thermocouple (Cole-Parmer Instrument Co., Vernon Hills, IL) was inserted rectally to monitor core temperature (**Figure 40**).

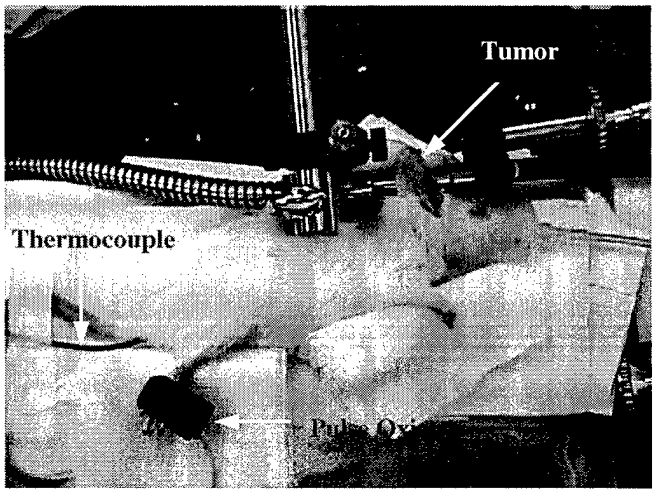


**Figure 40** A photo of the NIRS system experimental setup.

The experiments were performed in transmittance optical mode. In this configuration, the light source and detector were positioned on opposite sides of the tumor and stabilized by a mechanical mechanism. The light passed through and was attenuated by the tumor. The transmitted light was then collected by the detector. In this way, the NIRS measured $\Delta[HbO_2]$ and $\Delta[Hb]_{Total}$ in both peripheral and central regions of the tumor, yielding an average $\Delta[HbO_2]$ and $\Delta[Hb]_{Total}$ (**Figure 41**). It was important to

position the light source and detector in such a way that they made very good optical contact with the tumor, but did not exert excessive force on it. This was because excessive pressure on the tumor could hinder the tumor blood flow and thus, affect $\Delta[HbO_2]$ and $\Delta[Hb]_{Total}$ measurements. In this study, the following respiratory challenge paradigm was employed:

***Air*** $\rightarrow$ ***Carbogen*** $\rightarrow$ ***Air*** $\rightarrow$ ***Carbogen*** $\rightarrow$ ***Air***

(21% $O_2$) (95% $O_2$ + 5% $CO_2$)

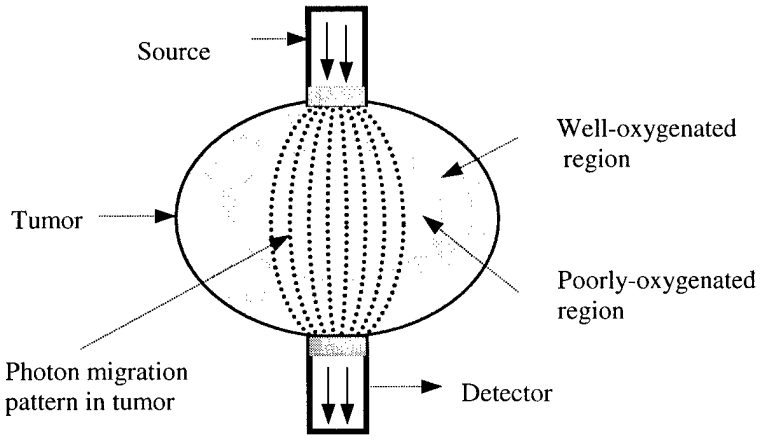


**Figure 41** A schematic diagram of transmittance optical mode.

Prior to the *in vivo* NIRS experiments, the I&Q system was warmed up for about 30 minutes. Then, 5 ~ 10 minute test data were acquired to check the stability of the system using a tissue equivalent phantom [**80**]. Once the system reached a steady state, a series of NIRS experiments was performed to determine tumor vascular $\Delta[HbO_2]$ and $\Delta[Hb]_{Total}$ according to the respiratory challenge paradigm described above. Rats breathed medical grade air (1 l/min) as a baseline for about 10 ~ 15 minutes for the first phase and then breathed each gas for about 20 ~ 25 mimutes for each of the subsequent phases. The five-phase experiment took about 90 ~ 115 minutes, acquiring a total of 12,000 ~ 16,000 data points at a sampling frequency of 2.22 Hz. During the course of the experiment, rat core temperature was closely monitored as a change in temperature would cause a change in the affinity of hemoglobin for oxygen, thus, a change in $\Delta[HbO_2]$, and also purturb extinction coefficient $\varepsilon$. To investigate the relationship between tumor vascular $\Delta[HbO_2]$ and tumor growth, each tumor was examined three times at different sizes during its growth (< 2, 5, and 10 $cm^3$, respectively).

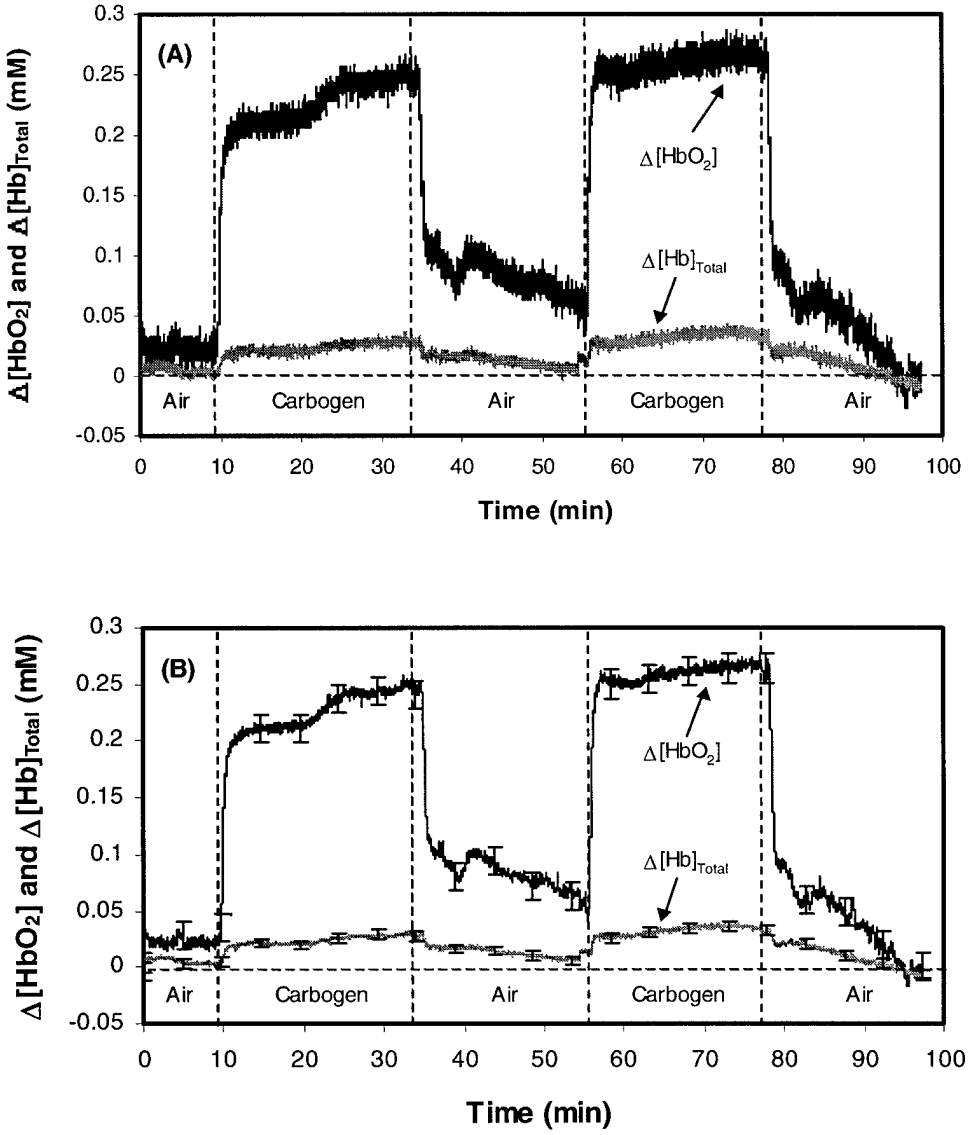


**Figure 42** Time course profiles of $\Delta[HbO_2]$ and $\Delta[Hb]_{Total}$ in response to respiratory challenge for breast tumor No. 1 (**A**) and corresponding postprocessed curves (**B**)

**Figure 42(A)** shows the time course impacts of inhaled gases on changes in tumor vascular hemoglobin oxygen saturation $\Delta[HbO_2]$ and total hemoglobin concentration $\Delta[Hb]_{Total}$ for a representative 13762NF breast tumor (14.8 $cm^3$) (tumor No. 1). The data were acquired in transmittance mode with a source-to-detector distance of 2.0 cm using the respiratory challenge paradigm described earlier. To show the quality of the raw data, averaging and filtering were not applied to the curve. The vertical dotted lines mark the beginning of each gas switch. The raw data were also smoothed using a seven-point

moving average routine. **Figure 42(B)** shows the corresponding post-processed data. The measurement uncertainties in $\Delta[HbO_2]$ and $\Delta[Hb]_{Total}$ were estimated using baseline data and were only labeled at representative locations.

For tumor No.1, the initial mean baseline $\Delta[HbO_2]$ value was $0.0 \pm 0.004$ (mM) when the rat was breathing air over a period of 10 minutes. Immediately following a gas switch from air to carbogen, $\Delta[HbO_2]$ rose rapidly and significantly ($p < 0.0001$) to about 0.223 (mM) within the first 70 seconds and then increased further at a slower rate, but still significant ($p < 0.0001$) for the next 20 minutes until an apparent saturation of 0.273 (mM) was reached. After the gas was switched back to air, $\Delta[HbO_2]$ did not decrease until about 30 – 40 seconds later, when a sudden and significant drop occurred ($p < 0.0001$), followed by a gradual return to the baseline. Note that there was a small overshoot in $\Delta[HbO_2]$ (~ 0.025 mM) as it was returning to the baseline and this overshoot also appeared in the second carbogen intervention. The second baseline $\Delta[HbO_2]$ value was a little higher than the initial baseline value ($p < 0.01$). This phenomenon was observed in several breast tumors. A very similar time course response pattern was observed for the next cycle of carbogen intervention, illustrating an excellent reproducibility of the dynamic changes in $\Delta[HbO_2]$ in response to respiratory challenge. $\Delta[Hb]_{Total}$ showed a similar time course profile in response to carbogen intervention, but at a less significant level in terms of amplitude ($p < 0.001$). $\Delta[Hb]_{Total}$ increased from a mean baseline value of $0.005 \pm 0.002$ (mM) to a final mean value of $0.028 \pm 0.004$ (mM) after the gas was switched to carbogen for the first cycle of intervention. A similar change in $\Delta[Hb]_{Total}$ was also observed for the second cycle of intervention. Assuming that $\Delta[Hb]_{Total}$ is proportional to total blood volume in the tumor, an increase in $\Delta[Hb]_{Total}$ showed that carbogen increased the total tumor blood volume. However, the total change in $\Delta[Hb]_{Total}$ was only 10% of that in $\Delta[HbO_2]$, indicating that the major portion of the increase in oxyhemoglobin concentration was contributed by increased hemoglobin loading reflecting an increased $pO_2$ in inhaled gas rather than by increased total blood volume. It is important to point out that similar time course response patterns were observed in most of 13762NF breast tumors, though the time constants and amplitudes of $\Delta[HbO_2]$ and $\Delta[Hb]_{Total}$ varied with tumor size.

To quantitatively characterize the dynamic features of $\Delta[HbO_2]$, the time constants and amplitudes of $\Delta[HbO_2]$ were computed using both a mono-exponential model and a bi-exponential model. The models were fitted to the rising portion of the raw data corresponding to each gas switch. **Figure 43 (A)** shows the result of the mono-exponential curve fit and **Figure 43 (B)** shows that of the bi-exponential curve fit for the first cycle of carbogen intervention. The solid curves represent the best fits to the $\Delta[HbO_2]$ data. The arrows mark the onset of carbogen intervention. The mono-exponential model yielded one time constant and one amplitude: $A = 0.1851 \pm 0.0002$

(mM) and $\tau = 0.530 \pm 0.006$ (min) with $R > 0.97$. The bi-exponential model gave two time constants and two amplitudes: $\tau_1 = 0.29 \pm 0.02$ (min), $\tau_2 = 3.99 \pm 0.06$ (min), $A_1 = 0.2 \pm 0.1$ (mM), and $A_2 = 0.482 \pm 0.006$ (mM) with $R > 0.99$. In this case, the bi-exponential model gave a better fit.

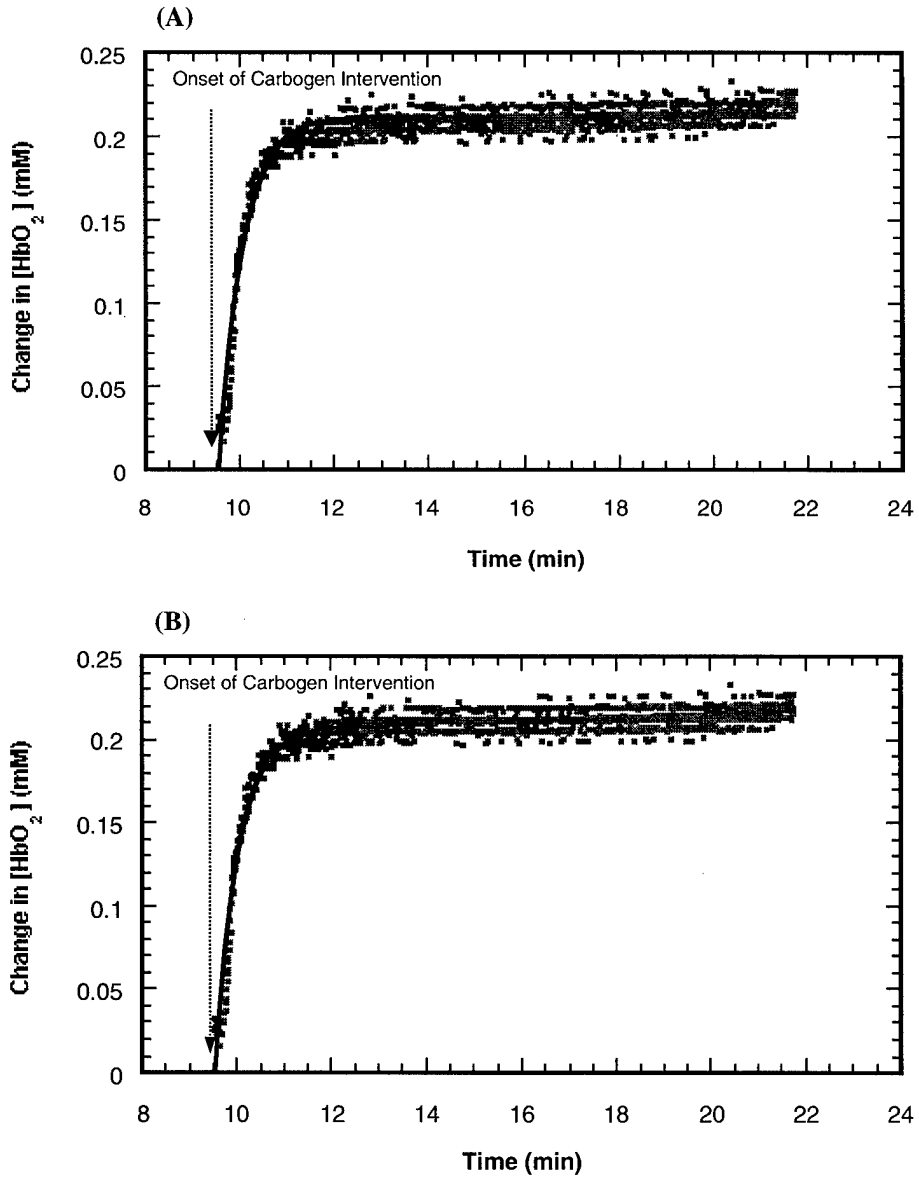


**Figure 43 (A)** Mono-exponential and **(B)** bi-exponential curve fits for tumor No. 1

**Figure 44** shows the time course profiles of $\Delta[HbO_2]$ and $\Delta[Hb]_{Total}$ in response to carbogen intervention for breast tumor No. 2 (9.9 $cm^3$). Again, similar response patterns were observed. After the gas was switched from air to carbogen, $\Delta[HbO_2]$ rose sharply and significantly ($p < 0.0001$) from the initial mean baseline $0.0 \pm 0.018$ (mM) to about 0.725 (mM) within the first 2.5 minutes. $\Delta[HbO_2]$ then continued to increase further at a slower rate for the rest duration of carbogen administration until a final maximum value of $0.79 \pm 0.03$ (mM) was reached. This was a three-fold increase in amplitude compared with breast tumor No. 1, suggesting that breast tumor No. 2 was better perfused. After the gas was switched back to air, $\Delta[HbO_2]$ decreased monotonically and exponentially back to baseline value. Here, I did not observe the small overshoot as seen in breast tumor No. 1 during the course of air breathing. $\Delta[HbO_2]$ exhibited a similar response pattern for the second cycle of carbogen intervention. $\Delta[Hb]_{Total}$ was found to respond to carbogen intervention differently from tumor No. 1 in terms of time course profile. It did not show a regular response pattern, as observed with most of the tumors. Initially, $\Delta[Hb]_{Total}$ increased sharply and significantly ($p < 0.001$) from 0.0 to $0.248 \pm 0.006$ (mM) in response to carbogen intervention, but changed very little thereafter. However, $\Delta[Hb]_{Total}$ began to decrease at the onset of the second carbogen intervention. It is important to point out that the decoupling of $\Delta[HbO_2]$ and $\Delta[Hb]_{Total}$ suggests the validity of the changes. Again, the dynamic response in $\Delta[HbO_2]$ was analyzed using both the mono-exponential and the bi-exponential models. The bi-exponential model gave: $\tau_1 = 0.854 \pm 0.008$ (min), $\tau_2 = 7.56 \pm 0.09$ (min), $A_1 = 0.8 \pm 0.3$ (mM), and $A_2 = 0.25 \pm 0.05$ (mM) with $R > 0.99$, whereas the mono-exponential model gave: $\tau = 1.65 \pm 0.02$ (min) and $A1 = 0.863 \pm 0.001$(mM) with $R = 0.938$. In this case, the bi-exponential model provided a better curve fit, too, as illustrated in **Figure 45**.

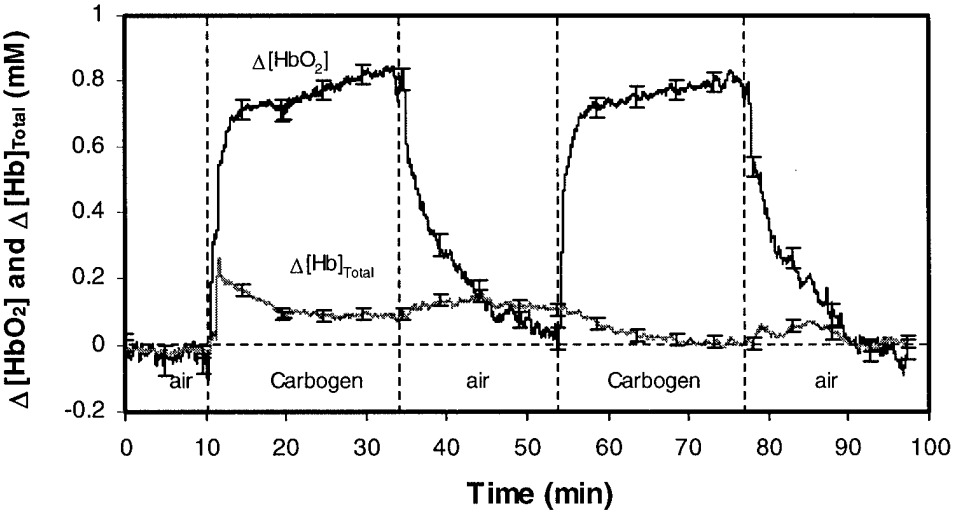


**Figure 44** Time course profiles of $\Delta[HbO_2]$ and $\Delta[Hb]_{Total}$ in response to carbogen intervention for breast tumor No. 2 (9.9 $cm^3$).

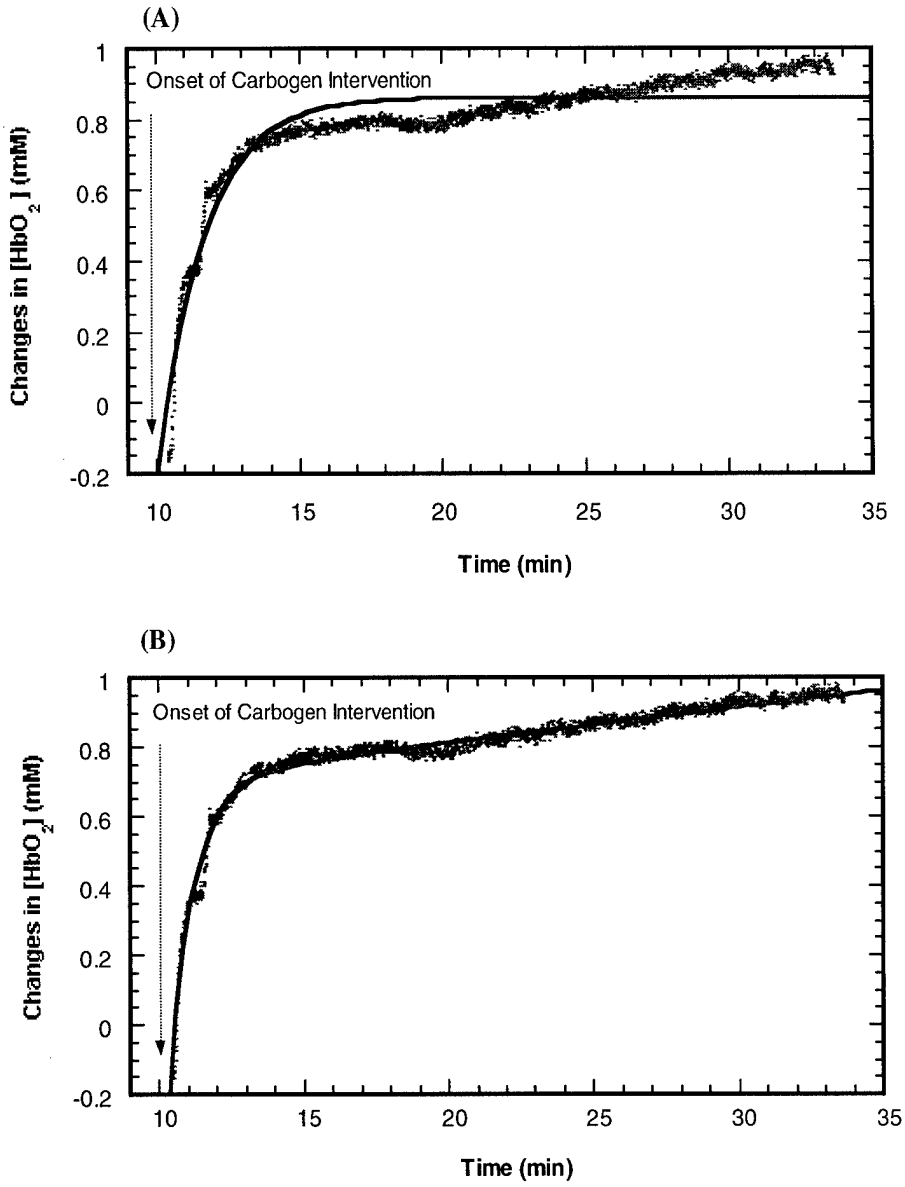


**Figure 45 (A)** Mono-exponential and **(B)** bi-exponential curve fits for tumor No. 2 (9.9 $cm^3$).

To determine whether the bi-exponential model gave an overall better performance than the mono-exponential model, the $R$ values were compared and the results are summarized in **Table 17**.

**Table 17** Comparison of the performance between the bi-exponential model and the mono-exponential model.

| Performance | No. of Bi-Exp Fits (%) | | No. of Mono-Exp Fits (%) | |
|---|---|---|---|---|
| Better | 34 | (90 %) | 2 | (5 %) |
| Equally Well | 2 | (5 %) | 2 | (5 %) |
| Worse | 2 | (5 %) | 34 | (90 %) |
| **Total** | **38** | | **38** | |

The effects of tumor volume on vascular oxygen dynamic parameters and $\Delta[HbO_2]$ and $\Delta[Hb]_{Total}$ were analyzed using a statistical method called the simple regression model. In this model, tumor volume of each individual tumor was treated as an independent variable and vascular oxygen dynamic parameters were the dependent variables. Based on this model, the linear correlation coefficients ($R$) between tumor volume and vascular oxygen dynamic parameters were computed and the results are summarized in **Table 18**.

**Table 18** Summary of linear correlation coefficients ($R$) determined by the linear regression analysis.
p = positive linear correlation, n = negative linear correlation.
No. of $R$(p) = number of positive linear correlations with $R > 0.500$.
No. of $R$(n) = number of negative linear correlations with $R > 0.500$.
x = does not have enough data

| Tumor | Vol vs. $\tau$1(min) | Vol vs. $\tau$2 (min) | Vol vs. $\tau$1/$\tau$2 | Vol vs. A1(mM) |
|---|---|---|---|---|
| No.1 | 1.000 (n) | 1.000 (n) | 1.000 (n) | 1.000 (n) |
| No.2 | 0.853 (p) | 0.846 (p) | 0.697 (p) | 0.984 (p) |
| No.3 | 0.750 (n) | 0.192 (p) | 0.679 (n) | 0.692 (p) |
| No.4 | 0.120 (p) | 0.055 (p) | 0.163 (n) | 0.695 (n) |
| No.5 | 1.000 (p) | 1.000 (n) | 1.000 (p) | 1.000 (p) |
| No.6 | 0.582 (p) | 0.994 (p) | 0.324 (n) | 0.986 (p) |
| No.7 | 0.178 (n) | 0.039 (n) | 0.275 (n) | 0.270 (n) |
| No.8 | 0.981 (p) | 0.996 (p) | 0.830 (p) | 0.719 (n) |
| No.9 | x | x | x | x |
| No.10 | x | x | x | x |
| No.11 | 0.947 (p) | 0.357 (p) | 0.289 (n) | 0.684 (n) |
| No. of (p, n) | (6, 3) | (6, 3) | (3, 6) | (4, 5) |
| No. of $R$(p) > 0.5 | 5 | 3 | 3 | 4 |
| No. of $R$(n) > 0.5 | 2 | 2 | 2 | 4 |

**Table 18 (cont.)** Summary of linear correlation coefficients ($R$) determined by the linear regression analysis.
p = positive linear correlation, n = negative linear correlation.
No. of $R$(p) = number of positive linear correlations with $R > 0.500$.
No. of $R$(n) = number of negative linear correlations with $R > 0.500$.
x = Does not have enough data

| Tumor | Vol vs. A2 (mM) | Vol vs. A1/A2 | Vol vs. $(A_1/A_2)/(\tau_1/\tau_2)$ |
|---|---|---|---|
| No.1 | 1.000 (n) | 1.000 (n) | 1.000 (n) |
| No.2 | 1.000 (n) | 0.997 (p) | 0.120 (p) |
| No.3 | 0.616 (p) | 0.160 (n) | 0.611 (p) |
| No.4 | 0.388 (n) | 0.232 (n) | 0.107 (n) |
| No.5 | 1.000 (n) | 1.000 (p) | 1.000 (p) |
| No.6 | 0.374 (p) | 0.855 (p) | 0.794 (p) |
| No.7 | 0.930 (p) | 0.975 (n) | 0.397 (n) |
| No.8 | 0.621 (n) | 0.028 (n) | 0.098 (n) |
| No.9 | x | x | x |
| No.10 | x | x | x |
| No.11 | 0.715 (n) | 0.244 (n) | 0.392 (n) |
| No. of (p, n) | (3, 6) | (3, 6) | (4, 5) |
| No .of $R$(p) > 0.5 | 2 | 3 | 3 |
| No. of $R$(n) > 0.5 | 5 | 2 | 1 |

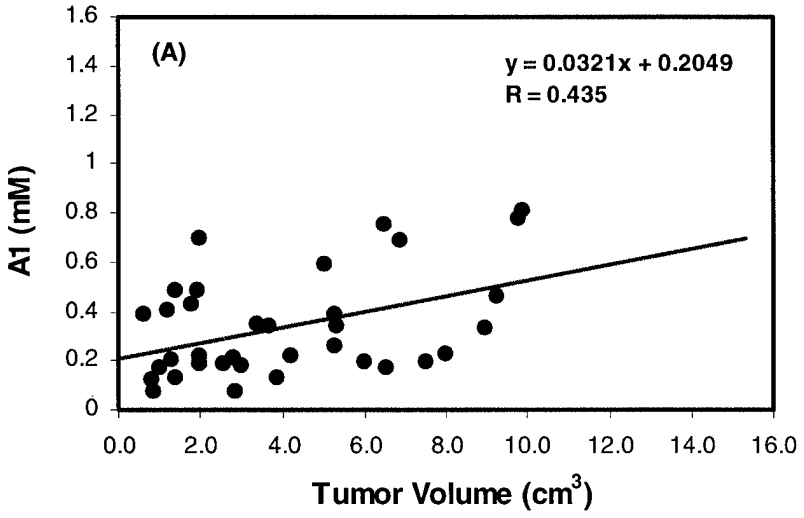

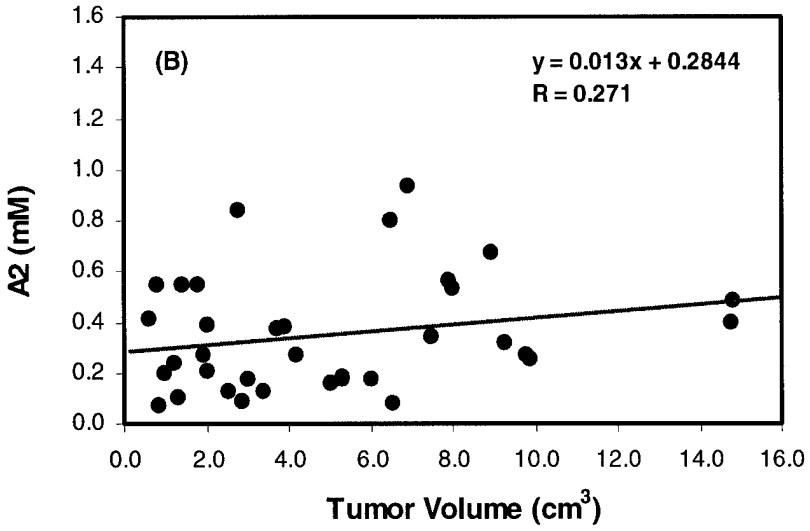


**Figure 46** Relationships between A1 (**A**), A2 (**B**) and tumor volume.

In addition, to determine whether tumor volume had significant effects on vascular oxygen dynamic parameters among the tumor population, all tumor data were pooled and analyzed as a random sample of the tumor population using the simple regression model. **Figure 46** (**A**) shows the relationship between tumor volume and A1, the response in $\Delta[HbO_2]$ corresponding to well-oxygenated tumor regions. The straight line represents the best fit. In this case, a linear correlation coefficient of $R = 0.435$ was obtained. **Figure 46** (**B**) shows the relationship between tumor volume and A2. In this example, a weak linear correlation coefficient was obtained ($R = 0.271$). However, both cases demonstrated the same trend toward increasing response in $\Delta[HbO_2]$ with increasing tumor volume, but at different rates. A1 increased faster than A2.

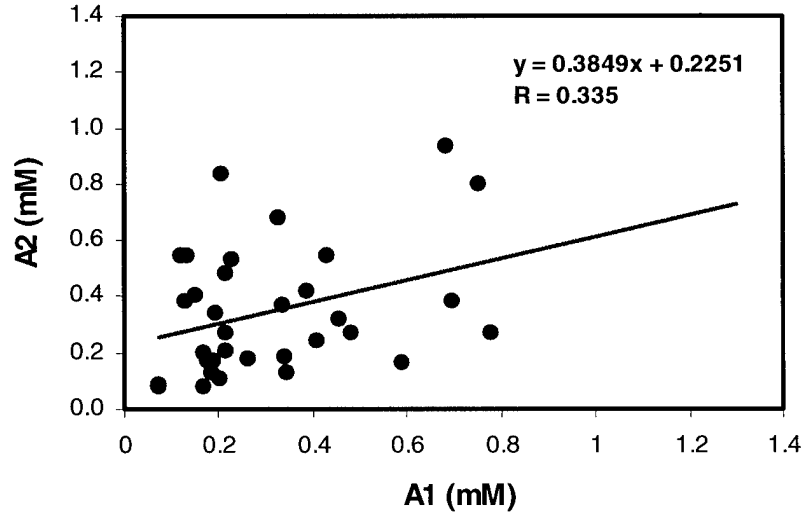


**Figure 47** Relationship between A1 and A2.

The relationship between A1 and A2 is illustrated in **Figure 47**. The result indicates that there was a weak linear relationship ($R$ = 0.335) between the two, suggesting that A1 and A2 are interdependent to some extent. The ratio of the two vasculature coefficients $\gamma 1/\gamma 2$ = A1/A2 is an important hemodynamic quantity. Its relationship with tumor volume is presented in **Figure 48**. **Figures 49** (**A**) and **49** (**B**) show the relationship between $\tau 1$, $\tau 2$, the time constants for the well- and poorly-oxygenated tumor regions, respectively, and tumor volume. Mathematically, the linear regression fit shown in (**A**) does not necessarily represent the best function, but it does indicate an inverse relationship between $\tau 1$ and tumor volume. As is seen in (**A**), the logarithmic function yielded a better fit, as indicated by the dotted line.

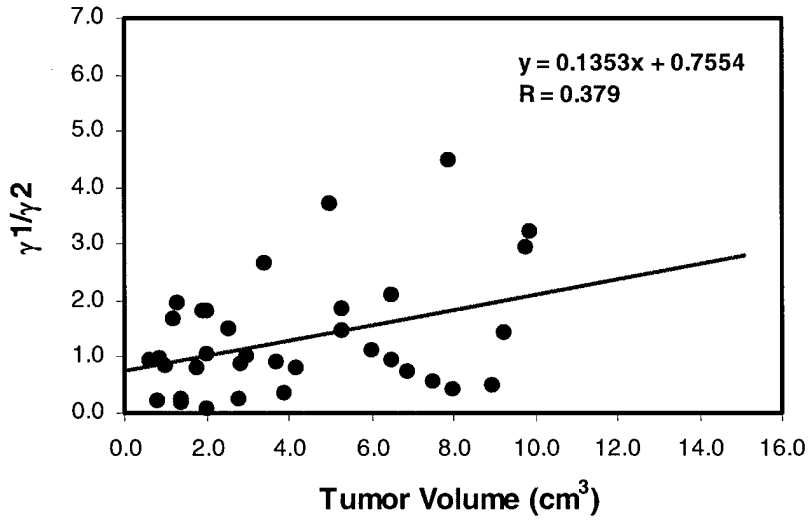


**Figure 48** Relationship between $\gamma 1/\gamma 2$ and tumor volume.

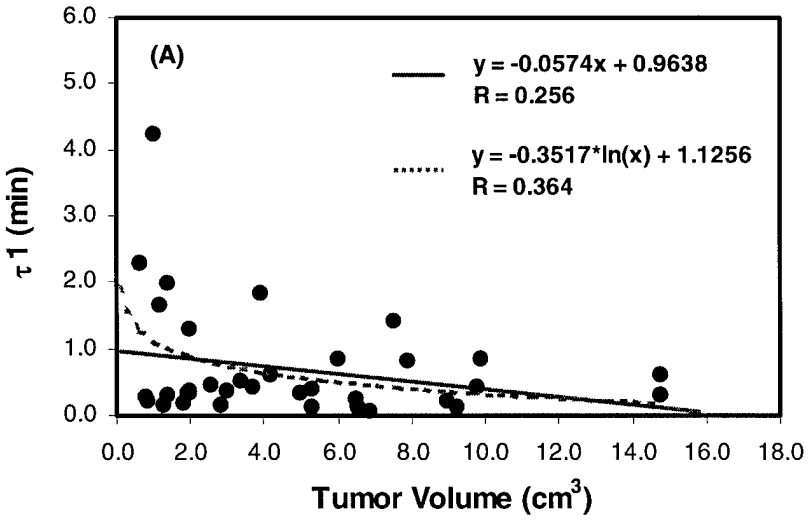

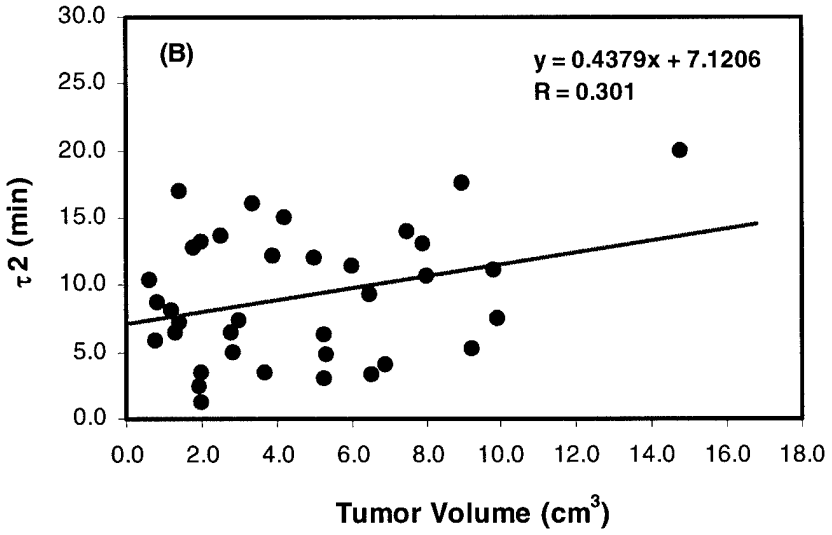


**Figure 49** Relationship between $\tau 1$, $\tau 2$, and tumor volume.

**Figure 50** shows the relationship between $\tau 1$ and $\tau 2$. In this case, a fairly strong linear relationship was observed ($R$ = 0.744). Since the slope of the linear fit was much greater than 1, this indicates that $\tau 2$ increased much faster than $\tau 1$ with increasing tumor volume as seen in **Figure 51**.

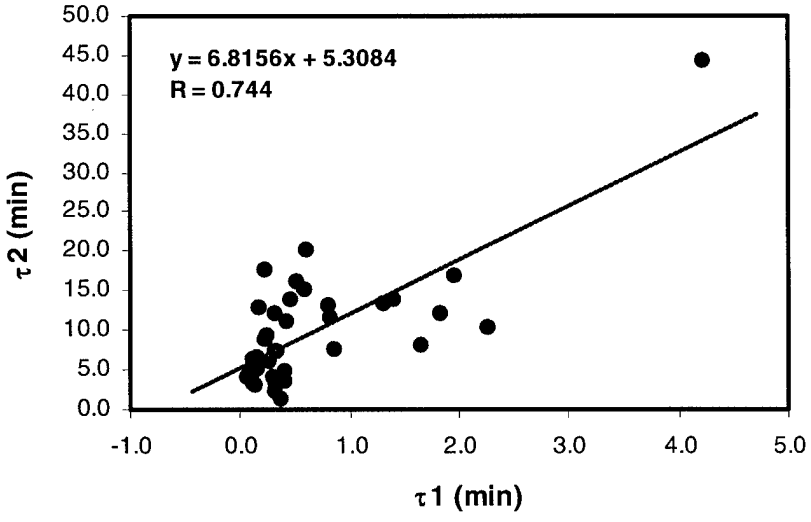


**Figure 50** Relationship between $\tau 1$ and $\tau 2$.

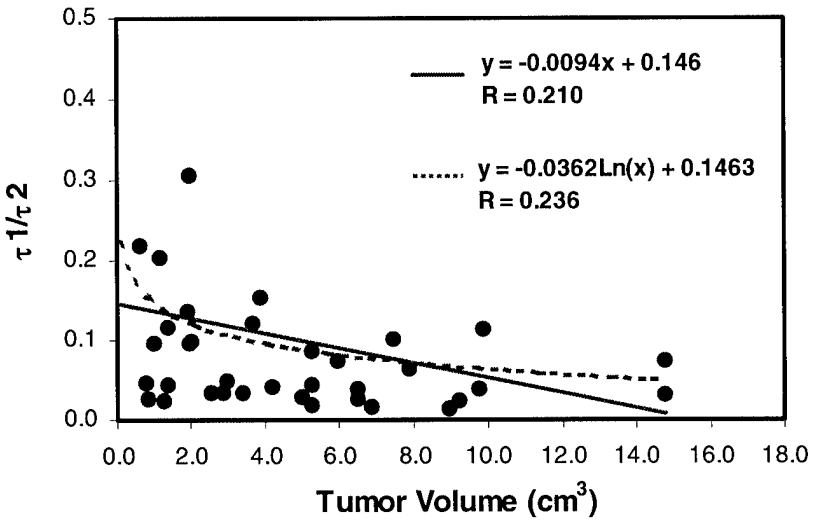


**Figure 51** Relationship between $\tau 1/\tau 2$ and tumor volume.

There was a fairly strong linear relationship between the ratio of the blood perfusion in the well-oxygenated tumor regions to that in the poorly-oxygenated tumor regions, $f1/f2 = (A_1/A_2)/(\tau_1/\tau_2)$, and tumor volume ($R = 0.512$), as seen in **Figure 52**.

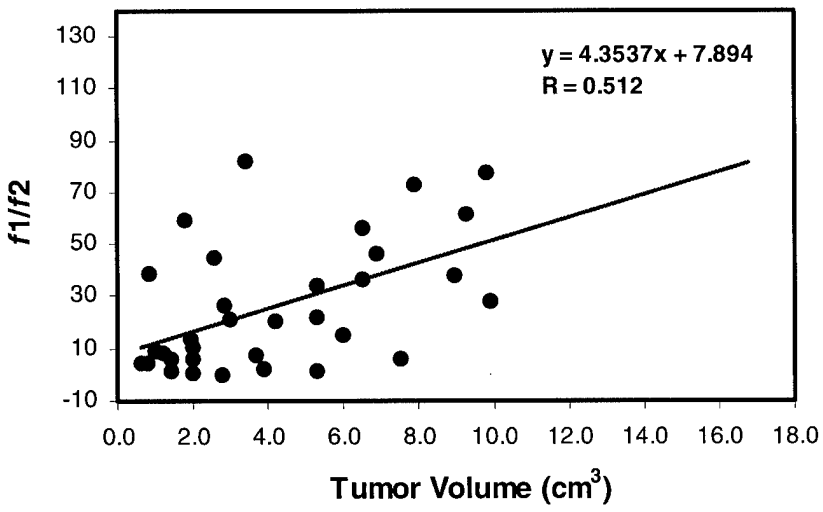


**Figure 52** Relationship between $f1/f2$ and tumor volume.

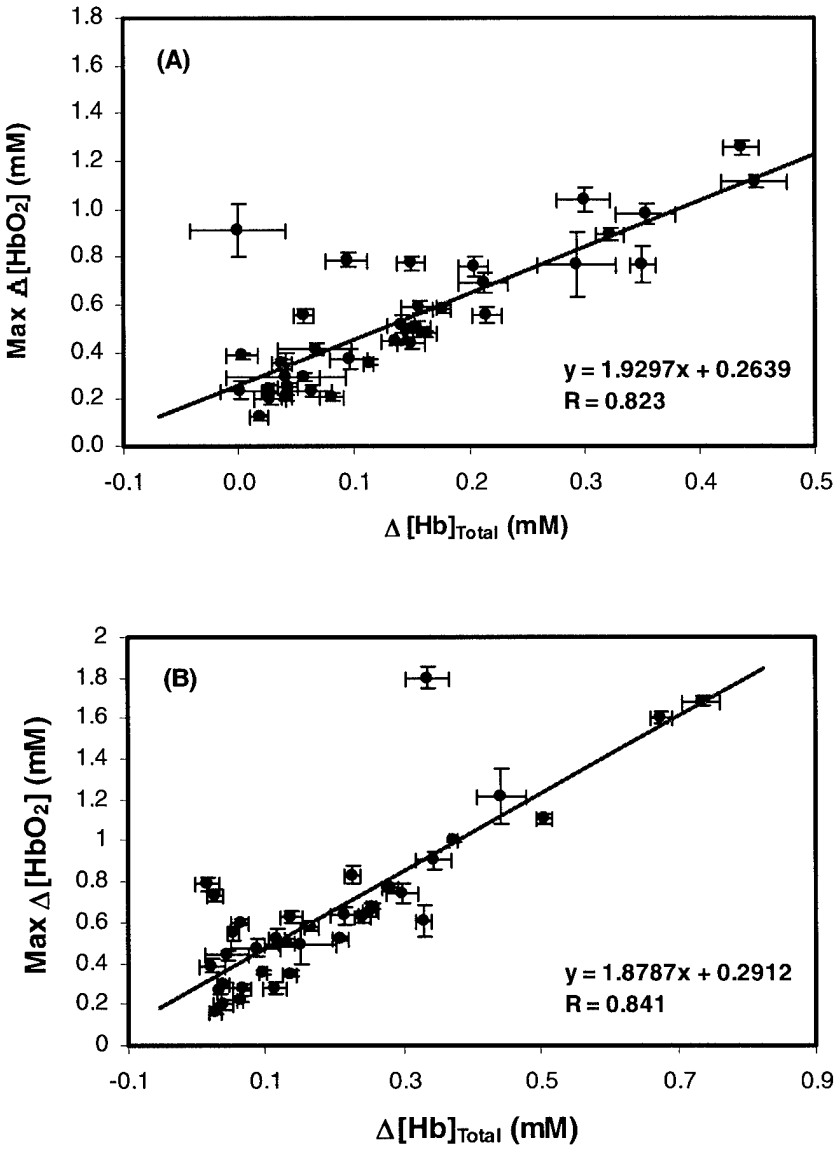


**Figure 53** Relationship between maximum $\Delta[HbO_2]$ and corresponding $\Delta[Hb]_{Total}$ for the first cycle (**A**) and second cycle of carbogen intervention (**B**).

To determine whether there was any significant relationship between $\Delta[HbO_2]$ and $\Delta[Hb]_{Total}$, I computed the maximum response in $\Delta[HbO_2]$ and corresponding $\Delta[Hb]_{Total}$ during carbogen intervention. It was found that there was a strong linear relationship between the two quantities (**Figure 53** (**A**)). This strong correlation was also observed for the second cycle of carbogen intervention as shown in **Figure 53** (**B**). The two slopes and intercepts of the linear regression fits differed by only 2.6% and 9.3%, respectively, an indication of good reproducibility of the I&Q system. The error bars in the plots represent

measurement uncertainties in max $\Delta[HbO_2]$ and corresponding $\Delta[Hb]_{Total}$ for each measurement, estimated using baseline data. **Figure 54** shows the relationship between the first Max $\Delta[HbO_2]$ and the second Max $\Delta[HbO_2]$. Again, a strong linear relationship was observed ($R$ = 0.90). The slope of the linear regression fit approached to unity, suggesting a good reproducibility of the I&Q system.

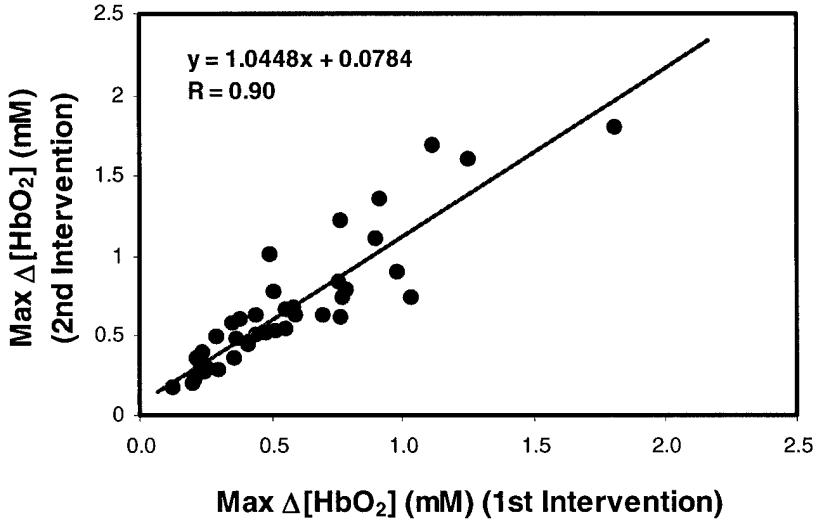


**Figure 54** shows the relationship between the first Max $\Delta[HbO_2]$ and the second Max $\Delta[HbO_2]$

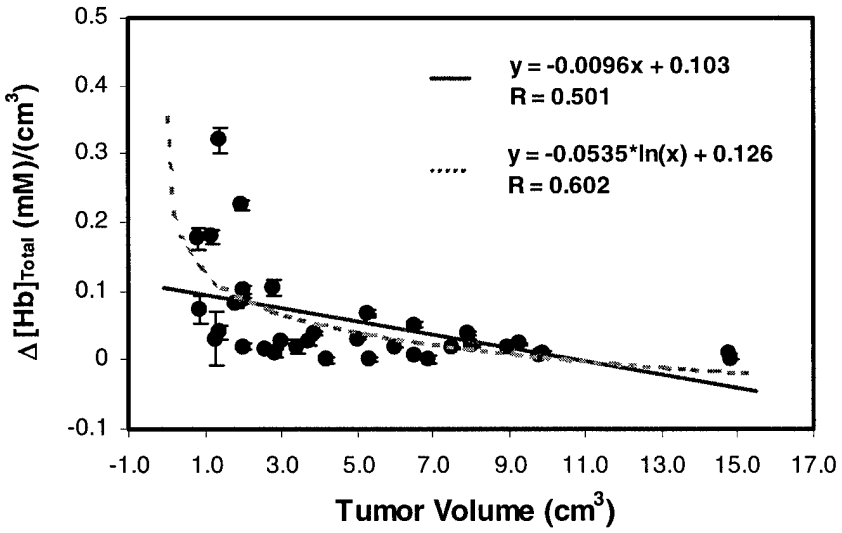


**Figure 55** A plot of volume-weighted $\Delta[Hb]_{Total}$ vs. tumor volume.

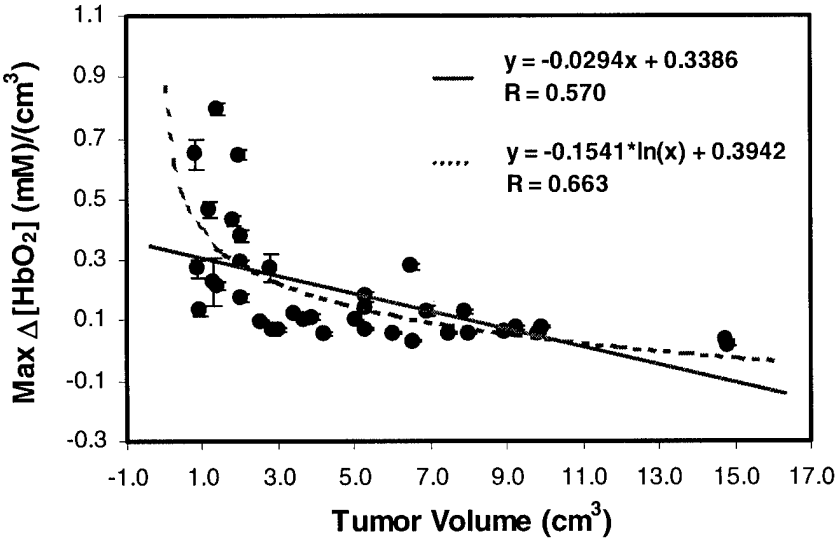


**Figure 56** A plot of volume-weighted max $\Delta[HbO_2]$ vs. tumor volume. Clearly, the logarithmic function gave a better fit (dotted line).

Furthermore, volume-weighted max $\Delta[HbO_2]$ and $\Delta[Hb]_{Total}$ were also calculated. **Figure 55** is a plot of volume-weighted $\Delta[Hb]_{Total}$ vs. tumor volume and **Figure 56** shows a plot of volume-weighted max $\Delta[HbO_2]$ vs. tumor volume. Clearly, in both cases, the linear regression fits did not represent the best functions although the *R* values were fairly large. To improve the goodness of the curve fits, the data were also fitted using a logarithmic function indicated by the dotted lines. In spite of the different mathematical models used in the curve fits, the results did indicate the overall relationship between volume-weighted max $\Delta[HbO_2]$, $\Delta[Hb]_{Total}$, and tumor volume was inverse.

- **Discussion**

Many factors contribute to the poor response of solid malignant tumors to conventional radiotherapy and many chemotherapeutic agents [**9**]. The most prominent one is the poor tumor oxygenation status or hypoxia. So far, however, few techniques have the capability of providing completely non-invasive and real-time oxygenation measurement with high sensitivity and reasonable accuracy. Currently, the techniques of good standard are based on polarographic oxygen electrodes. However, because of their high invasiveness, their potential routine clinical applications have been compromised. This is especially true when repeated measurements are desired. In this work, I have successfully measured $\Delta[HbO_2]$ and $\Delta[Hb]_{Total}$ in rat breast tumors in response to carbogen intervention using frequency-domain NIRS. The technique is non-invasive, real-time, and very sensitive to changes in hemoglobin and oxyhemoglobin concentrations. The technique interrogates all vasculature within the light field, thus,

yielding an average measurement of $\Delta[HbO_2]$ and $\Delta[Hb]_{Total}$. The results of this study show that under normobaric conditions, carbogen breathing had a significant impact on tumor oxygenation and total hemoglobin concentration i.e. total tumor blood volume within the light field compared to air breathing. Although changes in $\Delta[HbO_2]$ and $\Delta[Hb]_{Total}$ were highly variable and tumor-dependent, among the 38 experiments, carbogen breathing induced significant changes in $\Delta[HbO_2]$ in all cases and significant changes in $\Delta[Hb]_{Total}$ in 36 cases, accounting for 94.7% of the measurements. However, the magnitudes of the latter were much smaller than the former and could be contributed partially by blood redistribution within the tumor. Despite the fact that absolute values of $\Delta[HbO_2]$ and $\Delta[Hb]_{Total}$ could not be determined using the current system, statistical theory has shown that linear transformation of all ratio or interval scale data does not affect the results of hypothesis tests [**81**]. Therefore, the statistical conclusions of this study are still valid. These results suggest that (1) carbogen breathing can increase tumor blood volume at least during the period of carbogen administration and (2) the major portion of the increase in oxyhemoglobin concentration was contributed by increased hemoglobin loading reaction due to increased $pO_2$ in inhaled gas rather than by increased total blood volume.

Carbogen breathing has been studied extensively in its utility and mechanisms in improving tumor oxygenation [**82**]. Currently, carbogen breathing, combined with nicotinamide injection, is being investigated in clinical trials [**83**]. The widely accepted rationale for using carbogen in improving tumor vascular oxygenation is threefold [**84**]. First of all, 95% $O_2$ can increase the arterial blood $pO_2$, therefore, resulting in an increased $sO_2$ by a shift to the right of the oxyhemoglobin dissociation curve (ODC). Secondly, 5% $CO_2$ can increase the arterial blood $pCO_2$, leading to an increased stimulation of ventilation and, thus, an increased pulmonary $O_2$ uptake. Thirdly, 5% $CO_2$ can induce vasodilation of the afferent tumor vessels, thus, resulting in an increased tumor blood inflow and causing pooled, deoxygenated venous blood in tumor sinusoids to be flushed out by fresh, oxygenated blood. Synergistic actions of these mechanisms gave rise to an increased oxyhemoglobin saturation of the circulation system and an increased tumor oxyhemoglobin saturation and blood volume.

A growing body of data obtained with other established techniques supports these arguments. For example, Rodrigues *et. al.* [**85**], using $^{31}P$ MRS, found that carbogen breathing caused an enhanced uptake of ifosfamide, a chemotherapeutic agent, into subcutaneous GH3 prolactinomas compared with 2.5% $CO_2$ in $O_2$ and 5% $CO_2$ in air. The authors concluded that (1) hypercapnia could increase blood flow, and thus, drug uptake to the tumor and (2) hyperoxia could cause vasoconstriction to normal tissue and, therefore, induce some diversion in blood flow from systemic to tumor vasculature, resulting in a further enhancement of drug uptake. Honess *et. al.* [**86**] also reported a similar increase in blood perfusion during carbogen breathing in the RIF-1 tumor. The

results of my study clearly show that tumor vascular oxygenation could be improved and tumor blood volume can be increased by carbogen breathing. These findings were also consistent with the results of my $^{19}F$ MRS study using a perfluorooctylbromide (PFOB) ($C_8F_{17}Br$) emulsion.

Recently, Hull *et. al.* [**87**] published their results of carbogen-induced changes in rat mammary adenocarcinomas R3230 using reflectance NIRS. They also observed an increase in hemoglobin oxygen saturation in response to carbogen intervention. However, they only observed an increase in total hemoglobin concentration in 3 out of 16 measurements. As a matter of fact, the majority of measurements (10 of 16) showed decrease in total hemoglobin concentration in response to carbogen intervention at the time corresponding to maximum $sO_2$. In three tumors, the total hemoglobin concentration remained approximately constant. The authors argued that this phenomenon could be the "steal effect", i.e., vasodilation in the normal circulation resulting in a loss of blood volume in the tumor. Their observations were in sharp contrast to the results described here, reflecting markedly different vascular characteristics between the two tumor cell lines. Indeed, there is a substantial body of evidence to suggest that variations in tumor parameters between different tumor lines, such as distribution of tumor vessels and temporal characteristics in microcirculation, be often more pronounced than intra-tumor differences [**2**].

One of the possible explanations for the enhanced $\Delta[HbO_2]$ was an increase in the total tumor hemoglobin concentration, i.e., the total tumor blood volume, caused by vasoconstriction in the normal circulation in response to carbogen breathing. Indeed, the vast majority of the measurements in this study showed a significant increase in the total tumor hemoglobin concentration. Overall, there was a strong linear relationship ($R > 0.8$) between max $\Delta[HbO_2]$ and corresponding $\Delta[Hb]_{Total}$ for this particular tumor model (**Figure 53**). Meanwhile, in my study with Dunning prostate adenocarcinomas R3327-AT1, the same relationship was also observed (**Figure 57**). A comparison of **Figure 53** and **Figure 57** revealed that the latter has a larger slope, suggesting that an increased total hemoglobin concentration played a less important role in an increased $\Delta[HbO_2]$ for Dunning prostate tumors. Not surprisingly, Hull *et. al.* did not observe a clear correlation between max $\Delta[HbO_2]$ and corresponding $\Delta[Hb]_{Total}$ with rat mammary adenocarcinomas R3230 as the inter-tumor variations were expected to be pronounced. However, the data did demonstrate the same trend toward increasing response in $\Delta[HbO_2]$ with increasing $\Delta[Hb]_{Total}$.

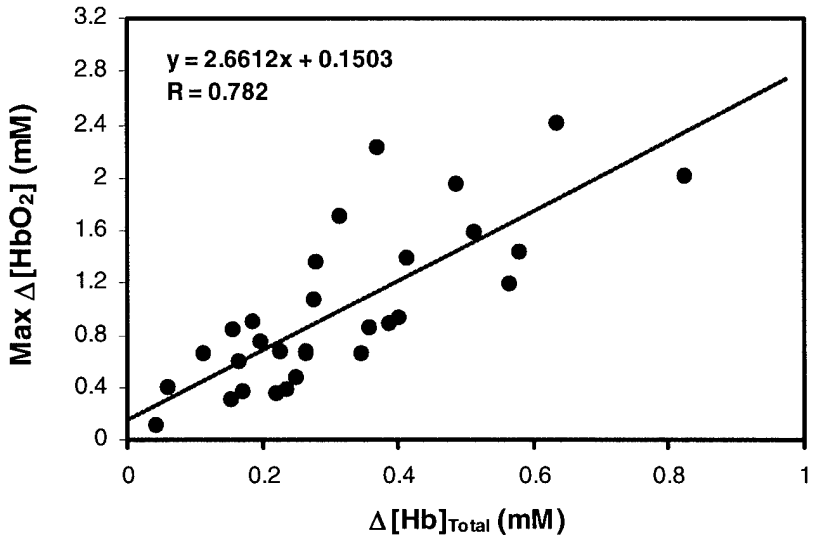


**Figure 57** Relationship between maximum $\Delta[HbO_2]$ and corresponding $\Delta[Hb]_{Total}$ for Dunning prostate adenocarcinomas R3327-AT1 in response to carbogen intervention.

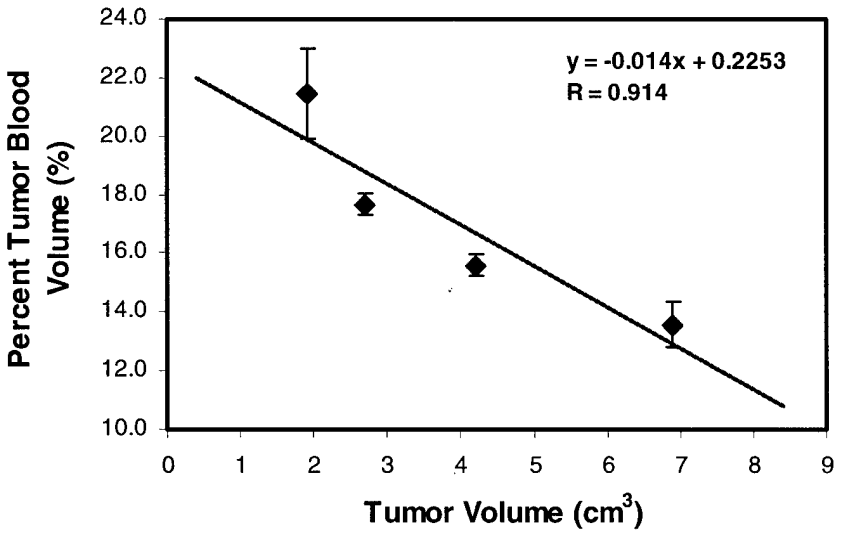


**Figure 58** Relationship between percent tumor blood volume and tumor volume determined by $^{19}F$ MRS of PFOB.

As seen in **Figures 55** and **56**, volume-weighted max $\Delta[HbO_2]$ and $\Delta[Hb]_{Total}$ correlated well with tumor volume using both linear and logarithmic models. The volume-weighted $\Delta[Hb]_{Total}$ is a quantity resembling the percent tumor blood volume that frequently appears in the literature. These overall inverse relationships clearly indicate that (1) tumor blood becomes increasingly poorly oxygenated and (2) tumor vasculature

deteriorates as the tumor increases in size. These findings have been independently confirmed by the results of my $^{19}F$ MRS study using a PFOB emulsion (**Figure 58**) and were also consistent with results reported by Baldwin *et. al.* [**88**], Steen *et. al.* [**54**], and Meyer *et. al.* [**89**] in different tumor types. The most popular hypothsis for this inverse relationship is the central necrosis. In solid tumors, new blood vessels are formed by the stimulation of angiogenic factors in order to meet the metabolic needs. However, as the tumor grows, the central necrosis develops due to an imbalance between the faster rate of tumor cell proliferation, and the slower proliferation and branching of the tumor blood vessels. Usually, the necrotic fraction increases as the tumor grows in size, resulting in a decreased percent tumor blood volume. Indeed, the histological H&E stained sections obtained from several of these tumors showed extensive central necrosis

In this study, the differential pathlength factor (*DPF*) was assumed to be 1 for simplicity. However, in reality, *DPF* could be much larger than 1 for solid tumors because of light scattering by tumor tissues. So far, *DPF* has not been systematically studied for solid tumors and there are very limited data available regarding its numerical values. To determine *DPF*, we need to know not only the absorption coefficient $\mu_a$, but also the reduced scattering coefficient $\mu_s'$. The difficulty in determining *DPF* arises from the fact that $\mu_s'$ is not easy to obtain for solid tumors. Based on the available data reported in the literature, *DPF* for solid tumors can be estimated as follows.

According to the diffusion approximation of transport theory, the mean optical pathlength <*L*> of light traveling within a highly scattering medium before detection is [**90**].

$$< L >= \frac{\sqrt{3}}{2} \cdot d \cdot \sqrt{\frac{\mu_s'}{\mu_a}} \cdot \left[ \frac{1}{1 + \frac{1}{d[3\mu_a \mu_s']^{1/2}}} \right], \tag{39}$$

where $d$ is the direct source-detector separation and $\mu_a$ and $\mu_s'$ are the absorption and reduced scattering coefficients of tumor tissues, respectively. Comparing Equation (39) with the definition of *DPF*, <*L*> = *DPF* × *d*, gives

$$DPF = \frac{\sqrt{3}}{2} \sqrt{\frac{\mu_s'}{\mu_a}} \cdot \left[ \frac{1}{1 + \frac{1}{d[3\mu_a \mu_s']^{1/2}}} \right], \tag{40}$$

To estimate *DPF* for solid tumors, I use the $\mu_a$ and $\mu_s'$ values for a human back tumor published by Fishkin *et al.* [**65**]: $\mu_a = 0.177$ ($cm^{-1}$) and $\mu_s' = 9.23$ ($cm^{-1}$). Thus,

$$DPF = \frac{\sqrt{3}}{2} \cdot \sqrt{\frac{9.23}{0.177}} \cdot \left[ \frac{1}{1 + \frac{1}{d \cdot [3 \times 0.177 \times 9.23]^{1/2}}} \right], \quad \text{or}$$

$$DPF = \left[ \frac{6.2538}{1 + \frac{1}{2.2138 \cdot d}} \right], \tag{4.18}$$

**Figure 59** shows the relationship between *DPF* and *d* for the range of *d* values used in my NIRS experiments. *DPF* spans from 3.28 to 5.19 for the *d* values ranging from 0.5 to 2.2 cm. Furthermore, according to Equation (4.18), the maximum *DPF* is 6.2538 as *d* goes to infinity. Thus, depending on *d*, a proper *DPF* should be applied to the NIRS data in order to estimate the absolute $\Delta[HbO_2]$ and $\Delta[Hb]_{Total}$.

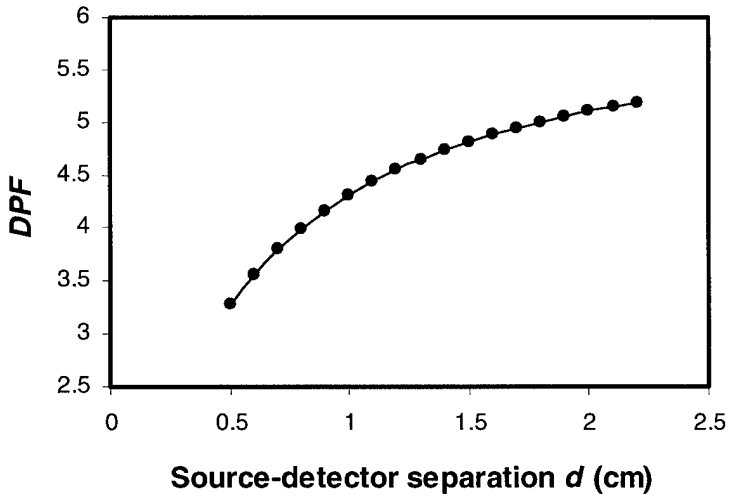


**Figure 59** Relationship between *DPF* and *d*.

**Investigation of Tumor Physiology in Response to Irradiation**

One of the reasons for the birth of modern fractionated radiotherapy was to exploit tumor reoxygenation that had been found to occur following each irradiation [**91**]. The phenomenon of reoxygenation is the process by which hypoxic cells in tumors become oxygenated during fractionated radiotherapy. Failure to reoxygenate during radiotherapy could be one of the important reasons for treatment failure due to hypoxia. So far, the exact mechanisms by which reoxygenation occurs have not been fully understood. It is believed that reoxygenation may be related to reduced respiration in radiation-damaged cells, recirculation through temporarily closed blood vessels, the resorption of damaged cells so that the hypoxic cells become closer to functional vessels, and a reduction in tissue pressure as the tumor shrinks, leading to a decrease in the intermittent closure of vessels [**92**, **93**]. Tumor reoxygenation has been measured using different techniques, such as polarographic needle electrodes [**94**, **95**, **96**] and positron emission tomography (PET) [**97**]. However, there is evidence to suggest that reoxygenation varies widely in extent from tumor to tumor [**94, 98**]. Since early 1980s, many new fractionation protocols have been designed, including hyperfractionation and accelerated fractionation [**99**]. Currently, however, the timing of successive doses is not optimized for individual tumors, but rather is based on experience with cell culture, animal tumor model systems, and clinical trials. In addition, recent clinical studies have shown that there is a positive linear relationship between hemoglobin concentrations and therapeutic outcome [**100-102**] and that the higher hemoglobin concentrations correlate with improved local tumor control and a higher overall survival rate [**103-105**]. These findings strongly suggest that hemoglobin concentration could be an independent prognostic factor.

- **Animal Preparation**

Mammary adenocarcinomas 13762NF were implanted in pedicles as described earlier. When tumors reached about 1 cm diameter, they were divided into two groups. One of the groups was used as the experimental group and the other one was used as the control group. Rats were anesthetized with 200 μl ketamine hydrochloride i.p. and maintained under general gaseous anesthesia with air (1.0 l/min) and 1.0% isoflurane (Ohmeda PPD Inc., Fort Dodge, IA). The body temperature was maintained at about 37° C by a warm water blanket connected to a water pump (K-MOD 100, Baxter Healthcare Co., Deerfield, IL). A fiber optic pulse oximeter (Nonin Medical, Inc., Plymouth, MN) was placed on the hind foot to monitor arterial hemoglobin oxygen saturation ($s_aO_2$) and heart rate (HR), and a thermocouple (Cole-Parmer Instrument Co., Vernon Hills, IL) was inserted rectally to monitor core temperature. Prior to irradiation, baseline tumor vascular $\Delta[HbO_2]$ and $\Delta[Hb]_{Total}$ were measured using the experimental protocol described earlier with NIRS.

- **Irradiation**

Following the baseline NIRS experiments, the irradiation was carried out using a Varian CLINAC 4-100 (4 MV photon beam) in the Department of Radiation Oncology outside normal business hours. Prior to irradiation, tissue equivalent bolus material was

placed around the tumors to ensure uniformity of dose to the tumors. A treatment plan was computed based on a source-to-axis distance (SAD) of 100 cm and a field size of 4 × 4 cm (**Table 19**). Tumors were irradiated with a 4 MV photon beam with 10 Gy delivered from each side at a rate of 2 Gy/min, giving a total dose of 20 Gy. Following irradiation, the NIRS measurements were then performed at 2 hours, 24 hours, 48 hours, and 96 hours to examine the extent and time course of tumor vascular hypoxiation and reoxygenation. Tumor size was measured once every two day following irradiation. Tumor growth delay was compared with the control group.

**Table 19** Parameters of the treatment plan for irradiation

| Parameter | Value |
|---|---|
| Field No. | 1 |
| Field Description | AP |
| Treatment Machine | CL4 |
| Energy | 4X |
| Collimator Width | 4.0 |
| Collimator Length | 4.0 |
| Eq. Square Col. | 4.0 |
| Output Factor | 0.961 |
| Eq. Square Field | 4.0 |
| Actual SSD | 100.00 |
| Actual Depth | 2.00 |
| Effective SSD | 100.00 |
| Effective Depth | 2.00 |
| SAD = SSD + Depth | 102 |
| Off-Axis Distance | 0.0 |
| Wedge Off-Axis Distance | 0.0 |
| TMR | 0.9754 |
| OF = Sc x Sp | 0.961 |
| INVSQ = $(SCD/SAD)^2$ | 0.961 |
| Tray Factor, TF | 1.000 |
| Wedge | 0.0 deg |
| Wedge Factor, WF | 1.000 |
| Wedge Off-Axis Factor | 1.000 |
| Off-Axis Factor | 1.000 |
| OAF Corr. | 1.000 |
| Isodose Line | 100% |
| Other | 1.000 |
| TD/MU | 0.9010 |
| Prescribed Dose | 2000 |
| MU Calc. Check | 2219.9 |
| 4X Backup Timer | 13.32 |
| Diode Low | 0.0 |
| Diode High | 0.0 |

**Figure 60** shows tumor vascular $\Delta[HbO_2]$ and $\Delta[Hb]_{Total}$ in response to carbogen intervention before irradiation for breast tumor No.1. The data were acquired in transmittance mode. As seen in the plot, carbogen intervention induced a rapid and significant change ($p < 0.0001$) in $\Delta[HbO_2]$ (0.59 ± 0.03) (mM). In contrast, the maximum change in $\Delta[Hb]_{Total}$ (0.11 ± 0.02 ) (mM) was much less than that in $\Delta[HbO_2]$, but was still significant ($p < 0.0001$). For hemodynamic analysis, the bi-exponential model was fitted to the first rising portion of the raw data, giving $\tau_1 = 0.241 \pm 0.007$ (min), $\tau_2 = 5.4 \pm 0.7$ (min), $A_1 = 0.471 \pm 0.005$ (mM), and $A_2 = 0.161 \pm 0.006$ (mM) with $R = 0.947$. **Figure 61** shows tumor vascular $\Delta[HbO_2]$ and $\Delta[Hb]_{Total}$ two hours after a single dose irradiation (20 Gy) for breast tumor No.1. The irradiation caused both $\Delta[HbO_2]$ (1.17 ± 0.05) (mM) and $\Delta[Hb]_{Total}$ (0.55 ± 0.03) (mM) to increase significantly ($p < 0.0001$) as compared to the pre-irradiation case, suggesting that reoxygenation occurred. In this case, the bi-exponential curve fit yielded $\tau_1 = 0.256 \pm 0.004$ (min), $\tau_2 = 61 \pm 98$ (min), $A_1 = 1.024 \pm 0.003$ (mM), and $A_2 = 0.3 \pm 0.4$ (mM) with $R = 0.951$. **Figure 62** shows tumor vascular $\Delta[HbO_2]$ and $\Delta[Hb]_{Total}$ 48 hours after the single dose irradiation for breast tumor No.1. By this time, the tumor volume had shrunk by 1.4 $cm^3$. However, tumor reoxygenation was not observed here although the changes were significant ($p < 0.0001$ for $\Delta[HbO_2]$ and $p < 0.0001$ for $\Delta[Hb]_{Total}$). Tumor vascular $\Delta[HbO_2]$ (0.103 ± 0.006) (mM) and $\Delta[Hb]_{Total}$ (0.044 ± 0.003) (mM) were much less than the pre-irradiation values. In this case, the bi-exponential curve fit gave $\tau_1 = 0.113 \pm 0.007$ (min), $\tau_2 = 4.18 \pm 0.05$ (min), $A_1 = 0.032 \pm 0.001$ (mM), and $A_2 = 0.080 \pm 0.001$ (mM) with $R = 0.987$. **Table 20** summarizes the changes in $\Delta[HbO_2]$ pre- and post-single dose irradiation for the experimental group. **Table 21** summarizes the changes in $\Delta[Hb]_{Total}$. The $p$ values were obtained in comparison to the pre-irradiation measurements.

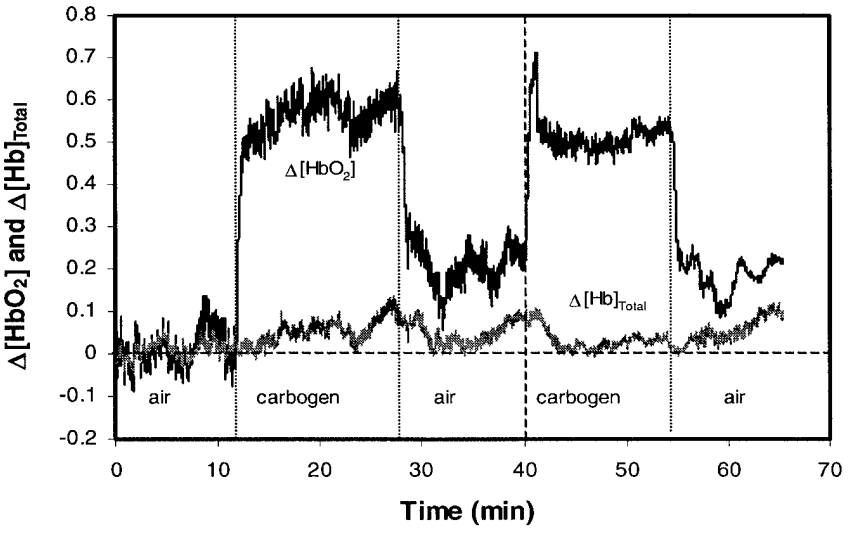


**Figure 60** Tumor $\Delta[HbO_2]$ and $\Delta[Hb]_{Total}$ before the irradiation for tumor No.1.

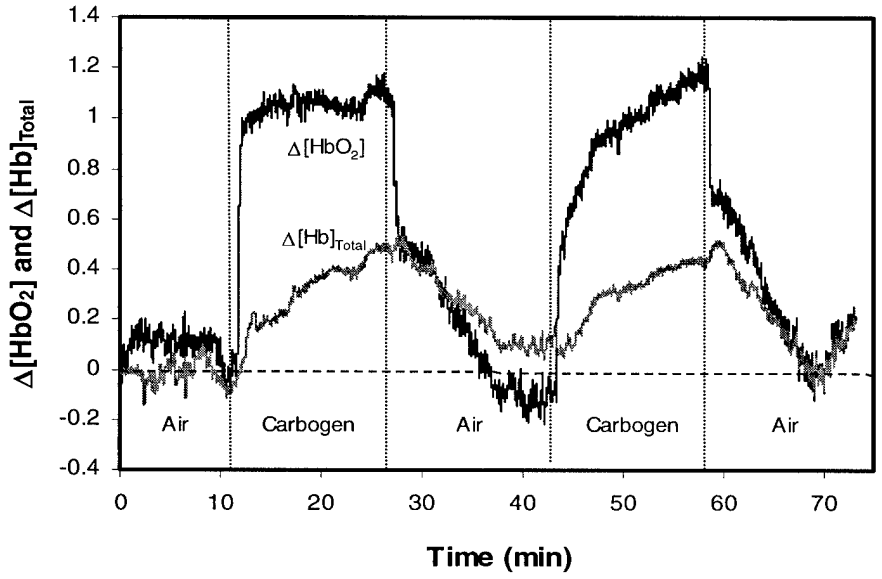


**Figure 61** Changes in tumor vascular $\Delta[HbO_2]$ and $\Delta[Hb]_{Total}$ two hours after the single dose irradiation (20 Gy) for breast tumor No.1.

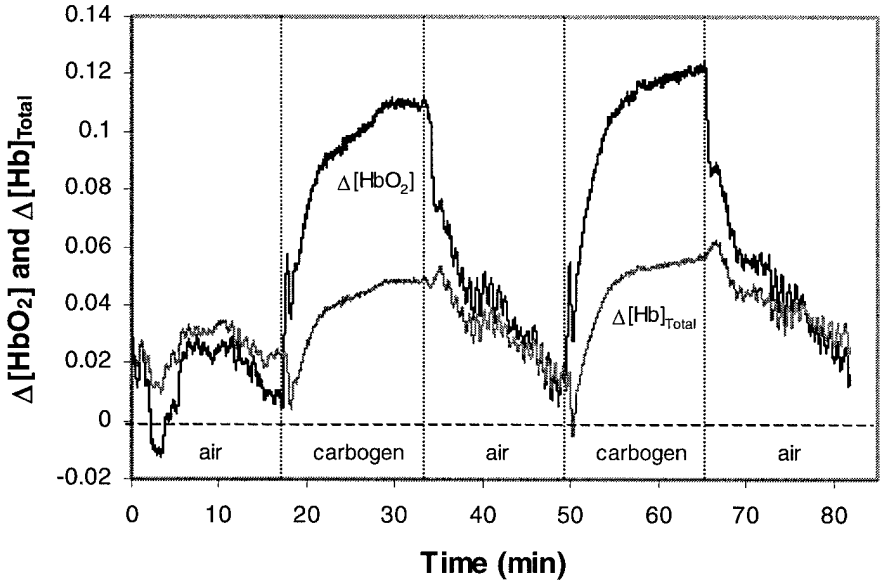


**Figure 62** Changes in tumor vascular $\Delta[HbO_2]$ and $\Delta[Hb]_{Total}$ 48 hours after the single dose irradiation (20 Gy) for breast tumor No.1.

**Table 20** Changes in $\Delta[HbO_2]$ before and after the single dose irradiation (20 Gy) for the experimental group. The *p* values were obtained using ANOVA in comparison to pre-irradiation measurements. (x = not applicable).

| | Vol ($cm^3$) | Max $\Delta[HbO_2]$ ± Err (mM) | *p* - value |
|---|---|---|---|
| Pre-Irradiation | 3.9 | 0.59 ± 0.03 | x |
| 2 Hrs Post-Irradiation | 3.9 | 1.17 ± 0.05 | < 0.0001 |
| 24 Hrs Post-Irradiation | 2.9 | 0.45 ± 0.02 | < 0.0001 |
| 48 Hrs Post-Irradiation | 2.5 | 0.103 ± 0.006 | < 0.0001 |
| 96 Hrs Post-Irradiation | 2.0 | 0.212 ± 0.008 | < 0.0001 |

**Table 21** Changes in $\Delta[Hb]_{Total}$ before and after the single dose irradiation (20 Gy) for the experimental group. The *p* values were obtained using ANOVA in comparison to pre-irradiation measurements. (x = not applicable).

| Time | Vol ($cm^3$) | Max $\Delta[Hb]_{Total}$ ± Err (mM) | *p* - value |
|---|---|---|---|
| Pre-Irradiation | 3.9 | 0.11 ± 0.02 | x |
| 2 Hrs Post-Irradiation | 3.9 | 0.55 ± 0.03 | < 0.0001 |
| 24 Hrs Post-Irradiation | 2.9 | 0.21 ± 0.02 | < 0.0001 |
| 48 Hrs Post-Irradiation | 2.5 | 0.044 ± 0.003 | < 0.0001 |
| 96 Hrs Post-Irradiation | 2.0 | 0.080 ± 0.004 | < 0.0001 |

**Figure 63** compares the maximum tumor vascular $\Delta[HbO_2]$ values and **Figure 64** compares the maximum tumor vascular $\Delta[Hb]_{Total}$ values pre- and post-irradiation for the experimental group. As seen in the plots, tumor vascular $\Delta[HbO_2]$ and $\Delta[Hb]_{Total}$ changed significantly post-irradiation as compared to the pre-irradiation values. Tumor reoxygenation occurred 2 hours post-irradiation and then oxygenation decreased for the next 48 hours. The same trend was also seen in $\Delta[Hb]_{Total}$. Tumor vascular $\Delta[HbO_2]$ and $\Delta[Hb]_{Total}$ were highly correlated with tumor volume post-irradiation ($R = 0.941$ and $R = 0.952$, respectively), as shown in **Figures 65** and **66**. However, these relationships were opposite to those observed with the non-irradiated tumors, suggesting the irradiation had

damaged the tumor vasculature and thus changed the tumor response pattern. **Table 22** is a summary of the parameters of the tumor vascular oxygen dynamics before and after irradiation for the experimental group. The parameters were determined by the bi-exponential model.

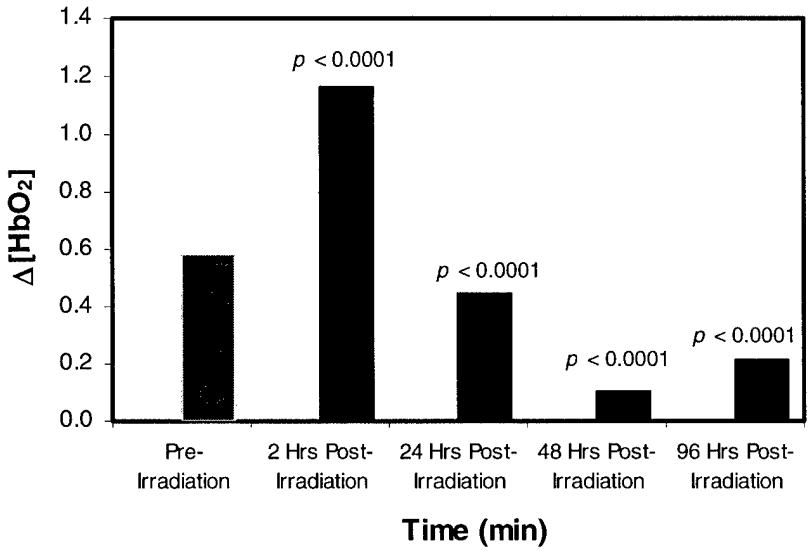


**Figure 63** Comparison of tumor vascular $\Delta[HbO_2]$ before and after the single dose irradiation (20 Gy) for the experimental group.

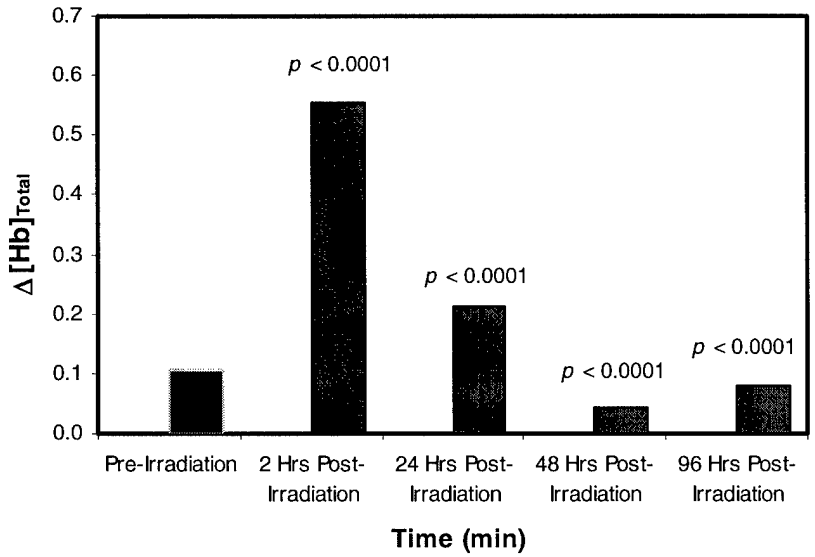


**Figure 64** Comparison of tumor vascular $\Delta[Hb]_{Total}$ before and after the single dose irradiation (20 Gy) for the experimental group.

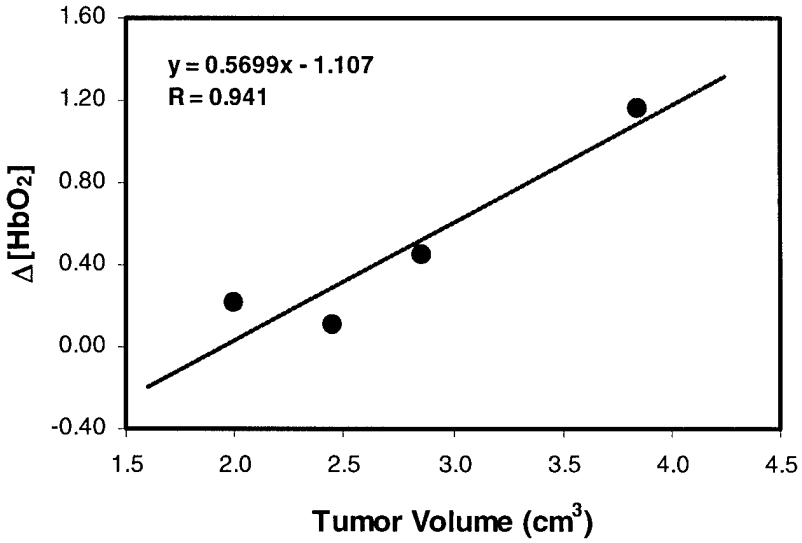


**Figure 65** Relationship between $\Delta[HbO_2]$ and tumor volume after the single dose irradiation (20 Gy) for the experimental group.

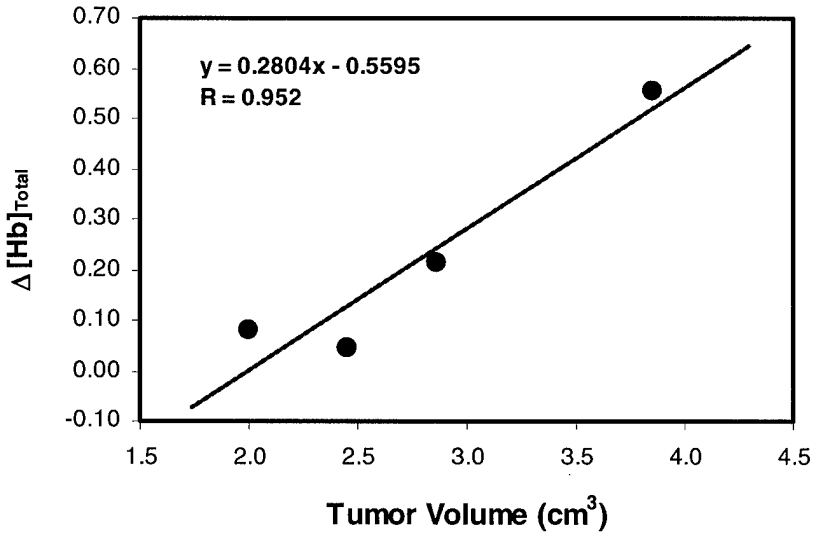


**Figure 66** Relationship between $\Delta[Hb]_{Total}$ and tumor volume after the single dose irradiation (20 Gy) for the experimental group.

**Table 22** Summary of the parameters of the vascular oxygen dynamics ($\Delta[HbO_2]$) before and after the single dose irradiation (20 Gy), determined by the bi-exponential model: $\Delta[HbO_2]=A_1 \cdot \exp[(t-t_0)/\tau_1]+A_2 \cdot \exp[(t-t_0)/\tau_2]$. (x = failed to fit).

| Time | Vol ($cm^3$) | $A_1 \pm$ Err (mM) | $A_2 \pm$ Err (mM) |
|---|---|---|---|
| Pre-Irradiation | 3.9 | 0.471 ± 0.005 | 0.161 ± 0.006 |
| 0 Hrs Post-Irradiation | 3.9 | 1.024 ± 0.003 | 0.3 ± 0.4 |
| 24 Hrs Post-Irradiation | 2.9 | 0.140 ± 0.003 | 0.348 ± 0.003 |
| 48 Hrs Post-Irradiation | 2.5 | 0.032 ± 0.001 | 0.080 ± 0.001 |
| 96 Hrs Post-Irradiation | 2.0 | x | x |

**Table 22** (**cont.**) Summary of the parameters of the vascular oxygen dynamics ($\Delta[HbO_2]$) before and after the single dose irradiation (20 Gy), determined by the bi-exponential model: $\Delta[HbO_2]=A_1 \cdot \exp[(t-t_0)/\tau_1] + A_2 \cdot \exp[(t-t_0)/\tau_2]$. (x = failed to fit).

| Tumor | Vol ($cm^3$) | $\tau_1 \pm$ Err (min) | $\tau_2 \pm$ Err (min) | $R$ |
|---|---|---|---|---|
| Pre-Irradiation | 3.9 | 0.241 ± 0.007 | 5.4 ± 0.7 | 0.947 |
| 0 Hrs Post-Irradiation | 3.9 | 0.256 ± 0.004 | 61 ± 98 | 0.951 |
| 24 Hrs Post-Irradiation | 2.9 | 0.07 ± 0.01 | 4.16 ± 0.09 | 0.957 |
| 48 Hrs Post-Irradiation | 2.5 | 0.113 ± 0.007 | 4.18 ± 0.05 | 0.987 |
| 96 Hrs Post-Irradiation | 2.0 | x | x | x |

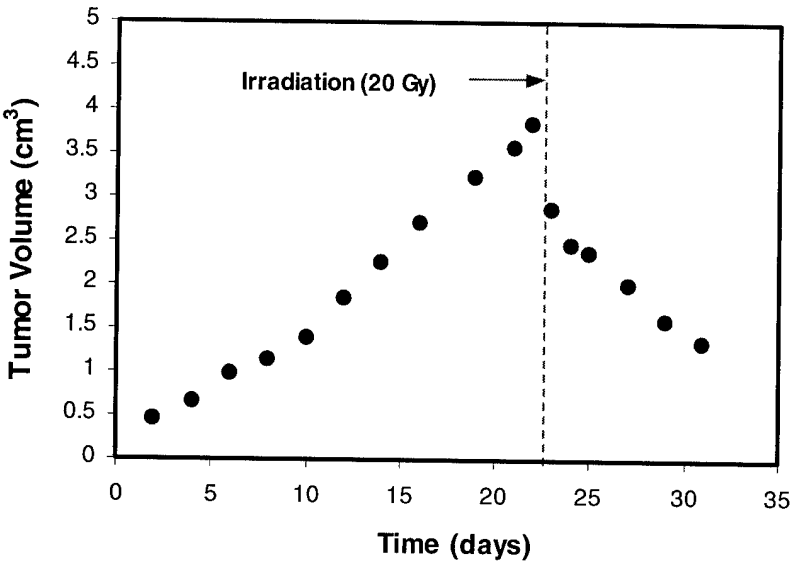


**Figure 67** Tumor volume as a function of time before and after the single dose irradiation (20 Gy) for the experimental group.

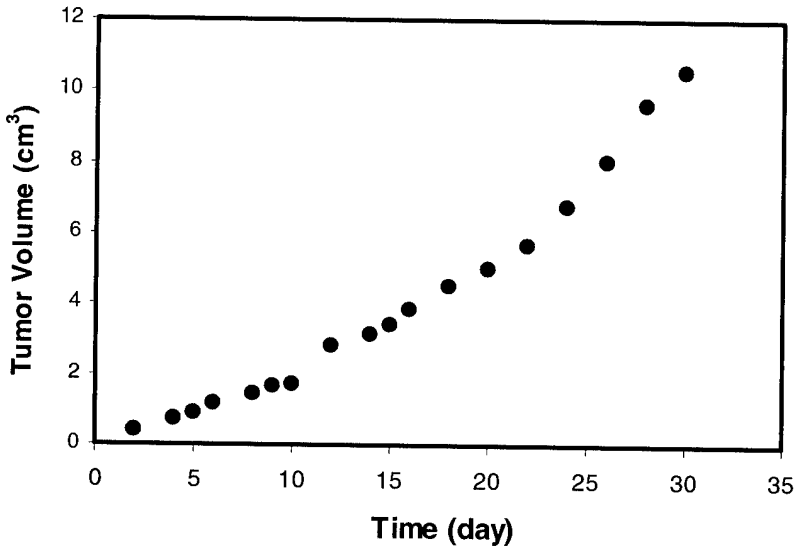


**Figure 68** Tumor volume as a function of time for the control group.

**Figure 67** shows the tumor growth curve for the experimental group before and after the single dose irradiation. Pre-irradiation, the tumor grew exponentially. Post-irradiation, tumor volume began to shrink for about 10 days and the shrinkage was significant ($p < 0.007$). By contrast, the non-irradiated tumors continued to grow until they approached a limiting maximum volume, as illustrated in **Figure 68**.

- **Discussion**

In this study, changes in tumor vascular $\Delta[HbO_2]$ and $\Delta[Hb]_{Total}$ in mammary adenocarcinomas 13762NF were measured with NIRS following a single dose irradiation (20 Gy). The study found that tumor reoxygenation occurred two hours post-irradiation. After this point, however, vascular oxygenation decreased significantly compared to the pre-irradiation value. The same response pattern was also observed in $\Delta[Hb]_{Total}$ and tumor vascular $\Delta[HbO_2]$ and $\Delta[Hb]_{Total}$ were highly correlated. In addition, there were strong linear relationships between tumor vascular $\Delta[HbO_2]$, $\Delta[Hb]_{Total}$, and tumor volume post-irradiation, contrary to those observed with the non-irradiated tumors. Furthermore, the irradiation also changed the rate of tumor response to carbogen intervention. The fast time constant $\tau 1$ increased with time post-irradiation, suggesting the tumor perfusion deteriorated following the irradiation, as evidenced by a decreasing trend in tumor vascular oxygenation post-irradiation. This phenomenon could be due to the late irradiation damage to the tumor vasculature. At the end of the irradiation, there could be a great deal of latent damage in the tumor vasculature. This latent damage was not expressed until the cells were called upon to divide [**91**]. The results presented here were consistent with those published by Grau *et al.* [**106**].

To explain the phenomenon of tumor reoxygenation, a number of possible mechanisms have been proposed. These include improved tumor blood flow, decreased metabolic rate of radiation damaged cells, reduced interstitial pressure, and decreased tumor volume resulting in surviving cells being closer to blood vessels [**91**]. However, there is evidence to suggest that decreased tumor oxygen consumption and increased tumor blood flow may be the dominant factors in reoxygenation [**107**]. Finally, This study demonstrated the possibility of investigating tumor reoxygenation using NIRS and laid a foundation for further investigation.

## 7) Dissertation

The studies described in this report constitute a part of my dissertation, which was defended successfully in the Spring Semester 2001.

# 4. KEY RESEARCH ACCOMPLISHMENTS

- The pedicle tumor model was proven to be ideally suited for *in vivo* NIRS and MRI studies, therapy, and manipulation.

- The pedicle tumor model allowed accurate measurement of tumor size and had no significant difference from the traditional subcutaneous site in the thigh in terms of growth.

- Mammary adenocarcinomas 13762NF were found to have a viable, well-oxygenated peripheral region, and a necrotic, poorly-oxygenated central region.

- Mammary adenocarcinomas 13762NF were found to have a silent phase ranging from 2 to 3 weeks and a mean volume doubling time (VDT) of ~ 4 days.

- The first order, autonomous differential equation was proven to be a good tumor growth model at least for a short period of growth for mammary adenocarcinomas 13762NF.

- For the birdcage resonator, laboratory bench testing indicated that the unloaded $Q$s for both proton and fluorine resonant modes were similar and relatively low. The loaded $Q$ dropped by about 36% for fluorine and 39% for proton. Phantom imaging found that the $\boldsymbol{B}_1$ fields were somewhat heterogeneous across usable volume of the resonator for both resonant modes.

- The slotted tube resonator had the capability of being continuously tuned in the frequency range of 150 MHz ~ 220 MHz. The resonator had high $Q$ values and short $90^0$ pulse widths for both proton and fluorine. In addition, the $\boldsymbol{B}_1$ field homogeneity was found to be excellent for proton resonance and reasonably good for fluorine resonance.

- Both resonant frequencies of the slotted tube resonator were stable and immune to external electromagnetic interference.

- The copper shield not only lowered the $Q$ value of the resonator, but also increased the RF pulse width.

- For the slotted tube resonator, NMR samples had a much stronger effect on the $^{19}F$ resonance than on the $^{1}H$ resonance.

- The HFB signal intensity was found to decay exponentially with a typical biological half-life ranging from $T_{1/2}$ = 700 to 1200 min, which, we believe, would provide an indication of relative tumor blood flow (TBF).

- The global and regional clearance and redistribution of HFB within the tumors did not interfere with $^{19}F$ MR EPI oximetry.

- Tumor voxels with high baseline $pO_2$ had significantly different response characteristics from those with initially low $pO_2$, with voxels of high baseline $pO_2$ showing significant changes in $pO_2$ while voxles of low baseline $pO_2$ showing small changes.

- Time constants ($\tau$) of well-oxygenated voxels (10 ~ 20 min) were much shorter than those of hypoxic voxels (> 50 min).

- NIR spectroscopy showed significant changes in tumor vascular oxygenation $\Delta[HbO_2]$ accompanying respiratory interventions. $^{19}F$ MR-EPI showed significant changes in tumor tissue $pO_2$, with considerable regional heterogeneity in both absolute values and rate of change accompanying interventions. Changes in tumor vascular $\Delta[HbO_2]$ preceded tumor tissue $pO_2$, particularly for smaller tumors.

- Strong correlation existed between the maximum $pO_2$ value attained during the course of an experiment and mean baseline $pO_2$ and between mean $pO_2$ and mean baseline $pO_2$.

- Strong correlation was observed between the time constant and the initial mean baseline $pO2$, indicating the faster the time constant, the higher the $pO_2$ in a particular voxel.

- There was a fairly strong linear relationship between baseline hypoxic fraction and baseline $pO_2$.

- There was a fairly strong linear relationship between baseline hypoxic fraction correlated and tumor volume.

- There was also a fairly strong linear relationship between mean baseline $pO_2$ and tumor volume.

- $^{19}F$ EPI oximetry of HFB was proven to be a useful technique for measuring tumor oxygenation.

- $pO_2$ and the distribution of $pO_2$ in breast adenocarcinomas 13762 NF changed with tumor growth and there existed heterogeneity in $pO_2$ distribution.

- Tumor oxygenation could be manipulated by inhaling different gases for breast adenocarcinomas 13762 NF.

- We found that breathing elevated $FO_2$ had a significant effect on arterial $s_aO_2$, tumor vascular $\Delta[HO_2]$, and tumor tissue $pO_2$. $s_aO_2$ had the fastest response, followed by $\Delta[HO_2]$, and $pO_2$.

- NIR spectroscopy is completely non-invasive, inexpensive, portable, and amenable to real-time measurements.

- Carbogen breathing significantly increased tumor vascular $\Delta[HbO_2]$.

- Carbogen breathing also significantly increased tumor $\Delta[Hb]_{Total}$,. However, the change in magnitude was much smaller than that in $\Delta$[HbO2].

- There was a fairly strong positive linear relationship between A1 and tumor volume

- We found that there was a strong linear relationship between $\Delta Hb]_{Total}$ and maximum $\Delta[HbO_2]$ following carbogen intervention.

- There was a fairly strong positive linear relationship between $\tau 1$ and $\tau 2$.

- Irradiation caused a significant decrease in tumor volume ($p < 0.007$).

- Tumor reoxygenation occurred two hours post-irradiation. After this point, however, vascular oxygenation decreased significantly compared to the pre-irradiation value.

# 5. REPORTABLE OUTCOMES

## ----PUBLICATIONS:

### Manuscripts

1) **"Tumor Oximetry: A Comparison between Near-infrared Frequency-Domain Spectroscopy of Hemoglobin Saturation and $^{19}$F MRI of Hexafluorobenzene"**
Katherine L. Worden, **Yulin Song**, Xin Jiang, Anca Constantinescu, Ralph P. Mason, and Hanli Liu, SPIE Vol. 3597:601-610, 1999.
(Presented in part at the International Symposium on Biomedical Optics, sponsored by the Society of Photo-Optical Instrumentation Engineers (**SPIE**), 1998).

2) **"Tumor Oxygen Dynamics: Comparison of $^{19}$F MR EPI and Frequency Domain NIR Spectroscopy"**
**Yulin Song**, Kate L. Worden, Xin Jiang, Dawen Zhao, Anca Constantinescu, Hanli Liu, and Ralph P. Mason, **ISOTT**, 1999.

3) **"Tumor Oximetry: Comparison of $^{19}$F MR EPI and Electrodes"**
Ralph P. Mason, Sandeep Hunjan, Anca Constantinescu, **Yulin Song**, Dawen Zhao, Eric W. Hahn, Peter P. Antich, and Peter Peschke, **ISOTT**, 1999.

4) **"Noninvasive Investigation of Blood Oxygenation Dynamics of Tumors by Near-Infrared Spectroscopy"**
Hanli Liu, **Yulin Song**, Katherine L. Worden, Xin Jiang, Anca Constantinescu, and Ralph P.Mason, Applied Optics, October, 2000.

5) **"Interplay of Tumor Vascular Oxygenation and $pO_2$ in Tumors Using NIRS and Needle Electrode"**
Jae G. Kim, **Yulin Song**, Dawen Zhao, Anca Constantinescu, Ralph P.Mason, and Hanli Liu, SPIE, 2001 (in the press).

6) **"Interplay of Tumor Vascular Oxygenation and Tumor $pO_2$ Observed Using NIRS, Oxygen Electrode, and $^{19}$F MR $pO_2$ Mapping"**
Jae G. Kim, **Yulin Song**, Dawen Zhao, Anca Constantinescu, Ralph P.Mason, and Hanli Liu, J. of Biomedical Optics, 2001 (submitted).

### Abstracts

1) **"Regional Tumor Oxygen Tension and Blood Flow: Correlation Studies Using 19F PBSR-EPI of Hexafluorobenzene"**
**Yulin Song**, Ralph P. Mason, Sandeep Hunjan, Anca Constantinescu, Eric Hahn, and Peter Antich.
(Presented at the Workshop on Magnetic Resonance in Experimental and Clinical Cancer Research, sponsored by the International Society for Magnetic Resonance in Medicine (**ISMRM**), St. Louis, November, 1998).

2) **"Tumor Oxygen Dynamics: Comparison between $^{19}$F MR-EPI of Hexafluorobenzene and Frequency Domain NIR Spectroscopy"**
**Yulin Song**, Kate L. Worden, Xin Jiang, Dawen Zhao, Anca Constantinescu, Hanli Liu, and Ralph P. Mason.

(Presented at the 27th Annual Meeting of International Society on Oxygen Transport to Tissue (**ISOTT**), Proc 27th, **ISOTT**, Dartmouth, NH, August, 1999).

3) **"Tumor Oximetry: Comparison of $^{19}F$ MR EPI and Electrodes"**
Ralph P. Mason, Sandeep Hunjan, Anca Constantinescu, **Yulin Song**, Dawen Zhao, Eric W. Hahn, Peter P. Antich, and Peter Peschke.
(Presented at the 27th Annual Meeting of International Society on Oxygen Transport to Tissue (**ISOTT**), Proc 27th, **ISOTT**, Dartmouth, NH, August, 1999).

4) **"Tumor Oxygenation and Measurement of Regional Dynamic Changes"**
Ralph P. Mason, Sandeep Hunjan, Anca Constantinescu, **Yulin Song**, Eric W. Hahn, Peter P. Antich, Christian Blum, and Peter Peschke.
(Presented at International Conference on Molecular Determinants of Sensitivity to Antitumor Agents, sponsored by **A**merican **A**ssociation for **C**ancer **R**esearch (**AACR**), Whistler, Canada, March, 1999).

7) **"Regional Tumor Tissue $pO_2$ and Blood $sO_2$ : Comparison of $^{19}F$ MR EPI and Frequency Domain NIR Spectroscopy"**
**Yulin Song**, Xin. Jiang, Dawen. Zhao, Anca Constantinescu, Hanli. Liu, and Ralph. P. Mason.
(Presented at the Eighth Scientific Meeting and Exhibition of the **ISMRM**, Denver, Colorado, April, 2000).

8) **"Noninvasive Measurement of Tumor Hemoglobin Dynamics Using Near-Infrared Spectroscopy"**
Hanli Liu, **Yulin Song**, Katherine L. Worden, Anca Constantinescu, and Ralph P.Mason.
(Presented at the Biomedcal Topical Meetings of Optical Society of America (**OSA**), Miami Beach, FL, April 2-5, 2000)

7) **"Tumor Oximetry: An Enhanced Dynamic Mapping Procedure Using $^{19}F$ Echo Planar MRI"**
Dawen Zhao, Sandeep Hunjan, Anca Constantinescu, **Yulin Song**, Eric W. Hahn, Peter P. Antich, and Ralph P. Mason.
(Presented at Radiation Research Meeting, Albuquerque, May 2000).

8) **"Regional Tumor Oxygen Dynamics: Relating Tissue $_pO_2$ to the Vasculature"**
**Yulin Song**, Xin Jiang, Dawen Zhao, Anca Constantinescu, Hanli Liu, and Ralph P. Mason.
(Presented at the Era of Hope Meeting sponsored by the Department of Defense, Atlanta, GA, June 8-11, 2000).

9) **"FREDOM (Fluorine Relaxometry using Echo planar imaging for Dynamic Oxygen Mapping): a contextual review"**
Ralph P. Mason, Dawen Zhao, Anca Constantinescu, **Yulin Song**, Lan Jiang and Eric W. Hahn
(Presentated at ISMRM Workshop on MR in Experimental and Clinical Cancer Research in the New Millennium).

10) **"Diverse Approaches to Monitoring Oxygen Dynamics in Rat Breast and Prostate Tumors"**
Dawen. Zhao, **Yulin Song**, Han Liu, Amca. Constantinescu, Eric W. Hahn, and Ralph. P. Mason,
(Presented at the Conference on Chemical Modifiers of Cancer Treatment, Banff, Canada, Oct. 2000).

**----DEGREE OBTAINED THAT IS SUPPORTED BY THIS AWARD:**
Ph.D. in Biomedical Engineering

**----EMPLOYMENT OR RESEARCH OPPORTUNITIES RECEIVED ON TRAINING SUPPORTED BY THIS AWARD**
Post-doctoral fellow in the Department of Radiation Oncology, School of Medicine, Stanford University (started on March 1, 2001)

# 6. CONCLUSIONS

Regional tumor tissue $pO_2$, vascular $\Delta[HbO_2]$ or $sO_2$, and $[Hb]_{Total}$ are critical physiological parameters in radiotherapy and some forms of chemotherapy. The capability to measure and manipulate them will provide insight into progressive physiological changes in a tumor accompanying interventions and enhance therapeutic outcomes. NIRS has the advantages of being entirely noninvasive, inexpensive, portable, and real-time. But the $^{19}F$ MR EPI approach clearly reveals detailed oxygenation heterogeneity. The correlation of NIRS and $^{19}F$ MR EPI technologies will help us understand issues of oxygen transport, perfusion, and consumption. I believe that synergistic application of multiple approaches to tumor oxygenation can lead to optimized tumor therapy.

# 7. REFERENCES


1. Vaupel, P., Thews, O, Kelleher, D. K., and Höckel, M., "Current status of knowledge and critical issues in tumor oxygenation", *In*: Hudetz and Bruley (eds), *Oxygen Transport to Tissue XX*, Plenum Press: New York, 591-602 (1998).
2. Vaupel, P., "Vascularization, blood flow, oxygenation, tissue *p*H, and bioenergetic status of human breast cancer", *In*: Nemoto and LaManna (eds), *Oxygen Transport to Tissue XVIII*, Plenum Press: New York, 243-253 (1997).
3. Vaupel, P., "Oxygen transport in tumors: Characteristics and clinical implications", *Adv. Exp. Med. Biol.*, **388**:341-351 (1996).
4. Hirst, D. G., "Anemia: A problem or an opportunity in radiotherapy?", *Int. J. Radiat. Oncol. Biol. Phys.*, **12:**2009-2017 (1986).
5. Busch, O. R., Hop, W. C., Hoynck van Papendrecht, M. A., Marquet, R. L., Jeekel, J., "Blood transfusions and prognosis in colorectal cancer", *N. Engl. J. Med.*, **328**:1372-1376 (1993).
6. Lavey, R. S., Dempsey, W. H., "Erythropoietin increases hemoglobin in cancer patients during radiation therapy", *Int. J. Radiat. Oncol. Biol. Phys.*, **27**:1147-1152 (1993).
7. Thomlinson, R. H., and Gray, L. H., "The histological structure of some human lung cancers and the possible implications for radiotherapy", *Br. J. Cancer,* **9**:539-549 (1955).
8. Brizel, D. M, Sibley, G. S., Prosnitz, L. R., Scher, R. L, and Dewhirst, M.W., "Tumor hypoxia adversely affects the prognosis of carcinoma of the head and neck", *Int. J. Radiat. Oncol. Biol. Phys.*, **38**:285-289 (1997).
9. Höckel, M., Knoop, C., Schlenger, K., "Intratumoral $pO_2$ predicts survival in advanced cancer of the utertine cervix", *Radiother. Oncol.*, **26**:45-50 (1993).
10. Fyles, A. W., Milosevic, M., Wng, R., Kavanagh, M. C., Pintile, M., Sun, A., Chapman, W., Levin, W., Manchul, L., Keane, T. J., and Hill, R. P., "Oxygenation predicts radiation response and survival in patients with cervix cancer", *Radiother. Oncol.*, **48**:149-156 (1998).
11. Teicher, B., Lazo, J., and Sartorelli, A., "Classification of antineoplastic agents by their selective toxicities toward oxygenated and hypoxic tumor cells", *Cancer Res.*, **41**:73-81 (1981).
12. Siemann, D. W., "Potentiation of chemotherapy by hypoxic cell radiation sensitizers – a review", *Int. J. Radiat. Oncol. Biol. Phys.*, **8**:1029-1034 (1982).
13. Chapman, J. D., Stobbe, C. C., Arnfield, M. R., Santus, R., Lee, J., and McPhee, M. S., "Oxygen dependency of tumor cell killing *in vitro* by light activated photofrin II", *Radiat. Res.*, **126**:73-79 (1991).
14. Pötgens, A. J. G., Westphal, H. R., de Waal, R. M. W, and Ruiter, D. J., "The role of vascular permeability factor and basic fibroblast growth factor in tumor angiogenesis", *Biol. Chem.*, Hopper-Seyler, **376**:57-70 (1995).

15. Blancher, C., and Harris, A. L., "The molecular basis of the hypoxia response pathway: tumor hypoxia as a therapy target", *Cancer Metastasis Rev.*, **17**:187-194 (1998).
16. Höckel, M., Schlenger, K., Aral, B., Mitze, M., Schäffer, U., and Vaupel, P., "Association between tumor hypoxia and malignant progression in advanced cancer of the uterine cervix", *Cancer Res.*, **56**:4509-15 (1996).
17. Brizel, D. M., Scully, S. P., Harrelson, J. M., "Tumor oxygenation predicts for the likelihood of distant metastases in human soft tissue sarcoma", *Cancer Res.*, **56**:941-943 (1996).
18. Sundfor, K., Lyng, Rofstad, E. K., "Tumor hypoxia and vascular density as predictors of metastasis in squamous cell carcinoma of the uterine cervix", *Br. J. Cancer*, **78**:822-827 (1998).
19. Young, S. D., Marshall, R. S., and Hill, R. P., "Hypoxia induces DNA overreplication and enhances metastatic potential of murine tumor cells", *Proc. Natl. Acad. Sci. USA*, **85**:9533-9537 (1988).
20. Reynolds, T. Y., Rockwell, S., and Glazer, P. M., "Genetic instability induced by the tumor microenvironment", *Cancer Res.*, **56**:5754-5757 (1996).
21. Graeber, T. G., Osmanian, C., and Jacks, T., "Hypoxia-mediated selection of cells with diminished apoptotic potential in solid tumors", *Nature*, **379**:88-91 (1996).
22. Nordsmark, M., Overgaard, M., and Overgaard, J., "Pretreatment oxygenation predicts radiation response in advanced squamous cell carcinoma of the head and neck", *Radiother. Oncol.*, **41**:31-39 (1996).
23. Stadler, P., Becker, A., Feldmann, H. J., Hansgen, G., Dunst, J., Wurschmid, F., Molls, M., "Influence of the hypoxic subvolume on the survival of patients with head and neck cancer," *Int. J. Radiat. Oncol. Biol. Phys.*, **44**:749-754 (1999).
24. Dusenbery, K. E., McGuire, W. A., Holt, P. J., Carson, L. F., Fowler, J. M, Twiggs, L. B., Potish, R. A., "Erythropoietin increases hemoglobin during radiation therapy for cervical cancer", *Int. J. Radiat. Oncol. Biol. Phys.*, **29**:1079-1084 (1994).
25. Henke, M., Guttenberger, R., Baker, A., Pajonk, F., Pötter, R., Frommhold, H., "Erythropoietin for patients undergoing radiotherapy: A pilot study", *Radiother. Oncol.*, **50**:185-190 (1999).
26. Overgaard, J., Horsman, M., "Modification of hypoxia-induced radioresistance in tumors by the use of oxygen and sensitizers", *Semin. Radiat. Oncol.*, **6:**10-21 (1996).
27. Guttenberger, R., Lutterbach, J., Roth, A., Röser, S., Schindler, R., Henke, M., Frommhold, H., "Hemoglobin levels predict local regional control after postoperative radiotherapy for advanced head and neck cancer", *Eur. J. Cancer,* **33** (suppl):102-103 (1997).
28. Vaupel, P., Kelleher, D. K., and Thews, O, "Modulation of tumor oxygenation ", *Int. J. Radiat. Oncol. Biol. Phys.*, **42**:843-848 (1998).
29. Pederson, D., Sogaard, H., and Overgaard, J., "Prognostic value of pretreatment factors in patients with locally advanced carcinoma of the uterine cervix treated by radiotherapy alone", *Acta Oncol.*, **34**:787-795 (1995).

30. Ludwig, H., and Pecorelli, S., "Suboptimal hemoglobin levels: Do they impact patients and their therapy? Audience responses", *Semin. Oncol.*, **27**(suppl):18-19 (2000).
31. Vaupel, P., Schlenger, K., Knoop, C., and Höckel, M., "Oxygenation of human tumors: evaluation of tissue distribution in breast cancers by computerized $O_2$ tension measurements", *Cancer Res.*, **51**:3316-22 (1991).
32. Collingridge, D. R., Young, W. K., Vojnovic, B., Wardman, P., Lynch, E. M., Hill, S. A., and Chaplin, D. J., "Measurement of tumor oxygenation: a comparison between polarographic needle electrodes and a time-resolved luminescence-based optical sensor", *Radiat. Res.*, **147**:329-34 (1997).
33. Swartz, H. M., Bacic, G., Friedman, B., Goda, F., Grinberg, O., Hoopes, P. J., Jiang, J., Liu, K. J., Nakashima, T., O'Hara, J. A., and Walczak, T., "Measurement of $pO_2$ *in vivo*, including human subjects by electron paramagnetic resonance", *In*: P. Wagner (ed), *Oxygen Transport to Tissue XIV*, P. Plenum Press: New York, 221-223 (1994).
34. O'Hara, J. A., Goda, F., Liu, K. J., Bacic, G., Hoopes, P. J., and Swartz, H. M., "The $pO_2$ in a murine tumor after irradiation: an *in vivo* electron paramagnetic resonance oximetry study", *Radiat. Res.*, **144**:222-229 (1995).
35. Olive, P. L., and Durand, R. E., "Detection of hypoxic cells in a murine tumor with the use of the comet assay", *J. Natl. Cancer Inst.*, **84**:707-711 (1992).
36. Helmlinger, G., F., Yuan, F., Dellian, M., and Jain, R. K., "Interstitial *p*H and $pO_2$ gradients in solid tumors *in vivo*: high resolution measurements reveal lack of correlation", *Nature Medicine*, **3**(**2**):177-182 (1997).
37. Kavanagh, M. C., Sun, A., Hu, Q., and Hill, R. P., "Comparing techniques of measuring tumor hypoxia in different murine tumors: Eppendorf $pO_2$ histograph, [$^3$H] nitroimidazole binding and paired survival assays", *Radiat. Res.*, **145**:491-500.
38. Vaupel, P., Okunieff, P., Kallinowski, F., and Neuringer, L. J., "Correlation between $^{31}$P NMR and tumor $pO_2$ in a murine fibrosarcoma", *Radiat. Res.*, **120**:477-493.
39. Mason, R. P., Constantinescu, A., Hunjan, S., Le, D., Hahn, E. W., Antich, P. P., Blum, C., and Peschke, P., "Regional tumor oxygenation and measurement of dynamic change", *Radiat. Res.*, **152**:239-245 (1999).
40. Hunjan, S., Mason, R. P., Constantinescu, A., Peschke, P., Hahn, E. W., and Antich, P. P., "Regional tumor oximetry: $^{19}$F NMR spectroscopy of hexafluorobenzene", *Int. J. Radiat. Oncol. Biol. Phys.*, **41**:161-171 (1998).
41. Steen, R., "Characterization of tumor hypoxia by $^{31}$P spectroscopy", *Am. J. Roentgenol*, **157**:243-248 (1991).
42. Lee, A. T., Glover, G. H., and Meyer, C. H., "Discrimination of large venous vessels in time-course spiral blood-oxygen-level-dependent magnetic resonance functional neuroimaging", *Magn. Reson. Med.*, **33**:745-754 (1995).
43. Ogawa, S., Menon, R. S., Tank, D. W., Kim, S., Ellermann, J. M., and Ugurbil, K., "Functional brain mapping by blood oxygenation level-dependent magnetic resonance imaging", *Biophys. J.*, **64**:803-812 (1993).

44. Mason, R. P., "Non-invasive physiology: $^{19}F$ NMR of perfluorocarbon", *Art. Cell Blood Sub. & Immob. Biotech.*, **22**:1141-1153 (1994).
45. Mason, R. P., Constantinescu, A., Hunjan, S., Le, D., Hahn, E. W., Antich, P. P., Blum, C., Peschke, P., "Regional tumor oxygenation and measurement of dynamic change", *Radiat. Res.*, **152**:239-245 (1999).
46. Hunjan, S., Mason, R. P., Constantinescu, A., Peschke, P., Hahn, E. W., Antich, P. P., "Regional tumor oximetry: $^{19}F$ NMR spectroscopy of hexafluorobenzene", *Int. J. Radiat. Oncol. Biol. Phys.*, **41**:161-171 (1998).
47. Chance, B., Nioka, S., Kent, J., McCully, K., Fountain, M., Greenfield, R., and Holtom, G., "Time resolved spectroscopy of hemoglobin and myoglobin in resting and ischemic muscle", *Anal. Biochem.*, **174**:698-707 (1988).
48. Homma, S., Fukunaga, T., and Kagaya, A., "Influence of adipose tissue thickness on near infrared spectroscopic signals in the measurement of human muscle", *J. Biomed. Opt.*, **1**(4): 418-424 (1996).
49. Ferrari, M., Wei, Q., Carraresi, L., De Blasi, R. A., and Zaccanti, G., "Time-resolved spectroscopy of the human forearm", *J. Photochem. Photobiol. B: Biol.* **16**:141-153 (1992).
50. Chance, B., Anday, E., Nioka, S., Zhou, S., Hong, L., Worden, K., Li, C., Murray, T., Ovetsky, Y., Pidikiti, D., and Thomas, R., "A novel method for fast imaging of brain function non-invasively with light", *Optics Express*, **2**(10): 411-423 (1998).
51. Wenzel, R., Obrig, H., Ruben, J., Villringer, K., Thiel, A., Bernarding, J., Dirnagl, U., and Villringer, A., "Cerebral blood oxygenation changes induced by visual stimulation in humans", *J. Biomed. Opt.*, **1**(4):399-404 (1996).
52. Cope, M., and Delpy, D. T., "A system for long term measurement of cerebral blood and tissue oxygenation in newborn infants by near infrared transillumination", *Med. Biol. Eng. Comp.*, **26**:289-294 (1988).
53. Steen, R. G., Wilson, D. A., Bowser, C., Rajan, S. S., Wehrle, J. P., and Glickson, J. D., "$^{31}P$ NMR spectroscopic and near-infrared spectrophotometric studies of effects of anesthetics on *in vivo* RIF-1 tumors: relationship to tumor radiosensitivity", *NMR in Biomed.*, **2**:87-92 (1989).
54. Steen, R. G., Kitagishi, K., and Morgan, K., "*In vivo* measurement of tumor blood oxygenation by near-infrared spectroscopy: immediate effects of pentobarbital overdose or carmustine treatment", *J. Neuro-Oncol.*, **22**:209-220 (1994).
55. Sostman, H. D., Rockwell, S., Sylvia, A. L., Madwed, D., Cofer, G., Charles, H. C., Negro-Vilar, R., and Moore, D., "Evaluation of BA1112 rhabdomyosarcoma oxygenation with microelectrodes, optical spectrophotometry, radiosensitivity, and magnetic resonance spectroscopy", *Magn. Reson. Med.*, **20**:253-267 (1991).
56. Mariya, Y., Seinberg, F., Streffer, C., Fuhrmann, C., and Abe, Y., "Oxygenation status and tumor response during fractionated irradiation in two murine tumor cell lines of same origin but different intrinsic radiosensitivities", *Radiat. Med.*, **17**(2):175-179 (1999).

57. Hoon, D. B. S., "Circulating immune complexes in rats bearing 6-thioguanine-resistant variants of the 13762 mammary adenocarcinoma", *Cancer Res.* **44**:2406-2409 (1984).
58. Hahn, E. W., Peschke, P., Mason, R. P., Babcock, E. E., and Antich, P. P., "Isolated Tumor Growth in a Surgically Formed Skin Pedicle in the Rat: A New Tumor Model for NMR Studies", *Magn. Reson. Imaging*, **11**:1007-1017 (1993).
59. Adam, J. A., "General aspects of modeling tumor growth and immune response" in *A Survey of Models for Tumor-Immune System Dynamics*, Adam, J. A. and Bellomo, N., eds., *Birkhäuser* (1996).
60. Steel, G. G., "Growth Kinetics of Tumors", *Clarendon Press, Oxford*, (1977).
61. Bassukas, I. D., "Comparative Gompertzian analysis of alterations of tumor growth patterns", *Cancer Res.*, **54**:4385-4392 (1994).
62. Hayes, C. E., Edelstein, W. A., Schenck, J. F., Mueller, O. M., and Eash, M., "An efficient, highly homogeneous radiofrequency coil for whole-body NMR imaging at 1.5 T", *J. Magn. Reson.*, **63**:622 - 628 (1985).
63. Pascone, R., Vullo, T., Farrelly, J., and Cahill, P. T., "Explicit treatment of mutual inductance in eight-column birdcage resonators", *Magn. Reson. Imag.*, **10**:401 - 410 (1992).
64. Cross, T. A., Muller, S., and Aue, W. P., "Radiofrequency resonators for high-field imaging and double-resonance spectroscopy", *J. Magn. Reson.*, **62**: 87 - 98 (1985).
65. Press, W. H., Teukolsky, S. A., Vetterling, W. T., and Flannery, B. P., *Numerical Recipes in C*, Cambridge University Press, 683 - 688 (1994).
66. Schneider, H. J., Dullenkopf, P., "Slotted tube resonator: a new NMR probe head at high observing frequencies", *Rev. Sci. Instrum.*, **48**:68 - 73 (1977).
67. Alderman, W., and Grant, D. M., "An efficient decoupler coil design which reduces heating in conductive samples in superconducting spectrometers", *J. Mag. Reson.*, **36**:447 - 451 (1979).
68. Ifeachor, E. C., Jervis, B. W., "Digital Signal Processing - A Practical Approach", *Addison-Wesley Publishing Company*, 374-483 (1993).
69. Mansfield, P., Pykett, I. L., "Biomedical and medical imaging by NMR", *J. Magn. Reson.*, **29**:355-373 (1978).
70. Barker, B. R., Mason, R. P., Peshock, R. M., "Echo planar imaging of perfluorocarbons", *Magn. Reson. Imaging*, **11**:1165-1173 (1993).
71. Barker, B. R., Mason, R. P., Bansal, N., Peshock, R. M., "Oxygen tension mapping by $^{19}F$ echo planar NMR imaging of sequestered perfluorocarbons", *JMRI*, **4**:595-602 (1994).
72. Le, D., Mason, R. P., Hunjan, S., Constantinescu, A., Barker, B. R., Antich, P. P., "Regional Tumor Oxygen Dynamics: $^{19}F$ PBSR EPI of Hexafluorobenzene", *Magn. Reson. Imaging*, **15**:971-981 (1997).
73. Sevick, E. M., Chance, B., Leigh, J., Nioka, S., and Maris, M., "Quantitation of time-and frequency-resolved optical spectra for the determination of tissue oxygenation", *Anal. Biochem.*, **195**:330-351 (1991).

74. Yunsong, Y., Liu, H., Li, X., and Chance, B., "Low-Cost Frequency-Domain Photon Migration Instrument for Tissue Spectroscopy, Oximetry, and Imaging", *Opt. Eng.*, **36(5)**:1562-1569 (1997).
75. "Data Acquisition Basics Manual", *National Instruments*, (1998).
76. Delpy, D. T. and Cope, M., "Quantification in near-infrared spectroscopy", *Phil. Trans. R. Soc. Lond. B.*, **952**:649-659 (1997).
77. Liu, H., Song, Y., Worden, K. L., Jiang, X., Constantinescu, A., and Mason, R. P., "Noninvasive Investigation of Blood Oxygenation Dynamics of Tumors by Near-Infrared Spectroscopy", *Applied Optics*, **39**(28):5231-5243 (2000).
78. Delpy, D. T., Cope, M., "A system for long term measurement of cerebral blood and tissue oxygenation in newborn infants by near infrared transillumination", *Med. Biol. Eng. Comp.*, **26**:289-294 (1988).
79. Zijlstra, W. G., Buursma, A., Meeuwsen-van der Roest, W. P., "Absorption spectra of human fetal and adult oxyhemoglobin, deoxyhemoglobin, carboxyhemoglobin, and methemoglobin", *Clin. Chem.*, **37**(9):1633-1638 (1991).
80. Liu, H., Matson, C. L., Lau, K., and Mapakshi, R. R., "Expeirmental validation of a backpropagation algorithm for three-dimensional breast tumor localization", *IEEE J. Select. Top. Quan. Elect.*, **5(4)**:1049-1057 (1999).
81. Zar, J. H., "Biostatistical Analysis", 3rd Edition, *Prentice Hall*, 179-275 (1996).
82. Falk, S. J., Ward, R., and Bleehen, N. M., "The influence of carbogen breathing on tumor tissue oxygenation in man evaluated by computerized $pO_2$ histography", *Br. J. Cancer*, **66**:919-924 (1992).
83. Fatigante, L. Ducci, F., Cartei, F., Colosimo, S., Marini, C., Prediletto, R., Danesi, R., Laddaga, M., Del Tacca, M., and Caciagli, P., "Carbogen and nicotinamide combined with unconventional radiotherapy in glioblastoma multiforme: A new modality treatment", *Int. J. Radiat. Oncol. Biol. Phys.*, **37**:499-504 (1997).
84. Robinson, S. P., Rodrigues, L, M., Ojugo, A. S. E., McSheehy, P. M., J., Howe, F. A., and Griffiths, J. R., "The response to carbogen breathing in experimental tumour models monitored by gradient-recalled echo magnetic resonance imaging", *Br. J. Cancer*, **75(7)**:1000-1006 (1997).
85. Rodrigues, L, M., Robinson, S. P., McSheehy, P. M., J., Stubbs, M., and Griffiths, J. R., "Relative roles of $O_2$ and $CO_2$ in the carbogen-enhanced-uptake of ifosfamide into tumours - an *in vivo* $^{31}$P MRS study", *Proc. Intl. Soc. Mag. Reson. Med.*, **8**:1046 (2000).
86. Honess, D. J., and Bleehen, N. M., "Perfusion changes in the RIF-1 tumor and normal tissues after carbogen and nicotinamide, individually and combined", *Br. J. Cancer*, **71**:1175-1180 (1995).
87. Hull, E. L., Conover, D. L., and Foster, T. H., "Carbogen-induced changes in rat mammary tumor oxygenation reported by near infrared spectroscopy," *Br. J. Cancer*, **79**:1709-1716 (1999).

88. Baldwin, N. J., Wang, Y., and Ng, T. C., "In situ $^{19}F$ MRS measurement of RIF-1 tumor blood volume: Corroboration by radioisotope-labeled [$^{125}I$]-albumin and correlation to tumor size", *Magn. Reson. Imaging*, **14**(3):275-280 (1996).
89. Meyer, K. L, Joseph, P. M., Mukherji, B., Livolsi, V. A., and Lin, R., "Measurement of vascular volume in experimental rat tumors by $^{19}F$ magnetic resonance imaging", *Investi. Radiol.* **28(8)**:710-719 (1993).
90. Liu, H., Beauvoit, B., Kimura, M., and Chance, B, "Dependence of tissue optical properties on solute-induced changes in refractive index and osmolarity", *J. Biomed. Opt.*, **1(2)**:200-211 (1996).
91. Hall, E. J., "The oxygen effect and reoxygenation", *In*: Hall (ed), *Radiotherapy for the radiologist*, 4th, Edition, Lippincott, Philadelphia, 133-152 (1994).
92. Kim, I. H., and Brown, J. M., "Reoxygenation and rehypoxiation in the SCCVII mouse tumor", *Int. J. Radiat. Oncol. Biol. Phys.*, **29**:492-497 (1994).
93. Kallman, R. F., and Dorie, M. J., "Tumor oxygenation and reoxygenation during radiation therapy: Their importance in predicting tumor response", *Int. J. Radiat. Oncol. Biol. Phys.*, **12**:681-685 (1986).
94. Fyles, A. W., Milosevic, M., Pintilie, M., and Hill, R, P., "Cervix cancer oxygenation measured following external radiation therapy", *Int. J. Radiation Oncology Biol. Phys.*, **42(4)**:751-753 (1998).
95. Lyng, H., Tanum, G., Evensen, J. F., and Rofstad, E. K., "Changes in oxygen tension during radiotherapy of head and neck tumors", *Acta Oncol.*, **38(8)**:1037-42 (1999).
96. Lartigau, E., Lusinchi, A., and Weeger, P., "Variations in tumor oxygen tension ($pO_2$) during accelerated radiotherapy of head and neck carcinoma", *Eur. J. Cancer*, **34**:856-861 (1998).
97. Koh, W., Bergman, K. S., and Rasey, J. S., "Evaluation of oxygenation status during fractionated radiotherapy in human non-small cell lung cancers using [F-18] fluoromisonidazole positron emission tomography", *Int. J. Radiat. Oncol. Biol. Phys.*, **33**:391-398 (1995).
98. Hill, R., "Experimental radiotherapy", *In*: Tannock and Hill (eds), *The basic science of oncology*, McGraw-Hill Inc., New York, 276-301 (1992).
99. Fowler, J. F., "Fractionation and therapeutic gain", *In*: Steel, Adams, and Horwich (eds), *The Biological Basis of Radiotherapy*, 2nd Edition, Elsevier Science Publishers: Amsterdam, 181-207 (1989).
100. Henke, M., Guttenberger, R., Baker, A., Pajonk, F., Pötter, R., Frommhold, H., "Erythropoietin for patients undergoing radiotherapy: A pilot study", *Radiother. Oncol.*, **50**:185-190 (1999).
101. Overgaard, J., Horsman, M., "Modification of hypoxia-induced radioresistance in tumors by the use of oxygen and sensitizers", *Semin. Radiat. Oncol.*, **6:**10-21 (1996).
102. Guttenberger, R., Lutterbach, J., Roth, A., Röser , S., Schindler, R., Henke, M., Frommhold, H., "Hemoglobin levels predict local regional control after

postoperative radiotherapy for advanced head and neck cancer", *Eur. J. Cancer,* **33** (suppl):102-103 (1997).

103. Vaupel, P., Kelleher, D. K., and Thews, O, "Modulation of tumor oxygenation", *Int. J. Radiat. Oncol. Biol. Phys.*, **42**:843-848 (1998).
104. Pederson, D., Sogaard, H., and Overgaard, J., "Prognostic value of pretreatment factors in patients with locally advanced carcinoma of the uterine cervix treated by radiotherapy alone", *Acta Oncol.*, **34**:787-795 (1995).
105. Ludwig, H., and Pecorelli, S., "Suboptimal hemoglobin levels: Do they impact patients and their therapy? Audience responses", *Semin. Oncol.*, **27**(suppl):18-19 (2000).
106. Grau, C., Overgard, J., "The influence of radiation dose on the magnitude and kinetics of reoxygenation in C3H mammary carcinoma", *Radiat. Res.*, **122**:309-315 (1990).
107. Olive, P. L, "Radiation-induced reoxygenation in the SCCVII murine tumor: Evidence for a decrease in oxygen consumption and an increase in tumor perfusion", *Radiother. Oncol.*, **32**:37-46 (1994).

# 8. APPENDICES

## ----COPIES OF MANUSCRIPTS AND ABSTRACTS

# Tumor Oximetry: A comparison between near-infrared frequency-domain spectroscopy of hemoglobin saturation and $^{19}$F MRI of hexafluorobenzene

Katherine L. Worden[*], Yulin Song[*ϕ], Xin Jiang[*], Anca Constantinescu[ϕ], Ralph P. Mason[ϕ], Hanli Liu[*]

[*]Joint Biomedical Engineering Program
University of Texas at Arlington/University of Texas Southwestern Medical Center at Dallas
Dallas, TX 75235

[ϕ]Department of Radiology
University of Texas Southwestern Medical Center at Dallas
Dallas, TX 75235

## ABSTRACT

Studies have shown that hypoxic tumor cells are relatively more resistant to radiotherapy, chemotherapy, and photodynamic therapy. Tumor oximetry, e.g., measurement of oxygen tension ($pO_2$) of tissue and/or blood oxygenation ($SO_2$) of the vascular bed, could be valuable for optimizing treatment plans.

In this study, we employed a recently developed homodyne system to measure changes in hemoglobin saturation ($SO_2$) and concentration in the vascular bed of rat prostate and breast tumors. For comparison, tissue $pO_2$ values were measured using $^{19}$F MR EPI of hexafluorobenzene, providing a map of regional tumor oxygenation tension. Both $SO_2$ and $pO_2$ measurements were taken while the inhaled gas was alternated between 33% oxygen, 100% oxygen and carbogen (95% oxygen, 5% $CO_2$).

The results obtained for both techniques showed significant changes in tumor oxygenation accompanying respiratory challenge, with changes in vascular $SO_2$ preceding tissue $pO_2$ change. The combined use of these two techniques provides new insight into the dynamics of tumor oxygenation by making available a method of obtaining regional information of the state of the tissue, as well as a non-invasive, real-time method for determining changes in the vascular bed.

**Keywords:** Frequency-Domain Spectroscopy, NIR spectroscopy, $^{19}$F MRI, Hexafluorobenzene, Oximetry

## 1. INTRODUCTION

Frequently, blood vessel formation is unable to keep up with the rapid growth of a tumor. If this occurs, the cells in the tumor furthest from a fresh blood supply will suffer a lack of oxygen and hypoxic areas will form (chronic hypoxia). These regions can be as much as 3 times more resistant to radiotherapy.[1] In addition to studies in vitro and in animal tumors, there is increasing evidence from clinical trials that poorly oxygenated tumors indicate poor prognosis for patients.[2,3] Methods of determining the oxygen content of a tumor could, therefore, be helpful in the development of an optimal treatment plan. This paper will present the experimental results of two such methods: NIR spectroscopy to determine blood oxygenation ($SO_2$) of the tumor's vascular bed and $^{19}$F MRI of hexafluorobenzene (HFB) to determine tissue $pO_2$.

NIR spectroscopy, through use of a recently developed frequency-domain system, based on an in-phase and quadrature (IQ) demodulator chip[4], is attractive as a non-invasive, inexpensive, portable, real-time system that can provide global $SO_2$ values. We show that this IQ system can be used to determine the $SO_2$ in a tumor's vascular bed and measure the

Part of the SPIE Conference on Optical Tomography and Spectroscopy of Tissue III
San Jose, California • January 1999 SPIE Vol. 3597 • 0277-786X/99/$10.00

response of blood volume and oxygen saturation to inhaled gas. The technique of using $^{19}F$ MRI relaxometry to map tissue $pO_2$ is also relatively new.[5] The spin-lattice relaxation rate of hexafluorobenzene is particularly sensitive to oxygen while being insensitive to temperature.[6] Following direct injection of HFB into a tumor, $^{19}F$ MRI maps tissue $pO_2$ at millimeter resolution. This method facilitates measurements of dynamic changes in $pO_2$ accompanying therapeutic interventions and allows the fate of individual voxels to be traced.

Through comparison of these two techniques, it is possible to examine the relationship between $SO_2$ of the vascular bed and $pO_2$ of the tissue. Blood oxygenation, blood volume, arterial $SO_2$ and temperature may also be compared.

## 2. METHODS AND INSTRUMENTATION

### 2.1 Tumor Model

Dunning prostate adenocarcinoma R3327-AT1 was implanted in adult male Copenhagen rats and NF13762 breast tumor in female Fisher rats. The tumors were grown in pedicles[7] on the forebacks of the rats until they were approximately 2 cm in diameter. Rats were anesthetized with 200 µl ketamine hydrochloride (100 mg/ml) and maintained under general gaseous anesthesia with 33 % inhaled $O_2$ [0.3 $dm^3$/min $O_2$, 0.6 $dm^3$/min $N_2O$, and 0.5% methoxyflurane] through a mask placed over the mouth and nose. Body temperature was maintained by a warm water blanket. A fiber optic pulse oximeter was placed on the hind foot to monitor arterial oxygenation ($A_{SO2}$) and a fiber optic probe was inserted rectally to measure temperature. Inhaled gas was alternated between 33% oxygen, 100% oxygen and carbogen (95% oxygen, 5% carbon dioxide). NIR and EPI measurements were performed sequentially for comparison.

### 2.2 NIR Spectroscopy

As shown in **figure 1**, we used a new homodyne system able to determine amplitude and phase changes of light.[4] In this setup, an RF source modulates the light from two laser diodes (wavelengths 758 nm and 782 nm) at 140 MHz. The light passes through fiber optic cables, is transmitted through the tumor tissue, and is collected by a second fiber bundle. The light is then detected by a PMT and is demodulated with a commercially available in-phase and quadrature (IQ) demodulator chip into I and Q components. Once these components are put through a low pass filter, they can be used to calculate amplitude and phase changes caused by the tumor. These steps can be seen mathematically in equations 1-4.

(1) $I(t) = 2A \sin(\omega t+\theta)\sin(\omega t) = A\cos(\theta) - A\cos(\omega t+\theta)$ ---> low pass filter ---> $I_{dc} = A\cos(\theta)$

(2) $Q(t) = 2A \sin(\omega t+\theta)\cos(\omega t) = A\sin(\theta) + A\sin(\omega t+\theta)$ ---> low pass filter ---> $Q_{dc} = A\sin(\theta)$

(3) $\theta = \tan^{-1}(Q_{dc} / I_{dc})$

(4) $A = (I_{dc}^2 + Q_{dc}^2)^{1/2}$

A = amplitude of detected light; θ = phase of detected light; ω = modulation frequency (140 MHz)

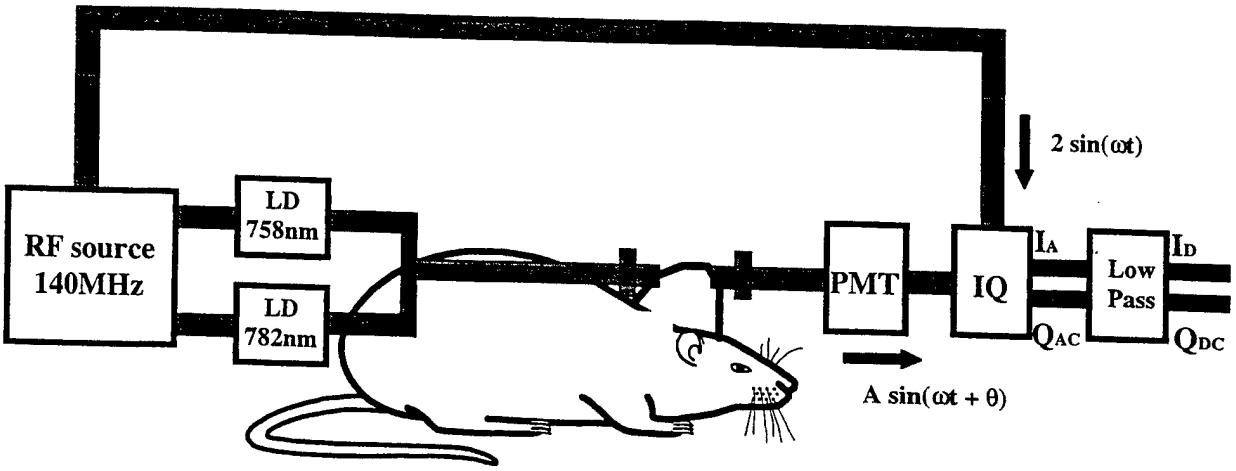


**Figure 1:** Setup for NIR experiment.

NIR spectroscopy can be used to determine hemoglobin saturation because the extinction coefficient values of deoxygenated hemoglobin differ from those of oxygenated hemoglobin at the wavelengths selected (758 nm and 782 nm). At this point in our algorithm calculations, we have assumed background absorbance to be negligible and estimated that the absorption coefficients were composed of the extinction coefficients for deoxy-hemoglobin and oxy-hemoglobin multiplied by their respective concentrations (equations 5&6).

(5) $\mu_a^{758} = \varepsilon_{Hb}^{758}[Hb] + \varepsilon_{HbO2}^{758}[HbO_2]$

(6) $\mu_a^{782} = \varepsilon_{Hb}^{782}[Hb] + \varepsilon_{HbO2}^{782}[HbO_2]$

The IQ system does give both phase and amplitude values, but given the tumor's small size and our fiber configuration, we haven't yet derived a suitable algorithm to compute $\mu_a$ and $\mu_s$. The data presented in this paper were analyzed using Beer-Lambert's law and the amplitude values to find trends in the changing absorption coefficients (equation 7). By manipulating equations 5-7, we can calculate changes in blood volume and saturation from the transmitted amplitude of the light through the tumor (equations 8&9).

(7) $\mu_{aC} - \mu_{aI} = 1/L * \log (A_I/A_C)$

(8) $\Delta[Hb]_{total} = -3.63 * \log (A_I/A_C)^{758} + 8.68 * \log (A_I/A_C)^{782}$

(9) $\Delta[HbO_2] - \Delta[Hb] = -18.49 * \log (A_I/A_C)^{758} + 21.20 * \log (A_I/A_C)^{782}$

$A_I$ = initial amplitude (amplitude of baseline); $A_C$ = current amplitude; L = optical pathlength between source/detector; The constants were computed with extinction coefficients for oxy- and deoxy- hemoglobin at the two wavelengths used.

## 2.3 MRI Instrumentation and Procedure

MRI experiments were performed on an Omega CSI 4.7 T 40 cm system with actively shielded gradients. A homebuilt tunable $^1H/^{19}F$ single turn solenoid coil was placed around the tumor. HFB (40 µl) was administered directly into the tumor using a fine sharp (32 G) needle with deliberate dispersion along several tracks to interrogate both central and peripheral tumor regions. HFB is ideal for the imaging of $pO_2$ because it has a single resonance and its relaxation rate varies linearly with oxygen concentration. $^1H$ images were acquired for anatomical reference using a traditional 3D spin-echo pulse sequence as seen in **figure 2a**. Conventional $^{19}F$ MR images (**figure 2b**) were then taken to show the 3D distribution of the HFB in the tumor. **Figure 2b** may be directly overlaid over **figure 2a** to show the position of the HFB in that slice.

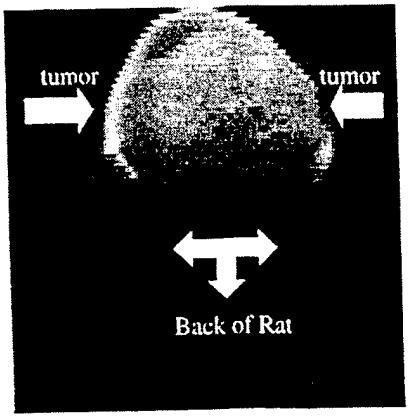


**Figure 2a:** Proton ($^1H$) coronal image of a representative slice through a breast tumor (NF13762): TR = 250 ms, TE = 8 ms, NA = 2, FOV = 48 x 48 mm, slice thickness = 4 mm, and matrix size = 128 x 64 x 8.

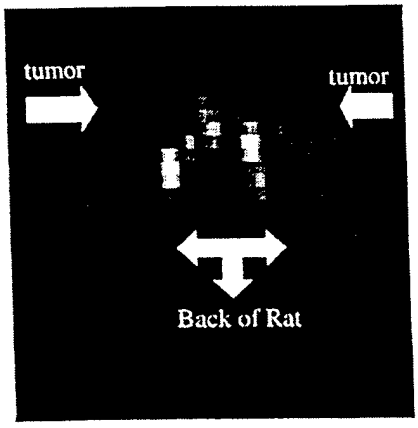


**Figure 2b:** Corresponding $^{19}F$ MR Image showing distribution of HFB within the tumor: TR = 150 ms, TE = 8 ms, FOV = 48 x 48 mm, matrix size = 128 x 64x8.

Tumor oxygenation was assessed using $^{19}$F PBSR-EPI of HFB.[8] The PBSR preparation pulse sequence consists of a series of 20 non-spatially selective saturating 90° pulses with 20 ms spacing to saturate the $^{19}$F nuclei. Following a variable delay time $\tau$, a single spin echo EPI sequence with "blipped" phase encoding was applied.[9] A PBSR-EPI image corresponding to the images shown in **figures 2a and 2b** is shown in **figure 2c**. Fourteen $32\times 32$ PBSR-EPI images, with $\tau$ ranging from 200 ms to 90 sec and an FOV of $40\times 40$ mm, were acquired in eight minutes. An $R1$ map was obtained by fitting signal intensity of each voxel of the fourteen images to a three parameter relaxation model by Levenberg-Marquardt least squares algorithm (equation 10):

$$(10)\qquad y_n(i,j) = A(i,j)\cdot[1-(1+W)\cdot\exp(-R1(i,j)\cdot\tau_n)]$$
$$(n=1,2,\cdots\cdots,14)$$
$$(i,\ j=1,2,\cdots\cdots,32)$$

where $y_n(i,j)$ is the measured signal intensity corresponding to delay time $\tau_n$ (the $n$th images) for voxel $(i,j)$, $A(i,j)$ is the fully relaxed signal intensity amplitude of voxel $(i,j)$, $W$ is a dimensionless scaling factor allowing for imperfect signal conversion, and $R1(i,\mathrm{j})$ is the relaxation rate of voxel $(i,j)$ in unit of $\mathrm{sec}^{-1}$. A, W and R1 are the three fit parameters.

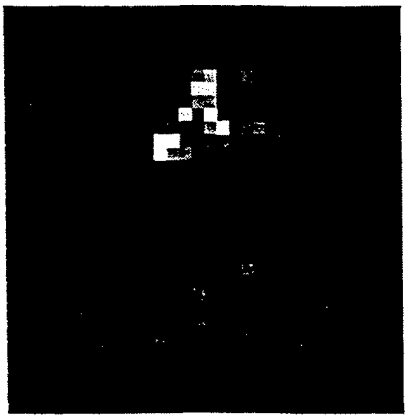

**Figure 2c:** $^{19}$F PBSR-EPI projection image obtained from the tumor in **figure 1** in a single acquisition ($\tau$ = 90 s). Fourteen images were acquired with variable relaxation delays ($\tau$) ranging from 200 ms to 90 sec. Using a 32 x 32 matrix, FOV of 40 x40 mm, $pO_2$ maps were generated with 1.25 x 1.25 mm resolution.

$pO_2$ maps were then generated by applying the calibration curve: $pO_2(\mathrm{torr}) = [R1(s^{-1}) - 0.074]/0.0016$ to the $R1$ maps.[10] The map shown in **figure 2d** focuses on a region of the same slice that was presented in figures 2a-2c.

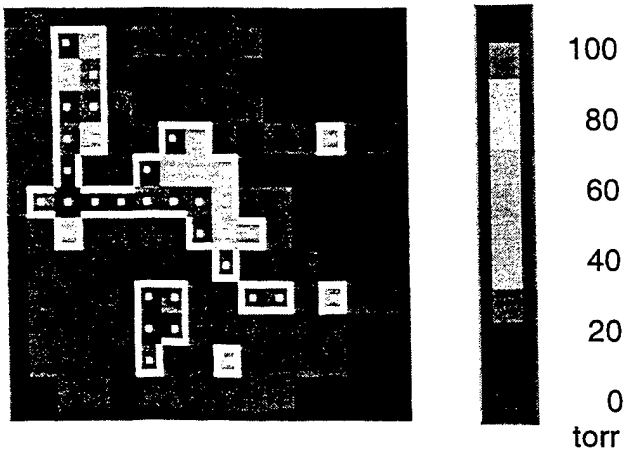


**Figure 2d:** Typical $pO_2$ map, composed of fourteen PBSR images from the tumor presented in **figure 2a-c.** Using a 32 x 32 matrix, FOV of 40 x40 mm, $pO_2$ maps were generated with 1.25 x 1.25 mm resolution.

## 3. RESULTS

### 3.1 NIR Results

The effects of the inhaled gas on hemoglobin saturation and concentration, as recorded by the IQ system, are shown below in **figures 3a & 3b**. The X-axis shows time in minutes from the start of the experiment and the dotted vertical lines mark the point when the gas was changed. Hemoglobin saturation and concentration are presented as unit-less, relative trends. It can easily be seen that hemoglobin saturation begins to increase almost immediately after a gas switch from baseline (33% oxygen) to either carbogen or 100% oxygen and increases steadily for several minutes. Total hemoglobin change is quite small in comparison, indicating relatively constant blood volume in the tumor. These trends seem fairly consistent for both breast and prostate tumors. Typical responses of a breast tumor and prostate tumor are presented in **figures 3a & 3b**, respectively.

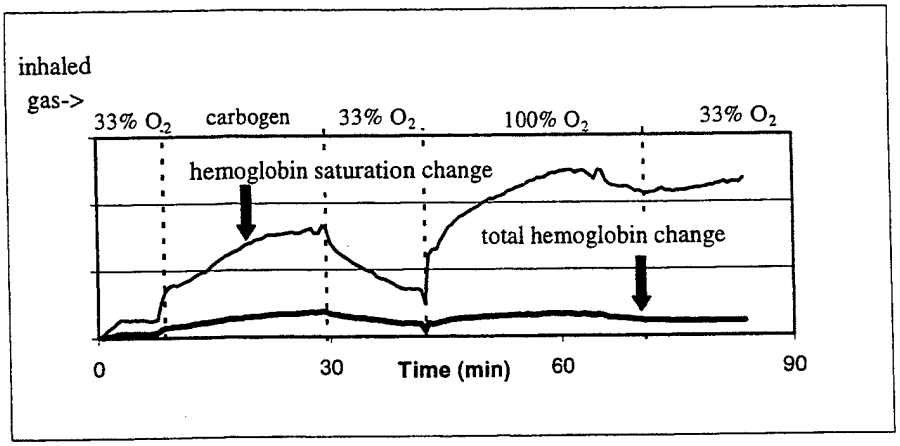


**Figure 3a:** Hemoglobin saturation and concentration change in a breast tumor.

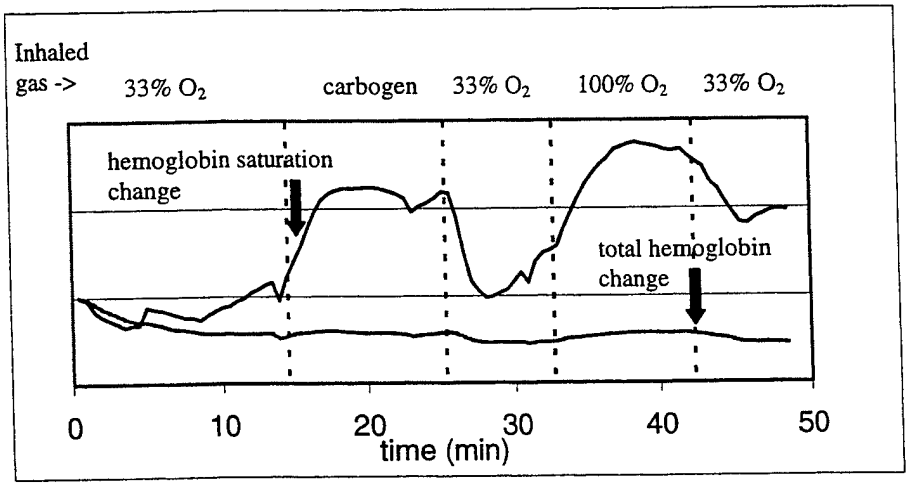


**Figure 3b:** Hemoglobin saturation and concentration change in a prostate tumor.

It is also worthwhile to compare the saturation changes measured in the tumors vascular bed by the IQ system with the arterial saturation changes measured by a pulse oximeter from the rat's hind foot. One such comparison taken from a prostate tumor is presented below as **figure 4**. Hemoglobin saturation in the vascular bed is again represented as a unit-less trend and arterial saturation values are presented to the right. Again, the X-axis gives the time from the beginning of the experiment in minutes and the dotted lines mark the time of gas change. In this case, the arterial saturation follows the same trend as the tumor vascular bed's hemoglobin saturation, but shows a faster change. Such close similarity wasn't always observed.

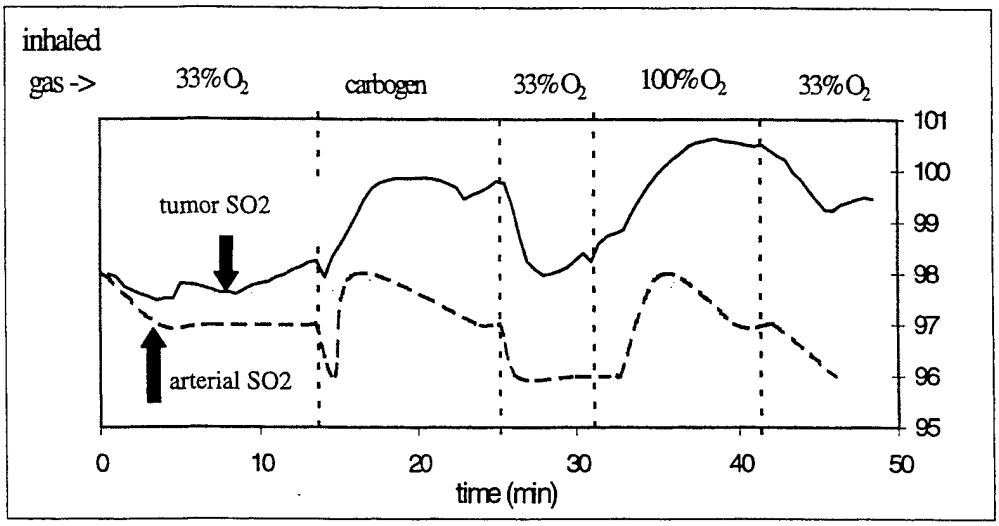


**Figure 4:** In the prostate tumor presented in Figure 4, both arterial $SO_2$ and the $SO_2$ in the tumor increased for inhaled carbogen and 100% $O_2$ and decreased for 33% $O_2$. Arterial $SO_2$ in hind foot measured by a commercial pulse oximeter and $SO_2$ in tumor using IQ system.

### 3.2 MRI Results

MRI provides the advantage of being able to look at regional changes in $pO_2$ values. Histograms, such as those presented in **figure 5**, are able to show the heterogeneity of $pO_2$ values within the tumor as well as the average $pO_2$ values. The data presented here were taken from a breast tumor and show the average values from the data of several $pO_2$ maps that were taken throughout the administration of each gas. In **figure 5a**, we see that when the rat was breathing 33% oxygen, the average $pO_2$ value was about 40 torr. When the rat was breathing carbogen (**figure 5b**), there was a large shift towards higher $pO_2$ values leading to a mean value of about 99 torr. These values increased further while the rat was breathing 100% oxygen (**figure 5c**) such that the average voxel now had a $pO_2$ value of about 145 torr. The time course of these changes is presented later in the paper in **figure 7b**.

**Figure 5a:**
$pO_2$ range while the rat was breathing 33% oxygen.
Average value = 40 ± 3 torr

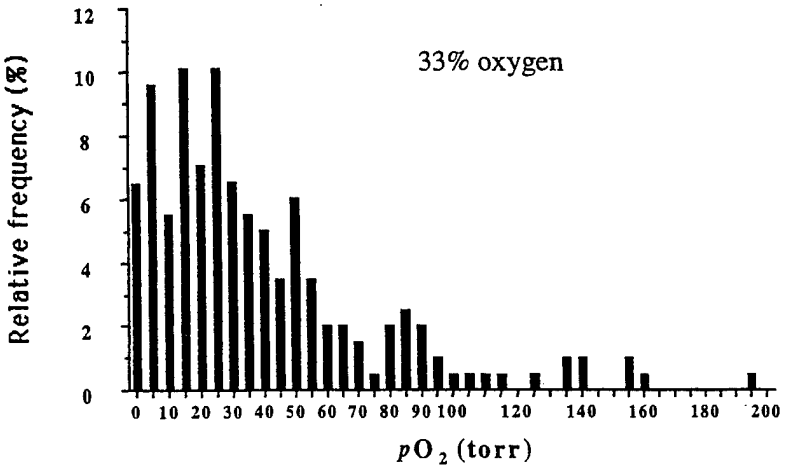


**Figure 5b:**
$pO_2$ range while the rat was breathing carbogen.
Average value = 99 ± 4 torr

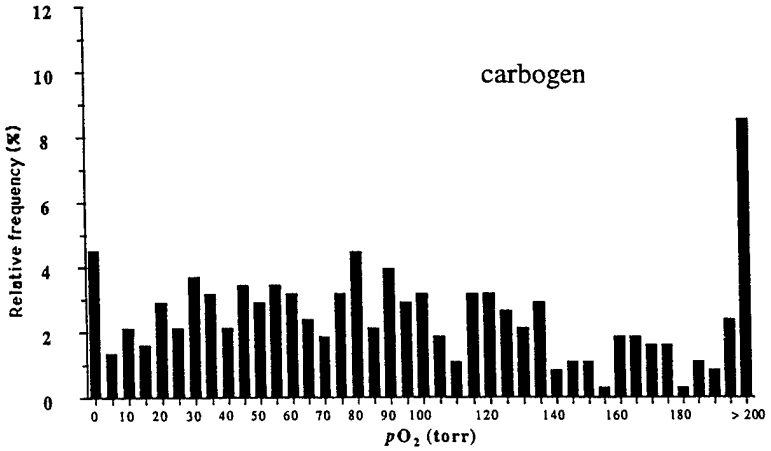


**Figure 5c:**
$pO_2$ range while the rat was breathing 100% oxygen.
Average value = 145 ± 4 torr

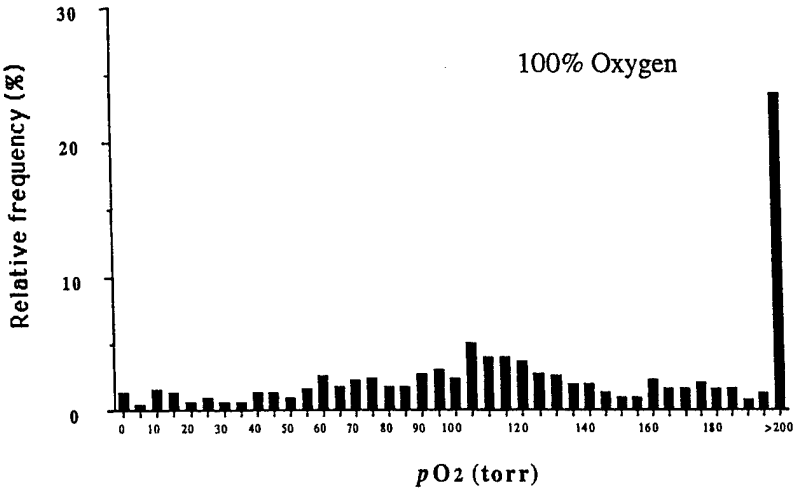

### 3.3 Comparison

While absolute $pO_2$ values are important for investigating hypoxia, dynamic changes may be more interesting for investigation of response to intervention. In **figures 6 & 7**, the dynamic changes in $pO_2$ and $SO_2$ are compared. These plots show that $pO_2$ reacts in a very similar fashion to blood saturation, but that the effect is slower. Since the IQ system provides a global measure across the whole tumor, $pO_2$ measurements are presented here as mean values attained from the pixels of each $pO_2$ map. The NIR and MRI data shown are for the same rat undergoing the same procedure, but on consecutive days. Data from two breast tumors of various size are presented. The larger tumor was about 2.1 x 2.4 x 2.2 cm whereas the smaller tumor was 1.9 x 2.2 x 2 cm. Inhaling carbogen and 100% oxygen each consistently resulted in increased $SO_2$ and $pO_2$ over 33% oxygen. The $pO_2$ and $SO_2$ measurements were plotted against the same X-axis to allow rate of change to be compared.

**Figure 6a: Saturation from IQ**

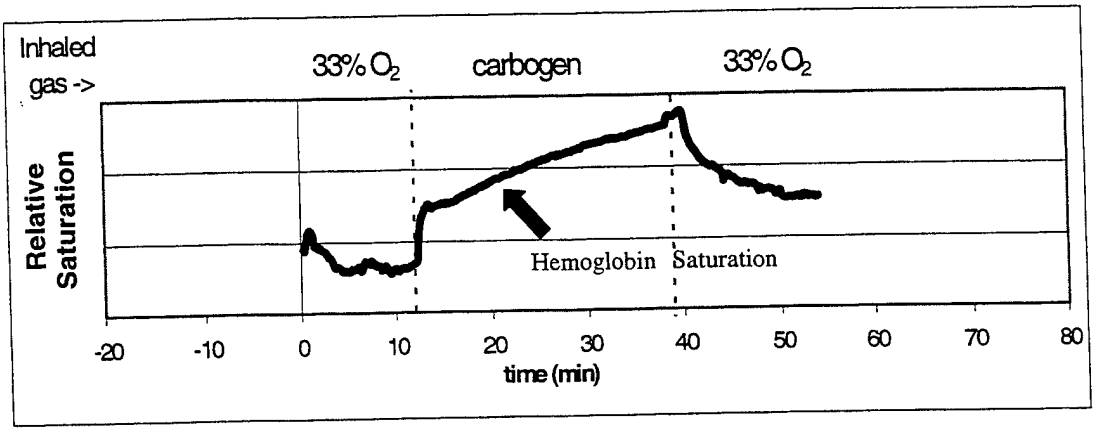


**Figure 6b: $pO_2$ from MRI**

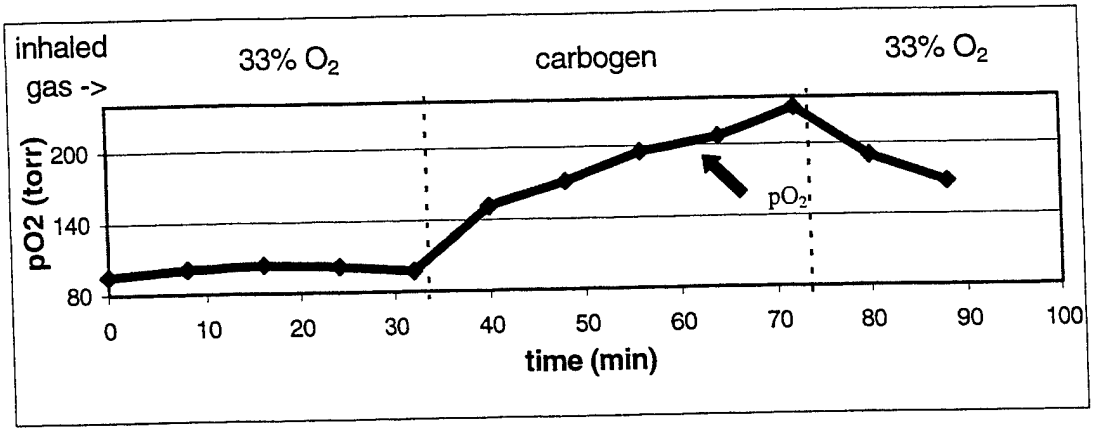


**Figure 6:** These two sets of data were taken from the small rat breast tumor on consecutive days. Both the $pO_2$ and blood saturation increased with a transition from 33% to carbogen, and decreased when switched back to 33%.

**Figure 7a: Saturation from IQ**

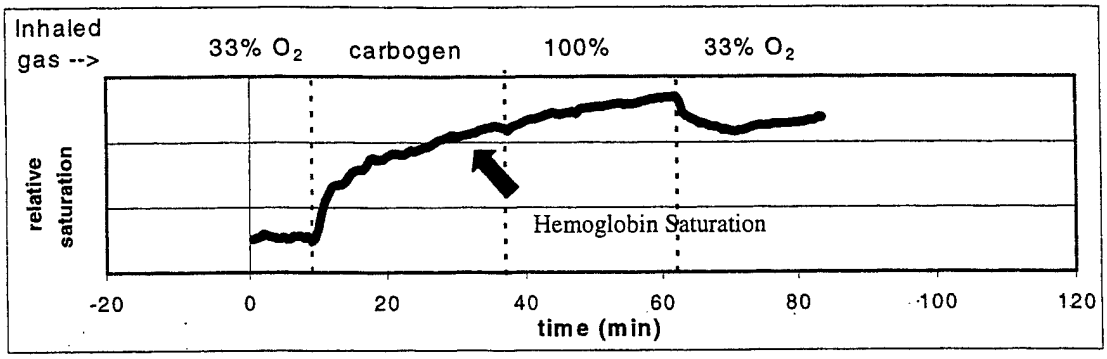


**Figure 7b: $pO_2$ from MRI**

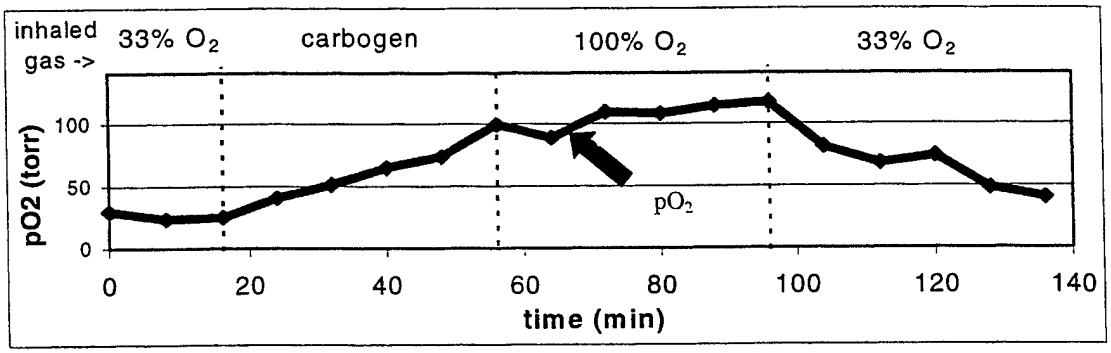


**Figure 7:** These two sets of data were taken from the large rat breast tumor on consecutive days. Both the $pO_2$ and blood saturation increased with a transition from 33% to carbogen, and then further increased slightly when switched from carbogen to 100% oxygen. Values began to decrease when switched back to 33%.

To further study the temporal response, the changes in $pO_2$ and $SO_2$ were modeled using the exponential equations 11 and 12. A non-linear curve fitting method was used to obtain $\tau$.

(11) For increasing values: $\text{Saturation} = a + b*(1-e^{-t/\tau})$

(12) For decreasing values: $\text{Saturation} = a + b*(e^{-t/\tau})$

Generally, blood saturation effects had a much shorter time constant than oxygen tension in the tissue (**Figure 8**). For the larger tumor, the rate of increase and decrease were much faster for $SO_2$ than $pO_2$. Less difference was seen in the smaller tumor. Further study for confirmation is underway.

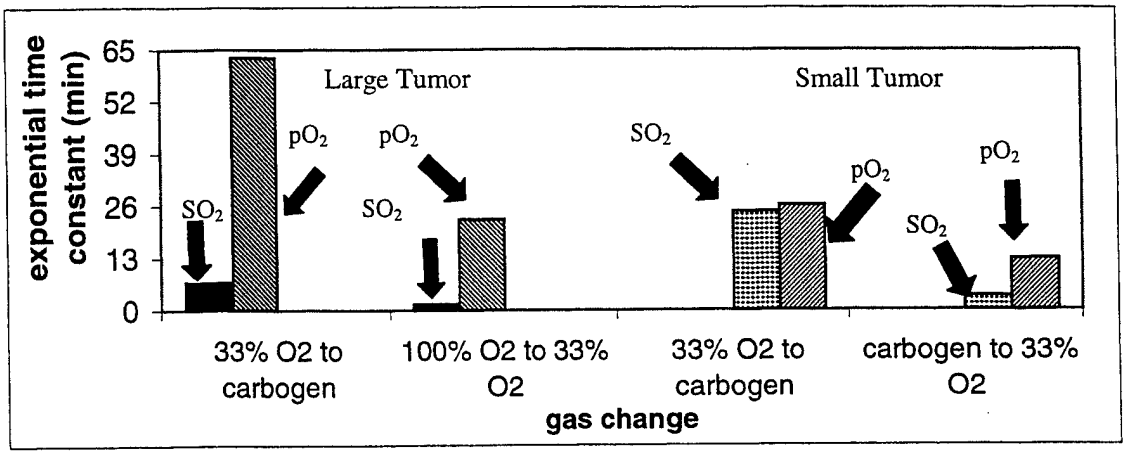


**Figure 8:** Time constants for the data presented in **Figures 6&7.**

## 4. CONCLUSION

The data suggest interesting correlations between several physiological parameters. Both tumor vascular Hb saturation and mean $pO_2$ increased in response to inhaling an elevated percent $O_2$, either through carbogen or 100% $O_2$. Arterial $SO_2$ and tumor $SO_2$ respond similarly to changes in inhaled gas, with arterial changes preceding changes in the tumor vascular bed. Changes in $SO_2$ are generally faster than $pO_2$, though absolute values are highly variable and suggest heterogeneity amongst the tumor population. Given the distinct heterogeneity among tumors even of a given type and size,[11] further investigations are required to form a sound picture of the interplay of multiple physiological parameters.

## ACKNOWLEDGEMENTS

This work was supported in part by The Whitaker Foundation (HL, RPM), The American Cancer Society RPG-97-116-010CCE (RPM), and the Department of Defense Breast Cancer Initiative BC962357 (YS). MRI experiments were performed at the Mary Nell & Ralph B. Rogers MR Center, an NIH BRTP Facility no. 5-P41-RR02584. We are very grateful to Sandeep Hunjan for assistance with data analysis.

## REFERENCES

[1] Denekamp, J. Physiological hypoxia and its influence on radiotherapy. *The Biological Basis of Radiotherapy, Second Edition*, Eds. G.G. Steel, G.E. Adams & A. Horwich (Elsevier Science Plblishers B.V., 1989)

[2] M. Höckel , K. Schlenger, B Aral, M. Mitze, U. Schäffer and P. Vaupel, Association between tumor hypoxia and malignant progression in advanced cancer of the uterine cervix. *Cancer Res.* **56**, 4509-15 (1996).

[3] A.W. Fyles, M. Milosevic, R. Wng, M.C. Kavanagh, M. Pintile, A. Sun, W. Chapman, W. Levin, L. Manchul, T.J. Keane and R. P. Hill, Oxygenation predicts radiation response and survival in patients with cervix cancer. *Radiother. Oncol.* **48**, 149-56 (1998).

[4] Y.Yunsong, H. Liu, X. Li, B. Chance, Low-cost frequency-domain photon migration instrument for tissue spectroscopy, oximetry, and imaging. *Opt. Eng.* 36(5) 1562-1569 May 1997

[5] R. P. Mason, Non-invasive physiology: $^{19}F$ NMR of perfluorocarbon. *Art. Cells, Blood Sub. & Immob. Biotech.* **22**, 4, 1141-1153 (1994).

[6] R.P. Mason, W. Rodbumrung and P.P. Antich, Hexafluorobenzene: a sensitive $^{19}F$ NMR indicator of tumor oxygenation. *NMR in Biomed.* **9**, 125-134 (1996).

[7] E. W. Hahn, P. Peschke, R. P. Mason, E. E. Babcock and P. P. Antich, Isolated tumor growth in a surgically formed skin pedicle in the rat: a new tumor model for NMR studies. *Magn. Reson. Imaging* **11**, 1007-1017 (1993).

[8] D. Le, R. P. Mason, S. Hunjan, A. Constantinescu, B. R. Barker and P. P. Antich, Regional tumor oxygen dynamics: $^{19}F$ PBSR EPI of hexafluorobenzene. *Magn. Reson. Imaging* **15**, 8, 971-81 (1997).

[9] B. R. Barker, R. P. Mason, N. Bansal and R. M. Peshock, Oxygen tension mapping by $^{19}F$ echo planar NMR imaging of sequestered perfluorocarbon. *JMRI* 4, 595-602 (1994).

[10] D. Le, R. P. Mason, S. Hunjan, A. Constantinescu, B. R. Barker and P. P. Antich, Regional tumor oxygen dynamics: $^{19}F$ PBSR EPI of hexafluorobenzene. *Magn. Reson. Imaging* **15**, 8, 971-81 (1997).

[11] R. P. Mason, A. Constantinescu, S. Hunjan, D. Le, E. W. Hahn, P. P. Antich, C, Blum and P. Peschke, Regional tumor oxygenation and measurement of dynamic changes. *Radiat. Res.* (submitted 1998).

# TUMOR OXIMETRY: COMPARISON OF $^{19}F$ MR EPI AND ELECTRODES

Ralph P. Mason, Sandeep Hunjan, Anca Constantinescu, Yulin Song, Dawen Zhao,

Eric W. Hahn, Peter P. Antich, and Peter Peschke[+].

U.T. Southwestern Medical Center, Dallas, TX and [+]DKFZ, Heidelberg, Germany

*address correspondence to:

Ralph P. Mason, Ph.D., C. Chem.,

Department of Radiology,

U.T. Southwestern Medical Center,

5323 Harry Hines Blvd.,

Dallas, TX 75235-9058

Tel: (214) 648-8926

Fax (214) 648-2991

E. mail: Ralph.Mason@email.swmed.edu

## ABSTRACT

We recently described a novel approach to measuring regional tumor oxygen tension using $^{19}F$ pulse burst saturation recovery NMR echo planar imaging relaxometry of hexafluorobenzene. We have now compared oxygen tension measurements in a group of size matched Dunning prostate rat tumors R3327-AT1 made using this FREDOM (Fluorocarbon Relaxometry using Echo planar imaging for Dynamic Oxygen Mapping). approach with a traditional polarographic method: the Eppendorf Histograph. We also compare MR and electrode approaches to monitoring dynamic changes with respect to interventions and demonstrate extension of the MR technique to rat breast tumors.

**Key words:** echo planar imaging, electrode, MRI, oxygen, prostate, tumor

**Abbreviations** ARDVARC (Alternated Relaxation Delays with Variable Acquisitions to Reduce Clearance effects); EPI (echo planar imaging); FREDOM (Fluorocarbon Relaxometry using Echo planar imaging for Dynamic Oxygen Mapping); HFB (hexafluorobenzene); i.t (intra tumoral)

**Acknowledgments**

This work was supported in part by The American Cancer Society (RPG-97-116-010CCE; RPM), DOD Breast Cancer initiative (YS), Verein zur Forderung der Krebserkennung and Krebshandlung e.V. Heidelberg (PP) and the NIH BRTP Facility #5-P41-RR02584.

## Introduction

It is widely appreciated that tumor oxygenation may significantly influence therapeutic success. In particular, the efficacy of radiotherapy [1], photodynamic therapy [2] and hypoxia selective chemotherapeutic agents [3] depend on $pO_2$. It had been suggested that the ability to measure tumor oxygenation in patients could allow therapy to be individualized and optimized [4], and indeed, several recent studies have found significant prognostic value based on the Eppendorf Histograph in assessing clinical tumors [5-7]. While electrodes may be considered a "gold standard", they have certain shortcomings and there is clearly a need for alternative methods [8]. We have been developing a new approach based on $^{19}F$ NMR of perfluorocarbons [9-12] and believe the method can now provide useful measurements of tumor oxygen dynamics *in vivo*.

The FREDOM approach exploits the exceptional response of the $^{19}F$ NMR spin lattice relaxation rate, R1, of fluorocarbons to changes in oxygen tension. Fluorocarbons act as ideal liquids and solvation of gases is directly proportional to the partial pressure of the gas (Henry' law). Since oxygen ($O_2$) is paramagnetic it induces relaxation in solution directly proportional to the concentration of oxygen, and hence, $pO_2$ [13]. The highly hydrophobic nature of fluorocarbons ensures both a high solubility of gases, providing molecular amplification, and minimal solvation of other materials (*e.g.*, metal ions) minimizing interference from other environmental factors. We, and others, have explored the use of numerous PFC reporter molecules and various routes of administration [14]. We believe that direct intra tumoral (i.t.) injection of HFB provides an optimal approach to tumor oximetry, and should provide measurements comparable to those obtained using electrodes. In addition, this minimally invasive approach facilitates mapping of dynamic changes in $pO_2$ with respect to interventions.

## Methods

Dunning prostate adenocarcinomas (R3327-AT1) were implanted in male Copenhagen rats (~250 g), as described in detail previously [15]. Tumors were divided

into two groups and allowed to grow to about ~2 $cm^3$ or > 3.5 $cm^3$ volume. For MR investigations rats were placed under general gaseous anesthesia with 33% inhaled $O_2$ (0.3 $dm^3$/min $O_2$, 0.6 $dm^3$/min $N_2O$, and 0.5% methoxyflurane. Hexafluorobenzene (25 - 40 µl) was injected directly into the tumors in both central and peripheral regions using a Hamilton syringe with a custom made fine sharp needle (32 G). A fiber optic probe was placed rectally to monitor core temperature. NMR experiments were performed using an Omega CSI 4.7 Tesla horizontal bore magnet system with actively shielded gradients with a tunable ($^1H/^{19}F$) single turn size-matched solenoid coil placed around the tumor. Following traditional imaging to establish the distribution of HFB, tumor oxygenation was estimated on the basis of $^{19}F$ PBSR EPI relaxometry of the HFB [10] with a typical 1.25 mm in plane resolution. For initial work three consecutive R1 measurements were made over a period of 1 hour to investigate reproducibility, and stability of the system when the rats breathed 33% $O_2$ (baseline). Since R1 is a linear function of $pO_2$ at constant temperature, $pO_2$ was estimated on a voxel by voxel basis using the relationship $pO_2$ (torr) = (R1 - 0.074)/0.0016 [10]. The inhaled gas was then altered to 100% oxygen, and relaxation measurements (three) were immediately repeated over a period of 1 hour. Finally, the gas was switched back to the baseline state and three further $pO_2$ determinations were immediately performed over 1 hour. Our initial studies required 20 mins to produce a $pO_2$ map, but more recent introduction of the ARDVARC acquisition protocol [12] provides enhanced maps in 8 mins. Breast 13762 NF adenocarcinomas were examined similarly.

Histography was applied to groups of size matched tumors, which did not receive HFB. Halothane was used in place of methoxyflurane. Using the Eppendorf Histograph 100 to 200 individual $pO_2$ determinations were made in each tumor ,as recommended by the manufacturer. For dynamic measurements a Diamond General micro-electrode (700 µm) was inserted to a specific location. Baseline $pO_2$ was measured and the inhaled gas altered to 100% $O_2$ or carbogen (95%$O_2$/5%$CO_2$) for 30 mins. At this stage $pO_2$ was

again measured. Following a series of measurements with different gases at one location, the needle was moved and the gases cycled again.

Statistical significance of changes in oxygenation was assessed using analysis of variance (ANOVA) on the basis of Fisher PLSD. Experiments were approved by the Institutional Animal Care and Advisory Committee conducted in accordance with National Laws.

**Results**

Both FREDOM and electrode methods indicated similar oxygen tension distributions for the AT1 tumors (Fig. 1). Moreover, both techniques showed that tumors with volume $> 3.5$ $cm^3$ were significantly ($p < 0.0001$) less well oxygenated than smaller tumors (volume $< 2$ $cm^3$). For the large tumors FREDOM indicated median $pO_2 = 2$ torr and fraction $< 10$ torr ($HF_{10}$) = 82 %, while the Eppendorf electrode indicated median $pO_2 =$ 3 torr and $HF_{10} = 84\%$. For the small tumors the match was less good with median = 15 v 8 torr and $HF_{10} = 44$ versus 66% for FREDOM and electrode, respectively. Examination of the MR images showed that for 1 small tumor most of the HFB resided very close to the tumor edge and may have biased the apparent $pO_2$. Indeed, if this tumor was excluded there was no significant difference between the respective $pO_2$ distributions.

Using the FREDOM approach we also examined response to respiratory challenge. Increasing the concentration of inspired oxygen from 33% to 100% $O_2$ produced a significant increase ($p < 0.0001$) in tumor oxygenation for the group of small tumors. In contrast no change was observed in the mean $pO_2$ for the group of large tumors. A strength of the FREDOM approach is the ability to follow individual tumor regions, with respect to intervention, in this case respiratory challenge. Six representative regions were selected from a single tumor (Fig. 2a). Three regions, which were initially well oxygenated ($pO_2 > 10$ torr) showed rapid and significant increases within 8 minutes of switching from 33% $O_2$ to 100% $O_2$. Changes in relatively poorly oxygenated regions

were much slower, although 2 of 3 regions did show a significant change in $pO_2$ after 24 mins.

Electrode investigation of dynamic changes in $pO_2$ also showed 3 of six regions with significant changes in switching from 33% $O_2$ to 100% $O_2$, but only 1 region was also significantly different with carbogen (Fig. 2b).

In a representative large breast tumor (~ 4 $cm^3$) we found significant changes in $pO_2$ ($p < 0.0001$) with respect to respiratory challenge with baseline mean $pO_2 = 40 \pm 3$ rising to mean $pO_2 = 99 \pm 4$, when rat inhaled carbogen and mean $pO_2 = 145 \pm 4$ for oxygen inhalation.

**Discussion**

These results demonstrate the similarly of measurements obtained using traditional electrodes or the new FREDOM approach to tumor oximetry. In each case there was a significant difference in $pO_2$ observed in small versus large AT1 tumors. For larger tumors the hypoxic fraction, mean and median were very similar, together with the range of typical $pO_2$ values. In smaller tumors MR suggested a larger range with a number of measurements in excess of 100 torr. This may have arisen from measurements close to the tumor periphery, which are less common using electrodes.

A significant strength of the FREDOM approach is the ability to monitor dynamic changes in regional $pO_2$ in response to acute interventions. Others have used the Eppendorf system to examine acute chnages [16], but this required reintroduction of the needle electrode and generation of new tracks. Not only was this invasive, but it also led to sampling of parallel tissue regions rather than the fate of specific regions. Given the extensive heterogeneity encountered in tumors and steep local gradients in $pO_2$ we believe it will be valuable to follow individual tumor regions. Historically, regional response to intervention was assessed by placing an electrode at a specific location and monitoring changes in $pO_2$ [17]. We have now performed such experiments with a micro

electrode and found a range of baseline $pO_2$ values and response to respiratory challenge similar to those seen using MRI.

We have now shown both that there is distinct intra tumoral heterogeneity in baseline oxygenation in the Dunning prostate AT1 tumor and also in the response to intervention. In common with our previous observations a three fold change in $FO_2$ seems to lead to a threefold response in tumor $pO_2$. However, the rate of change in highly variable. Preliminary data with 8 min time resolution suggest that well oxygenated regions respond rapidly, whereas those poorly oxygenated require much longer. Such observations could have significant implications for patient inhalation times prior to therapy: while previous work had shown that Pre Irradiation Breathing Times (PIBT) could substantially influence the effect of oxygen or carbogen breathing [18], the differential response of individual tumor regions may not have been fully appreciated.

In developing a new technique it is important demonstrate its reliability, robustness and general application. We and several other groups have now applied the FREDOM approach to tumor oximetry. Initially investigators favored intra venous or intra peritoneal administration of emulsions of fluorocarbons. While material became trapped in tumors and could be used to report $pO_2$ [19-22], it became increasingly apparent that material delivered via the vasculature tended to bias measurements towards well perfused tumor regions [22]. Indeed, recent measurements by Griffiths *et al.* have confirmed such a bias [23]. Furthermore, the use of emulsions to carry the PFCs tend to lead to extensive uptake by the reticuloendothelial system with hepatomegaly. Intra tumoral administration is minimally invasive provided that a fine sharp needle is applied, as we have used here. We have now extended our work from the Dunning prostate R3327-AT1 tumor, which is poorly differentiated, has only microscopic necrotic foci and is firm, to the 13762 breast tumor, which has less structure and considerable cystic fluid. Here, we have simply reported the ability to measure dynamic changes in the breast tumor oxygenation, but in the accompanying work (Song *et al.*, this volume), we show more extensive results.

Since the MR and electrode approaches appear to give similar results one may debate the relative their merits. Clearly, MR is very expensive, with a typical imaging system costing upwards of $1 M, compared with $60 000 for the Eppendorf and < $5 000 for a laboratory micro electrode system. However, MR facilitates the simultaneous measurements of dynamic changes in response to intervention at multiple points within a tumor. While we were able to follow changes in $pO_2$ at specific regions using a needle electrode with placement at sequential locations accompanied by cycling of the intervention, such an approach would be less satisfactory for other interventions, and even here, may have led to some conditioning or hysteresis. The FREDOM approach may be readily combined with other measurements such as blood flow/perfusion [24], pH [25] or metal ions by infusion of appropriate reporter molecules [26].

As a reporter molecule HFB has many advantageous properties. It is cheap, readily available, and exhibits minimal acute toxicity ($LD_{50}$ > 25 g/kg) [27]. No signs of renal or hepatic toxicity have been found [28] and others have tested doses as high as 50 g/kg (twice weekly) orally in rats over 35 weeks [29]. We typically find substantial clearance from tumors within 24 h, though this does limit our measurements to acute response to interventions [12]. High symmetry within the molecule leads to a single $^{19}F$ MR resonance providing optimal SNR. The R1 (=1/T1) is highly sensitive to $pO_2$ while showing little response to temperature [9]. Long T1s up to 14 s appear to make HFB less efficient for spin lattice relaxometry, but use of the pulse burst saturation recovery approach minimizes the length of th experiment [10] and a large range of T1 values is a requisite for sensitivity to changes in $pO_2$. The long transverse relaxation time (T2) is ideally suited to echo planar imaging.

The ultimate value of a novel technique will depend on its adoption by multiple laboratories, and the significance of the results that can be generated. We believe that the FREDOM approach is versatile and we are demonstrating increasing applications, and thus, we foresee expanded future application of the technique.

**Reference**:

1. Hall EJ. The oxygen effect and reoxygenation. In: Hall EJ, ed. Radiobiology for the Radiologist. 3 ed. Philadelphia: Lippincott, J. B., 1994: 133-152.

2. Chapman JD, Stobbe CC, Arnfield MR, Santus R, Lee J, McPhee MS. Oxygen Dependency of Tumor Cell Killing *In Vitro* by Light Activated Photofrin II. Radiat. Res. 1991;126:73-79.

3. Brown JM, Giaccia AJ. Tumor hypoxia: the picture has changed in the 1990s. Int. J. Radiat. Biol. 1994;65:95-102.

4. Vaupel PW, Höckel M. Oxygenation status of human tumors: a reappraisal using computerized $pO_2$ histography. In: Vaupel PW, Kelleher DK, Günderoth M, eds. Tumor Oxygenation. Stuttgart: Gustav Fischer, 1995: 219-232. (Thews G, ed. Funktionsanalyse biologischer Systeme; vol 24).

5. Fyles AW, Milosevic M, Wong R, et al. Oxygenation predicts radiation response and survival in patients with cervix cancer. Radiother. Oncol. 1998;48:149-56.

6. Höckel M, Schlenger K, Aral B, Mitze M, Schäffer U, Vaupel P. Association between tumor hypoxia and malignant progression in advanced cancer of the uterine cervix. Cancer Res. 1996;56:4509-15.

7. Nordsmark M, Overgaard M, Overgaard J. Pretreatment oxygenation predicts radiation response in advanced squamous cell carcinoma of the head and neck. Radiother. Oncol. 1996;41:31-40.

8. Stone HB, Brown JM, Phillips T, Sutherland RM. Oxygen in human tumors: correlations between methods of measurement and response to therapy. Radiat. Res. 1993;136:422-434.

9. Mason RP, Rodbumrung W, Antich PP. Hexafluorobenzene: a sensitive $^{19}F$ NMR indicator of tumor oxygenation. NMR in Biomed. 1996;9:125-134.

10. Le D, Mason RP, Hunjan S, Constantinescu A, Barker BR, Antich PP. Regional tumor oxygen dynamics: $^{19}F$ PBSR EPI of hexafluorobenzene. Magn. Reson. Imaging, 1997;15(8):971-81.

11. Mason RP, Constantinescu A, Hunjan S, et al. Regional tumor oxygenation and measurement of dynamic changes. Radiat. Res. 1999;152:239.

12. Hunjan S, Mason RP, Constantinescu A, Peschke P, Hahn EW, Antich PP. Regional tumor oximetry: $^{19}F$ NMR spectroscopy of hexafluorobenzene. Int. J. Radiat. Oncol. Biol. Phys. 1998;40(5):161-71.

13. Delpuech J-J, Hamza MA, Serratice G, Stébé M-J. Fluorocarbons as oxygen carriers. I. An NMR study of oxygen solutions in hexafluorobenzene. J. Chem. Phys. 1979;13:399.

14. Mason RP. Non-invasive physiology: $^{19}F$ NMR of perfluorocarbon. Art. Cells, Blood Sub. & Immob. Biotech. 1994;22(4):1141-1153.

15. Hahn EW, Peschke P, Mason RP, Babcock EE, Antich PP. Isolated tumor growth in a surgically formed skin pedicle in the rat: a new tumor model for NMR studies. Magn. Reson. Imaging 1993;11:1007-1017.

16. Laurence V, Ward R, Bleehen N. Tumor $pO_2$ distribution in patients treated with the combination of nicotinamide and carbogen breathing. In: P. W. Vaupel, D. K. Kelleher, M. Günderoth, eds. Tumor Oxygenation. Stuttgart: Gustav Fischer,, 1995: 185-193.

17. Cater D, Silver I. Quantitative measurements of oxygen tension in normal tissues and in the tumors of patients before and after radiotherapy. Acta Radiol. 1960;53:233-256.

18. Chaplin DJ, Horsman MR, Siemann DW. Further evaluation of nicotinamide and carbogen as a strategy to reoxgenate hypoxic cells *in vivo*: importance of nicotinamide dose and pre-irradiation breathing time. Br. J. Cancer 1993;68:269-73.

19. Dardzinski BJ, Sotak CH. Rapid tissue oxygen tension mapping using $^{19}F$ Inversion-recovery Echo-planar imaging of Perfluoro-15-crown-5-ether. Magn. Reson. Med. 1994;32(1):88-97.

20. Baldwin NJ, Ng TC. Oxygenation and metabolic status of KHT tumors as measured simultaneously by $^{19}F$ magnetic resonance imaging and $^{31}P$ magnetic resonance spectroscopy. Magn. Reson. Imaging 1996;14(5):514-551.

21. Fishman JE, Joseph PM, Carvlin MJ, Saadi-Elmandjra M, Mukherji B, Sloviter HS. *In vivo* measurements of vascular oxygen tension in tumors using MRI of a fluorinated blood substitute. Invest. Radiol. 1989;24:65-71.

22. Mason RP, Antich PP, Babcock EE, Constantinescu A, Peschke P, Hahn EW. Non-invasive determination of tumor oxygen tension and local variation with growth. Int. J. Radiat. Oncol. Biol. Phys. 1994;29: 95-103.

23. McIntyre DJO, McCoy CL, Griffiths JR. Tumour oxygenation measurements by $^{19}F$ MRI of perfluorocarbons. Curr. Sci. 1999;76:753-762.

24. Brown SL, Ewing JR, Lolozsvary A, Butt S, Cao Y, Kim JH. Magnetic Resonance Imaging of perfusion in rat cerebral 9L tumor after nicotinamide administration. Int. J. Radiat. Oncol. Biol. Phys. 1999;43:627-33.

25. Mason R, Hunjan S, He S, et al. Tumor trans membrane pH gradient and regional oxygen tension measured by fluorine magnetic resonance. In: Moraes M, Brentani R, Bevilacqua R, eds. 17th International Cancer Congress. Rio de Janeiro: Monduzzi, 1998: 1627-31. vol 2).

26. Mason RP. Transmembrane pH gradients *in vivo*: measurements using fluorinated vitamin B6 derivatives. *Curr. Med. Chem.* 1999;6:533-51.

27. Lancaster. Material Safety Data Sheet. In: Lancaster Synthesis Inc., 1998:

28. Hall LW, Jackson SRK, Massey GM. Hexafluorobenzene in veterinary anaesthesia. In: Arias A, Llaurado R, Nalda MA, Lunn JN, eds. Recent Progress in Anaesthesiology and Resuscitation. Oxford: Excerpta Medica, 1975: 201-204.

29. Rietjens IMCM, Steensma A, den Besten C, et al. Comparative biotransformation of hexachlorobenzene and hexafluorobenzene in relation to the induction of porphyria. Eur. J. Pharmacol. 1995;293:292-299.

**Figure legends**

**Figure 1**

Comparison of oxygenation in size-matched groups of AT1 tumors based on $^{19}F$ MR EPI relaxometry (left) and electrode polarography (right), when rats inhaled 33% $O_2$. Small tumors are shown at top (volume < 2 $cm^3$) and large tumors below (volume > 3.5 $cm^3$). Each method shows a significant difference in tumor oxygenation for small versus large tumors ($p < 0.0001$).

**Figure 2**

a) Dynamic changes in $pO_2$ of six specific regions of an AT1 tumor. The three high $pO_2$ regions had significantly different $pO_2$ (* $p < 0.05$) ) from those with low $pO_2$ at each time point. Within 8 mins of elevating inspired $O_2$ the three high $pO_2$ voxels had significantly increased $pO_2$ ($p < 0.05$) while the low $pO_2$ voxels required > 24 mins to show significant changes. All six regions were observed simultaneously using the FREDOM approach.

b) Dynamic changes in $pO_2$ of six specific regions of an AT1 tumor. The electrode was placed in one location at a time and inhaled gases cycled for subsequent locations.

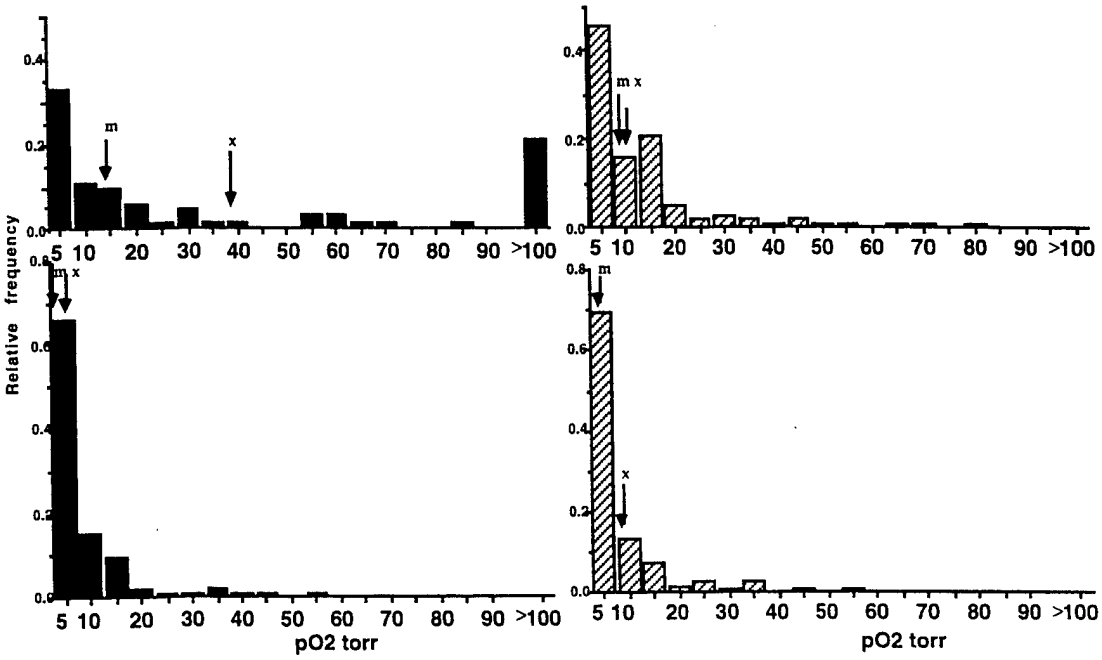
Relative frequency
m
x
m x
m x
m
x
5 10 20 30 40 50 60 70 80 90 >100
pO2 torr

Figure 1

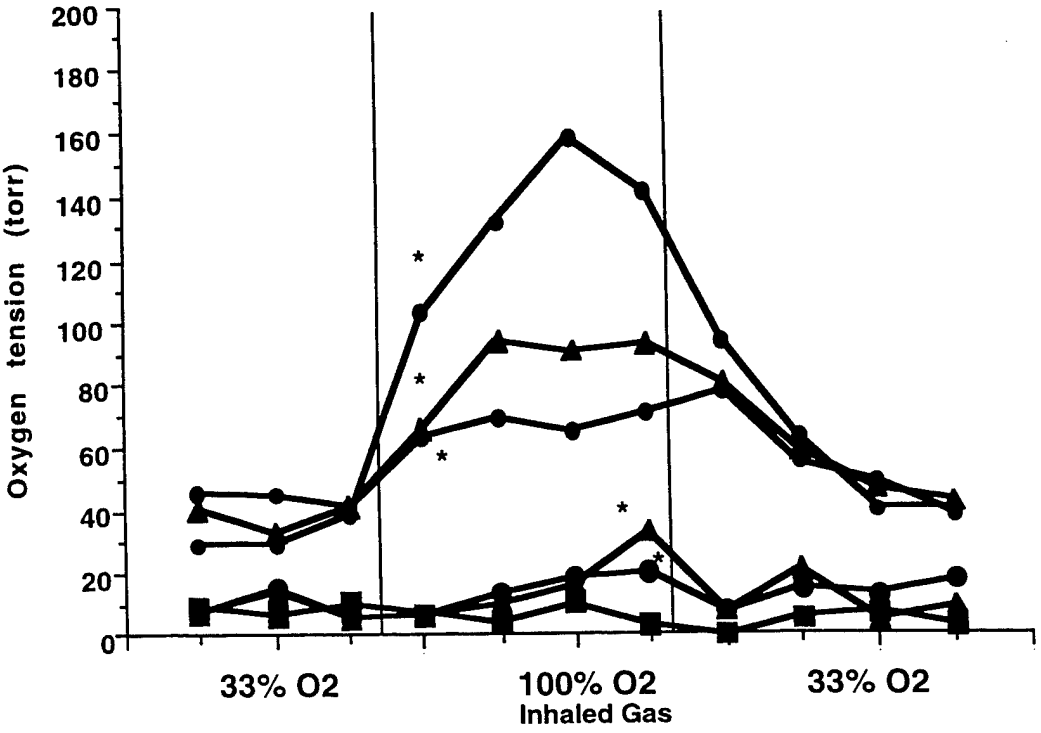


Figure 2a

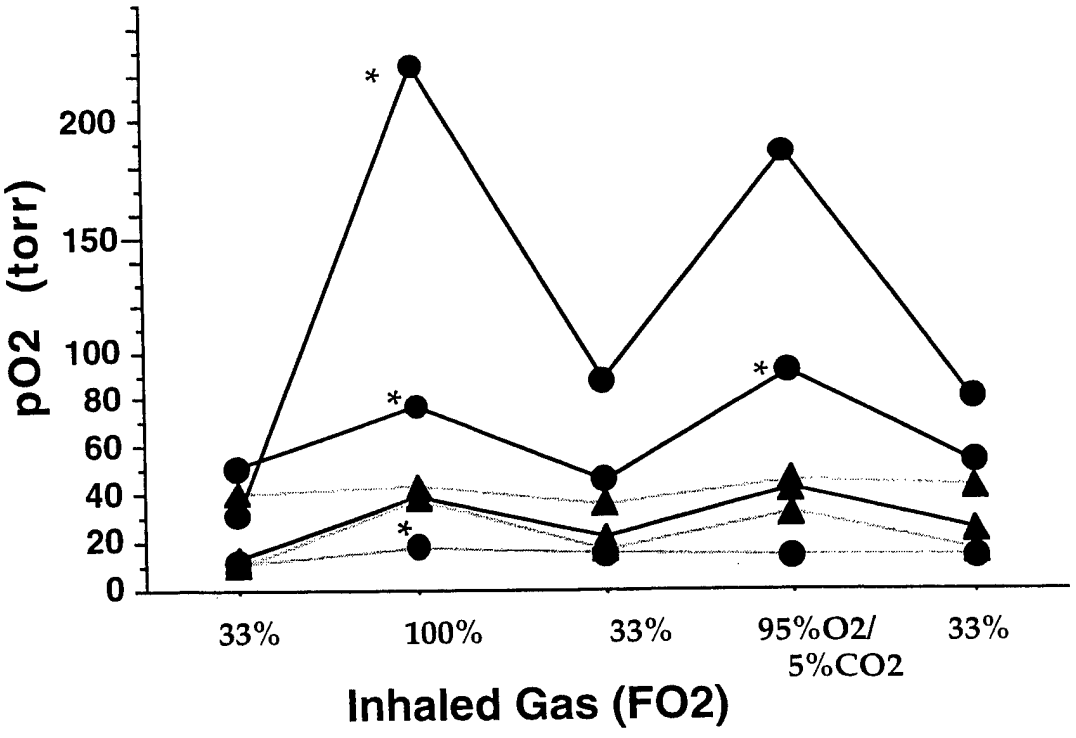


Figure 2b

ISOTT, 1999
All rights of reproduction in any form reserved

# Tumor Oxygen Dynamics: Comparison of $^{19}$F MR EPI and Frequency Domain NIR Spectroscopy

Yulin Song[1,2]; Kate L. Worden[1]; Xin Jiang[1]; Dawen Zhao[2]; Anca Constantinescu[2]; Hanli Liu[1]; and Ralph P. Mason[2]

[1]*Joint Graduate Program in Biomedical Engineering,*
[2]*Department of Radiology, UT Southwestern Medical Center, Dallas, TX 75235, USA*

## ABSTRCT

**Oxygen plays a key role in tumor therapy and may be related to tumor development: e.g., angiogenesis and metastasis. Using noninvasive techniques to accurately measure tumor oxygenation could assist in developing novel therapies. Here, we have used the FREDOM (Fluorocarbon Relaxometry using Echo planar imaging for Dynamic Oxygen Mapping) approach based on hexafluorobenzene (HFB) to monitor tissue oxygen tension ($pO_2$) of rat breast and prostate tumors and compared the results with changes in tumor vascular hemoglobin saturation ($sO_2$) and concentration observed using a new dual wavelength homodyne near-infrared (NIR) system. The dynamic changes in $pO_2$ and $sO_2$ were assessed while rats were breathing various gases. NIR showed significant changes in vascular oxygenation accompanying respiratory interventions. $^{19}$F MR-EPI also showed significant changes in tissue $pO_2$ and revealed considerable regional heterogeneity in both absolute values and rate of change accompanying interventions. Generally, changes in vascular $sO_2$ preceded tissue $pO_2$, particularly for smaller tumors.**

**Keywords: Oxygen tension, Echo planar imaging, MRI, Tumor, NIR spectroscopy**

## INTRODUCTION

The growth and development of tumors are greatly influenced by oxygen tension ($pO_2$), e.g., tumor hypoxia leads to increased expression of vascular endothelial growth factor (VEGF), and thus, angiogenesis [1]. Hypoxia reduces radiosensitivity [2], but chemotherapeutic approaches have been proposed to exploit the tumor hypoxia based on selective cytotoxicity of bioreductive drugs [3, 4]. In addition, increasing evidence from clinical trials has revealed that poorly oxygenated tumors have poor prognosis for patients [5, 6]. Therefore, accurate measurements of oxygenation could enhance cancer treatment planning. Here, we present two methods of measuring tumor oxygenation: the FREDOM approach to measure tumor tissue oxygen tension ($pO_2$) and NIR spectroscopy to measure changes in tumor vascular hemoglobin saturation ($sO_2$) and concentration [Hb]. By comparing these two techniques, we can examine the relationship between tumor tissue $pO_2$ and vascular $sO_2$.

Presented in part at the 27th annual meeting of the International Society of Oxygen Transport to Tissue (ISOTT), Dartmouth Medical School, Hanover, NH, USA, September 1999.
Correspondence to: Dr. R.P. Mason, Department of Radiology, UTSW, Dallas, USA. Tel: (214)-648-8926, Fax: (214)-648-2991,
E-mail: Ralph.Mason@email.swmed.edu

The FREDOM approach is based on $^{19}$F PBSR-EPI of hexafluorobenzene (HFB). It has been shown that the spin-lattice relaxation rate, $R1$ (1/T1), is linearly proportional to dissolved oxygen concentration [7]. HFB offers exceptional sensitivity to changes in $pO_2$ while having little response to temperature [8]. Because of structural symmetry, HFB has a single resonance and thus, is free from chemical shift artifact, providing an optimal signal-to-noise ratio (SNR). Maps of the tumor tissue $pO_2$ were obtained in 8 minutes with millimeter resolution, allowing the fate of individual voxels to be traced. NIR spectroscopy can be used to measure tumor vascular $sO_2$ because the absorption coefficients of deoxy-hemoglobin differ from those of oxy-hemoglobin at the wavelengths selected (758 nm and 782 nm) [9]. The system has many attractive features: completely non-invasive, inexpensive, portable, and real-time.

## METHODS

### Tumor Model

NF 13762 breast and Dunning prostate R3327-AT1 adenocarcinomas were implanted in skin pedicles on the forebacks of adult female Fischer and male Copenhagen rats (~250 g), respectively, as described

previously [10]. Once the tumors reached ~1 cm diameter, the rats were anesthetized with 200 µl ketamine hydrochloride (100 mg/ml) and maintained under general gaseous anesthesia (33% $O_2$, 66% $N_2O$ and 0.5%) through a mask placed over the mouth and nose. Body temperature was maintained at 37°C by a thermal blanket. A fiber optic pulse oximeter was placed on the hind foot to monitor arterial hemoglobin saturation and heart rate, and a fiber optic probe was inserted rectally to monitor core temperature. NIR spectroscopy and $^{19}F$ PBSR-EPI measurements were then performed sequentially, while inhaled gas was alternated between 33% $O_2$, carbogen (95% $O_2$ + 5% $CO_2$), and 100% $O_2$.

**NIR Spectroscopy**

The tumor vascular $sO_2$ was assessed by NIR spectroscopy using a new dual wavelength, homodyne system (wavelengths 758 nm and 782 nm). These wavelengths were selected because they not only allow the calculation of $sO_2$, but also fall into the range of wavelengths compatible with the low cost photo multiplier tube (PMT). The system uses only one RF source to determine amplitude and phase changes of light. Figure 1 shows a schematic diagram of the system. An RF source modulates the light from two laser diodes at 140 MHz. The light passes through fiber optic cables, is transmitted through the tumor tissue, and is collected by a second fiber bundle. The light is then detected, amplified, filtered, and demodulated into I and Q components. Amplitude and phase changes caused by the tumor are related to changes in hemoglobin concentration [Hb] and hemoglobin saturation [$HbO_2$], i.e., $sO_2$.

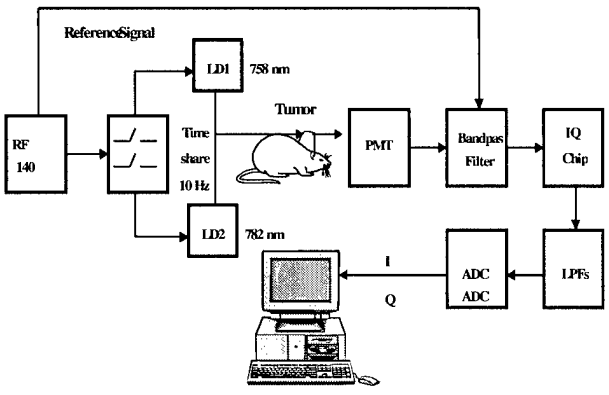


**Figure 1.** A schematic diagram of the NIR IQ system

To obtain the absorption coefficients of deoxy-hemoglobin and oxy-hemoglobin, we have assumed background absorbance to be negligible and estimated the absorption coefficients by multiplying the extinction coefficients for deoxy-hemoglobin and oxy-hemoglobin with their respective concentrations.

$$\mu_a^{758} = \varepsilon_{Hb}^{758}[Hb] + \varepsilon_{HbO2}^{758}[HbO_2] \quad (1)$$

$$\mu_a^{782} = \varepsilon_{Hb}^{782}[Hb] + \varepsilon_{HbO2}^{782}[HbO_2] \quad (2)$$

where $\mu_a^{758}$ and $\mu_a^{782}$ are the absorption coefficients, $\varepsilon_{Hb}^{758}$ and $\varepsilon_{Hb}^{782}$ the extinction coefficients for deoxy-hemoglobin, $\varepsilon_{HbO2}^{758}$ and $\varepsilon_{HbO2}^{782}$ the extinction coefficients for oxy-hemoglobin at the wavelengths 758 nm and 782 nm, respectively, and [Hb] and [$HbO_2$] are the deoxy-hemoglobin and oxy-hemoglobin concentrations, respectively.

Although the IQ system does give both phase and amplitude values, given the tumors' small sizes and our fiber configuration, conventional diffusion theory doesn't hold. To overcome this difficulty, we modified Beer-Lambert's law and used the amplitude values to find trends in the changing absorption coefficients.

$$\mu_{aC} - \mu_{aI} = (1/L)*\log (A_I/A_C) \quad (3)$$

where $A_I$ is the initial amplitude (amplitude of baseline), $A_C$ the current amplitude, and L the optical pathlength between source and detector.

By manipulating equations 1-3, we can compute changes in blood volume and saturation between the initial state and the intervention state from the transmitted amplitude of the light through the tumor.

$$\Delta[Hb]_{total} = -(3.63/L)*\log (A_I/A_C)^{758} + (8.68/L)*\log (A_I/A_C)^{782} \quad (4)$$

$$\Delta[HbO_2] - \Delta[Hb] = -(18.49/L)*\log (A_I/A_C)^{758} + (21.20/L)*\log (A_I/A_C)^{782} \quad (5)$$

where Δ[] represents change in concentration. The constants were computed with extinction coefficients for oxy- and deoxy-hemoglobin at the two wavelengths used.

Once stable baseline measurements were achieved, the inhaled gas was altered to pure oxygen or carbogen and dynamic changes were observed over a period of two hours. Both the magnitude and rate of change of $sO_2$ were examined. Following the NIR experiments, the MRI experiments were performed.

**$^{19}F$ MR-EPI**

All MRI experiments were performed on an Omega CSI 4.7 T 40 cm system with actively shielded

gradients. A tunable 2 cm $^{1}H/^{19}F$ single turn solenoid coil was placed around the tumor and 40 µl HFB were injected directly into both central and peripheral regions of the tumor using a 32 G needle. Shimming was performed on the $^{1}H$ signal of the tissue water to a typical linewidth of 50 Hz. 3D spin-echo (SE) $^{1}H$ images were acquired for anatomical reference and corresponding $^{19}F$ images were then obtained to show the distribution of HFB in the tumor. Regional tumor $pO_2$ maps were generated using $^{19}F$ PBSR-EPI based on the relationship: $pO_2(\text{torr}) = [R1 - 0.074]/0.0016$, where $R1$ is the spin lattice relaxation rate of HFB, as described in detail previously [11]. Twenty-three $pO_2$ maps were produced in 3 hours with respect to respiratory challenge.

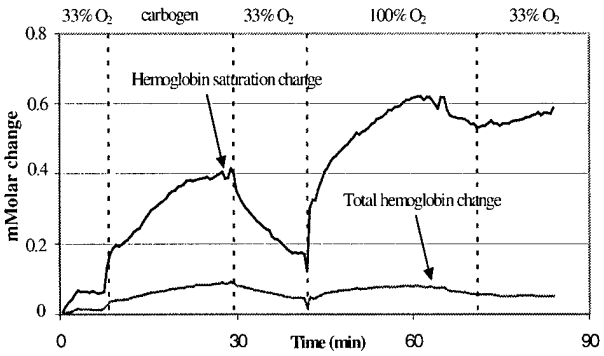


**Figure 2.** Hemoglobin saturation and concentration change in a 4.0 $cm^3$ breast tumor.

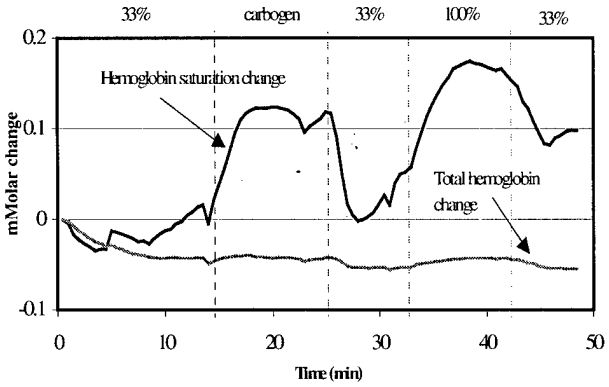


**Figure 3.** Hemoglobin saturation and concentration change in a 4.0 $cm^3$ prostate tumor.

## RESULTS

### NIR Results

Figure 2 shows the time course of changes in tumor vascular hemoglobin saturation and concentration accompanying alterations in inhaled gases for a breast tumor and Figure 3 shows the result for a prostate tumor. Hemoglobin saturation and concentration are presented as relative millimolar changes. Both tumors show significant changes in vascular oxygenation accompanying respiratory interventions. Hemoglobin saturation increased almost immediately after a gas switch from baseline (33% $O_2$) to either carbogen or 100% $O_2$ and increased steadily for several minutes, and then gradually returned to baseline after the gas was switched back to baseline. In contrast, total hemoglobin change is insignificant, indicating relatively constant blood volume in the tumor.

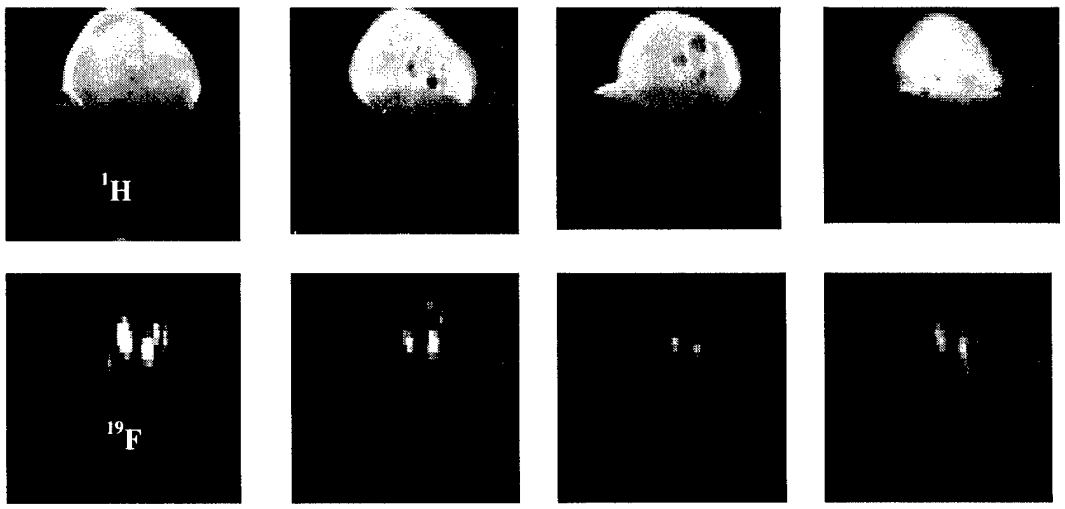


**Figure 4.** $^{1}H$ and $^{19}F$ coronal images of a breast tumor. FOV = 48 x 48 mm, matrix size = 128 x 64, and slice thickness = 4 mm.

## MRI Results

Figure 4 shows conventional spin echo (SE) $^{1}H$ images (upper) and corresponding $^{19}F$ images of a representative breast tumor. Figure 5a shows a $^{19}F$ PBSR-EPI projection image obtained from the tumor shown in Figure 4 in a single acquisition ($\tau$ = 90 s) and Figure 5b shows corresponding $pO_2$ map (expanded).

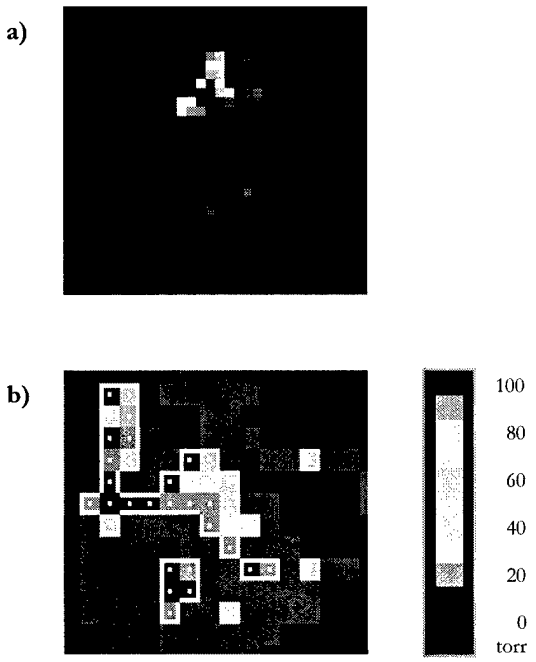


**Figure 5.** (**a**) A $^{19}F$ PBSR-EPI projection image obtained from the tumor shown in Figure 4 in a single acquisition = 90 s). Fourteen images were acquired with variable relaxation delays ($\tau$) ranging from 200 ms to 90 sec and 1.5 mm in plane resolution. (**b**) Corresponding $pO_2$ map (expanded).

The $^{19}F$ MR-EPI oximetry of tumor has the distinct advantage over other techniques that subsequent measurements are completely non-invasive. The greatest strength of this method is the ability to trace the fate of individual voxels (regions) with respect to therapeutic interventions. Figure 6 shows dynamic changes in $pO_2$ of six specific voxels of a breast tumor with respect to different inhaled gases. It is noteworthy that voxels with high baseline $pO_2$ had significantly different response characteristics from those with initially low $pO_2$, which showed small changes. Figure 7 shows $pO_2$ histograms obtained by FREDOM of HFB for a representative breast tumor. The histograms show the heterogeneity of $pO_2$ values within the tumor as well as the mean $pO_2$ values.

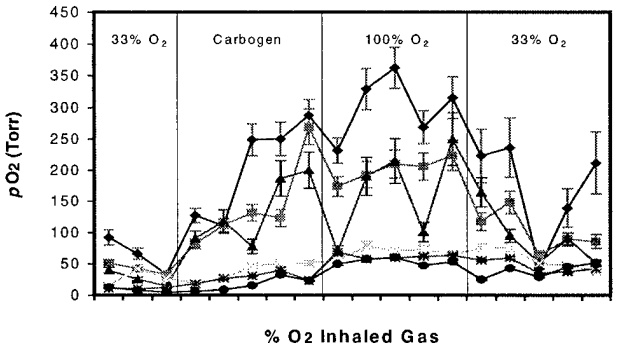


**Figure 6.** Dynamic changes in $pO_2$ of six specific voxels of a breast tumor.

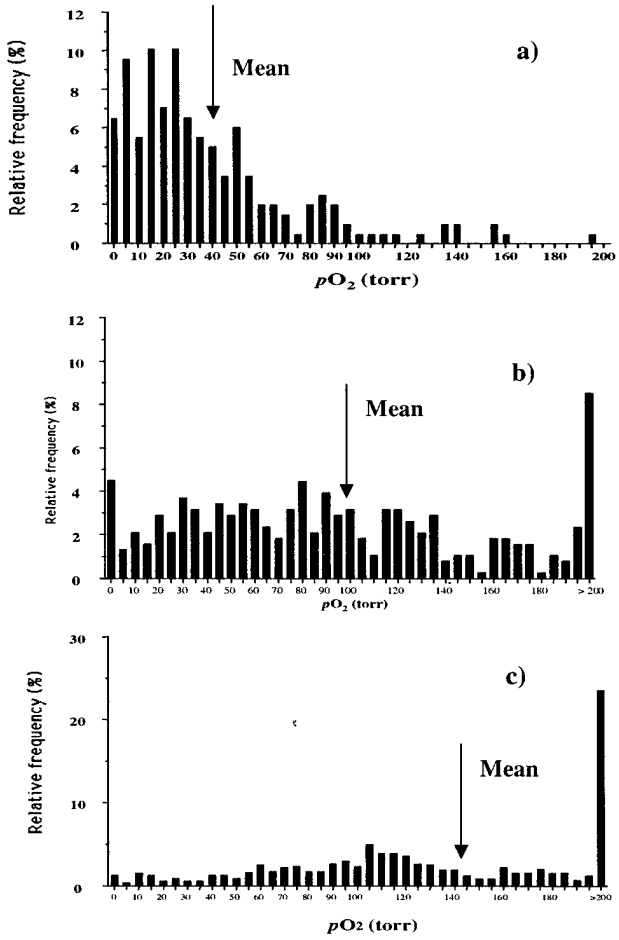


**Figure 7.** Histograms of oxygen tension for an NF13762 breast tumor determined by FREDOM of HFB. (**a**) $pO_2$ distribution while the rat breathed 33% $O_2$. Mean $pO_2$ = 44 ± 3 torr. (**b**) $pO_2$ distribution while the rat breathed carbogen (95% $O_2$ + 5% $CO_2$). Mean $pO_2$ = 99 ± 4 torr. ($p<0.0001$). (**c**) $pO_2$ distribution while the rat breathed 100% $O_2$. Mean $pO_2$ = 145 ± 4 torr.

**Comparison**

While absolute $pO_2$ values are important for investigating tumor hypoxia, dynamic changes may be more valuable for investigating tumor response to therapeutic interventions. Figure 8 shows comparisons between the dynamic changes in $pO_2$ and $sO_2$. Since the IQ system provides a global $sO_2$ value, each $pO_2$ data point is represented as an average over all voxels of each $pO_2$ map.

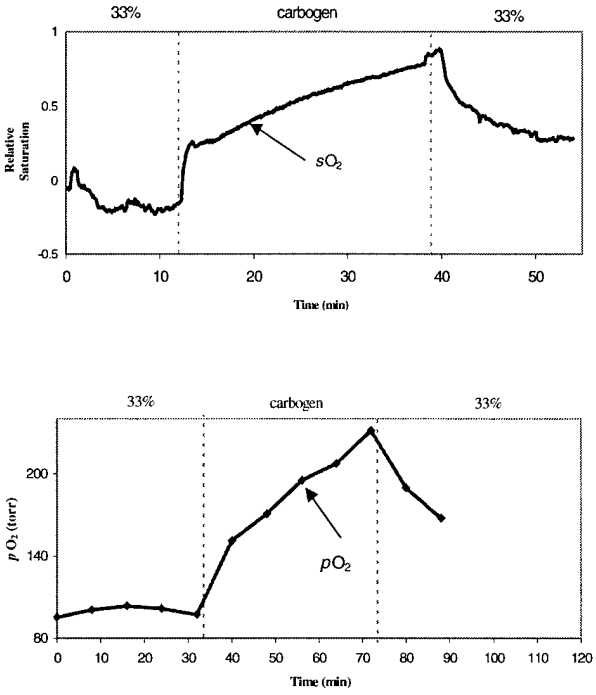


**Figure 8.** Comparison of $pO_2$ and hemoglobin saturation ($sO_2$) of a breast tumor. (**a**) $sO_2$ determined by NIR spectroscopy.(**b**) $pO_2$ determined by FREDOM. Both $pO_2$ and $sO_2$ increase with a transition from 33% to carbogen and begin to decrease when switched back to 33% $O_2$. Changes in vascular $sO_2$ precede tissue $pO_2$. The tumor size = 1.9 x 2.2 x 2.0 cm.

To further investigate the response, we modeled the temporal response in $pO_2$ and $sO_2$ using exponential equations:

$$y = a + b \cdot (1 - e^{-t/\tau}), \quad \text{for increasing trend} \qquad (6)$$

$$y = a + b \cdot e^{-t/\tau}, \quad \text{for decreasing trend} \qquad (7)$$

where $y$ is $pO_2$ or $sO_2$, $a$ and $b$ are two constants, $t$ is time, and $\tau$ is the time constant.

Changes in $sO_2$ were faster than $pO_2$ (Figure 9), especially in the case of larger tumor, which was found to be less well oxygenated and presumably less well perfused.

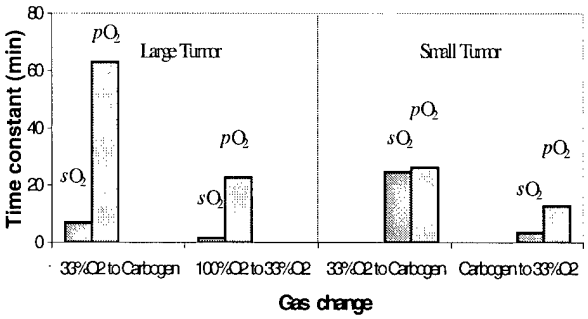


**Figure 9.** Comparison of $pO_2$ and $sO_2$ time constants of two breast tumors (small tumor = 1.9 x 2.2 x 2.0 cm, large tumor = 2.4 x 2.2 x 2.1 cm). The temporal responses in $pO_2$ and $sO_2$ were modeled using exponential equations.

## DISCUSSION

Since poorly oxygenated tumors tend to resist conventional therapy, there have been many efforts to re-oxygenate tumors prior to therapy. A simple intervention is respiratory challenge, i.e., attempting the elevated oxygen concentration of the inhaled gas. Past clinical trials were often disappointing, but it is now thought that results were significantly influenced by the inability to identify hypoxic tumors (i.e., those which would benefit from manipulation), a priori. As techniques become available to measure tumor oxygenation, it is appropriate to reevaluate approaches to manipulating tumor oxygenation. By increasing the oxygen tension of the inspired gas, the arterial $sO_2$ should increase, leading to increased hemoglobin saturation of the tumor vasculature, and hence, increased tumor tissue $pO_2$. Our data indicate that breathing elevated $O_2$ did indeed have a significant effect on both tumor vascular $sO_2$ and tissue $pO_2$. For a typical large breast tumor, significant changes were found in vascular $sO_2$ ($p<0.05$) and in tissue $pO_2$ ($p<0.0001$) by ANOVA in the case of carbogen inhalation, and ($p<0.01$) and ($p<0.0001$) in the case of oxygen inhalation. There has been a debate as to whether carbogen is more effective at modulating tumor oxygenation than 100% oxygen since $CO_2$ is a vasodilator. Indeed, recent work in a human glioma xenografts suggested that oxygen alone had no influence on tumor vascular oxygenation, whereas carbogen produced a pronounced effect [12]. Our preliminary results indicate that both gases produced changes in $sO_2$

and $pO_2$, with vascular $sO_2$ increasing more with 100% $O_2$ inhalation than with carbogen.

We recently showed that the FREDOM approach indicates similar $pO_2$ values in tumors to electrodes [13], especially on interstitial tissue $pO_2$. By contrast, NIR investigates vascular oxygenation. As expected, changes in vascular oxygenation ($sO_2$) were found to be more rapid than tumor tissue $pO_2$, with greater differences in large tumors. This probably reflects the extensive perfusion of the small tumors with lesser perfusion of large tumors as reflected by lower mean $pO_2$ and larger hypoxic fraction [13].

Regional tumor tissue $pO_2$ and blood $sO_2$ are important physiological parameters. The capability to measure them will provide insight into progressive physiological changes in a tumor accompanying interventions. NIR has the advantages of being entirely noninvasive, inexpensive, portable, and real-time. But the MRI approach clearly reveals detailed oxygenation heterogeneity. The correlation of NIR and MR technologies will provide insight into issues of oxygen delivery and consumption. We believe that application of multiple approaches to tumor oxygenation can lead to better understanding of tumor physiology and probably optimized tumor therapy.

## ACKNOWLEDGMENTS

This work was supported in part by grants from The American Cancer Society (RPG-97-116-010CCE; RPM), The Whitaker Foundation (RPM and HL), the DOD Breast Cancer Initiative (DAMD17-97-1-7261;YS), and NIH BRTP Facility #5-P41-RR02584.

## REFERENCES

1. P Ö tgens, A.J.G., Westphal, H.R., de Waal, R.M.W, and Ruiter, D.J., *The Role of Vascular Permeability Factor and Basic Fibroblast Growth Factor in Tumor Angiogenesis.* Biol. Chem. Hopper-Seyler, 1995, 376:57-70.

2. Gray, L.H., Conger, A.D., Ebert, M., Hornsey, S., and Scott, O.C.A., *The Concentration of Oxygen Dissolved in Tissues at the Time of Irradiation as a Factor in Radiotherapy.* Br. J. Radiol. 1953, 26:638-648.

3. Brown, J.M., Giaccia, A.J., *Tumor Hypoxia: the Picture has Changed in the 1990s.* Int. J. Radiat. Biol. 1994, 65:95-102.

4. Stratford, I., Adams, G., Bremmer, J., Cole, S., *et al.*, *Manipulation and Exploitation of the Tumor Environment for Therapeutic Benefit.* Int. J. Radiat. Biol. 1994, 85-94.

5. H Ö ckel, M., Schlenger, K., Aral, B., Mitze, M., Sch ä ffer, U., and Vaupel, P., *Association between Tumor Hypoxia and Malignant Progression in Advanced Cancer of the Uterine Cervix.* Cancer Res. 1996, 56:4509-15.

6. Fyles, A.W., Milosevic, M., Wng, R., Kavanagh, M.C., Pintile, M., Sun, A., Chapman, W., Levin, W., Manchul, L., Keane, T.J., and Hill, R.P., *Oxygenation Predicts Radiation Response and Survival in Patients with Cervix Cancer.* Radiother. Oncol. 1998, 48:149-56.

7. Mason, R.P., *Non-invasive Physiology: $^{19}F$ NMR of Perfluorocarbons.* Artif. Cells Blood Subs. Immob. Biotechnol. 1994, 22:1141-1153.

8. Mason, R.P., Rodbumrung, W., Antich, P.P., *Hexafluorobenzene: a Sensitive $^{19}F$ NMR Indicator of Tumor Oxygenation.* NMR in Biomed. 1996, 9:125-134.

9. Yunsong, Y., Liu, H., Li, X., and Chance, B., *Low-Cost Frequency-Domain Photon Migration Instrument for Tissue Spectroscopy, Oximetry, and Imaging.* Opt. Eng. 1997, 36(5):1562-1569.

10. Hahn, E. W., Peschke, P., Mason, R.P., Babcock, E.E., and Antich, P.P., *Isolated Tumor Growth in a Surgically Formed Skin Pedicle in the Rat: A New Tumor Model for NMR Studies.* Magn. Reson. Imaging. 1993, 11:1007-1017.

11. Le, D., Mason, R.P., Hunjan, S., Constantinescu, A., Barker, B.R., and Antich, P.P., *Regional Tumor Oxygen Dynamics: $^{19}F$ PBSR EPI of Hexafluorobenzene.* Magn. Reson. Imaging. 1997, 15:971-981.

12. van der Sanden, B.P.J., Heerschap, A., Simonetti, A.W., Rijken, P.F.J.W., Peters, H.P.W., St ü ben, G., and van der Kogel, A.J., *Characterization and Validation of Noninvasive Oxygen Tension Measurements in Human Glioma Xenografts by $^{19}F$-MR Relaxometry.* Int. J. Radiat. Oncol. Biol. Phys. 1999, 44(3):649-658.

13. Mason, R.P., Constantinescu, A., Hunjan, S., Le, D., Hahn, E.W., Blum, C., Antich, P.P., and Peschke, P., *Regional Tumor Oxygenation and Measurement of Dynamic Changes.* Radiat. Res. 1999, 152:239-249.

# Noninvasive investigation of blood oxygenation dynamics of tumors by near-infrared spectroscopy

Hanli Liu, Yulin Song, Katherine L. Worden, Xin Jiang, Anca Constantinescu, and Ralph P. Mason

The measurement of dynamic changes in the blood oxygenation of tumor vasculature could be valuable for tumor prognosis and optimizing tumor treatment plans. In this study we employed near-infrared spectroscopy (NIRS) to measure changes in the total hemoglobin concentration together with the degree of hemoglobin oxygenation in the vascular bed of breast and prostate tumors implanted in rats. Measurements were made while inhaled gas was alternated between 33% oxygen and carbogen (95% $O_2$, 5% $CO_2$). Significant dynamic changes in tumor oxygenation were observed to accompany respiratory challenge, and these changes could be modeled with two exponential components, yielding two time constants. Following the Fick principle, we derived a simplified model to relate the time constants to tumor blood-perfusion rates. This study demonstrates that the NIRS technology can provide an efficient, real-time, noninvasive means of monitoring the vascular oxygenation dynamics of tumors and facilitate investigations of tumor vascular perfusion. This may have prognostic value and promises insight into tumor vascular development. © 2000 Optical Society of America

*OCIS codes:* 170.1470, 170.3660, 170.4580, 170.5280, 290.1990, 290.7050.

## 1. Introduction

The presence and the significance of tumor hypoxia have been recognized since the 1950's. There is increasing evidence that tumor oxygenation is clinically important in predicting tumor response to radiation, tumor response to chemotherapy, overall prognosis, or all three. Hypoxic cells *in vitro* and in animal tumors *in vivo* are documented to be 3 times more resistant to radiation-induced killing compared with aerobic cells.[1] Recent studies show that hypoxia may have a profound impact on malignant progression and on responsiveness to therapy.[2,3] Numerous studies on tumor oxygen tension ($pO_2$) measurements have been conducted in recent years by use of a variety of methods, such as microelectrodes,[2] phosphors,[4] electron paramagnetic resonance,[5] or magnetic resonance imaging[6] (MRI). Comparing needle-based, oxygen-sensitive electrodes or electron paramagnetic resonance and MRI for measuring $pO_2$ shows that the latter two offer the advantage of facilitating multiple repeated measurements to map $pO_2$ noninvasively. However, magnets are large, and the methods are not readily portable. A versatile method for monitoring intratumor oxygenation rapidly and noninvasively is therefore very desirable for tumor prognosis and tumor treatment planning.

In the near-infrared (NIR) region (700–900 nm) the major chromophores in tissue are oxygenated hemoglobin and deoxygenated hemoglobin, which differ in their light absorption. Measurements of the absorption of light travelling through the tissue under study allow us to evaluate or quantify blood oxygenation, such as the concentrations of oxygenated hemoglobin ($HbO_2$), and deoxygenated hemoglobin (Hb) and the hemoglobin saturation $SO_2$. In the past decade, three forms of NIR spectroscopy (NIRS) that use pulsed-laser light in the time domain, amplitude-modulated laser light in the frequency domain, and cw light in a dc form were developed for blood oxygenation quantification in tissue.[7] Significant investigations in both laboratory and clinical settings by use of NIRS were conducted for noninvasive, quantitative measurements and imaging of cerebral oxygenation[8–12] and blood oxygenation of exercised

H. Liu (hanli@uta.edu), Y. Song, L. Worden, and X. Jiang are with the Joint Graduate Program in Biomedical Engineering, University of Texas at Arlington, Arlington, Texas 76109. A. Constantinescu and R. P. Mason are with the Department of Radiology, University of Texas Southwestern Medical Center, Dallas, Texas 75390.

Received 16 March 2000; revised manuscript received 25 June 2000.

0003-6935/00/285231-13$15.00/0

© 2000 Optical Society of America

muscle[13–17] *in vivo*. Although NIR techniques were used extensively in conjunction with cryospectrophotometry to investigate tumor blood-vessel oxygenation in biopsies,[18] only a few reports[19–22] were published on using the NIR techniques for monitoring tumor oxygenation *in vivo*. In principle, the theoretical model, i.e., the diffusion approximation to the photon transport theory, works well for only large and homogeneous media.[23,24] Accurate quantification of tumor oxygenation by use of the NIR approach is limited because of the considerable heterogeneity and the finite sizes of tumors.

It is understood and documented[25] that the NIR technique used for blood oxygenation monitoring is sensitive to vascular absorption in the measured organ. The NIR method is not limited to measurements of blood oxygenation in arteries (c.f., pulse oximetry) or in veins but interrogates blood in the entire vascular compartment, including capillaries, arterioles, and venules, i.e., the vascular bed. A variety of terms like cerebral oxygenation, tissue hemoglobin oxygenation, and mean hemoglobin oxygenation are used in the literature[7,24,26] to indicate this concept. Although tissue hemoglobin oxygenation is not rigorous because hemoglobin molecules are located in only blood, the term is used specifically to differentiate between the hemoglobin saturation in the tissue vascular bed, as measured by the NIR method, and the arterial hemoglobin saturation $S_aO_2$, as measured by a pulse oximeter.

The goal of this paper is to demonstrate the NIR technique as a real-time, noninvasive means of monitoring hemoglobin oxygenation dynamics, i.e., changes in the concentrations of total hemoglobin ($Hb_t$) and oxygenated hemoglobin ($HbO_2$), in the vascular bed of breast and prostate rat tumors in response to respiratory challenge. Compared with previous NIR studies of tumors *in vivo*, our approach has the following features: (1) The transmission mode, as opposed to the reflectance mode used by Hull *et al.*,[22] interrogates deeper regions (central parts) of the tumor. (2) Only two wavelengths, as opposed to the spectrum of 300–1100 nm used by Steen *et al.*,[21] are employed and provide a fast and low-cost instrument. (3) A source–detector separation of 1–2 cm interrogates a large tumor noninvasively, as opposed to the needlelike probe used by Steinberg *et al.*[20] More innovatively, on the basis of the experimental observation of tumor hemoglobin oxygenation dynamics, we developed a tumor hemoperfusion model that provides important insight into tumor blood perfusion.

This paper is organized as follows: In Section 2, we describe our animal model, the NIR instrument, and the algorithm for calculations of tumor blood oxygenation. In Section 3, we show experimental results measured from both breast and prostate tumors under respiratory interventions and calculate time constants for the hemoglobin oxygenation dynamics of the tumors. In Section 4, we develop a tumor hemoperfusion model to interpret the experimental data obtained in the tumor-intervention studies and to relate the time constants to tumor blood perfusion. Finally, in Section 5, we discuss the results, the future extensions, and the potential uses of the NIR technique as a novel diagnostic–prognostic tool for tumor therapy and cancer research.

## 2. Materials and Methods

### A. Animal Model and Measurement Geometry

NF13762 breast tumor was implanted in adult female Fisher rats, and Dunning prostate adenocarcinoma R3327-AT1 was implanted in adult male Copenhagen rats. The tumors were grown in pedicles[27] on the forebacks of the rats until the tumors were approximately 1–2 cm in diameter. Rats were anesthetized with 200-μl ketamine hydrochloride (100 mg/ml) and maintained under general gaseous anesthesia with 33% inhaled $O_2$ (0.3 $dm^3$/min $O_2$, 0.6 $dm^3$/min $N_2O$, and 0.5% methoxyflurane) through a mask placed over the mouth and nose. Tumors were shaved to improve the optical contact for transmitting light. Body temperature was maintained with a warm-water blanket. In some cases, a fiber-optic pulse oximeter (Nonin, Inc., Model 8600V) that was manufacturer calibrated was placed on the hind foot to monitor arterial oxygenation $S_aO_2$, and a fiber-optic probe was inserted rectally to measure temperature. The tumor volume $V$ (in centimeters cubed) was estimated as $V = (4\pi/3)\,[(L + W + H)/6]^3$, where $L$, $W$, and $H$ are the three respective orthogonal dimensions.

Most measurements were performed with 33% oxygen as inhaled gas to achieve a stable baseline for a period of 5 to 15 min. The inhaled gas was then switched to carbogen (95% oxygen, 5% carbon dioxide) for at least 20 min and then switched back to 33% $O_2$ for approximately 15 min. The complete cycle lasted 1 hour. Sometimes repeated carbogen interventions were performed sequentially to evaluate the reproducibility of the time profiles of the tumors. In certain cases alternative gases were used, as defined in the results and figures, and some rats were sacrificed by KCl-induced cardiac arrest.

Figure 1 shows the measurement geometry: Horizontally, the delivering and the detecting fiber bundles were face to face in the transmittance mode, and both were in contact with the tumor surface without hard compression. The separation of the two bundle surfaces was between 1.0 and 2.5 cm, depending on the tumor size. Vertically, the two bundle tips (with diameters of 0.5 cm) were placed around the middle of the tumor. Thus the current setup of the probes provides an optimal geometry for the NIR light to interrogate deep tumor tissue with minimal interference from the foreback of the rat.

### B. Near-Infrared Instrument and Data Analysis

As shown in Fig. 1, we used a homodyne frequency-domain photon-migration system[28,29] that was capable of determining the amplitude and the phase changes of amplitude-modulated light passing through tumors. In this setup a rf source modulates

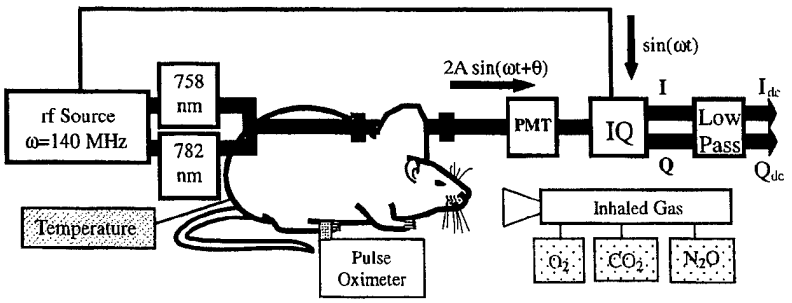


Fig. 1. Experimental setup of a one-channel, NIR, frequency-domain IQ instrument for tumor oxygenation measurement. PMT, photomultiplier tube for detecting light; IQ, in-phase and quadrature demodulator for retrieving amplitude and phase information; Low Pass, low-pass filter. The 5-mm-diameter fiber bundles deliver and detect the laser light through the tumor in transmittance geometry.

the light from two laser diodes (wavelengths of 758 and 782 nm) at 140 MHz. The laser light passes through a combined fiber-optic bundle, is transmitted through the tumor tissue, and is collected by a second fiber bundle. The light is then detected by a photomultiplier tube and demodulated with a commercially available in-phase and quadrature (IQ) demodulator chip into its $I$ and $Q$ components. After these components are put through a low-pass filter they can be used to calculate the amplitude and the phase changes caused by the tumor. These steps are expressed mathematically by

$$\begin{aligned} I(t) &= 2A\sin(\omega t + \theta)\sin(\omega t) \\ &= A\cos(\theta) - A\cos(\omega t + \theta) \xrightarrow[\text{pass}]{\text{low}} I_{dc} \\ &= A\cos(\theta), \end{aligned} \tag{1}$$

$$\begin{aligned} Q(t) &= 2A\sin(\omega t + \theta)\cos(\omega t) \\ &= A\sin(\theta) + A\sin(\omega t + \theta) \xrightarrow[pass]{\text{low}} Q_{dc} \\ &= A\sin(\theta), \end{aligned} \tag{2}$$

$$\theta = \tan^{-1}(Q_{dc}/I_{dc}), \tag{3}$$

$$A = (I_{dc}^2 + Q_{dc}^2)^{1/2}, \tag{4}$$

where $A$ and $\theta$ are the amplitude and the phase of the detected light, respectively, and $\omega$ is the angular modulation frequency ($=2\pi \times 140$ MHz).

The two laser lights were time shared, and the controlling process and the data acquisition both interfaced through a 12-bit analog-to-digital board (Real Time Devices, Inc., Model AD2100) with a maximum sampling rate of 4 Hz.[28] However, slower sampling rates were used in measurements to compensate for experimental noise. Simple time averaging among a few adjacent data points was performed during data analysis to further decrease the noise. However, data smoothing was not applied for (1) calculating the experimental uncertainty (error bars) or (2) fitting the time constants to prevent the fast-changing component from being oversmoothed and overlooked. The pulse-oximeter data were not averaged because they were recorded manually and appear discrete compared with the NIR data. The experimental uncertainties for arterial saturation and changes in hemoglobin concentrations were calculated by use of the baseline data taken over 5–10 min without respiratory perturbation to the rat. Nonlinear curve fitting based on the Marquardt algorithm[30,31] was performed by use of KaleidaGraph.[32] The software also provided the errors (or uncertainties) for each fitted parameter, the optimized $\chi^2$ values, and the fitting correlation coefficient $R$, together with the goodness of the fit $R^2$.[33] The significance of changes was assessed on the basis of Fisher protected-least-significant-difference analysis of variance by use of Statview software.

### C. Calculation for Changes in the Hemoglobin Concentration

It is well known that the NIRS of tissue can be used to determine the total hemoglobin concentration $Hb_t$ and the hemoglobin oxygen saturation $SO_2$ of an organ *in vivo*.[7] When two NIR wavelengths are used (758 and 782 nm, in this case) it is assumed that tissue background absorbance is negligible and that the major chromophores in organs are oxygenated and deoxygenated hemoglobin molecules. In principle, because the IQ system can give both phase and amplitude values, we should be able to obtain absolute calculations of $HbO_2$, Hb, and $SO_2$.[7,28] However, given the tumor's small size and large spatial heterogeneity, it is very difficult to obtain such absolute quantification accurately with conventional algorithms[34] that are based on the diffusion approximation. Instead, on the basis of the modified Beer–Lambert law, we can use the amplitude of the light transmitted through the tumor to calculate concentration changes in $HbO_2$, Hb, and $Hb_t$ (expressed as $\Delta HbO_2$, $\Delta Hb$, $\Delta Hb_t$, respectively) of the tumor that are caused by respiratory intervention. These changes can be derived[25] and expressed as (see Appendix A for derivations and justifications)

$$\begin{aligned} \Delta\text{Hb} &= \text{Hb(transient)} - \text{Hb(baseline)} \\ &= \frac{\epsilon_{HbO_2}^{\lambda_1}\log\left(\frac{A_b}{A_t}\right)^{\lambda_2} - \epsilon_{HbO_2}^{\lambda_2}\log\left(\frac{A_b}{A_t}\right)^{\lambda_1}}{L(\epsilon_{Hb}^{\lambda_2}\epsilon_{HbO_2}^{\lambda_1} - \epsilon_{Hb}^{\lambda_1}\epsilon_{HbO_2}^{\lambda_2})}, \end{aligned} \tag{5}$$

$$\Delta HbO_2 = HbO_2(\text{transient}) - HbO_2(\text{baseline})$$
$$= \frac{\epsilon_{Hb}^{\lambda_2} \log\left(\frac{A_b}{A_t}\right)^{\lambda_1} - \epsilon_{Hb}^{\lambda_1} \log\left(\frac{A_b}{A_t}\right)^{\lambda_2}}{L(\epsilon_{Hb}^{\lambda_2} \epsilon_{HbO_2}^{\lambda_1} - \epsilon_{Hb}^{\lambda_1} \epsilon_{HbO_2}^{\lambda_2})}, \quad (6)$$

where $\epsilon_{Hb}^{\lambda}$ and $\epsilon_{HbO_2}^{\lambda}$ are extinction coefficients[35] of deoxygenated and oxygenated hemoglobin, respectively, at wavelength $\lambda$; the variable $A_b$ is a constant amplitude of baseline; $A_t$ is the transient amplitude under measurement; and $L$ is the optical path length between the source and the detector.

Using the approach suggested by Cope and Delpy,[10] we can express $L$ as $L = \text{DPF} \times d$, where $d$ is the direct source–detector separation in centimeters and DPF is the ratio between the optical path length and the physical separation and is tissue dependent. The DPF for tumors has not been well studied; for simplicity, we assume the DPF to be 1 in our calculations. The justification for this simplification is given in Section 5. After substituting the extinction coefficients[35] at 758 and 782 nm in Eqs. (5) and (6) with values of $\epsilon_{Hb}^{758} = 0.359$, $\epsilon_{HbO_2}^{758} = 0.1496$, $\epsilon_{Hb}^{782} = 0.265$ and $\epsilon_{HbO_2}^{782} = 0.178$, respectively, in units of inverse millimoles times inverse centimeters, we arrive at

$$\Delta Hb = \frac{[7.34 \log(A_b/A_t)^{758} - 6.17 \log(A_b/A_t)^{782}]}{L}, \quad (7)$$

$$\Delta HbO_2 = \frac{[-10.92 \log(A_b/A_t)^{758} + 14.80 \log(A_b/A_t)^{782}]}{L}, \quad (8)$$

$$\Delta Hb_t = \Delta(HbO_2 + Hb) = \frac{[-3.58 \log(A_b/A_t)^{758} + 8.63 \log(A_b/A_t)^{782}]}{L}, \quad (9)$$

where the units are in millimoles. Equations (7) and (8) permit the calculation of changes in Hb and $HbO_2$ that are due to respiratory challenge, respectively, whereas Eq. (9) quantifies a relative increase in the total hemoglobin concentration that is caused by the intervention. The last quantity also reflects a change in blood volume because it is proportional to the total Hb concentration.

## 3. Results

### A. Instrument Drift Tests

The stability of the NIR instrument was tested in terms of baseline drift after a warm-up period of 30 min by use of a tissue phantom[25,36] with stable optical properties. Figure 2 shows an example of a phantom measurement that displays the variation of relative changes in apparent $HbO_2$ and $Hb_t$ concentrations, as calculated from Eqs. (8) and (9). In this example, the standard deviations over the entire period of 100 min were less than 0.007 and 0.004 mM, respectively, for $\Delta HbO_2$ and $\Delta Hb_t$. Furthermore, we calculated uncertainties for both of these quantities on the basis of the propagation of errors, and the results are consistent with those shown in Fig. 2.

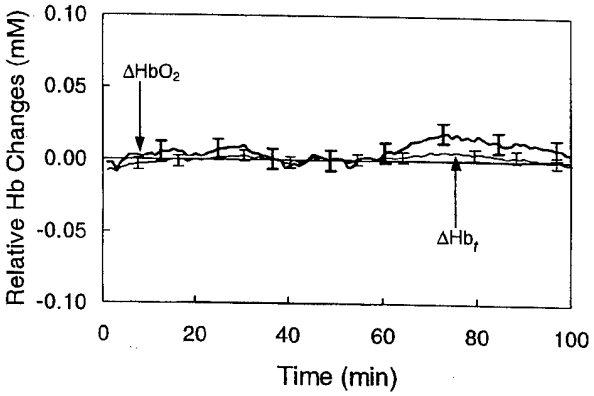


Fig. 2. Results of a drift test of the NIR instrument by use of a tissue phantom. The thicker solid curve represents relative changes in the oxygenated hemoglobin concentration, i.e., $\Delta HbO_2$, and the thinner solid curve represents relative changes in the total hemoglobin concentration, i.e., $\Delta Hb_t$. $\Delta HbO_2$ and $\Delta Hb_t$ were calculated by use of Eqs. (8) and (9), respectively.

### B. Breast Tumors

Figure 3(a) shows the results taken from a breast tumor (4.5 $cm^3$) with a source–detector separation of 1.8 cm. The data were smoothed, and the measurement uncertainties are shown at only discrete locations. The figure shows the relative changes in total hemoglobin concentration $\Delta Hb_t$ and oxygenated hemoglobin concentration $\Delta HbO_2$. The arterial Hb saturation was also obtained to show a relatively rapid change in arterial signals when the inhaled gas was switched from 33% $O_2$ to carbogen. Respiratory challenge caused a sharp rise in $\Delta HbO_2$ ($p < 0.01$ after 1 min, $p < 0.0001$ by 1.5 min) that was followed by a further slow, gradual, but significant, increase over the next 25 min ($p < 0.001$). $\Delta Hb_t$ also changed significantly ($p < 0.001$) within the first minute, but the total change was only approximately 10% of that of $\Delta HbO_2$. Given the exponential appearance of the rising part of $\Delta HbO_2$, we used single-exponential and double-exponential expressions to fit the data in the rising portion to better understand and quantify the dynamic features of $\Delta HbO_2$. The unsmoothed data and the fitted curves are shown in Figure 3(b). The double exponential appears to give a much better fit, as is confirmed by the respective $R$ values (0.98 versus 0.81). Time constants of 0.18 ± 0.02 min and 27.8 ± 3.9 min were obtained for fast and slow dynamic changes, respectively, in the tumor $HbO_2$ concentration.

Figure 4(a) was obtained from a second breast tumor (5.9 $cm^3$) with a source–detector separation of 1.6 cm. Here $\Delta HbO_2$ increased rapidly after the ini-

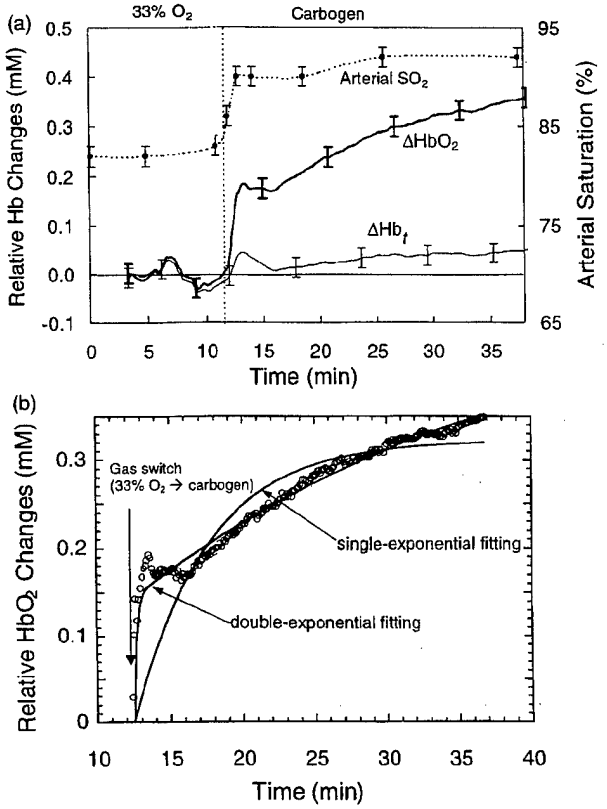


Fig. 3. (a) Results obtained with the NIR instrument from a 4.5-$cm^3$ rat breast tumor while the breathing gas was switched from 33% $O_2$ to carbogen. The thicker solid curve represents $\Delta HbO_2$, the thinner solid curve represents $\Delta Hb_t$, and the dashed curve with the filled circles represents arterial saturation. (b) The unsmoothed data and the fitted curves: The solid curves represent the best fits to the $\Delta HbO_2$ data at the rising portion. The best fit to the two exponential terms is $0.143\{1 - \exp[-(t - 12.5)/0.18]\} + 0.36\{1 - \exp[-(t - 12.5)/27.8]\}$, with $R = 0.98$, whereas the best fit with one exponential term is expressed as $0.322\{1 - \exp[-(t - 12.5)/5.1]\}$, with $R = 0.81$.

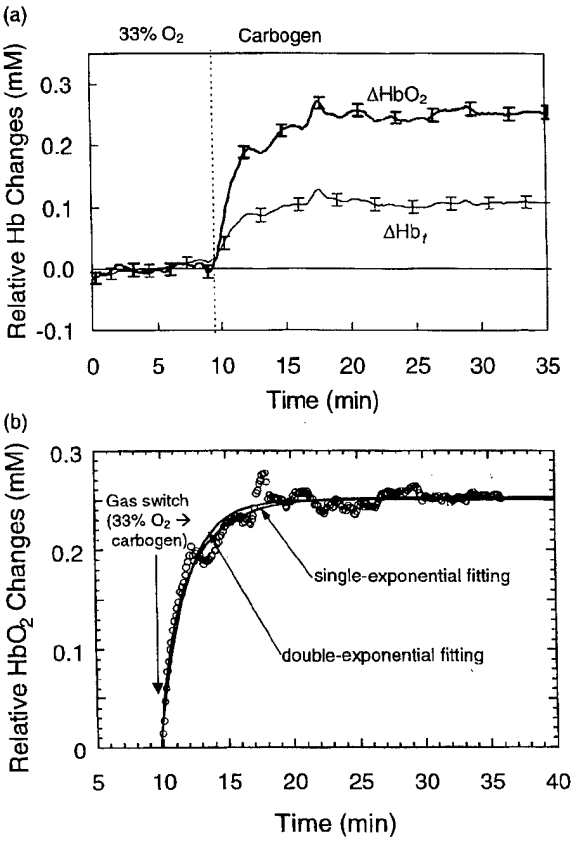


Fig. 4. (a) Results obtained with the NIR instrument from a 5.9-$cm^3$ rat breast tumor while the breathing gas was switched from 33% $O_2$ to carbogen. (b) The solid curves show the best fits to the $HbO_2$ data at the rising portion. In this case a double exponential with values of $0.09\{1 - \exp[-(t - 9.8)/0.8]\} + 0.16\{1 - \exp[-(t - 9.8)/3.0]\}$, with $R = 0.98$, and a single exponential with a value of $0.250\{1 - \exp[-(t - 9.8)/2.00]\}$, with $R = 0.97$, provided similarly good fits.

tial gas switch but did not exhibit the continued slow rise afterward. $\Delta Hb_t$ was found to increase with carbogen inhalation, although the magnitude was smaller than that of $\Delta HbO_2$ during the period of the intervention. Again, changes in $\Delta HbO_2$ were modeled by a single-exponential term that yielded a time constant of 2.00 ± 0.04 min ($R = 0.97$) and by a double-exponential formula with two time constants of 0.8 ± 0.2 min and 3.0 ± 0.3 min ($R = 0.98$). In this case both expressions fit the data well, as shown in Fig. 4(b).

To demonstrate the reproducibility of the dynamic changes in response to respiratory challenge, we subjected one animal to repeat carbogen inhalation. Figure 5(a) shows measurements taken from a breast tumor (6.7 $cm^3$) with a source–detector separation of 2 cm. In this case air with 1.2% isoflurane (anesthetic) was used as the baseline instead of 33% $O_2$. This figure shows a very consistent pattern in two repeated time responses with a fast and a slow increase in $\Delta HbO_2$. Here $\Delta Hb_t$ shows a similar dynamic pattern, i.e., a rapid rise followed by a slow continuation. Figures 5(b) and 5(c) show the unsmoothed data together with the fitted curves for the rising portions of the two repeated increases in $\Delta HbO_2$. Again, the double-exponential expression with two time constants produced much better fits than did the single-exponential term in both processes with two averaged time constants of $\tau_1$ (mean) = 0.26 ± 0.11 min and $\tau_2$ (mean) = 8.2 ± 1.8 min. Individual, respective time constants and coefficients are summarized in Table 1. Furthermore, single-exponential and double-exponential expressions were fitted to obtain time constants for the decay processes after the inhaled gas was switched repeatedly back to the baseline conditions. Similarly, the double-exponential expression fits the data better with two mean time constants of $\tau_1^{decay}$ (mean) = 0.17 ± 0.07 min and $\tau_2^{decay}$ (mean) = 12.2 ± 0.7 min for the two decay processes.

To further validate our experimental observations, we subjected some rats to cardiac arrest (with KCl) to observe the changes in $HbO_2$ and $Hb_t$ on death. Figure 6 shows an example of cardiac arrest on a rat with

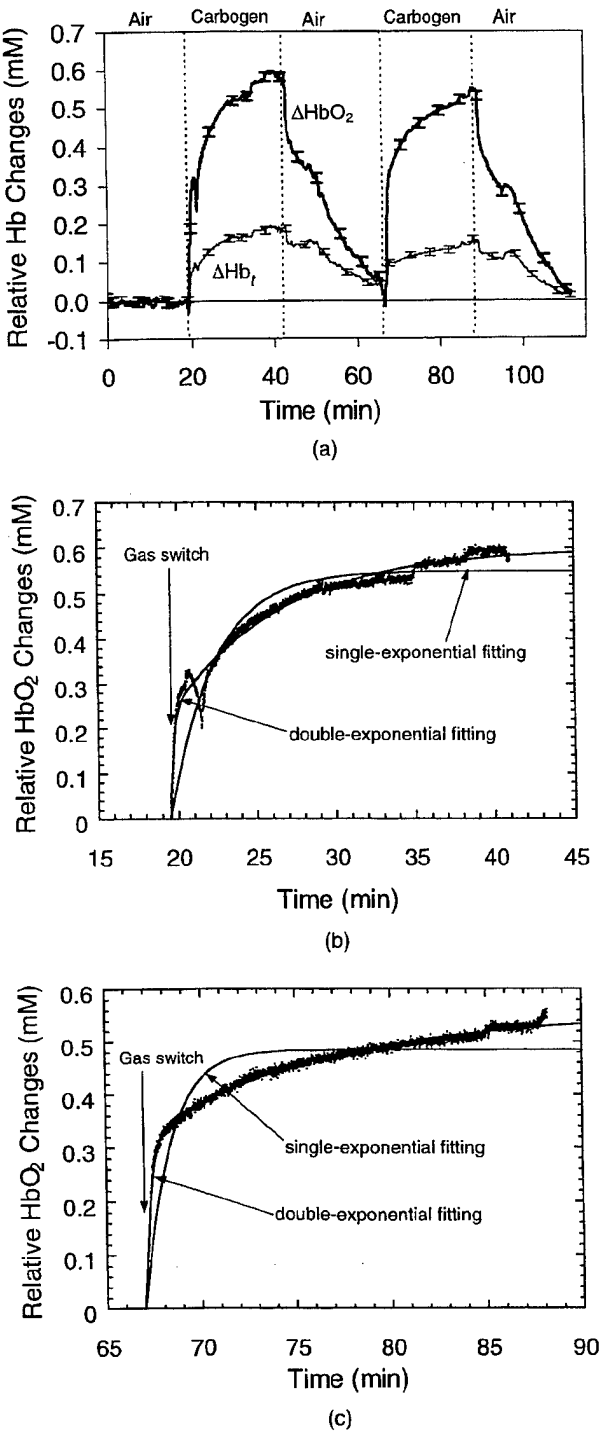


Fig. 5. (a) Relative changes in the $HbO_2$ detected with the NIR instrument from a rat breast tumor (6.7 $cm^3$) while the breathing gas was alternated between air (21% $O_2$) and carbogen. The best fits to the $HbO_2$ data by use of both the double-exponential and the single-exponential expressions for (b) the first and (c) the second respiratory challenges are shown. The fitted equations that were obtained from (b) are $0.232\{1 - \exp[-(t - 19.5)/0.18]\} + 0.368\{1 - \exp[-(t - 19.5)/6.93]\}$, with $R = 0.98$, and $0.550\{1 - \exp[-(t - 19.5)/2.80]\}$, with $R = 0.89$, respectively. The fitted equations that were obtained from (c) were $0.321\{1 - \exp[-(t - 67)/0.332]\} + 0.233\{1 - \exp[-(t - 67)/9.47]\}$, with $R = 0.99$, and $0.485\{1 - \exp[-(t - 67)/1.38]\}$, with $R = 0.81$, respectively.

Table 1. Summary of the Vascular Oxygen Dynamics

| Tumor | | | Double-Exponential Fitting $\Delta HbO_2 = A_1[1 - \exp(-t/\tau_2)] + A_2[1 - \exp(-t/\tau_2)]$ | | | | | | | | Single-Exponential Fitting $\Delta HbO_2 = A_1[1 - \exp(-t/\tau)]$ | | |
|---|---|---|---|---|---|---|---|---|---|---|---|---|---|
| Type | Volume ($cm^3$) | $\tau_1$ (min) | $\tau_2$ (min) | $A_1$ (mM) | $A_2$ (mM) | $R^2$ | $\tau_1/\tau_2$ | $\frac{\gamma_1}{\gamma_2} = \frac{A_1}{A_2}$ | $\frac{f_1}{f_2} = \frac{A_1/A_2}{\tau_1/\tau_2}$ | $\tau$ (min) | $A$ (mM) | $R^2$ |
| Breast (Fig. 3) | 1.5 | 1.8 ± 0.02 | 27.8 ± 3.9 | 0.143 ± 0.003 | 0.36 ± 0.03 | 0.96 | 0.006 ± 0.001 | 0.40 ± 0.03 | 61.35 ± 0.01 | 5.1 ± 0.3 | 0.322 ± 0.005 | 0.66 |
| Breast (Fig. 4) | 5.9 | 0.8 ± 0.2 | 3.0 ± 0.3 | 0.09 ± 0.02 | 0.16 ± 0.02 | 0.96 | 0.27 ± 0.07 | 0.56 ± 0.14 | 2.11 ± 0.18 | 2.00 ± 0.04 | 0.250 ± 0.001 | 0.94 |
| Breast (Fig. 5) | 6.7 | 0.18 ± 0.01 | 6.93 ± 0.09 | 0.232 ± 0.002 | 0.368 ± 0.002 | 0.97 | 0.026 ± 0.001 | 0.63 ± 0.01 | 24.27 ± 0.01 | 2.80 ± 0.03 | 0.550 ± 0.001 | 0.80 |
| | 6.7 | 0.332 ± 0.003 | 9.47 ± 0.12 | 0.321 ± 0.001 | 0.233 ± 0.001 | 0.99 | 0.035 ± 0.001 | 1.38 ± 0.01 | 39.30 ± 0.01 | 1.38 ± 0.02 | 0.485 ± 0.001 | 0.66 |
| Prostate (Fig. 7) | 8.2 | 0.265 ± 0.007 | 6.02 ± 0.15 | 0.090 ± 0.001 | 0.064 ± 0.001 | 0.93 | 0.044 ± 0.001 | 1.41 ± 0.03 | 31.95 ± 0.01 | 1.13 ± 0.02 | 0.140 ± 0.001 | 0.67 |
| Prostate (Fig. 8) | 10.8 | 0.3 ± 4.5 | 15.6 ± 3.1 | 0.004 ± 0.01 | 0.38 ± 0.03 | 0.94 | 0.02 ± 0.20 | 0.01 ± 0.03 | 0.6 ± 1.2 | 14.8 ± 1.6 | 0.37 ± 0.02 | 0.94 |

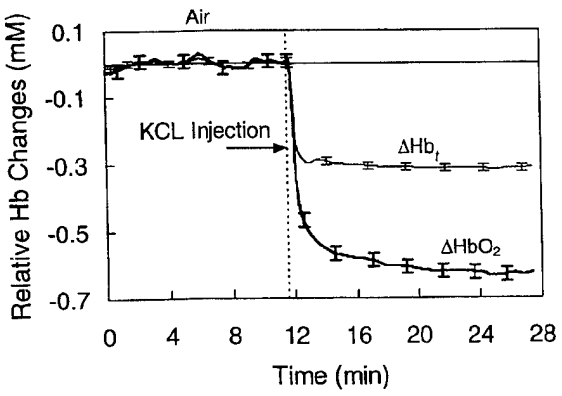


Fig. 6. Influence of KCl-induced cardiac arrest on the values of $HbO_2$ and $Hb_t$ of a breast tumor (5.3 $cm^3$), while the rat was breathing air.

a breast tumor (5.3 $cm^3$). Both $\Delta Hb_t$ and $\Delta HbO_2$ dropped significantly, immediately after KCL was admitted intravenously. Within 1 min $\Delta Hb_t$ reached a plateau, whereas $\Delta HbO_2$ decreased rapidly within the first 30 s and then was followed by a slow prolongation.

### C. Prostate Tumors

Figure 7(a) was obtained from a large prostate tumor (8.2 $cm^3$). In common with the breast tumors, $\Delta HbO_2$ showed a rapid initial increase that was followed by a slower continuation. $\Delta Hb_t$ increased rapidly and then reached a plateau. Figure 7(b) shows that the double-exponential equation fits the unsmoothed data better ($R = 0.96$) than does the single-exponential term ($R = 0.82$). Here the fast and the slow time constants are $0.265 \pm 0.007$ min and $6.02 \pm 0.15$ min, respectively.

Figure 8(a) was obtained from another large prostate tumor (10.8 $cm^3$ with a source–detector separation of 2.5 cm). Here $\Delta HbO_2$ displayed a gradual increase throughout the entire period of carbogen inhalation, whereas the increase in $\Delta Hb_t$ was considerably delayed. Variations in arterial hemoglobin saturation $S_aO_2$ are also shown and were very rapid in comparison with $\Delta HbO_2$, in common with Fig. 3. $\Delta HbO_2$ dropped rapidly when the inhaled gas was switched back from carbogen to 33% $O_2$. Both the single-exponential and the double-exponential expressions were used to obtain time constants for the rising portion of $\Delta HbO_2$ that was due to carbogen intervention. In this case both expressions gave equally good fits, as shown in Fig. 8(b) and Table 1. For the decay process, we obtained $\tau_1^{decay} = 0.6 \pm 0.2$ min and $\tau_2^{decay} = 6.6 \pm 1.7$ min with $R = 0.94$ for the double-exponential fitting, whereas the single-exponential fitting resulted in $\tau = 2.8 \pm 0.4$ min with $R = 0.88$. For comparison the rat was also challenged with 100% $O_2$.

In summary, we observed dynamic changes in $HbO_2$ that were due to carbogen intervention for both breast and prostate tumors. In most cases these changes were modeled better by a double-exponential

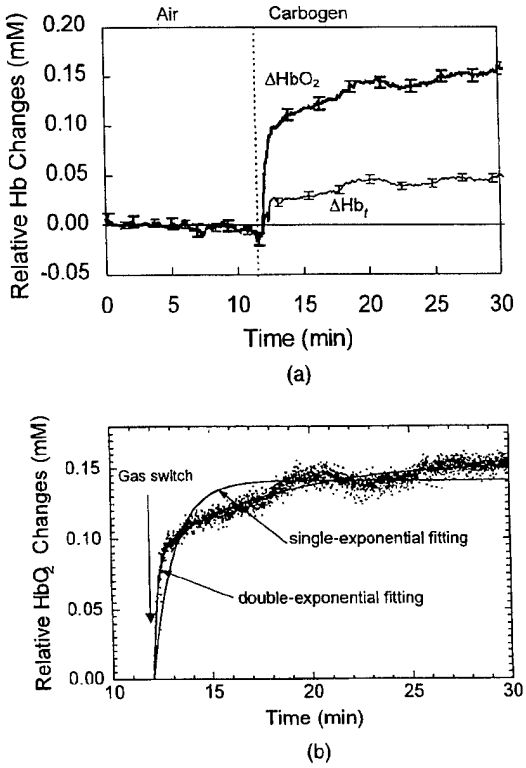


Fig. 7. (a) Influence of respiratory challenges (switching from air to carbogen) on the values of $HbO_2$ and $Hb_t$ of a large rat prostate tumor (8.2 $cm^3$). (b) The best-fitted equations are $0.090\{1 - \exp[-(t - 12)/0.265]\} + 0.064\{1 - \exp[-(t - 12)/6.02]\}$, with $R = 0.96$, and $0.140\{1 - \exp[-(t - 12)/1.13]\}$, with $R = 0.82$, for the double-exponential and the single-exponential expressions, respectively.

expression with a fast and a slow time constant than they were by a single-exponential fitting. Dynamic changes in arterial saturation preceded those in $HbO_2$. The detailed parameters regarding tumor size, fitted time constants, corresponding magnitudes, and $R^2$ are listed in Table 1.

## 4. Model for the Blood Oxygenation Dynamics of Tumors

As was shown in Section 3, the temporal changes in $HbO_2$ caused by respiratory challenge can be fitted with an exponential equation that has either one or two time constants (fast and slow). In this section, we further derive and simplify a hemoperfusion model to interpret these time constants and to correlate the experimental findings with the physiology of the tumors.

To develop the model, we follow an approach used to measure regional cerebral blood flow (rCBF) with diffusible radiotracers, as originally developed by Kety[37] in the 1950's. The basic model was modified in a variety of ways to adapt it to positron emission tomography studies.[38,39] By analogy, we can evaluate tumor hemodynamics such as tumor blood flow (perfusion) by using the respiratory-intervention gas as a tracer.

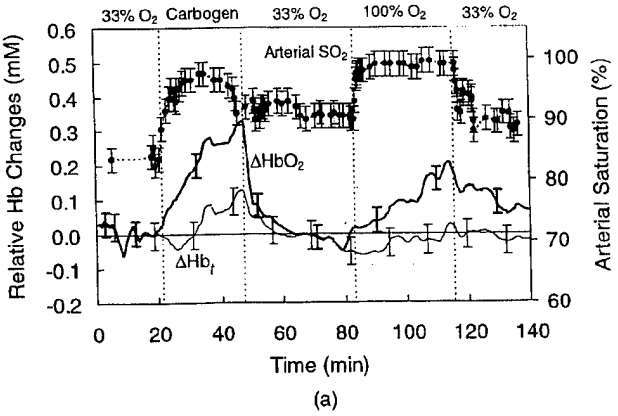


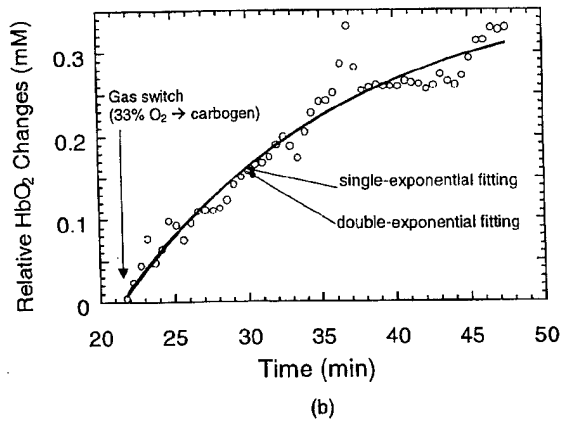


Fig. 8. (a) Variations in $S_aO_2$, $\Delta HbO_2$, and $Hb_t$ of which the latter two were detected with the NIR instrument, from a large rat prostate tumor (10.8 $cm^3$) during respiratory challenge. (b) The solid curves represent the best fits to the $\Delta HbO_2$ data at the rising portion during carbogen inhalation. The fitted equations are $0.004\{1 - \exp[-(t - 21.5)/0.3]\} + 0.38\{1 - \exp[-(t - 21.5)/15.6]\}$ and $0.37\{1 - \exp[-(t - 21.5)/14.8]\}$ for the double-exponential and the single-exponential expressions, respectively, with $R = 0.97$ for both.

In general, the Fick principle can be stated as follows[38]: The rate of change of tracer concentration in a regional area of an organ equals the rate at which the tracer is transported to the organ in the arterial circulation minus the rate at which it is carried away into the venous drainage, i.e.,

$$\frac{dC_t}{dt} = f(C_a - C_v), \tag{10a}$$

where $f$ is the blood flow (or perfusion rate), $C_t$ is the tracer concentration in tissue, and $C_a$ and $C_v$ are the time-varying tracer concentrations in the arterial input and the venous drainage, respectively. $C_a$ can be measured from a peripheral artery, but $C_v$ is relatively difficult to obtain regionally. Therefore a brain–blood partition coefficient, $\lambda = C_t/C_v$, was developed by Kety, and Eq. (10a) becomes[37]

$$\frac{dC_t}{dt} = f\left(C_a - \frac{C_t}{\lambda}\right). \tag{10b}$$

In Eq. (10b), $f$ and $\lambda$ are constants, whereas $C_t$ is a time-dependent variable that is written as $C_t(t)$. In principle, the arterial-tracer concentration $C_a$ is a time-varying quantity. If a certain concentration of the arterial tracer is administrated continuously starting at time 0, $C_a$ can be expressed mathematically as a constant value of $C_a(0)$ after time 0. Then Eq. (10b) can be solved as

$$C_t(t) = \lambda C_a(0)[1 - \exp(-ft/\lambda)]. \tag{11}$$

Equation (11) indicates that, at time $t$ after the onset of tracer administration, the local tissue (traditionally brain) $C_t(t)$ concentration depends on the blood flow $f$, the arterial time–activity curve $C_a(0)$, and the partition coefficient $\lambda$.

In response to respiratory intervention, a sudden small change is introduced into the arterial $O_2$ saturation $S_aO_2$, and the resulting increase in arterial $HbO_2$ concentration ($\Delta HbO_2^{artery}$) can be considered as an intravascular tracer.[40] Following Kety's method and assuming that changes in dissolved $O_2$ are negligible,[40] we have

$$\frac{d}{dt}(\Delta HbO_2^{vasculature}) = f\left(\Delta HbO_2^{artery} - \frac{\Delta HbO_2^{vasculature}}{\gamma}\right). \tag{12}$$

where $f$ still represents blood flow (or perfusion rate) and $\gamma$ is defined as a vasculature coefficient of the tumor. The coefficient $\gamma$ is the ratio of the $HbO_2$ concentration change in the vascular bed to that in veins and equals $(\Delta HbO_2^{vasculature})/(\Delta HbO_2^{vein})$. This definition implies that a change in the venous blood oxygenation $\Delta HbO_2^{vein}$ is proportional to a change in the Hb oxygenation in the vascular bed, $\Delta HbO_2^{vasculature}$.

In Eq. (12), $f$ and $\gamma$ are constants, whereas $\Delta HbO_2^{vasculature}$ is a time-dependent variable. By analogy to Eq. (11), $\Delta HbO_2^{vasculature}$ can be solved rigorously given a constant input $H_0$ for $\Delta HbO_2^{artery}$ after time 0. Our data (Figs. 3 and 8) demonstrate that changes in the arterial $HbO_2$ ($S_aO_2$) are much faster than in the vascular bed. Then solving Eq. (12) leads to

$$\Delta HbO_2^{vasculature}(t) = \gamma H_0[1 - \exp(-ft/\gamma)]. \tag{13}$$

Equation (13) indicates that, at time $t$ after the onset of respiratory intervention, the change in oxygenated hemoglobin concentration in the tumor vasculature $\Delta HbO_2^{vasculature}(t)$ depends on the blood perfusion rate $f$, the arterial oxygenation input $H_0$, and the vasculature coefficient of the tumor $\gamma$.

As indicated by Eq. (8), our NIR instrument is able to measure an increase in the vascular $HbO_2$ concentration $\Delta HbO_2^{vasculature}$. Equation (13) gives an exponential of the same form as that used to fit our experimental data, indicating that the measured

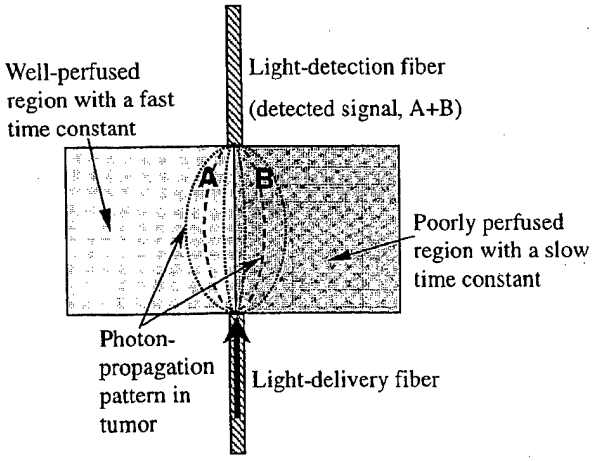


Fig. 9. Schematic diagram showing (1) a tumor model with two vascular perfusion regions, (2) the source and the detector fibers and their geometry with respect to the tumor model, and (3) the light patterns that propagate in the tumor tissue. *A* represents a portion of the detected signal, which interrogates the well-perfused region, and *B* represents another portion of the detected signal, which passes mainly through the poorly perfused region. We have assumed that the total detected signal is the sum of *A* and *B*.

time constant is associated with the blood perfusion rate $f$ and the vasculature coefficient $\gamma$ of the tumor in the measured area. If the measured volume involves two distinct regions, we then involve with two different blood-perfusion rates $f_1$ and $f_2$, two different vasculature coefficients $\gamma_1$ and $\gamma_2$, or all four. Here it is reasonable to assume that the measured signal results from both regions, as illustrated in Fig. 9. Consequently, Eq. (13) can be modified with a double-exponential expression and two time constants as

$$\begin{aligned}\Delta HbO_2{}^{vasculature}(t) &= \gamma_1 H_0[1 - \exp(-f_1 t/\gamma_1)] \\ &\quad + \gamma_2 H_0[1 - \exp(-f_2 t/\gamma_2)] \\ &= A_1[1 - \exp(-f_1 t/\gamma_1)] \\ &\quad + A_2[1 - \exp(-f_1 t/\gamma_2)], \quad (14)\end{aligned}$$

where $f_1$ and $\gamma_1$ are the blood-perfusion rate and the vasculature coefficient, respectively, in region 1, $f_2$ and $\gamma_2$ are the same for region 2, $A_1 = \gamma_1 H_0$, and $A_2 = \gamma_2 H_0$. The two time constants are equal to $\tau_1 = \gamma_1/f_1$ and $\tau_1 = \gamma_2/f_2$. Then, if $A_1$, $A_2$, and the two time constants are determined from our measurements, we arrive at the ratios for the two vasculature coefficients and the two blood-perfusion rates:

$$\frac{\gamma_1}{\gamma_2} = \frac{A_1}{A_2}, \qquad \frac{f_1}{f_2} = \frac{A_1/A_2}{\tau_1/\tau_2}. \quad (15)$$

With these two ratios, we can obtain insight into the tumor vasculature and blood perfusion. For example, a ratio of $\gamma_1/\gamma_2$ near 1 from a measurement implies that the vascular structure of the measured tumor volume is rather uniform. Then the coexistence of two time constants reveals two mechanisms of regional blood perfusion in the tumor. A large time constant implies slow perfusion through a poorly perfused area, whereas a small time constant indicates fast perfusion through a well-perfused area. In the meantime, the ratio of the perfusion rates in these two areas can also be obtained quantitatively. Furthermore, a ratio of $\gamma_1/\gamma_2 > 1$ (i.e., $A_1/A_2 > 1$) means that the measured signal results more from region 1 than from region 2 within the measured tumor volume. Therefore, by studying tumor blood oxygenation dynamics and obtaining time constants together with their amplitudes, we can gain important information on regional blood perfusion and vascular structures of the tumor within the measured volume.

Our experimental data (Table 1) reveal that all the measurements can be fitted with the double-exponential model equivalently to or better than the single-exponential fitting. Ratios of $\tau_1/\tau_2$, $\gamma_1/\gamma_2$, and $f_1/f_2$ are also shown in Table 1 for respective cases.

## 5. Discussion

Using NIRS, we have measured relative changes in $Hb_t$ and $HbO_2$ in breast and prostate rat tumors in response to respiratory intervention. We have observed that respiratory challenge caused the $HbO_2$ concentration to rise promptly and significantly in both breast and prostate tumors but that the total concentration of hemoglobin sometimes increased and sometimes remained unchanged. The dynamic changes of tumor oxygenation can be modeled by either one exponential term with a slow time constant or two exponential terms with fast and slow time constants. This relation suggests that there may be two vascular mechanisms in the tumor that are detected by the NIRS measurement. As indicated by Eqs. (13) and (14), these time constants are inversely proportional to the blood-perfusion rates of the measured volumes of the tumors. Based on the double-exponential model, determination of the two time constants and their corresponding amplitudes allows us to determine the relations between the two perfusion rates and between the vascular structures, as expressed in Eq. (15). Further investigation with more measured quantities may lead to quantification of each parameter individually by use of the NIR technique.

To develop a model for interpreting the NIR data taken during carbogen inhalation, we have defined a vasculature coefficient $\gamma$. It is a proportionality factor between $\Delta HbO_2{}^{vein}$ and $\Delta HbO_2{}^{vasculature}$, i.e., $\Delta HbO_2{}^{vein} = \Delta HbO_2{}^{vasculature}/\gamma$. We expect that $\gamma$ depends on (1) the oxygen consumption and (2) the capillary density of the tumor. If the oxygen consumption, the capillary density, or both of the tumor are large, changes in the venous $HbO_2$ concentration will be small; if the oxygen consumption, the capillary density, or both of the tumor are small, changes in the venous $HbO_2$ concentration will be large. Further studies are necessary to learn more about this coefficient and to confirm our speculation.

Our current NIR system allows us to quantify the

ratio of $\gamma/f$ by using the single-exponential model or to quantify the ratios of $\gamma_1/\gamma_2$ and $f_1/f_2$ by using the double-exponential model. We can obtain important information on the blood perfusion of the tumor: a large time constant usually represents slow blood perfusion, whereas a small time constant indicates fast blood perfusion. The coexistence of two time constants implies a combination of well-perfused and poorly perfused mechanisms of blood perfusion. Indeed, some tumor lines have only 20% to 85% of vessels perfused.[41] Furthermore, tumor structures and oxygen distribution[6,42] are highly heterogeneous. Therefore it is likely that our measurement detects a well-perfused region, or a poorly perfused region, or a mixture of both in the tumor, depending on the position or the location of the source and the detector of the NIR instrument.

Hull *et al.*[22] reported carbogen-induced changes in rat mammary tumor oxygenation by using spatially resolved NIRS. To compare our results to theirs, we applied our curve-fitting procedure to their published hemoglobin saturation curve and obtained a time constant of 0.27 min (or 16 s) for the rising edge, which is consistent with our fast component. Their data do not show a slow component, suggesting that their measurement was dominated by active tumor vasculature. This difference may be explained as follows:

(1) The tumor volume mentioned in the paper by Hull *et al.*[22] was approximately 1.5 $cm^3$, much smaller than the volumes of the tumors that we measured (in Figs. 3 to 8, the largest tumor was 10.8 $cm^3$, whereas the smallest tumor was 4.5 $cm^3$).

(2) Their measurement was in reflectance geometry with multiple detectors located at distances 1 to 20 mm away from the source, and in the calculation the tumor was assumed to be homogenous in order to use diffusion theory. Thus their measurement was more sensitive to the superficial area of the tumor, emphasizing the tumor periphery, which is often better vascularized than the central part of the tumor.[42,43]

The fast component observed in our tumors is consistent with the rapid changes detected in $S_aO_2$ in the leg as measured by use of the pulse oximeter, providing further evidence that this relates to the well-vascularized, highly perfused region of the tumor.

The data shown in Fig. 8 in this paper are representative of the measurement of a poorly perfused region in which the measured tumor was large and the portion for the fast oxygenation response was small. The data given in Figs. 3–5 and 7 resulted from a mixture of well-perfused and poorly perfused areas in the tumors and exhibited a mixture of fast and slow oxygenation responses to hyperoxygen conditions. It is reasonable to expect that larger tumors have more poorly perfused regions than do smaller tumors. The time constant of the slow component observed here approaches that observed previously for changes in tissue $pO_2$ in an AT1 prostate tumor measured by use of $^{19}F$ nuclear magnetic resonance spectroscopy to interrogate interstitial oxygenation.[44] In general, well-oxygenated tumor regions had a large and rapid response to respiratory challenge, whereas poorly oxygenated regions were much more sluggish.[45] One would indeed expect changes in vascular oxygenation to precede changes in the tissue, and combined investigations by NIRS and nuclear magnetic resonance spectroscopy in the future will provide further insight into the delivery of oxygen to tumors.

Dynamic changes in vascular oxygenation have been assessed previously by several other techniques. Following the infusion of Green 2W dye intravenously into EMT-6 tumor-bearing mice, Vinogradov *et al.*[4] were able to image changes in the surface vascular $pO_2$. On switching from air to carbogen inhalation, they observed a very rapid increase in $pO_2$ with a rate similar to the fast component, which we have seen here. Although the phosphorescence method provides vascular $pO_2$, NIR methods generally provide $HbO_2$ or $SO_2$ because there is some uncertainty in the local affinity of hemoglobin for tumor oxygen: the $pO_2$–$SO_2$ dissociation curve is subject to pH, temperature, and other allosteric effectors, such as 2,3-diphosphoglycerate in the immediate milieu. A promising new approach is the blood-oxygen-level–dependent (BOLD) contrast $^1H$ MRI, which is sensitive to vascular perturbations. Robinson *et al.*[46] explored the response to respiratory challenge in various tumors and showed reversible regional changes on switching from air to carbogen inhalation. In common with our NIR data, their changes were often biphasic with a large change occurring within the first 2 min and followed by slower increases.[46] However, interpreting the BOLD MRI results is complicated by variations in vascular volume and flow, and there is no direct measure of $HbO_2$ in tumors.

The time constants are not source–detector separation sensitive. Equations (8) and (9) have demonstrated that $\Delta HbO_2$ and $\Delta Hb_t$ are proportional to $1/d$, where $d$ is the source–detector separation. This relation indicates that a different $d$ value will only stretch or compress the entire temporal profile of $\Delta HbO_2$, but it does not change the transient behavior of the time response. The same argument can apply to the DPF. In this study, we have assumed a DPF ratio of 1 for simplicity. If the DPF value is larger than 1, the values of $\Delta HbO_2$ and $\Delta Hb_t$ will decrease by a factor of DPF. But this modification does not affect the time constants $\tau_1$ and $\tau_2$, which constitute the dynamic responses of $\Delta HbO_2$ of the tumors to respiratory intervention.

Given the evidence for intratumoral heterogeneity from MRI[6,46] and histology,[47] we believe it will be important to advance our NIR system to have multiple sources, multiple detectors, or both to study not only dynamic but also spatial aspects of blood oxygenation in tumor vasculature. Nonetheless, we believe the preliminary results described here are a proof of principle for the technique, laying a foundation for more extensive tests to correlate tumor size

with the rates of change of $HbO_2$ and $Hb_t$ with respect to respiratory challenge. Although Hull *et al.*[22] and we have focused on respiratory challenge, we note that previous NIR studies of tumors also examined the influence of chemotherapy,[21] pentobarbital overdose,[21] ischemic clamping,[20] and infusion of perfluorocarbon blood substitute.[19] These studies demonstrate the potential versatility of the NIR approach and its application for diverse future studies.

In summary, we have demonstrated that the NIR technology can provide an efficient, real-time, noninvasive means for monitoring vascular oxygenation dynamics in tumors during hyperoxygen respiratory challenge. $HbO_2$ concentrations measured from both breast and prostate tumors often exhibit a prompt rise that is followed by a gradual persistence throughout the intervention. By developing a hemoperfusion model with two exponential terms and fitting the model to the increased $HbO_2$ data, we are able to recognize two mechanisms for blood perfusion in the tumor and to quantify the ratios of the two perfusion rates and those of the two vasculature coefficients. Thus the technique can enhance our understanding of the dynamics of tumor oxygenation and the mechanisms of tumor physiology under baseline and perturbed conditions. Moreover, it appears that the NIRS may have a great potential for monitoring tumor angiogenesis because the method can provide information on blood perfusion and oxygen consumption of the measured tumor.

## Appendix A

### A. Derivation

It has been shown that, in the NIR range, the major light absorbers in tissue are oxygenated and deoxygenated hemoglobin molecules.[24,25] With this knowledge, the absorption coefficients (in inverse centimeters) at two wavelengths can be associated with the concentrations of $HbO_2$ and Hb by

$$\mu a^{\lambda 1} = \epsilon_{\mathrm{Hb}}^{\lambda 1}\mathrm{Hb} + \epsilon_{\mathrm{HbO_2}}^{\lambda 1}\mathrm{HbO_2}, \tag{A1}$$

$$\mu a^{\lambda 2} = \epsilon_{\mathrm{Hb}}^{\lambda 2}\mathrm{Hb} + \epsilon_{\mathrm{HbO_2}}^{\lambda 2}\mathrm{HbO_2}, \tag{A2}$$

where $\epsilon_{\mathrm{Hb}}^{\lambda}$ and $\epsilon_{\mathrm{HbO_2}}^{\lambda}$ are the extinction coefficients (in inverse centimeters times inverse millimoles) of deoxygenated and oxygenated hemoglobin, respectively, at wavelength $\lambda$, and $HbO_2$ and Hb are the oxyhemoglobin and the deoxyhemoglobin concentrations. Because $\epsilon_{\mathrm{Hb}}^{\lambda}$ and $\epsilon_{\mathrm{HbO_2}}^{\lambda}$ are constants, changes in $HbO_2$ and Hb in tissue vasculature result in changes in $\mu_a^{\lambda}$. In turn, changes in $HbO_2$ and Hb can be determined by measuring changes in $\mu_a^{\lambda}$ at two wavelengths and can be expressed as

$$\begin{aligned}\Delta\mathrm{Hb} &= \mathrm{Hb(transient)} - \mathrm{Hb(baseline)} \\ &= \frac{\epsilon_{\mathrm{HbO_2}}^{\lambda 1}\Delta\mu_a^{\lambda 2} - \epsilon_{\mathrm{HbO_2}}^{\lambda 2}\Delta\mu_a^{\lambda 1}}{\epsilon_{\mathrm{Hb}}^{\lambda 2}\epsilon_{\mathrm{HbO_2}}^{\lambda 1} - \epsilon_{\mathrm{Hb}}^{\lambda 1}\epsilon_{\mathrm{HbO_2}}^{\lambda 2}},\end{aligned} \tag{A3}$$

$$\begin{aligned}\Delta\mathrm{HbO_2} &= \mathrm{HbO_2(transient)} - \mathrm{HbO_2(baseline)} \\ &= \frac{\epsilon_{\mathrm{Hb}}^{\lambda 2}\Delta\mu_a^{\lambda 1} - \epsilon_{\mathrm{Hb}}^{\lambda 1}\Delta\mu_a^{\lambda 2}}{\epsilon_{\mathrm{Hb}}^{\lambda 2}\epsilon_{\mathrm{HbO_2}}^{\lambda 1} - \epsilon_{\mathrm{Hb}}^{\lambda 1}\epsilon_{\mathrm{HbO_2}}^{\lambda 2}},\end{aligned} \tag{A4}$$

where $\Delta$Hb and $\Delta HbO_2$ refer to the change in the deoxyhemoglobin and the oxyhemoglobin concentrations between the baseline condition and the transient, or perturbed, condition, respectively, and $\Delta\mu_a^{\lambda}$ represents the change in the absorption coefficient at $\lambda$ relative to the baseline condition. However, our current experimental setup with one source and one detector does not provide adequate information for quantifying $\mu_a^{\lambda}$ values for a solid rat tumor. Thus we take an approximate approach by using the modified Beer–Lambert relation to calculate $\Delta$Hb and $\Delta HbO_2$.

According to the modified Beer–Lambert law,[10] an optical density (OD) can be defined as $\mathrm{OD} = \log(I_0/I) = \mu_a L$, where $I_0$ and $I$ are the incident and the detected optical intensities, respectively, and $L$ is the optical path length traveled by light inside the tissue. When an organ or a tumor undergoes a change from its baseline condition to a transient condition under physiological perturbations, a change in the OD at wavelength $\lambda$ will occur and can be expressed as

$$\begin{aligned}\Delta\mathrm{OD}^{\lambda} &= \mathrm{OD}^{\lambda}\,\mathrm{(transient)} - \mathrm{OD}^{\lambda}\,\mathrm{(baseline)} \\ &= \log(I_b/I_t)^{\lambda} = \Delta\mu_a^{\lambda}L^{\lambda},\end{aligned} \tag{A5}$$

where $I_b$ and $I_t$ are measured optical intensities under baseline and transient conditions, respectively. Thus we arrive at

$$\Delta\mu_a^{\lambda} = \log(I_b/I_t)^{\lambda}/L^{\lambda}. \tag{A6}$$

With our current NIR instrument, we can obtain the ratios of $(I_b/I_t)^{\lambda 1}$ and $(I_b/I_t)^{\lambda 2}$ from the tumor measurement. By assuming a constant path length, i.e., $L^{\lambda 1}\,\mathrm{(baseline)} \approx L^{\lambda 2}\,\mathrm{(baseline)} \approx L^{\lambda 1}\,\mathrm{(transient)} \approx L^{\lambda 2}\,\mathrm{(transient)} \approx L$, we next substitute Eq. (A6) into Eqs. (A3) and (A4) and arrive at Eqs. (5) and (6) for calculations of tumor hemoglobin oxygenation dynamics. Note that $I_b, I_t$ have been replaced with $A_b, A_t$ in Eqs. (5) and (6).

### B. Justification

The assumption of a constant path length as given above makes it possible to use relatively simple equations, for example, Eqs. (5) and (6), to quantify the $\Delta$Hb and the $\Delta HbO_2$ of tumors under respiratory intervention. However, in principle, the optical path length $L$ through tissue is wavelength dependent and could be variable under physiological perturbations. Therefore it is useful to know whether the relative error for calculated $\Delta$Hb and $\Delta HbO_2$ caused by this assumption is within a reasonable range.

According to the diffusion approximation, the optical path length $L$ of the NIR light traveling in tissue can be expressed approximately as[24]

$$L = \frac{\sqrt{3}}{2}\,d\left(\frac{\mu_s'}{\mu_a}\right)^{1/2}, \tag{A7}$$

where $d$ is the source–detector separation and $\mu_a$ and $\mu_s'$ are the absorption and the reduced scattering coefficients, respectively. Because in the NIR region the $\mu_s'$ of tissue is not sensitive to either wavelength or perturbation, we assume that a change in $L$ results from only a change in $\mu_a$, which is both wavelength and perturbation dependent. With this assumption, Eq. (A7) leads to

$$\frac{\Delta L}{L} = -\frac{1\Delta\mu_a}{2\mu_a}. \tag{A8}$$

Equation (A8) allows us to determine the relative errors of $\Delta L/L$ that are caused by (a) the wavelength dependence of $\mu_a$ and (b) the perturbation dependence of $\mu_a$ in the tumor. For case (a), we calculated this error by using

$$\frac{\mu_a^{758} - \mu_a^{782}}{2\mu_a^{758}}$$

under the baseline and the perturbed conditions; for case (b), we employed

$$\frac{\mu_a^{\lambda}\,(\text{transient}) - \mu_a^{\lambda}\,(\text{baseline})}{2\mu_a^{\lambda}\,(\text{baseline})}$$

at both $\lambda = 758$ nm and $\lambda = 782$ nm for the error calculation. The $\mu_a$ values used here were taken from Hull *et al.*[22] Although the rat tumor used in their study was different from ours, the absorption coefficients of the tumors should be in a similar order and follow a similar dynamic trend. The calculation shows that, with 758 and 782 nm under carbogen perturbation, the maximum value of $\Delta L/L$ is 12%. This result implies that the assumption of a constant path length that was used for Eqs. (5) and (6) gives rise to a maximal relative error of 12% in $L$.

On the basis of Eqs. (5) and (6) [or Eqs. (7) and (8)], we arrive at $\Delta X/X = -\Delta L/L$, where $X$ can be $\Delta HbO_2$, $\Delta Hb$, or $\Delta Hb_t$. Thus the assumption of a constant path length leads to a maximal relative error of 12% for the magnitude of the changes that we detected with regard to respiratory challenge. Although 12% is not completely negligible, the measurement and the calculation with the assumption of a constant path length are still worthwhile. Such an approach makes it possible, as a first-order approximation, to quantify the $\Delta Hb_t$ and the $\Delta HbO_2$ of tumors under respiratory intervention, providing deep insight into tumor vascular phenomena and mechanisms of modulating tumor physiology for therapeutic enhancement.

This study was supported in part by The Whitaker Foundation RG-97-0083 (H. Liu), The American Cancer Society RPG-97-116-010CCE (R. P. Mason), and The Department of Defense Breast Cancer Initiative BC962357 (Y. Song). We thank Peter P. Antich and Eric W. Hahn for their continued collegial support.

## References

1. L. Gray, A. Conger, M. Ebert, S. Hornsey, and O. Scott, "The concentration of oxygen dissolved in tissues at time of irradiation as a factor in radio-therapy," Br. J. Radiol. **26,** 638–648 (1953).
2. M. Höckel, K. Schlenger, B. Aral, M. Mitze, U. Schaffer, and P. Vaupel, "Association between tumor hypoxia and malignant progression in advanced cancer of the uterine cervix," Cancer Res. **56,** 4509–4515 (1996).
3. T. Y. Reynolds, S. Rockwell, and P. M. Glazer, "Genetic instability induced by the tumor microenvironment," Cancer Res. **56,** 5754–5757 (1996).
4. S. A. Vinogradov, L.-W. Lo, W. T. Jenkins, S. M. Evans, C. Koch, and D. F. Wilson, "Noninvasive imaging of the distribution of oxygen in tissues *in vivo* using near-infrared phosphors," Biophys. J. **70,** 1609–1617 (1996).
5. J. A. O'Hara, F. Goda, K. J. Liu, G. Bacic, P. J. Hoopes, and H. M. Swartz, "The $pO_2$ in a murine tumor after irradiation: an *in vivo* electron paramagnetic resonance oximetry study," Radiat. Res. **144,** 222–229 (1995).
6. R. P. Mason, A. Constantinescu, S. Hunjan, D. Le, E. W. Hahn, P. P. Antich, C. Blum, and P. Peschke, "Regional tumor oxygenation and measurement of dynamic changes," Radiat. Res. **152,** 239–245 (1999).
7. D. T. Delpy and M. Cope, "Quantification in tissue near-infrared spectroscopy," Philos. Trans. R. Soc. London B **952,** 649–659 (1997).
8. M. Fabiani, G. Gratton, and P. M. Corballis, "Noninvasive near-infrared optical imaging of human brain function with subsecond temporal resolution," J. Biomed. Opt. **1,** 387–398 (1996).
9. R. Wenzel, H. Obrig, J. Ruben, K. Villringer, A. Thiel, J. Bernarding, U. Dirnagl, and A. Villringer, "Cerebral blood oxygenation changes induced by visual stimulation in humans," J. Biomed. Opt. **1,** 399–404 (1996).
10. M. Cope and D. T. Delpy, "A system for long-term measurement of cerebral blood and tissue oxygenation in newborn infants by near-infrared transillumination," Med. Biol. Eng. Comput. **26,** 289–294 (1988).
11. B. Chance, E. Anday, S. Nioka, S. Zhou, L. Hong, K. Worden, C. Li, T. Murray, Y. Ovetsky, D. Pidikiti, and R. Thomas, "A novel method for fast imaging of brain function, noninvasively, with light," Opt. Express **2,** 411–423 (1998), http://www.epubs.osa.org/opticsexpress.
12. A. M. Siegel, J. A. Marota, J. Mandeville, B. Rosen, and D. A. Boas, "Diffuse optical tomography of rat brain function," in *Optical Tomography and Spectroscopy of Tissue III*, B. Chance, R. R. Alfano, and B. J. Tromberg, eds., Proc. SPIE **3597,** 252–261 (1999).
13. S. Homma, T. Fukunaga, and A. Kagaya, "Influence of adipose tissue thickness on near-infrared spectroscopic signals in the measurement of human muscle," J. Biomed. Opt. **1,** 418–424 (1996).
14. M. Ferrari, Q. Wei, L. Carraresi, R. A. De Blasi, and G. Zaccanti, "Time-resolved spectroscopy of the human forearm," J. Photochem. Photobiol. B: Biol. **16,** 141–153 (1992).
15. M. Ferrari, R. A. De Blasi, S. Fantini, M. A. Franceschini, B. Barbieri, V. Quaresima, and E. Gratton, "Cerebral and muscle oxygen saturation measurement by a frequency-domain near-infrared spectroscopic technique," in *Optical Tomography, Photon Migration, and Spectroscopy of Tissue and Model Media: Theory, Human Studies, and Instrumentation*, B. Chance and R. R. Alfano, eds., Proc. SPIE **2389,** 868–874 (1995).
16. H. Long, G. Lech, S. Nioka, S. Zhou, and B. Chance, "CW imaging of human muscle using near-infrared spectroscopy," in *Advances in Optical Imaging and Photon Migration*, J. G. Fujimoto and M. S. Patterson, eds., Vol. 21 of OSA Trends in

Optics and Photonics Series (Optical Society of America, Washington, D.C., 1998), pp. 256–259.
17. B. Chance, S. Nioka, J. Kent, K. McCully, M. Fountain, R. Greenfield, and G. Holtom, "Time-resolved spectroscopy of hemoglobin and myoglobin in resting and ischemic muscle," Anal. Biochem. **174,** 698–707 (1988).
18. B. M. Fenton, S. F. Paoni, J. Lee, C. J. Koch, and E. M. Lord, "Quantification of tumor vasculature and hypoxia by immunohistochemical staining and $HbO_2$ saturation measurements," Br. J. Cancer **79,** 464–471 (1999).
19. H. D. Sostman, S. Rockwell, A. L. Sylva, D. Madwed, G. Cofer, H. C. Charles, R. Negro-Villar, and D. Moore, "Evaluation of BA 1112 rhabdomyosarcoma oxygenation with microelectrodes, optical spectrometry, radiosensitivity, and MRS," Magn. Reson. Med. **20,** 253–267 (1991).
20. F. Steinberg, H. J. Röhrborn, T. Otto, K. M. Scheufler, and C. Streffer, "NIR reflection measurements of hemoglobin and cytochrome $aa_3$ in healthy tissue and tumors," Adv. Exp. Med. Biol. **428,** 69–77 (1997).
21. R. G. Steen, K. Kitagishi, and K. Morgan, "*In vivo* measurement of tumor blood oxygenation by near-infrared spectroscopy: immediate effects of pentobarbital overdose or carmustine treatment," J. Neuro-Oncol. **22,** 209–220 (1994).
22. E. L. Hull, D. L. Conover, and T. H. Foster, "Carbogen-induced changes in rat mammary tumor oxygenation reported by near-infrared spectroscopy," Br. J. Cancer **79,** 1709–1716 (1999).
23. M. S. Patterson, B. Chance, and B. C. Wilson, "Time-resolved reflectance and transmittance for the noninvasive measurement of tissue optical properties," Appl. Opt. **28,** 2331–2336 (1989).
24. E. M. Sevick, B. Chance, J. Leigh, S. Nioka, and M. Maris, "Quantitation of time- and frequency-resolved optical spectra for the determination of tissue oxygenation," Anal. Biochem. **195,** 330–351 (1991).
25. H. Liu, A. H. Hielscher, F. K. Tittel, S. L. Jacques, and B. Chance, "Influence of blood vessels on the measurement of hemoglobin oxygenation as determined by time-resolved reflectance spectroscopy," Med. Phys. **22,** 1209–1217 (1995).
26. S. J. Matcher, M. Cope, and D. T. Delpy, "*In vivo* measurements of the wavelength dependence of tissue-scattering coefficients between 760 and 900 nm measured with time-resolved spectroscopy," Appl. Opt. **36,** 386–396 (1997).
27. E. W. Hahn, P. Peschke, R. P. Mason, E. E. Babcock, and P. P. Antich, "Isolated tumor growth in a surgically formed skin pedicle in the rat: a new tumor model for NMR studies," Magn. Reson. Imaging. **11,** 1007–1017 (1993).
28. Y. Yang, H. Liu, X. Li, and B. Chance, "Low-cost frequency-domain photon migration instrument for tissue spectroscopy, oximetry, and imaging," Opt. Eng. **36,** 1562–1569 (1997).
29. H. Y. Ma, Q. Xu, J. R. Ballesteros, V. Ntziachristors, Q. Zhang, and B. Chance, "Quantitative study of hypoxia stress in piglet brain by IQ phase modulation oximetry," in *Optical Tomography and Spectroscopy of Tissue III*, B. Chance, R. R. Alfano, and B. J. Tromberg, eds., Proc. SPIE **3597,** 642–649 (1999).
30. P. R. Bevington, *Data Reduction and Error Analysis for the Physical Sciences* (McGraw-Hill, New York, 1969).
31. W. H. Press, B. P. Flannery, S. A. Teukolsky, and W. T. Vetterling, *Numerical Recipes* (Cambridge U. Press, Cambridge, 1988).
32. KaleidaGraph, Version 3.08 (Synergy Software, 2457 Perkiomen Avenue, Reading, Pa. 19606, 1996).
33. J. L. Hintze, *NCSS, Version 6.0, User's Guide II: Statistical System for Windows* (Number Cruncher Statistical Systems, Kaysville, Utah, 1996).
34. J. B. Fishkin and E. Gratton, "Propagation of photon-density waves in strongly scattering media containing an absorbing semi-infinite plane bounded by a straight edge," J. Opt. Soc. Am. A **10,** 127–140 (1993).
35. W. G. Zijlstra, A. Buursma, and W. P. Meeuwsen-van der Roest, "Absorption spectra of human fetal and adult oxyhemoglobin, deoxyhemoglobin, carboxyhemoglobin, and methemoglobin," Clin. Chem. **37,** 1633–1638 (1991).
36. H. Liu, C. L. Matson, K. Lau, and R. R. Mapakshi, "Experimental validation of a backpropagation algorithm for three-dimensional breast tumor localization," IEEE J. Select. Top. Quantum Electron. **5,** 1049–1057 (1999).
37. S. S. Kety, "The theory and applications of the exchange of inert gas at the lungs and tissue," Pharmacol. Rev. **3,** 1–41 (1951).
38. H. Watabe, M. Itoh, V. Cunningham, A. A. Lammertsma, P. Bloomfield, M. Mejia, T. Fujiwara, A. K. P. Johes, T. Johes, and T. Nakamura, "Noninvasive quantification of rCBF using positron emission tomography," J. Cerebr. Blood Flow Metab. **16,** 311–319 (1996).
39. S. S. Kety, "Cerebral circulation and its measurement by inert diffusible racers," Israel J. Med. Sci. **23,** 3–7 (1987).
40. A. D. Edwards, C. Richardson, P. Van Der Zee, C. Elwell, J. S. Wyatt, M. Cope, D. T. Delpy, and E. O. R. Reynolds, "Measurement of hemoglobin flow and blood flow by near-infrared spectroscopy," J. Appl. Physiol. **75,** 1884–1889 (1993).
41. H. J. J. A. Bernsen, P. F. J. W. Rijken, T. Oostendorp, and A. J. van der Kogel, "Vascularity and perfusion of human gliomas xenografted in the athymic nude mouse," Br. J. Cancer **71,** 721–726 (1995).
42. R. P. Mason, P. P. Antich, E. E. Babcock, A. Constantinescu, P. Peschke, and E. W. Hahn, "Noninvasive determination of tumor oxygen tension and local variation with growth," Int. J. Radiat. Oncol. Biol. Phys. **29,** 95–103 (1994).
43. B. P. J. van der Sanden, A. Heerschap, A. W. Simonetti, P. J. F. W. Rijken, H. P. W. Peters, G. Stuben, and A. J. van der Kogel, "Characterization and validation on noninvasive oxygen tension measurements in human glioma xenografts by 19F-MR relaxometry," Int. J. Radiat. Oncol. Biol. Phys. **44,** 649–658 (1999).
44. S. Hunjan, R. P. Mason, A. Constantinescu, P. Pescheke, E. W. Hahn, and P. P. Antich, "Regional tumor oximetry: $^{19}F$ NMR spectroscopy of hexafluorobenzene," Int. J. Radiat. Oncol. Biol. Phys. **41,** 161–171 (1998).
45. S. Hunjan, D. Zhao, A. Constantinescu, E. W. Hahn, P. P. Antich, and R. P. Mason, "Tumor oximetry: an enhanced dynamic mapping procedure using fluorine-19 echo planar magnetic resonance imaging," Int. J. Radiat. Oncol. Biol. Phys. (to be published).
46. S. P. Robinson, F. A. Howe, L. M. Rodrigues, M. Stubbs, and J. R. Griffiths, "Magnetic resonance imaging techniques for monitoring changes in tumor oxygenation and blood flow," Semin. Radiat. Oncol. **8,** 198–207 (1998).
47. B. M. Fenton, "Effects of carbogen plus fractionated irradiation on KHT tumor oxygenation," Radiother. Oncol. **44,** 183–190 (1997).

SPIE 2001
in the press

# Interplay of Tumor Vascular Oxygenation and $pO_2$ in Tumors Using NIRS and Needle Electrode

Jae Gwan Kim*, Yulin Song*$^{\phi}$, Dawen Zhao$^{\phi}$, Anca Constantinescu$^{\phi}$, Ralph P. Mason$^{\phi}$, Hanli Liu*

*Joint Graduate Program in Biomedical Engineering
University of Texas at Arlington/University of Texas Southwestern Medical Center at Dallas
Arlington, TX 76019

$^{\phi}$Advanced Radiological Sciences, Department of Radiology
University of Texas Southwestern Medical Center at Dallas
Dallas, TX 75390

## ABSTRACT

The effective measurement of dynamic changes of blood and tissue oxygenation of tumors could be valuable for optimizing tumor treatment plans. For this study, a near-infrared spectroscopy system and $pO_2$ needle electrode were used to measure simultaneously changes in total hemoglobin concentration ($[Hb]_{total}$), oxygenated hemoglobin concentration ($[HbO_2]$) and local oxygen tension ($pO_2$) in the vascular bed of prostate tumors implanted in rats in response to respiratory challenge. The inhaled gas was alternated between air and carbogen (95% oxygen, 5% $CO_2$). Significant changes in tumor vascular oxygenation were observed with an apparent threshold for variation in $[HbO_2]/[HbO_2]_{max}$. For comparison, a phantom study was undertaken with 1% intralipid solution and blood. The slope of $[HbO_2]/[HbO_2]_{max}$ vs. $pO_2$ in the phantom was ten times larger than in the tumor indicating that tumor cells are relatively resistant to oxygenation. This study demonstrates that the NIR technology can provide an efficient, real-time, non-invasive approach to monitoring tumor physiology and is compatible with additional techniques.

**Key Words**: Frequency-Domain Spectroscopy, NIR Spectroscopy, Tumor Vascular Oxygenation, $pO_2$ electrode

## 1. INTRODUCTION

Many cancer therapies are less effective for treating hypoxic tumor cells, in particular radiation therapy and photodynamic therapy. Hypoxic tumor cells are three times more resistant to radiation therapy than well oxygenated tumor cells.[1] Thus, measurement of tumor oxygenation could be important for tumor treatment planning and assessing methods designed to modulate tumor oxygenation.

While there are many methods to measure tissue oxygen tension[2], many are highly invasive precluding the detection of dynamic changes. Oxygen microelectrodes[3], fiber optical sensors[4], electron spin resonance[5], and nuclear magnetic resonance[6] do facilitate measurement of dynamic changes. MRI is particularly valuable since it allows dynamic maps of $pO_2$ to be obtained.[7] Near infrared spectroscopy (NIRS) does not provide quantitative measurements of $pO_2$ in tissue, but can indicate dynamic changes in vascular oxygenation and has the advantages of being entirely non-invasive and the instrumentation is cost effective and portable.

Oxygenated and deoxygenated hemoglobin are major chromophores in tissue in the near infrared region (700-900 nm) and they exhibit different light absorption characteristics. By measuring absorption and scattering of light by tissue, blood oxygenation, i.e. the concentration of oxygenated hemoglobin $[HbO_2]$, deoxygenated hemoglobin [Hb], oxygen saturation of hemoglobin $SO_2$ and total hemoglobin concentration $[Hb]_{total}$ can be determined. Based on attenuation and phase changes absolute values could be obtained, but currently our analysis of tumor oxygenation using the NIR technique is limited to relative changes.

Temperature was maintained at 37 °C using the electric heater, and a magnetic stirrer was used to make the solution homogeneous. NIRS amplitude and phase data were recorded, and after 5 minutes of baseline measurement, 2 ml of fresh rabbit blood was added to the solution. Air and nitrogen gas were used to oxygenate and deoxygenate the solution, respectively.

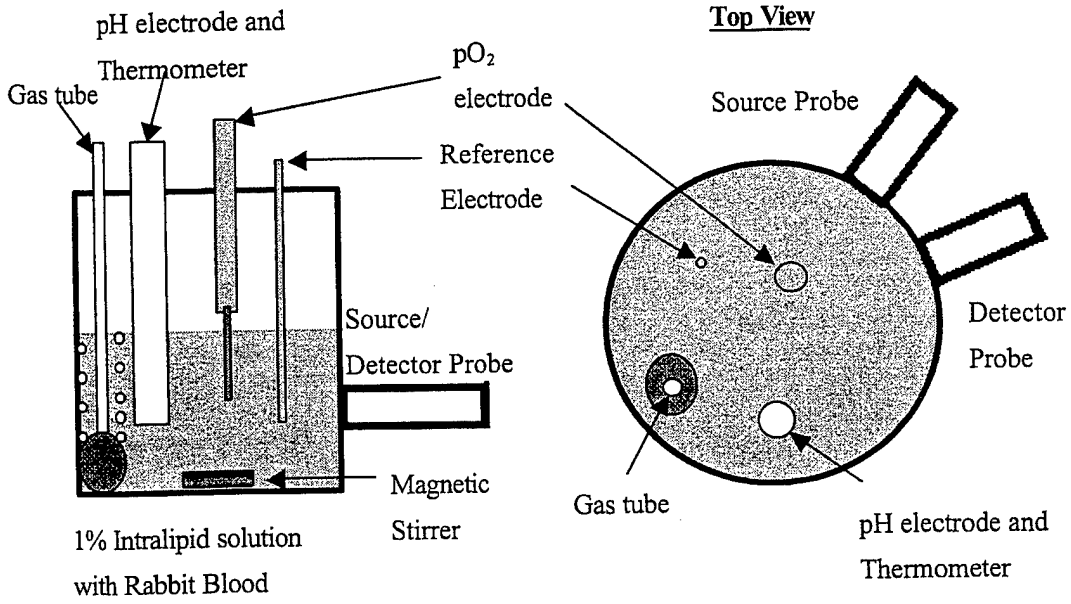


Figure 2: Experimental setup for phantom solution study.

**2.3 NIR Spectroscopy**

NIR spectroscopy can be used to measure the hemoglobin saturation because the extinction coefficients of oxygenated hemoglobin are different from deoxygenated hemoglobin at the wavelengths selected (758 nm and 782 nm). In common with our previous work[9], we assume that oxyhemoglobin and deoxyhemoglobin are the only significant absorbance materials in the blood. The absorption coefficients comprise the extinction coefficients for deoxyhemoglobin and oxyhemoglobin multiplied by their respective concentrations (Equations 1 and 2).

$$\mu_a^{758} = \varepsilon_{Hb}^{758}[Hb] + \varepsilon_{HbO2}^{758}[HbO_2], \quad (1)$$

$$\mu_a^{782} = \varepsilon_{Hb}^{782}[Hb] + \varepsilon_{HbO2}^{782}[HbO_2]. \quad (2)$$

The IQ system can give both amplitude and phase values[9], but we have not yet derived a suitable algorithm to compute $\mu_a$ and $\mu_s$' due to the small tumor size and heterogeneity. The data presented in this paper were analyzed using modified Beer-Lambert's law and amplitude values to find the changes of absorption (Equation 3). By manipulating Equations 1-3, changes of oxygenated hemoglobin and total hemoglobin concentrations were calculated from the transmitted amplitude of the light through the tumor (Equations 4 and 5).

$$\mu_{aB} - \mu_{aT} = \log (A_B/A_T) / L, \quad (3)$$

$$\Delta[HbO_2] = [-10.92*\log (A_B/A_T)^{758} + 14.80*\log (A_B/A_T)^{782}] / L, \quad (4)$$

$$\Delta[Hb]_{total} = \Delta[Hb] + \Delta[HbO_2] = [-3.58*\log (A_B/A_T)^{758} + 8.63*\log (A_B/A_T)^{782}] / L, \quad (5)$$

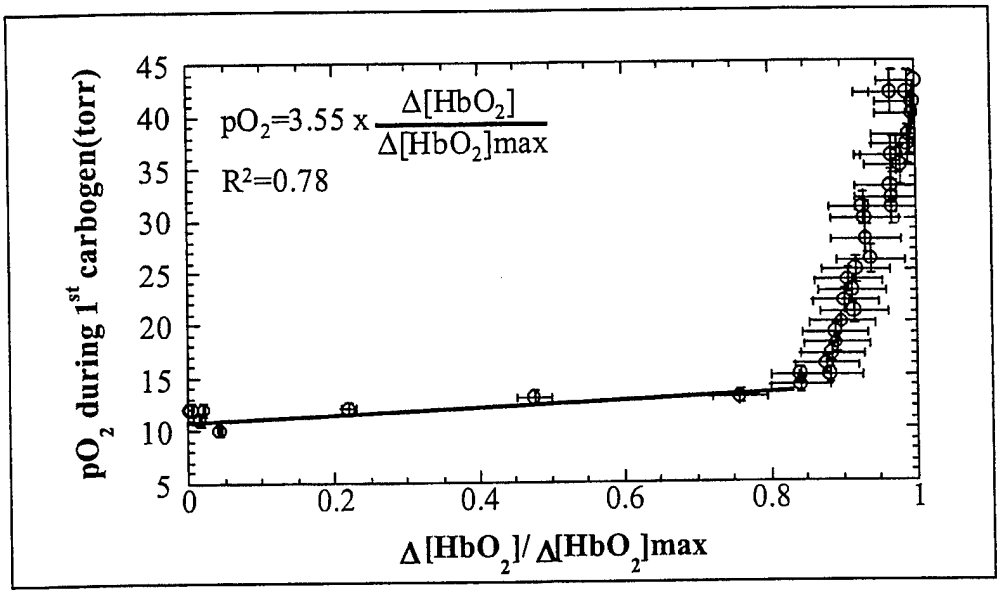


Figure 3b: Changes of tumor tissue $pO_2$ with hemoglobin oxygenation changes in tumor (case1). Notice that the slope between $pO_2$ and $\Delta[HbO_2]/\Delta[HbO_2]_{max}$ is 3.55 when $\Delta[HbO_2]/\Delta[HbO_2]_{max}$ is less than 0.8.

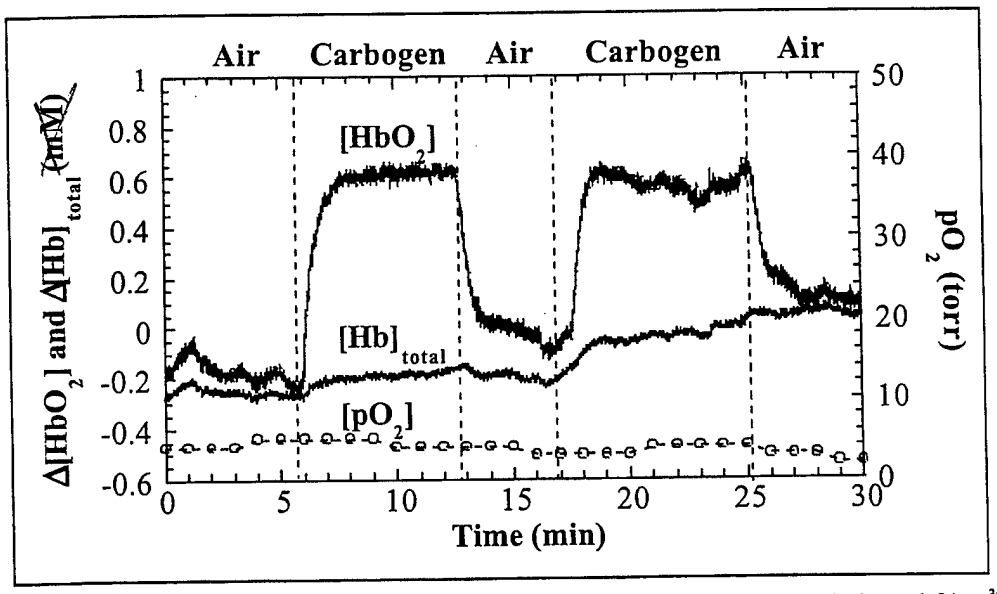


Figure 3c: Dynamic changes of $[HbO_2]$, $[Hb]_{total}$ and $pO_2$ in a second R3327-H rat prostate tumors (volume: 1.54 $cm^3$). In this case, $pO_2$ baseline was ~ 5 torr and did not respond to respiratory challenge.

### 3.2 Phantom Solution Study Results

Figure 4a shows the changes in $[HbO_2]$, $[Hb]_{total}$ and $pO_2$ measured in the phantom study. The first six minutes were measured without blood to show the effect of adding blood. Upon adding 2 ml of blood to the solution, immediate increases of both $\Delta[HbO_2]$ and $\Delta[Hb]_{total}$ were observed. Bubbling nitrogen deoxygenated the solution, and thus, $pO_2$ fell; oxyhemoglobin concentration declined also, but with a small lag. It is reassuring that changes were essentially as expected.

## 4. DISCUSSION

Tumor oxygenation involves a complex interplay of multiple compartments and parameters: blood flow, blood volume and oxygen consumption. NIRS provides a global non-invasive estimate of average vascular oxygenation encompassing arterial, venous and capillary compartments. In common with our previous results[9], the $\Delta[HbO_2]$ response is biphasic, which we believe represents rapid elevation of arterial oxygenation, followed by more sluggish capillary components. Meanwhile the electrode measurements are limited to a very local region. In common with many reports in the literature and our own previous observations in Dunning prostate tumors, $pO_2$ distributions are highly heterogeneous. Figures 3a and c show distinctly different baseline $pO_2$ values and perhaps more significantly different response to intervention. Using $^{19}F$ echo planar MRI of the reporter molecule hexafluorobenzene (FREDOM)[10], we have previously observed such differences in the faster growing undifferentiated Dunning prostate R3327-AT1 rat tumors. Indeed, such heterogeneity emphasizes the importance of mapping $pO_2$ at multiple locations, as opposed to a single electrode site, as reported here.

Previous investigations of the Dunning prostate R3327-H tumor have suggested that it is relatively well oxygenated[12] and very well vascularized[13]. The large and rapid changes observed in $\Delta[HbO_2]$ here are consistent with these previous reports. The actual electrode $pO_2$ measurements here are in the range of mean values reported previously for $pO_2$ distributions using the Eppendorf electrode system in this tumor line. [12] Given the high degree of differentiation and slow growth rate, the H tumor line is considered by many to be an excellent model for human prostate cancer. This tumor line has been used previously to investigate tumor physiological response to photodynamic therapy. In those studies the H tumor was found to be better perfused than the faster growing AT subline.[14] Both tumor types showed reduced perfusion following photodynamic therapy. However, we are unaware of any previous attempts to examine dynamic changes in oxygenation of this tumor in response to respiratory challenge.

The phantom measurements provide strong evidence for the reliability of the NIRS technique, although the minor apparent change in $\Delta[Hb]_{total}$ with gas remains to be evaluated. Both phantom and tumor measurements indicate a sharp response of $pO_2$ to oxyhemoglobin, once the $\Delta[HbO_2]$ reaches about 80% of maximum. This coincides with the recognized sigmoidal binding of oxygen to hemoglobin. The difference between the phantom and tumor cases is that the $pO_2$ response to $HbO_2$ changes in tumor is about 10 times smaller than that in tissue phantom. This demonstrates that it is much harder to deliver oxygen into the hypoxic regions of the tumor than into regular tissues. The small slope at low $\Delta[HbO_2]$ in tumor presumably also reflects oxygen consumption by the tumor tissues, as oxygen initially becomes available.

## 5. CONCLUSION

We could measure relative $[HbO_2]$, $[Hb]_{total}$ in tumor vasculature and tumor tissue $pO_2$ simultaneously using NIRS and needle type $pO_2$ electrode. NIRS data showed significant changes in vascular oxygenation accompanying respiratory interventions and changes in tumor vascular hemoglobin oxygenation preceded tumor tissue $pO_2$. Correlation between tumor $\Delta[HbO_2]$ and tumor tissue $pO_2$ shows that there is a threshold $[HbO_2]$ for tumor cells to be oxygenated. This indicates the difficulty of oxygen delivery into the hypoxic regions of tumor.

Clearly, future studies will require more detailed estimates of tumor heterogeneity, ideally applying both NIR imaging and MR $pO_2$ mapping.

## ACKNOWLEDGEMENTS

This work was supported in part by The Whitaker Foundation (HL), The American Cancer Society RPG-97-116-010CCE (RPM), NIH RO1 CA79515 (RPM), and the Department of Defense Breast Cancer Initiative grants BC962357 (YS) and BC990287 (HL). We are very grateful to Sherwin Yen and William McSweeny for assistance with data acquisition and Dr. Peter Peschke for providing the original tumor cells.

# Interplay of Tumor Vascular Oxygenation and Tumor $pO_2$ Observed Using NIRS, Oxygen Needle Electrode, and $^{19}F$ MR $pO_2$ Mapping

Jae G. Kim[+], Yulin Song[+ϕ], Dawen Zhao[ϕ], Anca Constantinescu[ϕ],
Ralph P. Mason[ϕ], and Hanli Liu[+*]

[+]Joint Graduate Program in Biomedical Engineering
University of Texas at Arlington/University of Texas Southwestern Medical Center at Dallas
Arlington, TX 76019

[ϕ]Advanced Radiological Sciences, Department of Radiology
University of Texas Southwestern Medical Center at Dallas
Dallas, TX 75390

## ABSTRACT

Breathing carbogen (95% $O_2$, 5% $CO_2$) to enhance tumor oxygenation may improve tumor response to therapy. However, few studies have been reported on the relationship between tumor oxygen tension ($pO_2$) and tumor vascular oxygenation. This study investigates the correlation of tumor blood oxygenation and tumor $pO_2$ with respect to carbogen inhalation and compares such correlation with that in tissue phantoms. We used near-infrared spectroscopy (NIRS) to measure changes of oxygenated hemoglobin concentration ($\Delta[HbO_2]$) and used an oxygen needle electrode and $^{19}F$ MRI for $pO_2$ measurements in tumors. The measurements were taken from Dunning prostate R3327 tumors implanted in rats, while the rats were anesthetized breathing air or carbogen. In the tissue-phantom study, 1% intralipid solution and rabbit blood were used. NIRS results showed significant changes in tumor vascular oxygenation in response to carbogen inhalation. Furthermore, the results show an apparent threshold for tumor $pO_2$ response. The slope of $pO_2$ versus normalized $\Delta[HbO_2]$ below the threshold obtained from the tissue phantom was ten times larger than the slope from the tumor, indicating that tumor cells are much harder to oxygenate. This study demonstrates that the NIRS technology can provide an efficient, real-time, non-invasive approach to monitoring tumor physiology and is complementary to other techniques.

**Key Words**: Frequency-Domain Spectroscopy, NIR Spectroscopy, $^{19}F$ MRI, Tumor Vascular Oxygenation, $pO_2$ electrode, Oxygen, Oximetry

* hanli@uta.edu; phone 1 817 272-2054; fax 1 817 272-2251; Joint Program of Biomedical Engineering, P.O. Box 19138, University of Texas at Arlington, Arlington, TX, USA 76019-0167

## 1. Introduction

It has long been known that hypoxic tumor cells are more resistant to radiation therapy than well-oxygenated tumor cells.[1] Breathing elevated oxygen (100%) or carbogen (95% $O_2$, 5% $CO_2$) has been used during therapy to improve oxygenation.[2, 3] However, little is known about oxygen transfer from the tumor vasculature to tumor tissue cells. In this study, we investigated the relationship between vascular oxygenation and tissue oxygenation during respiratory challenge in rat prostate tumors using Near-Infrared Spectroscopy (NIRS), $pO_2$ needle electrodes, and $^{19}F$ MRI for simultaneous or sequential measurements.

While various methods are available for measuring tissue oxygen tension[4], many of them are highly invasive precluding the detection of dynamic changes. Oxygen microelectrodes[5], fiber optic sensors[6], and electron spin resonance[7] do facilitate measurement of dynamic changes. MRI has the further advantage of providing dynamic maps of $pO_2$, which can reveal tumor heterogeneity.[8] While NIRS does not quantify $pO_2$, it can indicate dynamic changes in vascular oxygenation and has the advantage of being entirely non-invasive, providing real-time measurements, and being cost effective and portable.

Oxygenated and deoxygenated hemoglobin molecules are major chromophores in tissue in the near infrared region (700-900 nm), and they exhibit distinct absorption characteristics. In principle, by measuring light absorption and scattering in tissue, the concentrations of oxygenated hemoglobin, [$HbO_2$], deoxygenated hemoglobin, [Hb], and oxygen saturation of hemoglobin, $SO_2$, can be determined based on diffusion theory. However, the theory works well only for large and homogeneous media.[9, 10] Accurate quantification of tumor

oxygenation in our approach is currently limited to relative changes in $[HbO_2]$ and $[Hb]_{total}$ due to considerable heterogeneity and finite size of tumors.

The goal of this study was to investigate the correlation of tumor blood oxygenation and tumor $pO_2$ in response to carbogen intervention and to compare such correlation with that from regular tissues using phantoms.

## 2. Materials and Methods

### 2.1 Tumor Model and $pO_2$ needle electrode measurements

Dunning prostate rat tumors (three R3327-HI and two R3327-AT1)[11] were implanted in pedicles on the foreback of adult male Copenhagen rats, as described in detail previously.[12] Once the tumors reached approximately 2 cm in diameter, the rats were anesthetized with 0.2 ml ketamine hydrochloride (100 mg/mL; Aveco, Fort Dodge, IA) and maintained under general gaseous anesthesia with isoflurane in air (1.3% isoflurane at 1 $dm^3$/min air) through a mask placed over the mouth and nose. Tumors were shaved to improve optical contact for transmitting light. Body temperature was maintained by a warm water blanket and was monitored by a rectally inserted thermal probe connected to a digital thermometer (Digi-Sense, model 91100-50, Cole-Parmer Instrument Company, Vernon Hills, IL). A pulse oximeter (model 8600, Nonin, Inc., Plymouth, MN) was placed on the hind foot to monitor arterial oxygenation ($S_aO_2$).

Figure 1 shows the schematic setup for animal experiments using NIRS and a $pO_2$ needle electrode. A needle type oxygen electrode was placed in the tumor, and the reference electrode was placed rectally. The electrodes

were connected to a picoammeter (Chemical Microsensor, Diamond Electro-Tech Inc., Ann Arbor, MI) and polarized at - 0.75 V. Linear two-point calibrations were performed with air (21% $O_2$) and pure nitrogen (0% $O_2$) saturated saline buffer solutions before the electrode was inserted into the tumor, and we estimated an instrumental precision of 2-3 mmHg. $PO_2$ experimental data were manually recorded, while the NIRS data were acquired automatically. Measurements of $pO_2$ and NIRS were initiated while rats breathed air for ~10 minutes to demonstrate a stable baseline. The inhaled gas was then switched to carbogen for 15 minutes and switched back to air.

**2.2 NIR Spectroscopy**

NIR spectroscopy can be used to measure hemoglobin concentrations and oxygen saturation because light absorptions of $HbO_2$ and Hb are different at the wavelengths selected (758 nm and 785 nm). In common with our previous work[13], we assumed that $HbO_2$ and Hb are the only significant absorbing materials in tumors within the NIR range. The absorption coefficients comprise the extinction coefficients for deoxyhemoglobin ($\varepsilon_{Hb}$) and oxyhemoglobin ($\varepsilon_{HbO2}$) multiplied by their respective concentrations (Equations 1 and 2).

$$\mu_a^{758} = \varepsilon_{Hb}^{758}[Hb] + \varepsilon_{HbO2}^{758}[HbO_2], \quad (1)$$

$$\mu_a^{785} = \varepsilon_{Hb}^{785}[Hb] + \varepsilon_{HbO2}^{785}[HbO_2]\,. \quad (2)$$

An NIR homodyne frequency-domain photon migration system (NIM, Inc., Philadelphia, PA) allows one to obtain absorption and scattering properties of the measured sample[14]. Figure 1 indicates the working principle of the NIR system, and detailed information on the instrument is given elsewhere[13]. We have not yet completed a

suitable algorithm to compute $\mu_a$ and $\mu_s$' of rat tumors due to their finite size and high heterogeneity. The data presented here were analyzed using only amplitude values to find changes in $[HbO_2]$ and $[Hb]_{total}$, based on modified Beer-Lambert's law (Equation 3). By manipulating Equations 1-3, changes of $[HbO_2]$ and $[Hb]_{total}$ due to respiratory intervention were calculated from the transmitted amplitude of the light through the tumor (Equations 4 and 5).

$$\Delta\mu_a = \mu_{aT} - \mu_{aB} = Ln(A_B/A_T) / L, \quad (3)$$

$$\Delta[HbO_2] = [-5.73*Ln(A_B/A_T)^{758} + 9.67*Ln(A_B/A_T)^{785}] / L, \quad (4)$$

$$\Delta[Hb]_{total} = \Delta[Hb] + \Delta[HbO_2] = [-1.32*Ln(A_B/A_T)^{758} + 6.23*Ln(A_B/A_T)^{785}] / L, \quad (5)$$

where $A_B$ = baseline amplitude; $A_T$ = transient amplitude; L = optical pathlength between source/detector; the constants given in the equations were computed with the extinction coefficients for oxy- and deoxy-hemoglobin at the two wavelengths used.[15] In principle, the units of $\Delta[HbO_2]$ and $\Delta[Hb]_{total}$ are mM, and L is equal to the source–detector separation multiplied by a Differential Pathlength Factor (DPF)[16]. The DPF has been studied intensively for muscles[17]and brains[18] with approximate values of 4-6 and 5-6, respectively. Little is known about the DPF for tumors, though a DPF value of 2.5 has been used by others[19]. Since our focus is on dynamic changes and relative values of tumor $[HbO_2]$ with respect to carbogen intervention, we have taken the approach of including the DPF in the unit, i.e., modifying eq. (4) as follows:

$$\Delta[HbO_2] = [-5.73*Ln(A_B/A_T)^{758} + 9.67*Ln(A_B/A_T)^{785}] / d, \quad (6)$$

where d is the direct source-detector separation in cm, and the unit of $\Delta[HbO_2]$ in eq. (6) is mM/DPF. We further

will show that our conclusion on the relationship between tumor $\Delta[HbO_2]$ and $pO_2$ will not be affected by the DPF after normalizing the experimental $\Delta[HbO_2]$ data to its maximal value.

**2.3 MRI Instrumentation and Procedure**

To support the findings obtained from the $pO_2$ electrode measurements and NIRS, we conducted MRI experiments using an Omega CSI 4.7 T 40 cm system with actively shielded gradients. A homebuilt tunable $^1H/^{19}F$ single turn solenoid coil was placed around the tumor. 45 μL of hexafluorobenzene (HFB; Lancaster, Gainesville, FL) was administered directly into the tumor using a Hamilton syringe (Reno, NV) with a custom-made fine sharp (32 gauge) needle with deliberate dispersion along several tracks to interrogate both central and peripheral tumor regions as described in detail previous[6]. HFB is ideal for imaging $pO_2$, because it has a single resonance, and its relaxation rate varies linearly with oxygen concentration. $^1H$ images were acquired for anatomical reference using a traditional 3D spin-echo pulse sequence. Conventional $^{19}F$ MR images were then taken to show the 3D distribution of the HFB in the tumor. $^{19}F$ MR images were directly overlaid over $^1H$ images to show the position of the HFB in that slice.

Tumor oxygenation was assessed using FREDOM (Fluorocarbon Relaxometry using Echo planar imaging for Dynamic Oxygen Mapping) based on $^{19}F$ pulse burst saturation recovery (PBSR) echo planar imaging (EPI) of HFB. The PBSR preparation pulse sequence consists of a series of 20 non-spatially selective saturating 90° pulses with 20 ms spacing to saturate the $^{19}F$ nuclei. Following a variable delay time $\tau$, a single spin-echo EPI sequence with blipped phase encoding was applied.[20] Fourteen 32×32 PBSR-EPI images, with $\tau$ ranging from

200 ms to 90 sec and a field of view (FOV) of 40× 40 mm, were acquired in eight minutes using the ARDVARC (Alternated Relaxation Delays with Variable Acquisitions to Reduce Clearance effects) acquisition protocol[21]. An $R1$(=1/T1) map was obtained by fitting signal intensity of each voxel of the fourteen images to a three parameter relaxation model by Levenberg-Marquardt least squares algorithm (equation 6):

$$y_n(i,j) = A(i,j)\cdot[1-(1+W)\cdot\exp(-R1(i,j)\cdot\tau_n)] \quad (6)$$
$$(n=1,2,\cdots\cdots,14)$$
$$(i,j=1,2,\cdots\cdots,32)$$

where $y_n(i,j)$ is the measured signal intensity corresponding to delay time $\tau_n$ (the $n$th images) for voxel $(i,j)$, $A(i,j)$ is the fully relaxed signal intensity amplitude of voxel $(i,j)$, $W$ is a dimensionless scaling factor allowing for imperfect signal conversion, and $R1(i,j)$ is the relaxation rate of voxel $(i,j)$ in unit of $sec^{-1}$. $A$, $W$ and $R1$ are the three fit parameters for each of the 32 x 32 voxels. Finally, the $pO_2$ maps were generated by applying the calibration curve: $pO_2(mmHg) = [R1(s^{-1}) - 0.0835]/0.001876$ at 37 °C to the $R1$ maps.[21]

**2.4 Tissue Phantom Solution Model**

The tissue-simulating phantom comprised a solution of 1% Intralipid in saline buffer. The oxygen needle electrode, a pH electrode and a thermocouple probe (model 2001, Sentron, Inc., Gig Harbor, WA) were placed in the solution, and a gas tube was placed opposite the NIRS probes to minimize any liquid movement effects (Figure 2). Source and detector probes for the NIRS were placed in reflection geometry. The solution was stirred to maintain homogeneity at ~ 37 °C. Fresh whole rabbit blood (2 ml) was added to the 200 mL solution before baseline measurement. Nitrogen gas and air were used to deoxygenate and oxygenate the solution, respectively.

## 3. Results

### 3.1 Tumor Study Results

Figure 3a shows the temporal profiles of $\Delta[HbO_2]$ and $pO_2$ in a small Dunning prostate R3327-HI tumor (1.5 $cm^2$) with respiratory challenge measured simultaneously with NIRS and the $pO_2$ needle electrode. After a switch from air to carbogen, $\Delta[HbO_2]$ increased rapidly, along with tumor tissue $pO_2$. Figure 3b was obtained from a second large prostate tumor (3.1 $cm^2$) and now the NIRS response was biphasic, while the electrode showed a slower $pO_2$ response. In a third tumor NIRS behaved as before, but $pO_2$ did not change (Fig. 3c).

In two tumors from a separate subline (Dunning prostate R3327-AT1), NIRS and $^{19}F$ MRI were taken with carbogen challenge sequentially (Fig. 4). NIRS response showed vascular oxygenation changes as before, and FREDOM revealed the distinct heterogeneity of the tumor tissue response. Initial $pO_2$ was in the range of 1 to 75 mmHg, and carbogen challenge produced $pO_2$ values in the range of 6 to 360 mmHg. Representative voxels are shown.

### 3.2 Tissue Phantom Solution Study Results

Figure 5 shows a similar temporal profile for $\Delta[HbO_2]$ and $pO_2$ measured from the tissue phantom during a cycle of gas change from air to nitrogen and back. The first five minutes were measured as a baseline after adding 2 ml blood. Bubbling nitrogen deoxygenated the solution and caused the $pO_2$ values to fall; $\Delta[HbO_2]$ declined accordingly with a small time lag. After the bubbling gas was switched from nitrogen to air, both $\Delta[HbO_2]$ and $pO_2$ started to increase simultaneously, but the recovery time of $\Delta[HbO_2]$ to the baseline was faster than that of

$pO_2$. The small time lag between the changes of $\Delta[HbO_2]$ and $pO_2$ is probably due to the allosteric interactions between hemoglobin and oxygen molecules. According to the hemoglobin oxygen-dissociation curve[22, 23], oxyhemoglobin starts to lose oxygen significantly when $pO_2$ falls below 70 mmHg at standard conditions (pH=7.4 and temperature=37 °C). The same principle can explain why $\Delta[HbO_2]$ has a faster recovery than that of $pO_2$. Namely, $\Delta[HbO_2]$ became saturated as $pO_2$ increased from 0 to 70 mmHg, while the solution was being oxygenated. Importantly, $\Delta[Hb]_{total}$ remained unchanged, as expected, during the cycle of deoxygenation and oxygenation.

### 3.3 Correlation of $pO_2$ and $\Delta[HbO_2]/\Delta[HbO_2]_{max}$

To compare the data from tumors and from the phantom for the relationship between changes in tumor vascular oxygenation and tumor tissue $pO_2$, we normalized $\Delta[HbO_2]$ at the maximum value during the gas (carbogen/nitrogen) intervention, i.e., $\Delta[HbO_2]/\Delta[HbO_2]_{max}$. One advantage of using normalized $\Delta[HbO_2]$ is to eliminate the uncertainty of DPF.

Figure 6a replots the data given in figures 3a and 3b, showing a direct relationship between the normalized $\Delta[HbO_2]$ and $pO_2$ in the tumors. It shows that $pO_2$ in the tumors varied linearly with a slope of 4.1 in case 1 and a slope of 3.6 in case 2 before $\Delta[HbO_2]$ reached 60 % and 80 % of $\Delta[HbO_2]_{max}$ in cases 1 and 2, respectively. Thereafter, tumor $pO_2$ increased sharply, indicating a threshold for tumor tissue $pO_2$ to increase. While NIRS results tended to be similar for several tumors, $pO_2$ electrode measurements showed considerable variation even in the same tumor type, suggesting distinct tumor heterogeneity. This was substantiated by the $^{19}F$ MR $pO_2$

mappings: indeed, in some cases, $pO_2$ values did not change with respiratory challenge, especially when baseline $pO_2$ values were lower than 10 mmHg.

Figure 6b shows the relationship between normalized $\Delta[HbO_2]$ and $pO_2$ measured from the phantom. The threshold occurred at essentially the same value of $\Delta[HbO_2]/\Delta[HbO_2]_{max}$ (~80%) as observed for tumor case 2. However, the phantom showed a much larger slope between $pO_2$ and $\Delta[HbO_2]/\Delta[HbO_2]_{max}$, i.e., 39.5, prior to the threshold.

Figure 6c summarizes the data obtained from the tumors and phantom and plots them with reversed axes. In the phantom, $pO_2$ had increased from 0 mmHg to 70 mmHg by the stage that $\Delta[HbO_2]$ reached to 90% of $\Delta[HbO_2]_{max}$. This behavior is reminiscent of the hemoglobin oxygen dissociation curve. By comparison, the tumor $pO_2$ increased only from 14 mmHg to 30 mmHg in case 1 and from 10 mmHg to 21 mmHg in case 2 when $\Delta[HbO_2]$ approached to 90 % of $\Delta[HbO_2]_{max}$.

## 4. Discussion and conclusion

Tumor oxygenation involves a complex interplay of multiple compartments and parameters: blood flow, blood volume, blood vessel structure, and oxygen consumption. NIRS provides a global non-invasive estimate of average vascular oxygenation encompassing arterial, venous and capillary compartments. In agreement with our previous observations[13], the $\Delta[HbO_2]$ response is often biphasic, which we believe represents rapid elevation of arterial oxygenation, followed by more sluggish capillary components. Comparison with electrode measurements

indeed revealed that tumors are heterogeneous. Like NIRS measurements, $pO_2$ electrodes provide rapid assessment of $pO_2$ facilitating real time observation of dynamic changes. In Fig. 3a, $pO_2$ starts at a baseline value ~ 15 mmHg and increases rapidly in response to respiratory challenge with carbogen. Indeed, the rate approaches that of the vascular compartments. In a second tumor (Fig. 3b), where the interrogated location showed a slightly lower $pO_2$, the tissue response was more sluggish. For a third HI tumor, local baseline $pO_2$ was found to be < 5 mmHg, and this did not change with carbogen inhalation despite the response observed by NIRS. This suggests a danger of comparing a global vascular measurement with regional tumor $pO_2$, since tumors are known to be highly heterogeneous. This also demonstrates an essential need for NIR imaging of tumors to provide regional tumor vascular oxygenation details.

Indeed, FREDOM measurements in Fig. 4 revealed the heterogeneity in baseline oxygenation within individual tumors of this second tumor subline. Baseline $pO_2$ ranged from 1 – 75 mmHg, and response to carbogen was variable in terms of rate and extent, as seen for the HI subline using electrodes (Fig. 3). As with the electrodes, the better oxygenated tumor regions showed a faster and greater response to carbogen inhalation.

The phantom measurements indicate the reliability of the NIRS technique. Both phantom and tumor measurements indicate a sharp increase of $pO_2$ after the normalized $\Delta[HbO_2]$ reaches about 80% of its maximum. This coincides with the recognized sigmoidal binding of oxygen to hemoglobin. The difference between the phantom and tumor results reveals that the $pO_2$ response to $[HbO_2]$ changes in tumor is about 10 times smaller than that in tissue phantom when $pO_2$ values are relatively low (0 to 30 mmHg). This demonstrates a greater

hurdle to deliver oxygen from blood vasculature into the hypoxic regions of the tumor than into regular tissues. The slope at low $\Delta[HbO_2]/\Delta[HbO_2]_{max}$ in the tumors presumably also reflects oxygen consumption by the tumor tissues, as oxygen initially becomes available.

Both NIRS and electrodes offer essentially real time measurement of changes in oxygenation, which can be rapid (Fig. 3). Indeed, the inflow kinetics of vascular $O_2$ detected by NIRS are similar to those previously reported in the HI tumor line following a bolus of the paramagnetic contrast agents Gd-DTPA[24]. FREDOM has lower temporal resolution, but reveals the tumor heterogeneity and differential response of regions exhibiting diverse baseline $pO_2$. The results here correspond closely with more extensive observation[6, 8, 21]. While FREDOM currently requires 6½ minutes per $pO_2$ map, we have previously demonstrated alternative data acquisition protocol achieving 1 s time resolution in a perfused heart, albeit providing less precision in measurements and only a global determination.[25]

In conclusion, we have measured relative $[HbO_2]$ changes in tumor vasculature and tumor tissue $pO_2$ under carbogen intervention using NIRS and needle type $pO_2$ electrode, and the $pO_2$ data were also supported by the $^{19}F$ MR $pO_2$ mapping. The NIRS data showed significant changes in vascular oxygenation accompanying respiratory interventions, and changes in tumor vascular oxygenation preceded tumor tissue $pO_2$. The correlation between normalized tumor $\Delta[HbO_2]$ and tumor tissue $pO_2$ shows that there is a threshold of normalized $\Delta[HbO_2]$ for tumor cells to be efficiently oxygenated. This indicates the difficulty of oxygen delivery into the hypoxic regions of tumors. This study demonstrates that the NIRS technology can provide an efficient, real-time, non-invasive

approach to monitoring tumor physiology, and emphasizes the need to develop an imaging technique to reveal spatial heterogeneity.

**Acknowledgement**

This work was supported in part by NIH RO1 CA79515 (RPM), and the Department of Defense Breast Cancer Initiative grant BC990287 (HL). NMR experiments were conducted at the Mary Nell & and Ralph B. Rogers MR center, an NIH BRTP Facility no. 5-P41-RR02584. We are grateful to Sherwin Yen and William McSweeny for assistance with data acquisition and Dr. Peter Peschke for providing the original tumor cells.

**Figure Captions**

**Figure 1.** Schematic experimental setup of one channel, near infrared, frequency domain IQ instrument for tumor investigation *in vivo*. The 5-mm diameter fiber bundles deliver the laser light, comprising two wavelengths (758 and 785 nm), and detect the laser light transmitted through the implanted tumor. The $pO_2$ needle electrode measures tumor tissue $pO_2$.

**Figure 2.** Experimental setup for phantom study using 1% Intralipid in saline buffer. NIRS probes were placed in reflectance mode, while the gas bubbler was placed opposite to minimize liquid movement effects. After adding 2 ml of rabbit blood to a 200 ml solution, nitrogen gas and air were introduced to deoxygenate and oxygenate the solution, respectively.

**Figure 3.** Simultaneous dynamic changes of $\Delta[HbO_2]$ and $pO_2$ in R3327-HI rat prostate tumors using NIRS and $pO_2$ needle electrode; (a) A smaller tumor (1.5 $cm^3$) showed a rapid $pO_2$ response (Case 1), whereas (b) a bigger tumor (3.1 $cm^3$) showed a slower $pO_2$ response (Case 2). (c) In a third tumor where regional baseline $pO_2$ was < 5 mmHg, there was no $pO_2$ response (Case 3). The unit of $\Delta[HbO_2]$ is mM/DPF, where DPF is equal to the optical path length divided by the source-detector separation. Dotted vertical line marks the time when the gas was changed. The oxygen needle electrode was placed in tumors where $pO_2$ had a baseline value of about 10 mmHg.

**Figure 4.** Dynamic changes of $\Delta[HbO_2]$ and $pO_2$ in R3327-AT1 rat prostate tumors measured using NIRS and $^{19}F$ MR $pO_2$ mapping. The solid curves represent $\Delta[HbO_2]$, and the solid lines with solid circles represent mean $pO_2$ ± SE (Standard Error) of 21 (Fig. 4a) and 45 (Fig. 4b) voxels of each tumor. Dashed lines with open symbols are 4 representative voxels for each case. After a gas switched from air to carbogen, both the mean $pO_2$ of each tumor increased. Individual voxels showed totally different response, indicating heterogeneity. The tumor sizes were 3.2 $cm^3$ and 2.7 $cm^3$ for (a) and (b), respectively.

**Figure 5.** Simultaneous dynamic changes of $\Delta[HbO_2]$, $\Delta[Hb]_{total}$ and $pO_2$ in the phantom solution measured using NIRS and $pO_2$ needle electrode. The dark solid curve is for $\Delta[HbO_2]$, the lighter solid line is for $\Delta[Hb]_{total}$, and the solid circles show $pO_2$ values in the phantom solution. After ~3 minutes of baseline, the bubbling gas was changed from air to nitrogen to deoxygenate the solution and then switched back to air to reoxygenate the solution. The unit of $\Delta[HbO_2]$ is mM/DPF.

**Figure 6.** Changes of tumor tissue $pO_2$ with normalized changes of oxygenated hemoglobin (a) in tumors measured with NIRS and a $pO_2$ needle electrode, and (b) in the phantom solution using the same NIRS and $pO_2$ needle electrode. The slope between $pO_2$ and $\Delta[HbO_2]/\Delta[HbO_2]_{max}$ is 3.6 when $\Delta[HbO_2]/\Delta[HbO_2]_{max}$ is less than 0.8 in Case 2 tumor, while the slope obtained from the phantom solution is 39.5, which is ten times larger than that in Case 2. (c) Summarizing the relationship between $pO_2$ and normalized $\Delta[HbO_2]$ obtained from both tumors and the tissue phantom. Dotted horizontal line shows 90% of normalized $\Delta[HbO_2]$.

## References:


1. L. Gray, A. Conger, M. Ebert, S. Hornsey and O. Scott, "The concentration of oxygen dissolved in tissues at time of irradiation as a factor in radio-therapy," *Br. J. Radiol.*, **26**, pp. 638-648 (1953)

2. J. H. Kaanders, L. A. Pop, H. A. Marres, J. Liefers, F. J. van den Hoogen, W. A. van Daal, A. J. and van der Kogel, "Accelerated radiotherapy with carbogen and nicotinamide (ARCON) for laryngeal cancer," *Radiother. Oncol.*, **48**, pp. 115-22. (1998)

3. J. Overgaard and M. R. Horsman, "Modification of hypoxia-induced radioresistance in tumors by the use of oxygen and sensitizers," *Semin. Radiat. Oncol.*, **6**, pp. 10-21. (1996)

4. H. B. Stone, J. M. Brown and T. Phillips, "Oxygen in human tumors: correlations between methods of measurement and response to therapy," *Radiat. Res.*, **136**, pp. 422-434 (1993)

5. D. Cater and I. Silver, "Quantitative measurements of oxygen tension in normal tissues and in the tumors of patients before and after radiotherapy," *Acta Radiol.*, **53**, pp. 233-256 (1960)

6. D. Zhao, A. Constantinescu, E. W. Hahn and R. P. Mason. "Tumor oxygenation dynamics with respect to growth and respiratory challenge: Investigation of the Dunning prostate R3327-HI tumor," *Radiat. Res.*, **156(5)**, pp. 510-520 (2002)

7. J. A. O' Hara, F. Goda, E. Demidenko and H. M. Swartz, "Effect on regrowth delay in a murine tumor of scheduling split-dose irradiation based on direct $pO_2$ measurements by electron paramagnetic resonance

Oximetry," *Radiat. Res.*, **150**, pp. 549-56 (1998)

8. R. P. Mason, A. Constantinescu, S. Hunjan, D. Le, E. W. Hahn, P. P. Antich, C. Blum and P. Peschke, "Regional tumor oxygenation and measurement of dynamic changes," *Radiat. Res.*, **152**, pp. 239-249 (1999)

9. M. S. Patterson, B. Chance and B. C. Wilson, "Time resolved reflectance and transmittance for the non-invasive measurement of tissue optical properties," *Appl. Opt.*, **28**, pp. 2331-2336 (1986)

10. E. M. Sevick, B. Chance, J. Leigh, S. Nokia and M. Maris, "Quantitation of time- and frequency-resolved optical spectra for the determination of tissue oxygenation," *Anal. Biochem.*, **195**, pp. 330-351 (1991)

11. P. Peschke, E. W. Hahn, F. Lohr, F. Brauschweig, G. Wolber, I. Zuna and M. Wannenmacher, "Differential sensitivity of three sublines of the rat Dunning prostate tumor system R3327 to radiation and/or local tumor hyperthermia," *Radiat. Res.*,**150**, pp. 423-430 (1998)

12. E. W. Hahn, P. Peschke, R. P. Mason, E. E. Babcock and P. P. Antich, "Isolated tumor growth in a surgically formed skin pedicle in the rat: a new tumor model for NMR studies," *Magn. Reson. Imaging*, **11**, pp. 1007-1017 (1993)

13. H. Liu, Y. Song, K. L. Worden, X. Jiang, A. Constantinescu and R. P. Mason, "Noninvasive investigation of blood oxygenation dynamics of tumors by near-infrared spectroscopy," *Appl. Opt.*, **39**, pp. 5231-5243 (2000)

14. Y. Yang, H. Liu, X. Li and B. Chance, "Low-cost frequency-domain photon migration instrument for tissue spectroscopy, oximetry, and imaging," *Opt. Eng.*, **36**, pp. 1562-1569 (1997)

15. S. J. Matcher, C. E. Elwell, C. E. Cooper, M. Cope and D. T. Delpy, "Performance Comparison of Several Published Tissue Near-Infrared Spectroscopy Algorithms", *Anal. Biochem.*, **227**, pp. 54-68 (1995)

16. D.T. Delpy, M. Cope, P. van der Zee, S. Arridge, S. Wray, and J. Wyatt, "Estimation of optical pathlength through tissue from direct time of flight measurement," Phys. Med. Biol. 33(12), 1433-1442 (1988).

17. M. Ferrari, Q. Wei, L. Carraresi, R. A. De Blasi and G. Zaccanti, "Time-resolved spectroscopy of human forearm", *J. Photochem. Photobiol.*, **16**, pp. 141-153, (1992)

18. P. van der Zee, M. Cope, S. R. Arridge, M. Essenpreis, L. A. Potter, A. D. Edwards, J. S. Wyatt, D. C. McCormick, S. C. Roth, E. O. R. Reynolds and D. T. Delpy, "Experimentally measured optical pathlengths for the adult head, calf and forearm and the head of the newborn infants as a function of inter optode spacing", *Adv. Exp. Med. Biol.*, **316**, pp. 143-153, (1992)

19. R. G Steen, K. Kitagishi and K. Morgan, " *In vivo* measurement of tumor blood oxygenation by near-infrared spectroscopy: Immediate effects of pentobarbital overdose or carmustine treatment", *J. Neuro-Oncol.*, **22**, pp. 209-220 (1994)

20. B. R. Barker, R. P. Mason, N. Bansal and R. M. Peshock, "Oxygen tension mapping by $^{19}F$ echo planar NMR imaging of sequestered perfluorocarbon," *JMRI,* **4**, pp. 595-602 (1994)

21. S. Hunjan, D. Zhao, A. Constantinescu, E. W. Hahn, P. Antich and R. P. Mason, "Tumor oximetry: demonstration of an enhanced dynamic mapping procedure using fluorine-19 echo planar magnetic resonance

imaging in the dunning prostate R3327-AT1 rat tumor," *Int. J. Radiat. Oncol. Biol. Phys.*, **49**, pp. 1097-1108 (2001)

22. R. L. Fournier, "Oxygen transport in biological systems," Chap. 4 in Basic Transport Phenomena in Biomedical Engineering, pp. 87-94, Taylor & Francis, Lillington (1999)

23. S. I. Fox, "Respiratory physiology," Chap. 16 in Human Physiology, pp. 508-513, The McGraw-Hill companies, Inc., Boston (1999)

24. G. Brix, J. Debus, M. Mueller-Schimpfle, P. Peschke, P. Huber, H. J. Zabel and W. Lorenz, "MR-tomographische Quantifizierung struktureller und funktioneller Gewebeveraenderungen an stosswellen-therapierten Dunning-Prostata-Tumoren," *Z. Med. Phys.*, **3**, pp. 76-82 (1993)

25. R. P. Mason, F. M. H. Jeffrey, C. R. Malloy, E. E. Babcock and P. P. Antich, "A noninvasive assessment of myocardial oxygen tension: $^{19}F$ NMR sepectroscopy of sequestered perfluorocarbon emulsion," *Magn. Reson. Med.*, **27**, pp. 310-317 (1992)

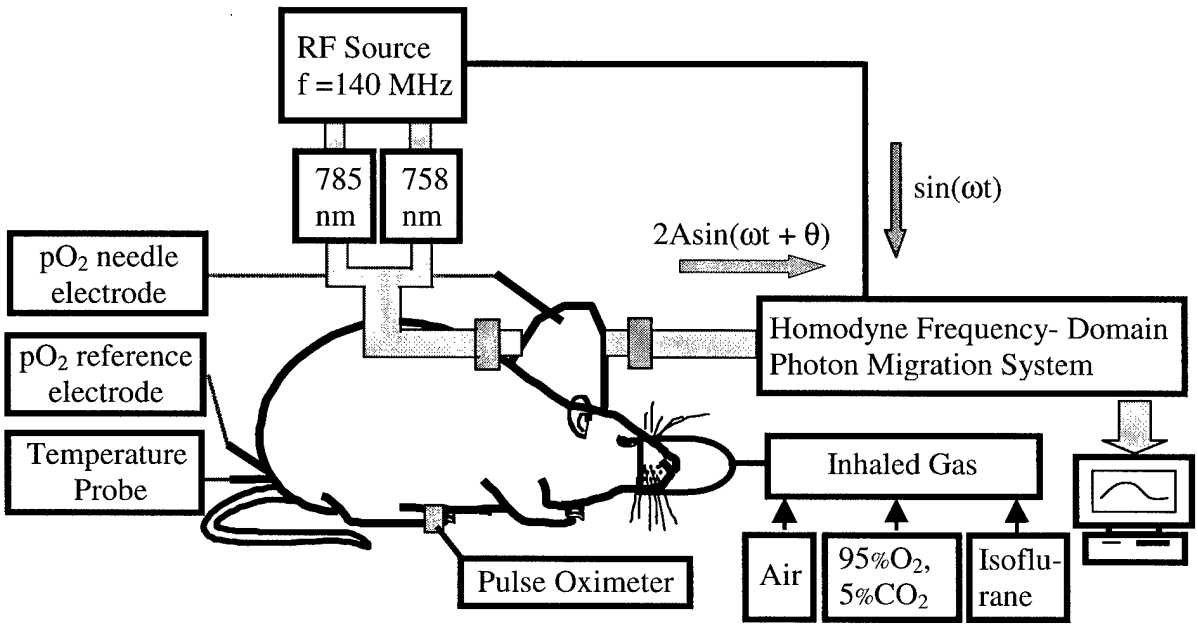
RF Source
f =140 MHz
785
nm
758
nm
sin(ωt)
2Asin(ωt + θ)
pO2 needle
electrode
pO2 reference
electrode
Temperature
Probe
Homodyne Frequency- Domain
Photon Migration System
Inhaled Gas
Air
95%O2,
5%CO2
Isoflu-
rane
Pulse Oximeter

Figure 1

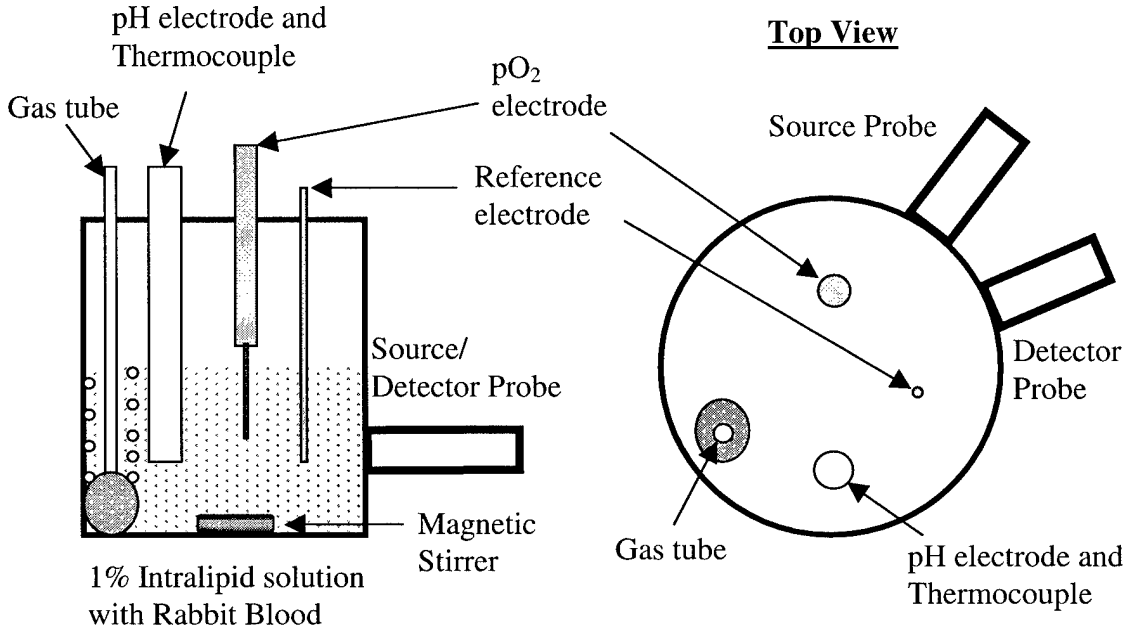
pH electrode and
Thermocouple
Gas tube
$pO_2$
electrode
Reference
electrode
Source/
Detector Probe
Magnetic
Stirrer
1% Intralipid solution
with Rabbit Blood
Top View
Source Probe
Detector
Probe
Gas tube
pH electrode and
Thermocouple

Figure 2

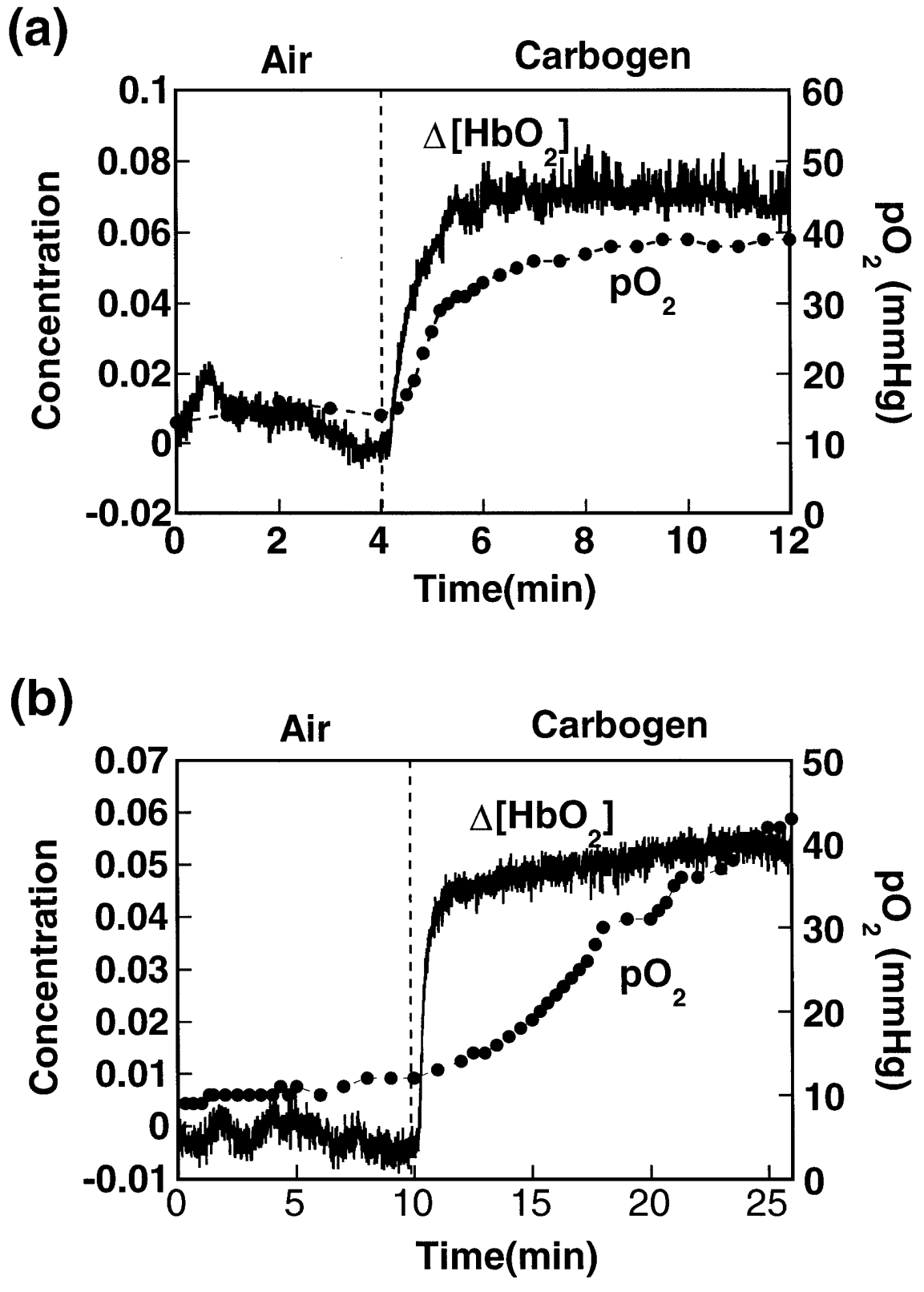
(a)
Air
Carbogen
0.1
0.08
0.06
0.04
0.02
0
-0.02
Concentration
Δ[HbO2]
pO2
60
50
40
30
20
10
0
pO2 (mmHg)
0
2
4
6
8
10
12
Time(min)
(b)
Air
Carbogen
0.07
0.06
0.05
0.04
0.03
0.02
0.01
0
-0.01
Concentration
Δ[HbO2]
pO2
50
40
30
20
10
0
pO2 (mmHg)
0
5
10
15
20
25
Time(min)

Figure 3

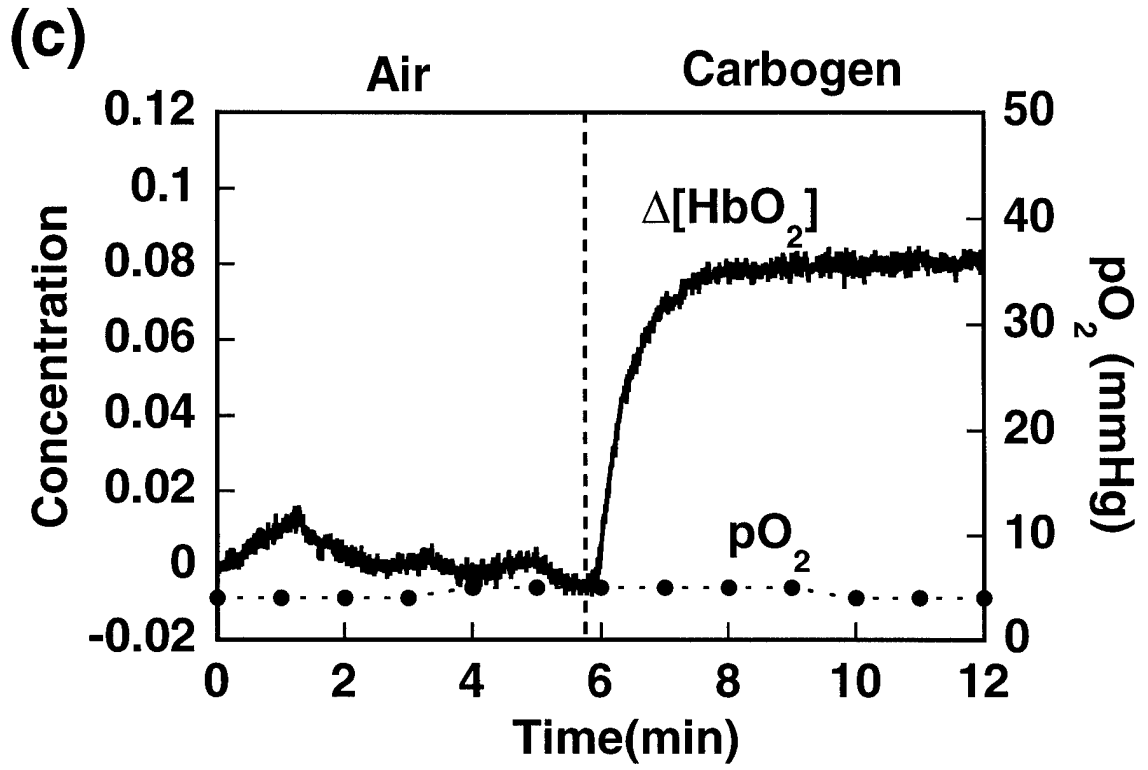
(c)
Air
Carbogen
0.12
0.1
0.08
0.06
0.04
0.02
0
-0.02
Concentration
50
40
30
20
10
0
pO2 (mmHg)
Δ[HbO2]
pO2
0
2
4
6
8
10
12
Time(min)

Figure 3

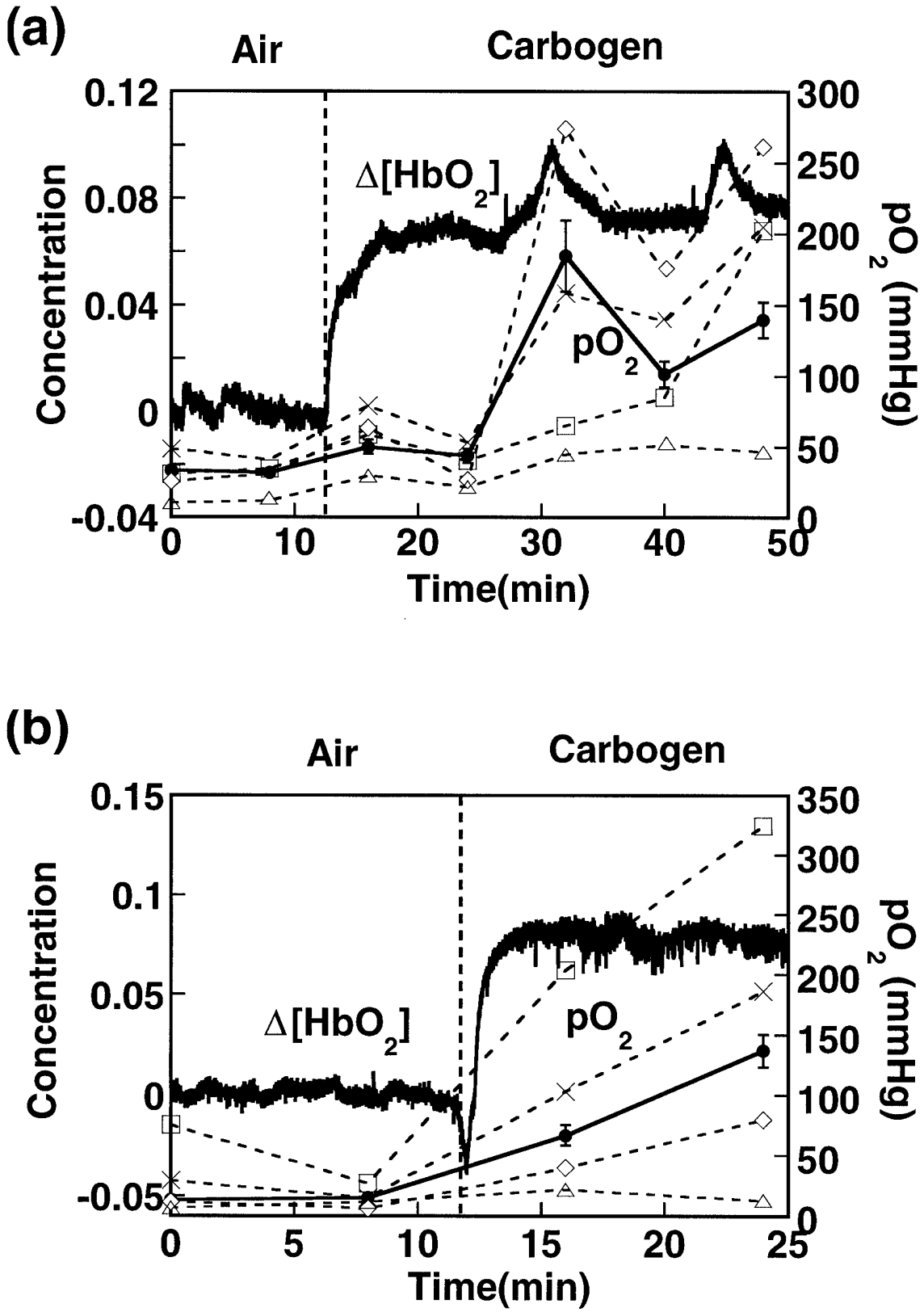
(a)
Air
Carbogen
0.12
0.08
0.04
0
-0.04
Concentration
Δ[HbO2]
pO2
300
250
200
150
100
50
0
pO2 (mmHg)
0
10
20
30
40
50
Time(min)
(b)
Air
Carbogen
0.15
0.1
0.05
0
-0.05
Concentration
Δ[HbO2]
pO2
350
300
250
200
150
100
50
0
pO2 (mmHg)
0
5
10
15
20
25
Time(min)

Figure 4

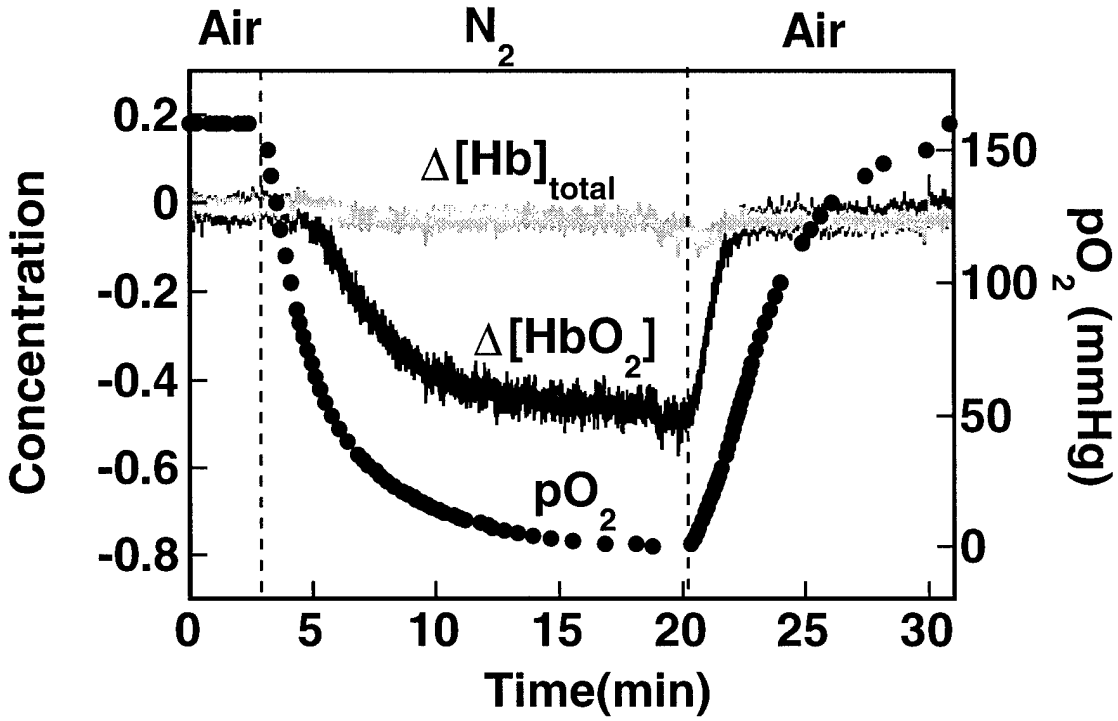
Air
N2
Air
0.2
0
-0.2
-0.4
-0.6
-0.8
Concentration
Δ[Hb]total
Δ[HbO2]
pO2
150
100
50
0
pO2 (mmHg)
0
5
10
15
20
25
30
Time(min)

Figure 5

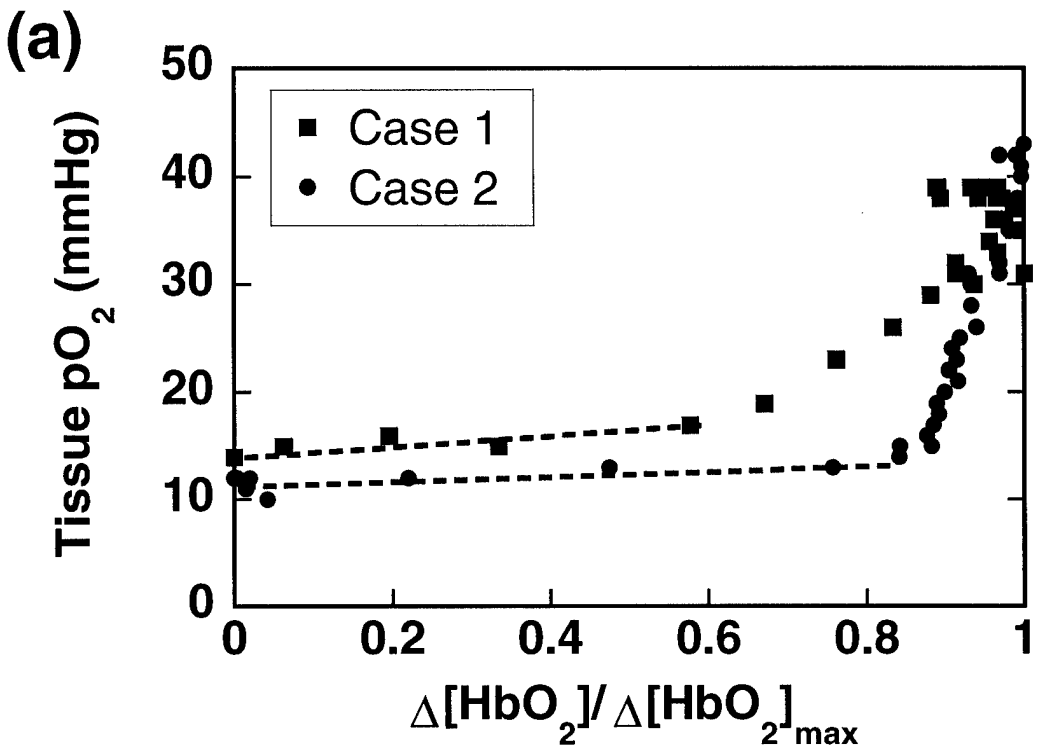
(a)
Tissue pO2 (mmHg)
50
40
30
20
10
0
Case 1
Case 2
0
0.2
0.4
0.6
0.8
1
Δ[HbO2]/Δ[HbO2]max

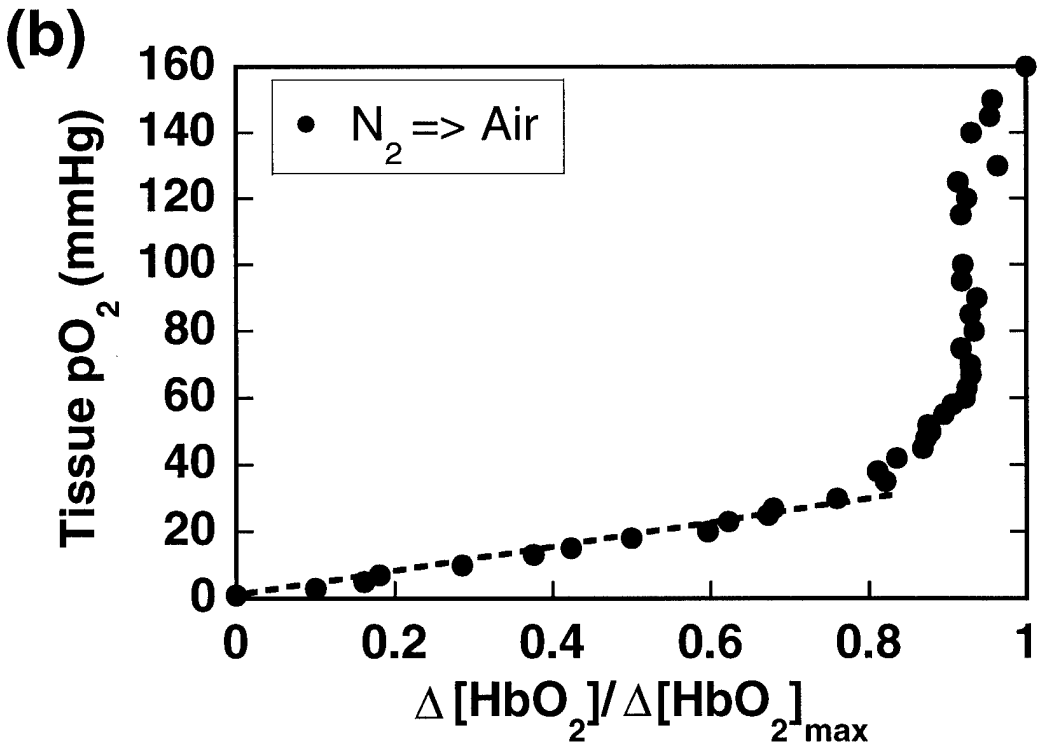
(b)
Tissue pO2 (mmHg)
160
140
120
100
80
60
40
20
0
N2 => Air
0
0.2
0.4
0.6
0.8
1
Δ[HbO2]/Δ[HbO2]max

Figure 6

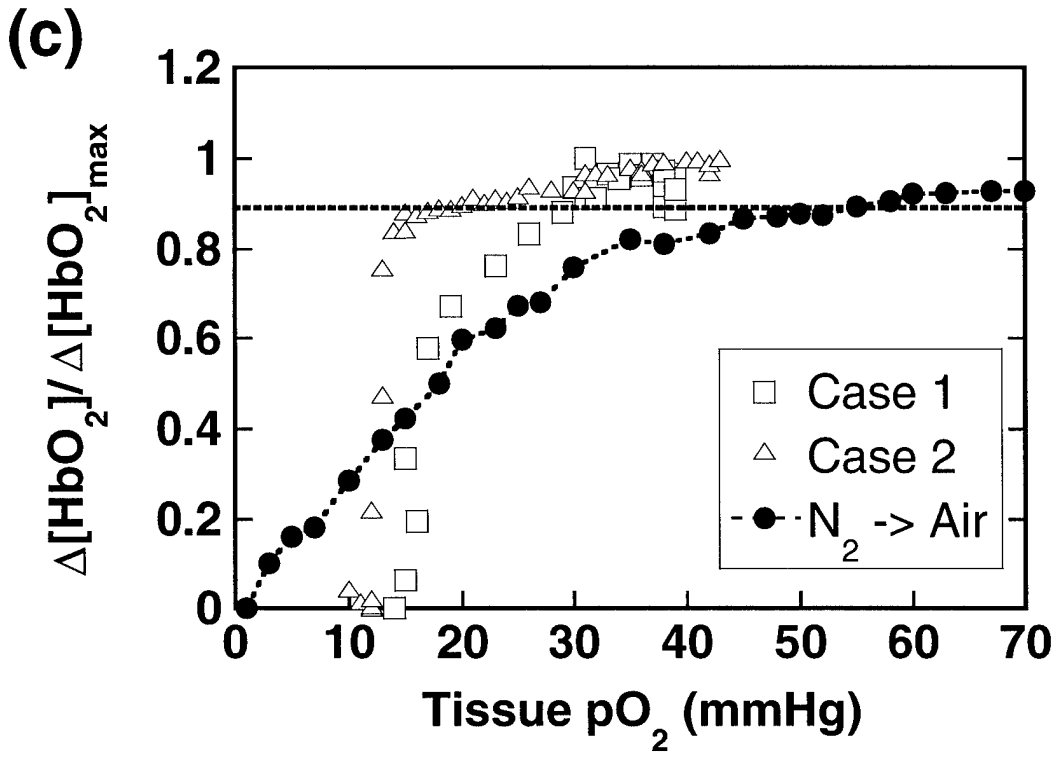
(c)
1.2
1
0.8
0.6
0.4
0.2
0
0
10
20
30
40
50
60
70
Δ[HbO2]/Δ[HbO2]max
Tissue pO2 (mmHg)
Case 1
Case 2
N2 -> Air

Figure 6

## Regional Tumor Oxygen Tension and Blood Flow: Correlation Studies Using $^{19}F$ PBSR-EPI of Hexafluorobenzene

Y. Song, R. P. Mason, S. Hunjan, A. Constantinescu, E. W. Hahn, and P. P. Antich,
*Department of Radiology, UT Southwestern Medical Center, Dallas, Texas, USA*

**Introduction:** It is recognized that therapeutic efficacy may be influenced by tumor oxygenation. In particular, hypoxic tumors resist radiotherapy. We have recently shown the feasibility of monitoring tumor oxygen tension based on $^{19}F$ PBSR-EPI of hexafluorobenzene (HFB) [1]. We also found that HFB clears from tumors over a period of hours [2]. Since HFB is a non-ionic freely diffusable tracer, it appeared that clearance rate would provide an indication of relative tumor blood flow (TBF). We have now investigated the feasibility of mapping the clearance rate of HFB and correlating this putative blood flow marker with corresponding $pO_2$.

**Methods:** Dunning prostate R3327-AT1 or breast 13762 NF adenocarcinoma was implanted in a skin pedicle on the foreback of a rat. When the tumor reached 1~2 cm diameter, 40 µl HFB were injected directly into the tumor (IT), both centrally and peripherally. The rat was maintained under general gaseous anesthesia (33% $O_2$, 66% $N_2O$ and 0.5% methoxyflurane). A homebuilt tunable 2 cm $^{1}H/^{19}F$ single turn solenoid coil was placed around the tumor and MR experiments were performed using a 4.7 T magnet equipped with actively shielded gradients. 3D $^{1}H$ images were acquired for anatomical reference and corresponding $^{19}F$ images were obtained to show the distribution of HFB. Tumor oxygenation was assessed using $^{19}F$ PBSR-EPI of HFB. By applying the acquisition protocol ARDVARC (Alternated Relaxation Delays with Variable Acquisitions to Reduce Clearance effects) [2], we achieved $R1$ maps in 8 min. A series of maps were acquired over a period of 2 hours with respect to respiratory challenges. $pO_2$ maps were then generated by applying the relationship: $pO_2(\text{torr}) = [R1(s^{-1}) - 0.074]/0.0016$ to the $R1$ maps. The data also allowed us to produce a clearance map based on EPI images with the longest delay (90 s).

**Results:** $pO_2$ maps were generated with a typical precision of 2 ~ 5 torr and 30 ~ 100 individual voxels within a tumor. For many regions, the HFB signal intensity was found to decline exponentially with a typical clearance half-life ranging from $T_{1/2}$ = 700 to 1200 min, though many voxels indicated no apparent changes.

**Discussion:** Regional tumor oxygen tension and blood flow are important physiological parameters and the opportunity to measure both simultaneously would be of value in physiological research. Based on the preliminary data presented here, we believe that clearance of HFB provides an indication of relative TBF by analogy with studies of cerebral blood flow using freon-23 [3]. In future studies, such measurements will be rigorously evaluated.

**References:**

[1] D. Le, *et al.*, *MRI*, 15, 971-981 (1997). [2] S. Hunjan, *et al.*, *IJROBP*, 41, 161-171 (1998)
[3] J. R. Ewing, *et al.*, *Stroke*, 21, 100-106 (1990).

This study was supported in part by grants from The American Cancer Society (RPM), The Whitaker Foundation (RPM), the DOD Breast Cancer Initiative (YS), and NIH BRTP.

# TUMOR OXYGEN DYNAMICS: COMPARISON BETWEEN $^{19}$F MR-EPI OF HEXAFLUOROBENZENE AND FREQUENCY DOMAIN NIR SPECTROSCOPY

Song[1,2], Y.; Worden[1], K. L.; Jiang[1], X.; Zhao[2], D.; Constantinescu[2], A.; Liu[1], H.; and Mason[2], R. P.
[1]*Joint Graduate Program in Biomedical Engineering,*
[2]*Department of Radiology, UT Southwestern Medical Center, Dallas, TX 75235, USA*

**Introduction:** Oxygen plays a key role in tumor therapy and may be related to tumor development: *e.g.*, angiogenesis and metastasis. Using noninvasive techniques to accurately measure oxygenation could assist in developing novel therapies. Here, we have used $^{19}$F MR-EPI relaxometry of hexafluorobenzene (HFB)[1] to monitor tissue oxygen tension ($pO_2$) of rat breast tumors and compared the results with changes in hemoglobin saturation ($sO_2$) and concentration in the vasculature of the tumors observed using a new dual wavelength homodyne near-infrared (NIR) system.

**Methods:** Breast 13762 NF adenocarcinomas were implanted in skin pedicles on the forebacks of adult female Fischer rats. Once the tumors reached ~1cm diameter, the tumor blood $sO_2$ was assessed by NIR spectroscopy using a dual wavelength NIR system (758 nm and 782 nm) in transmission geometry [2]. The tumor blood volume and $sO_2$ were calculated from the light amplitude. The rats were maintained under general gaseous anesthesia (33% $O_2$, 66% $N_2O$ and 0.5% methoxyflurane). Once stable baseline measurements were achieved, the inhaled gas was altered to pure oxygen or carbogen and dynamic changes were observed over a period of two hours. Both the magnitude and rate of change of $sO_2$ were examined. Following the NIR experiments, 40 µl HFB were injected directly into both central and peripheral regions of the tumors. A tunable 2 cm $^1$H/$^{19}$F single turn solenoid coil was placed around the tumor and MR experiments were performed using a 4.7 T magnet. Regional tumor $pO_2$ was estimated using the relationship: $pO_2(\text{torr}) = [R1 - 0.074]/0.0016$, where $R1$ is the spin lattice relaxation rate of HFB. Twenty-three $pO_2$ maps were produced in 3 hours with respect to respiratory challenge.

**Results:** NIR showed significant changes in vascular oxygenation accompanying respiratory interventions. $^{19}$F MR-EPI also showed significant changes in tissue $pO_2$, with considerable regional heterogeneity in both absolute values and rate of change accompanying interventions. Generally, changes in vascular $sO_2$ preceded tissue $pO_2$, particularly for smaller tumors.

**Discussion:** Regional tumor $pO_2$ and blood $sO_2$ are important physiological parameters. The capability to measure them will provide insight into progressive physiological changes in a tumor accompanying interventions. NIR has the advantage of being entirely noninvasive, but the MRI approach clearly reveals detailed oxygenation heterogeneity. We believe that better understanding and monitoring of tumor oxygenation can lead to improved tumor therapy.

**References:**

[1] D. Le, *et al.*, *MRI*, 15, 971-981 (1997). [2] K. Worden, *et al.*, SPIE, 3597 (1999)

**Acknowledgments:**

Supported in part by grants from The American Cancer Society (RPM), The Whitaker Foundation (RPM and HL), the DOD Breast Cancer Initiative (YS), and NIH BRTP.

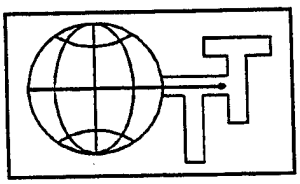

# TUMOR OXIMETRY: COMPARISON OF $^{19}F$ MR EPI AND ELECTRODES

Mason, Ralph; Hunjan, Sandeep; Constantinescu, Anca; Song, Yulin; Zhao, Dawen; Hahn, Eric; Antich, Peter; and Peschke, Peter+. U.T. Southwestern Medical Center, Dallas, TX and +DKFZ, Heidelberg, Germany

Therapeutic efficacy may be influenced by tumor oxygenation. In particular, hypoxic tumors resist radiotherapy and may be good candidates for hypoxia selective cytotoxic agents. We recently described a novel approach to measuring regional tumor oxygen tension using $^{19}F$ pulse burst saturation recovery (PBSR) nuclear magnetic resonance (NMR) echo planar imaging (EPI) relaxometry of hexafluorobenzene (HFB) (1). We have now compared oxygen tension measurements in a group of size matched Dunning prostate rat tumors R3327-AT1 made using this new method with a traditional polarographic method: the Eppendorf Histograph. We also demonstrate extension of the MR technique to rat breast tumors.

Methods: Dunning prostate R3327-AT1 or breast 13762 NF adenocarcinoma was implanted in a skin pedicle on the foreback of a rat. When the tumor reached a volume ~2 $cm^3$ or > 3.5 $cm^3$, 40 µl HFB were injected directly into both central and peripheral regions of the tumor. The rat was maintained under general anesthesia (33% $O_2$, 66% $N_2O$ and 0.5% methoxyflurane). A tunable 2 cm $^1H/^{19}F$ single turn solenoid coil was placed around the tumor and MR experiments were performed using a 4.7 T magnet equipped with actively shielded gradients. 3D $^1H$ images were acquired for anatomical reference and corresponding $^{19}F$ images were obtained to show the distribution of HFB. Tumor oxygenation was assessed using $^{19}F$ PBSR-EPI of HFB. A series of $pO_2$ maps was acquired over a period of 2 hours with respect to respiratory challenge using the relationship: $pO_2$ (torr) = (R1-0.074)/0.0016. Histography was applied to groups of size matched tumors, which did not receive HFB.

Results: Similar oxygen tension distributions were found using each method and both techniques showed that tumors with volume > 3.5 $cm^3$ were significantly ($p < 0.0001$) less well oxygenated than smaller tumors (volume < 2 $cm^3$). Using the $^{19}F$ EPI approach we also examined response to respiratory challenge. Increasing the concentration of inspired oxygen from 33% to 100% $O_2$ produced a significant increase ($p < 0.0001$) in tumor oxygenation for a group of small tumors. In contrast no change was observed in the mean $pO_2$ for a group of large tumors. Consideration of individual tumor regions, irrespective of tumor size showed a strong correlation between the maximum $pO_2$ observed when breathing 100% $O_2$, as compared with mean baseline $pO_2$.

Discussion: These results demonstrate the similarity of results obtained using electrode or MR approaches to tumor oximetry. They also indicate the feasibility of $^{19}F$ MR to monitor dynamic changes in regional $pO_2$ in response to acute interventions. The ability to measure $pO_2$ could be valuable in pre-clinical evaluation of novel therapies and could allow therapy to be individualized and optimized for patients.

Reference:

1. D. Le, R. P. Mason, S. Hunjan, A. Constantinescu, B. R. Barker and P. P. Antich, Regional tumor oxygen dynamics: $^{19}F$ PBSR EPI of hexafluorobenzene. *Magn. Reson. Imaging*, 15, 971-81 (1997).

This work was supported in part by The American Cancer Society (RPM), DOD Breast Cancer initiative (YS), Verein zur Forderung der Krebserkennung and Krebshandlung e.V. Heidelberg (PP) and the NIH BRTP Facility #5-P41-RR02584.

**Tumor oxygenation and measurement of regional dynamic changes**

Ralph P. Mason, Sandeep Hunjan, Anca Constantinescu, Yulin Song, Eric W. Hahn, and Peter P. Antich, Advanced Radiological Sciences, U.T. Southwestern Medical Center, Dallas, Texas and Christian Blum and Peter Peschke, Deutsches Krebsforschungszentrum, Heidelberg, Germany

Therapeutic efficacy may be influenced by tumor oxygenation. In particular, hypoxic tumors resist radiotherapy and may be good candidates for hypoxia selective cytotoxic agents. We recently described a novel approach to measuring regional tumor oxygen tension using $^{19}F$ pulse burst saturation recovery (PBSR) nuclear magnetic resonance (NMR) echo planar imaging (EPI) relaxometry of hexafluorobenzene (HFB) (1). We have now compared oxygen tension measurements in a group of size matched Dunning prostate rat tumors R3327-AT1 made using this new method with a traditional polarographic method: the Eppendorf Histograph. We also demonstrate extension of the MR techniques to rat breast tumors.

Methods: Rat Dunning prostate R3327-AT1 or breast 13762 NF adenocarcinomas were examined at a volume $<2$ cm$^3$ or $> 3.5$ cm$^3$: for MRI 40 µl HFB were injected directly into the tumor, both centrally and peripherally. The rat was maintained under general gaseous anesthesia (33% $O_2$, 66% $N_2O$ and 0.5% methoxyflurane). A tunable 2 cm $^1H/^{19}F$ single turn solenoid coil was placed around the tumor and MR experiments were performed using a 4.7 T magnet equipped with actively shielded gradients. Tumor oxygenation was assessed using $^{19}F$ PBSR-EPI of HFB. By applying the acquisition protocol ARDVARC (Alternated Relaxation Delays with Variable Acquisitions to Reduce Clearance effects), we achieved R1 maps in 8 min. A series of maps was acquired over a period of 2 hours with respect to respiratory challenges. $pO_2$ maps were then generated by applying the relationship: $pO_2$ (torr) = (R1 -0.074)/0.0016. In parallel experiments $pO_2$ was determined polarographically

Results: Similar oxygen tension distributions were found using $^{19}F$ MRI or polarography and both techniques showed that tumors with volume $> 3.5$ cm$^3$ were significantly ($p < 0.0001$) less well oxygenated than smaller tumors (volume $< 2$ cm$^3$). Using the $^{19}F$ EPI approach we also examined response to respiratory challenge. Increasing the concentration of inspired oxygen from 33% to 100% $O_2$ produced a significant increase ($p < 0.0001$) in tumor oxygenation for a group of small tumors. In contrast no change was observed in the mean $pO_2$ for a group of large tumors. Consideration of individual tumor regions, irrespective of tumor size showed a strong correlation between the maximum $pO_2$ observed when breathing 100% $O_2$, as compared with mean baseline $pO_2$.

Conclusions: These results further demonstrate the usefulness of $^{19}F$ EPI to assess changes in regional tumor oxygenation. The ability to measure $pO_2$ could be valuable in pre-clinical evaluation of novel therapies and ultimately allow therapy to be individualized and optimized for patients.

This work was supported in part by The American Cancer Society (RPM), The Whitaker Foundation (RPM), DOD Breast Cancer Initiative (YS), Verein zur Förderung der Krebserkennung und Krebshandlung e.V. Heidelberg (PP) and the NIH BRTP Facility #5-P41-RR02584.

1. D. Le, R. P. Mason, S. Hunjan, A. Constantinescu, B. R. Barker and P. P. Antich, Regional tumor oxygen dynamics: $^{19}F$ PBSR EPI of hexafluorobenzene. *Magn. Reson. Imaging*, **15**, 8, 971-81 (1997).

# Regional Tumor Tissue $pO_2$ and Blood $sO_2$ : Comparison of $^{19}F$ MR EPI and Frequency Domain NIR Spectroscopy

Y. Song[1,2]; X. Jiang[1]; D. Zhao[2]; A. Constantinescu[2]; H. Liu[1]; and R. P. Mason[2]
[1]*Joint Graduate Program in Biomedical Engineering,*
[2]*Department of Radiology, UT Southwestern Medical Center, Dallas, TX 75235, USA*

## INTRODUCTION

Tumor oxygenation has a profound effect on growth and development, and hypoxia reduces radiosen-sitivity. Moreover, increasing evidence from clinical trials has indicated that poorly oxygenated tumors have poor prognosis. Therefore, development of non-invasive techniques to accurately measure oxygenation is essential in cancer treatment planning and prognosis prediction. Here, we present and compare two such techniques: the FREDOM (Fluorocarbon Relaxometry using Echo planar imaging for Dynamic Oxygen Mapping) approach based on hexafluorobenzene (HFB)[1] to measure tumor tissue oxygen tension ($pO_2$) and NIR spectroscopy to measure changes in tumor vascular hemoglobin saturation ($sO_2$) and concentration [Hb]. The synergistic application of MR and NIR techniques could provide new insight into issues of tumor angiogenesis and perfusion.

## METHODS

NF 13762 breast and Dunning prostate R3327-AT1 adenocarcinomas were implanted in skin pedicles on the forebacks of adult female Fischer and male Copenhagen rats (~250 g), respectively. Once the tumors reached ~1 cm diameter, the rats were anesthetized with 200 µl ketamine hydrochloride (100 mg/ml) and maintained under general gaseous anesthesia (33% $O_2$, 66% $N_2O$ and 0.5% methoxyflurane). The tumor vascular $sO_2$ was assessed by NIR spectroscopy using a new dual wavelength, homodyne system (wavelengths 758 nm and 782 nm)[2], while inhaled gas was alternated between 33% $O_2$, carbogen (95% $O_2$ + 5% $CO_2$), and 100% $O_2$. The light amplitude and phase changes caused by the tumor are related to changes in hemoglobin concentration [Hb] and hemoglobin saturation [$HbO_2$], i.e., $sO_2$:

$$\Delta[Hb]_{total} = -[3.56 * \log(A_I/A_C)^{758} + 8.59 * \log(A_I/A_C)^{782}]/d \quad (1)$$

$$\Delta[HbO_2] - \Delta[Hb] = -[18.27 * \log(A_I/A_C)^{758} + 20.92 * \log(A_I/A_C)^{782}]/d \quad (2)$$

where $A_I$ is the initial amplitude (amplitude of baseline), $A_C$ the current amplitude, d the direct source-detector separation in cm, and Δ[] the change in concentration in mM.

Following the NIR experiments, a tunable 2 cm $^1H/^{19}F$ single turn solenoid coil was placed around the tumor and 40 µl HFB were injected directly into both central and peripheral regions of the tumor using a 32 G needle. 3D spin-echo (SE) $^1H$ images were acquired for anatomical reference and corresponding $^{19}F$ images were then obtained to show the distribution of HFB in the tumor. Regional tumor $pO_2$ maps were generated using $^{19}F$ PBSR-EPI based on the relationship: $pO_2(\text{torr}) = [R1 - 0.0836]/0.00188$, where $R1$ (1/T) is the spin lattice relaxation rate of HFB in 1/sec.

## RESULTS

Tumor vascular $sO_2$ increased almost immediately after a gas switch from baseline (33% $O_2$) to either carbogen or 100% $O_2$ and increased steadily for several minutes, and then gradually returned to baseline after the gas was switched back to baseline. In contrast, total hemoglobin change was insignificant, indicating relatively constant blood volume in the tumor. Tumor tissue $pO_2$ also showed significant changes, but with considerable regional heterogeneity in both absolute values and rate of change. Both carbogen and 100% $O_2$ inhalation produced significant changes in $sO_2$ and $pO_2$, especially with 100% $O_2$ inhalation. Temporal dynamic response in both $sO_2$ and $pO_2$ were modeled and exponential time constants were determined. The FREDOM technique also allowed us to compute the time constant on a voxel-by-voxel basis. It was found that $sO_2$ had a faster time constant than $pO_2$, especially in the cases of larger tumors, which were found to be less well oxygenated and presumably less well perfused. It was also found that some tumors showed a bimodal response (slow plus fast) in $sO_2$, as compared to a unimodal response (slow) in $pO_2$.

## DISCUSSION

An increase in inspired gas $FO_2$ should lead to increased tumor vascular $sO_2$, and hence, increased tumor tissue $pO_2$. Our data indicate that breathing elevated $O_2$ did indeed have a significant effect on both tumor vascular $sO_2$ and tissue $pO_2$. Vascular $sO_2$ values were found to have a faster time constant than tumor tissue $pO_2$, with greater differences in large tumors. This probably reflects the extensive perfusion of the small tumors with lesser perfusion of large tumors since time constant should be inversely proportional to tumor blood flow (TBF), as reflected by lower mean $pO_2$ and larger hypoxic fraction. We believe that application of multiple approaches to tumor oxygenation can lead to better understanding of tumor physiology and probably optimized tumor therapy.

## ACKNOWLEDGMENTS

This work was supported in part by grants from The American Cancer Society (RPG-97-116-010CCE; RPM), The Whitaker Foundation (HL), the DOD Breast Cancer Initiative (DAMD17-97-1-7261;YS), NIH 1RO1-CA79515 (RPM), and P41-RR02584.

## REFERENCES

1. Le, D., Mason, R.P., Hunjan, S., Constantinescu, A., Barker, B.R., and Antich, P.P., *Regional Tumor Oxygen Dynamics: $^{19}F$ PBSR EPI of Hexafluorobenzene*. Magn. Reson. Imaging. 15:971-981, 1997.
2. Yunsong, Y., Liu, H., Li, X., and Chance, B., *Low-Cost Frequency-Domain Photon Migration Instrument for Tissue Spectroscopy, Oximetry, and Imaging*. Opt. Eng. 36(5):1562-1569, 1997.

The Era of Hope Meeting, 2000
Atlanta, GA

# REGIONAL TUMOR OXYGEN DYNAMICS: RELATING TISSUE $pO_2$ TO THE VASCULATURE

**Y. Song[1,2], X. Jiang[1], D. Zhao[2], A. Constantinescu[2], H. Liu[1], and R. P. Mason[2]**

[1]*Joint Graduate Program in Biomedical Engineering,*
[2]*Department of Radiology, UT Southwestern Medical Center, Dallas, TX 75235, USA*

E-mail: song1058@hotmail.com

**INTRODUCTION** Tumor oxygenation has a critical influence on success in radiotherapy and is thought to play a key role in angiogenesis and metastasis. However, no non-invasive procedure for tumor oximetry has been established in clinical practice, so far. Here, we present and compare two oximetry techniques: the FREDOM (Fluorocarbon Relaxometry using Echo planar imaging for Dynamic Oxygen Mapping) approach based on hexafluorobenzene (HFB) to measure tumor tissue oxygen tension ($pO_2$) and near infrared (NIR) spectroscopy based on a new I/Q system to measure changes in tumor vascular hemoglobin saturation ($sO_2$) and concentration [Hb].

**METHODS** NF 13762 breast adenocarcinomas were implanted in skin pedicles on the forebacks of adult female Fischer rats. Once the tumors reached ~1 cm diameter, the dynamic characteristics of tumor vascular $sO_2$ in response to respiratory challenge were monitored by NIR spectroscopy. Then, 40 µl HFB were injected directly into the tumor. 3-D MR spin-echo $^1H$ images were acquired for anatomical reference and corresponding $^{19}F$ images were then obtained to reveal the distribution of HFB in the tumor. The dynamic characteristics of regional tumor $pO_2$ were assessed using FREDOM.

**RESULTS** Tumor vascular $sO_2$ increased rapidly after a gas switch from baseline (33% $O_2$) to either carbogen or 100% $O_2$ and then slowly returned to baseline after the gas was switched back to baseline. Total hemoglobin change was insignificant. Tumor tissue $pO_2$ also showed significant changes, but with considerable regional heterogeneity in both absolute values and rate of change. Changes in $sO_2$ preceded those in $pO_2$. Tumor voxels with high baseline $pO_2$ had significantly different response characteristics from those with initially low $pO_2$, with voxels of high baseline $pO_2$ showing significant changes in $pO_2$, while voxels of low baseline $pO_2$ showing small changes. Strong correlation existed between the maximum $pO_2$ value attained during the course of an experiment and mean baseline $pO_2$.

**CONCLUSIONS** Synergistic application of the FREDOM and NIR techniques will provide new insight into issues of tumor angiogenesis and perfusion, and could lead to improved tumor therapy.

**ACKNOWLEDGMENTS** This work was supported in part by The U.S. Army Medical Research and Materiel Command under DAMD17-97-1-7261 (YS), The American Cancer Society (RPG-97-116-010CCE; RPM), The Whitaker Foundation (HL), and NIH BRTP P41-RR02584.

# Noninvasive measurement of tumor hemoglobin dynamics using near-infrared spectroscopy

**Hanli Liu, Xin Jiang, Katherine L. Worden,**
*Joint Graduate Program in Biomedical Engineering, University of Texas at Arlington , Arlington, TX, 76109*
*Tel: (817) 272-2054; FAX: (817) 272-2251; e-mail address: hanli@uta.edu*

**Yulin Song, Anca Constantinescu, and Ralph Mason**
**Department of Radiology, University of Texas Southwestern Medical Center, Dallas, TX, 75235*
*Tel: (214) 648-8926; FAX: (214) 648-2991; e-mail address: Ralph.Mason@email.swmed.edu*

**Abstract:** Dynamic changes in blood oxygenation of tumor vasculature grown on rats are measured by near infrared spectroscopy. Significant temporal changes in tumor oxygenation accompanying respiratory challenge are modeled by exponential expressions with fast and slow time constants.

©1999 Optical Society of America
**OCIS codes:** (170.1470) blood/tissue constituent monitoring; (170.3660) light propagation in tissues; (170.4580) optical diagnostics for medicine; (170.5280) photon migration; (290.1990) diffusion; (290.7050)turbid media.

## 1. Introduction

Hypoxic cells *in vitro* and in animal tumors *in vivo* are documented to be three times more resistant to radiation-induced killing compared to aerobic cells. Recent studies show that hypoxia may have a profound impact on malignant progression and on responsiveness to therapy. Numerous studies on tumor oxygen tension ($pO_2$) measurements have been conducted in recent years using a variety of methods, such as microelectrodes, optical reflectance, EPR, or MRI. Although the latter one offers advantage of facilitating repeated measurements of $pO_2$ noninvasively, magnets are large and the methods not readily portable. A versatile method for monitoring intra-tumor oxygenation rapidly and non-invasively is therefore desirable for tumor treatment planning and prognosis.

Significant investigations in both laboratory and clinical settings using NIRS have been conducted for non-invasive, quantitative measurements and imaging of tissue oxygenation of brain and muscle *in vivo*. While NIR techniques have been used extensively in conjunction with cryospectrophotometry to investigate tumor blood vessel oxygenation in biopsy, only few recent reports[1] have been published on using the techniques for monitoring tumor oxygenation *in vivo*. Accurate quantification of tumor oxygenation using the NIR approach is complicated due to considerable heterogeneity and limited sizes of tumors.

The importance of angiogenesis for the growth of solid tumors is well recognized, and the field of "angiogenesis research" has spanned almost three decades. It does not occur under most conditions, but it is an inevitable process for tumors to grow and to spread. After a nest of cancer cells grows to 1-2 mm diameter, the oxygen and nutrient supply must develop for further expansion. Recent development for fighting cancer includes inhibiting new vessel formation and break up of the existing network of abnormal capillaries that feed the cancerous mass by using antiangiogenic drugs, or angiogenesis inhibitors. Liu et al previously showed that the NIR spectroscopy essentially measures the signals from small blood vessels, i.e., the capillary bed, in organs.[2] The technique could thus be a useful tool for monitoring angiogenesis and antiangiogenic therapy.

The goal of this paper is two fold. One is to present the NIR technique as a real-time, non-invasive means for monitoring changes in [$HbO_2$], [Hb], and $SO_2$ in the vascular bed of breast and prostate tumors in response to respiratory challenge. This technique can be a key to better tumor therapy planning and tumor prognosis. The second part is to investigate the possibility of using the NIR technique as a monitoring tool for studying tumor angiogenesis.

## 2. Materials and Methods

Animal Model

Dunning prostate adenocarcinoma R3327-AT1 was implanted in adult male Copenhagen rats and NF13762 breast tumor in female Fisher rats. The tumors were grown in pedicles on the forebacks of the rats until they were

approximately 2 cm in diameter. Rats were anesthetized with 200 µl ketamine hydrochloride (100 mg/ml) and maintained under general gaseous anesthesia with 33 % inhaled $O_2$ [0.3 $dm^3$/min $O_2$, 0.6 $dm^3$/min $N_2O$, and 0.5% methoxyflurane] through a mask placed over the mouth and nose. Body temperature was maintained by a warm water blanket. A fiber optic pulse oximeter was placed on the hind foot to monitor arterial oxygenation ($A_{SO2}$) and a fiber optic probe was inserted rectally to measure temperature. Inhaled gas was alternated between 33% oxygen and carbogen (95% oxygen, 5% carbon dioxide).

NIR Instrument and Hemoglobin Concentration Calculation

We used a homodyne frequency-domain photon migration system[3] able to determine amplitude and phase changes of light passing through tumors. In this setup, an RF source modulates the light from two laser diodes (wavelengths 758 nm and 782 nm) at 140 MHz. The light passes through fiber optic cables, is transmitted through the tumor tissue, and is collected by a second fiber bundle. The light is then detected by a PMT and is demodulated with an in-phase and quadrature (IQ) demodulator chip into I and Q components. Once these components are put through a low pass filter, they can be used to calculate amplitude and phase changes caused by the tumor. But given the tumor's small size and large spatial heterogeneity, it is very difficult to obtain absolute quantification accurately using conventional algorithms. Instead, based on modified Beer-Lambert's law, we can use the amplitude of the light transmitted through the tumor to calculate concentration changes in $HbO_2$, Hb, and $Hb_t$ of the tumor caused by respiratory intervention. Using the approach suggested by Delpy et al, we can obtain $\Delta[Hb]_{total}$ and $\Delta[HbO_2]$ - $\Delta[Hb]$ from two NIR wavelength measurement. For simplicity, we assume DPF to be 1 in our calculations. Such a simplification does not change the dynamic behavior of tumor $HbO_2$ concentration under respiratory intervention.

Theory for Tumor Hemo-Perfusion Calculations

In general, the Fick principle may be stated as follows: the rate of change of tracer concentration in a regional area of an organ equals the rate at which the tracer is transported to the organ in the arterial circulation minus the rate at which it is carried away into the venous drainage, i.e.,

$$\frac{dC_t}{dt} = f(C_a - C_v) \qquad (1)$$

where f is the tissue blood flow (or perfusion), $C_t$ is the tracer concentration in tissue, and $C_a$ and $C_v$ are the time-varying tracer concentrations in the arterial input and venous drainage. $C_a$ can be measured from a peripheral artery, but $C_v$ is relatively difficult to obtain regionally. Therefore, a brain-blood partition coefficient was developed by Kety as $\lambda = C_t/C_v$, and eq. (1) becomes[4]

$$\frac{dC_t}{dt} = f(C_a - \frac{C_t}{\lambda}). \qquad (2)$$

In response to respiratory intervention, a change occurs in arterial $O_2$ saturation, and the resulting increase in arterial $HbO_2$ concentration ($\Delta HbO_2^{artery}$) can be considered as an intravascular tracer. Our NIR instrument is able to detect an increase in capillary $HbO_2$ concentration ($\Delta HbO_2^{capillary}$). Following Kety's method and assuming that excessive changes in dissolved $O_2$ are negligible, we can have

$$\frac{d}{dt}(\Delta HbO_2^{capillary}) = f(\Delta HbO_2^{artery} - \frac{\Delta HbO_2^{capillary}}{\gamma}). \qquad (3)$$

where f still represents blood flow (or perfusion), and $\gamma$ is defined as a capillary-vein partition coefficient of the tumor and equal to $\gamma = (\Delta HbO_2^{capillary})/(\Delta HbO_2^{vein})$. Since the change of $HbO_2$ in artery is much faster than that in capillary bed, it is reasonable to simplify $\Delta HbO_2^{artery}$ to be the following condition:

$$\Delta HbO_2^{artery} = 0 \quad \text{when } T < 0$$
$$= \text{constant.} \quad \text{when } T \geq 0$$

where T=0 is the starting time for respiratory intervention tracer administration. Then solving eq. (3) leads to

$$\Delta HbO_2^{capillary}(T) = \gamma \times const. \times (1 - e^{-fT/\gamma}) = const. \times (1 - e^{-fT/\gamma}) \qquad (4)$$

Notice that the exponential term in eq. (4) has a time constant of $\gamma/f$, which can be determined from our experimental data. Although our current system allows us to quantify only the product of $\gamma/f$, from it we can still obtain important information on blood perfusion of the tumor. a large time constant represents a slow blood perfusion and a large capillary-vein partition coefficient, while a small time constant indicates a fast blood perfusion and a small capillary-vein partition coefficient. Coexistence of two time constants reveals two mechanisms of blood perfusion and two capillary-vein partition coefficients in tumors.

## 3. Results

Figure 1(a) was obtained from a large prostate tumor with a volume of 10.8 $cm^3$, and the source detector separation was 2.5 cm. The figure shows relative changes in total hemoglobin concentration ($\Delta Hb_{total}$), in oxygenated hemoglobin concentration ($\Delta HbO_2$), and absolute values of arterial hemoglobin saturation ($S_aO_2$). It can be seen that at time≅ 110 minute, $\Delta Hb_{total}$ changes very little in responding to a respiratory change from 33% $O_2$ to Carbogen, whereas $\Delta HbO_2$ displays a gradual increase throughout the period of carbogen inhalation. Since $\Delta HbO_{total}\cong 0$, in this case, $\Delta HbO_2$ - $\Delta Hb$ represents $2\Delta HbO_2$. In comparison to the increase in $HbO_2$, $S_aO_2$ exhibited much faster response after the inhaling gas was switched to carbogen. If we fit eq. (4) to the rising part of $\Delta HbO_2$, as shown in Figure 1(b), we can obtain a time constant of 9.4 minutes (with an uncertainty of 0.8 minute); figure 1(b) shows the fitted curve with the experimental data.

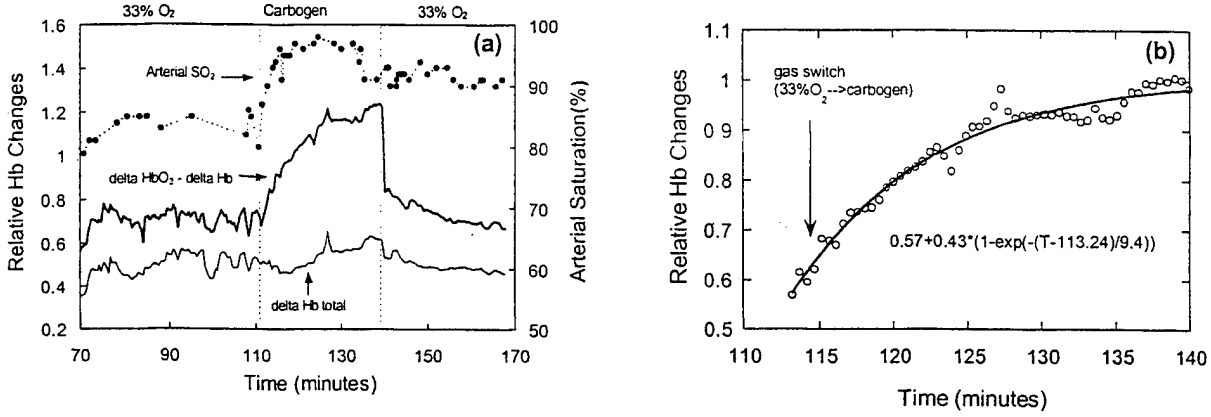


**Figure 1.** Results shown in (a) were taken with the NIR instrument from a large rat prostate tumor while the breathing gas for the rat was switched between 33% $O_2$ and carbogen. The darker solid curve is for $\Delta HbO_2$-$\Delta Hb$, the lighter solid curve is for $\Delta Hb_{total}$, and the dashed curve with solid circles is for arterial saturation. The unit for $\Delta HbO_2$-$\Delta Hb$ and $\Delta Hb_{total}$ are mM, assuming DPF to be 1 for simplicity. The solid curve shown in (b) is a best fit to $\Delta HbO_2$-$\Delta Hb$ data at the rising portion.

In some cases, generally for smaller tumors, we sometimes observed two exponential components with a small and large time constant, indicating fast and slow changes in hemoglobin concentration. Another set of data (not shown) was obtained from a 4.5 $cm^3$ breast tumor with a source-detector separation of 1.8 cm. In this case, the arterial Hb saturation had a relatively rapid change when the inhaled gas was switched from 33% $O_2$ to carbogen. Similarly to the case shown in Fig. 1, $\Delta Hb_{total}$ did not change much, as expected. But the data shows clearly that there was a sharp rise in $\Delta HbO_2$ followed by a slow/gradual increase throughout the entire period of gas inhalation of ~25 minutes. After switching the gas back to the baseline (33% $O_2$), $\Delta HbO_2$ went back to the baseline gradually. The corresponding fitted curve reveals that a small and large time constant of 0.47±0.03 minute and 23.8±1.8 minutes are obtained, respectively, for fast and slow dynamic changes in tumor $HbO_2$ concentration.

## 4. Summary

Using NIR spectroscopy, we have measured relative changes in hemoglobin concentration and saturation in tumors in response to respiratory intervention. In this study, we demonstrated the ability to detect dynamic changes in $HbO_2$ in the vascular bed of rat breast and prostate tumors. Furthermore, we found that the dynamic changes of tumor oxygenation can be modeled by either one exponential term with a slow time constant or by two exponential terms with a fast and slow time constant. This suggests that there may be two vascular mechanisms in the tumor "seen" by the NIR spectroscopy measurement. Moreover, it appears the NIR spectroscopy can provide insight into tumor angiogenesis.

## 5. References

[1] E. L. Hull, D. L. Conover, and T. H. Foster, "Carbogen-induced changes in rat mammary tumour oxygenation reported by near infrared spectroscopy," Br. J. Cancer **79**, 1709-1716, (1999).

[2] H. Liu, B. Chance, A. H. Hielscher, S. L. Jacques, and F. K. Tittel, "Influence of blood vessels on the measurement of hemoglobin oxygenation as determined by time-resolved reflectance spectroscopy," Med. Phys. **22**(8), 1209-1217 (1995).

[3] Y.Yunsong, H. Liu, X. Li, B. Chance, "Low-cost frequency-domain photon migration instrument for tissue spectroscopy, oximetry, and imaging." *Opt. Eng.* **36**(5), 1562-1569 (1997).

[4] S.S. Kety, "The theory and applications of the exchange of inert gas at the lungs and tissue," Pharmacol. Rev. **3**, 1-41 (1951).

# DIVERSE APPROACHES TO MONITORING OXYGEN DYNAMICS IN RAT BREAST AND PROSTATE TUMORS

**Dawen Zhao, Yulin Song, Hanli Liu[+], Anca Constantinescu, Eric W. Hahn, and Ralph P. Mason**, Department of Radiology, UT Southwestern, Dallas, TX 75390 and [+]BME, UT-Arlington, TX 76109

**Summary**: The increasing evidence that direct measurement of $pO_2$ in patient's tumors has prognostic value provides strong impetus to develop robust methods for measuring tumor oxygen dynamics. Using the *FREDOM* NMR approach (Fluorocarbon Relaxometry using Echo planar imaging for Dynamic Oxygen Mapping) we are able to examine regional variations in tumor $pO_2$ in response to interventions. To obtain a more complete view of vascular dynamics, we now incorporate Near Infrared (NIR) measurements of hemoglobin concentration [Hb] and saturation ($sHbO_2$) in tumors.

**Methods:** Dunning prostate R3327 (AT1 and HI) and 13762NF breast tumors were implanted in pedicles (1) on the foreback of syngeneic Copenhagen and Fisher rats, respectively. Once tumors reached ~ 1 cm diameter, rats were anesthetized (generally, 1.2% isoflurane in air) and examined using a homodyne dual wavelength NIR device in transmission mode, to monitor relative $\Delta$[Hb] and $\Delta sHbO_2$ (2). A pulse oximeter simultaneously provided $s_aO_2$ in the leg. Variations in these values were observed with respect to respiratory challenge and vasoactive drugs (oxygen, carbogen and hydralazine). The following day the same tumors were interrogated by $^{19}F$ NMR EPI with respect to the same interventions (3). Hexafluorobenzene (45 µl) was injected directly into both central and peripheral regions of the tumors using a fine sharp needle (32G) and $pO_2$ maps determined with 8 minute time resolution and 1.25 mm in plane spatial resolution using pulse burst saturation NMR echo planar imaging relaxometry (*FREDOM*). In some instances, additional studies were performed using oxygen microelectrodes and the OxyLite™ optical fiber sensor.

**Results:** As expected, the fastest changes in oxygenation in response to respiratory challenge occurred in the arterial saturation ($s_aO_2$) in the leg with a typical time constant $\tau$<20 s (Fig. 1). Small tumors often showed biphasic vascular response with a rapid $\Delta HbO_2$ component ($\tau$<30 s) approaching that of $s_aO_2$ and a more sluggish component increasing over 20 mins. The slow component alone was typical of larger tumors. Changes in $\Delta$[Hb] indicated that vascular volume was also modulated. Changes in tumor tissue $pO_2$ were highly variable. Well oxygenated regions responded significantly with a time constant in the range $\tau$ = 10 – 30 mins. The response of initially poorly oxygenated regions was highly tumor dependent. AT1 tumor regions initially <10 torr showed little response, whereas most regions in the slower growing HI responded, significantly reducing the hypoxic fraction with oxygen or carbogen (see accompanying abstract by Zhao *et al.*). Although the breast tumors grow rapidly, hypoxic regions were also found to respond in these tumors (Fig. 2). Both oxygen microelectrodes and the OxyLite™ showed changes in $pO_2$, which were comparable to the *FREDOM* results, in terms of both rates and magnitude of change.

**Conclusions:** The *FREDOM* approach allows dynamic changes in regional tumor $pO_2$ to be followed in diverse tumors. These data indicate that regional response to respiratory challenge depends not only on the baseline tumor oxygenation, but also the degree of tumor differentiation. By adding NIR, we are additionally able to probe changes in vascular volume and hemoglobin oxygen saturation. These preliminary data were obtained sequentially, but

simultaneous NIR and *FREDOM* investigations are imminently feasible to provide deeper insight into tumor vascular phenomena. We believe the complimentary applications of the two techniques will provide deeper insight into tumor physiology and mechanisms of modulating tumor physiology for therapeutic enhancement.

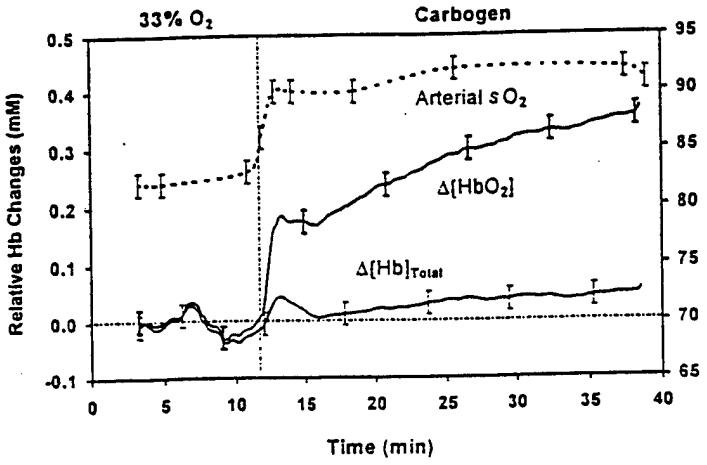


**Fig. 1** Dynamic response in $s_aO_2$, $\Delta HbO_2$, and $\Delta Hb_{Total}$ in 4.5-$cm^3$ rat breast tumor with respect to respiratory challenge observed using NIR instrument. A bi-exponential curve fit for changes in $\Delta HbO_2$ gave time constants $\tau_1$=11 s and $\tau_2$ = 27.8 mins, respectively.

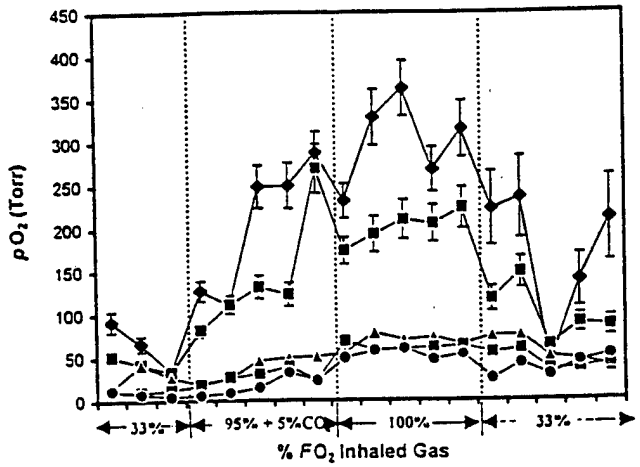


**Fig. 2** Dynamic changes in $pO_2$ measured using *FREDOM* of representative regions in a second breast tumor (3.5 $cm^3$). The local response depended strongly on initial baseline $pO_2$, both in terms of rate and magnitude (measurements at 8 min intervals).

## References


1. Hahn, E. W., Peschke, P., Mason, R. P., Babcock, E. E., and Antich, P. P. Isolated tumor growth in a surgically formed skin pedicle in the rat: A new tumor model for NMR studies., Magn. Reson. Imaging. *11:* 1007-1017, 1993.
2. Liu, H., Song, Y., Worden, K. L., Jiang, X., Constantinescu, A., and Mason, R. P. Noninvasive Investigation of Blood Oxygenation Dynamics of Tumors by Near-Infrared Spectroscopy, *Appl. Optic*, in the press 2000.
3. Mason, R. P., Constantinescu, A., Hunjan, S., Le, D., Hahn, E. W., Antich, P. P., Blum, C., and Peschke, P. Regional tumor oxygenation and measurement of dynamic changes, Radiat. Res. *152:* 239-249, 1999.



Supported by The American Cancer Society (RPG-97-116-010CCE), The Whitaker Foundation, The Department of Defense Breast Cancer Initiative BC962357 and NIH R01-CA79515 and P41-RR02584.